Fakultät für Elektrotechnik und Informationstechnik

Professur für Computational Photonics

Modeling and simulations of quantum cascade lasers for frequency comb generation

Petar Tzenov

Vollständiger Abdruck der von der Fakultät für Elektrotechnik und Informationstechnik der Technischen Universität München zur Erlangung des akademischen Grades

Doktor-Ingenieurs

genehmigten Dissertation.

Vorsitzender: Prof. Dr.-Ing. Norbert Hanik

Prüfer der Dissertation:

1. Prof. Dr.-Ing. Christian Jirauschek
2. Prof. Dr. Hans-Joachim Bungartz

Die Dissertation wurde am 19.04.2018 bei der Technischen Universität München eingereicht und durch die Fakultät für Elektrotechnik und Informationstechnik am 05.09.2018 angenommen.

I hereby declare that this thesis is entirely the result of my own work except where otherwise indicated. I have only used the resources given in the list of references.

München, March 18, 2019

Petar Tzenov

Acknowledgments

First and foremost I would like to thank my family for their endless support, who have always been there for me. Specifically, I want to thank Woobinn for always being on my side with her infinite love and patience, and also for sacrificing so much for me. I would like to thank my Parents for their love and the solid foundations which they have laid out for me, giving me so many great opportunities in life. Last, but not least, I would like to thank my Sister, for many things, but mostly for being so strong through the difficult times we had, taking many of the "blows" of life upon herself to protect me (and of course for being such a great friend). I am forever indebted to you all.

I would also like to thank Professor Jirauschek for guiding me throughout the whole process. He was always ready to pass on to us his knowledge and experience, which undoubtedly made the PhD-experience not only easier, but also much more valuable. His knowledge and competence on this and many other topics never ceases to amaze me. I would also like to thank the whole Computational Photonics group: Michael, Mark and Jesus, for being such fun lab-mates, engaging in productive and interesting discussions, and sharing some of their beers with me.

Finally, big THANK YOU to the whole institute, to current and former colleagues, who made the academic environment such a productive and fun place to be, especially in the framework of those "mostly scientific" conferences.

Abstract

English

Quantum cascade lasers (QCLs) are unipolar, semiconductor devices emitting coherent radiation in the underdeveloped far- and mid-infrared portions of the electromagnetic spectrum. QCLs achieve lasing in those frequencies by "quantum engineering" of the optical transition in epitaxially grown quantum well heterostructures. Sub-nano scale control over the quantum well thickness ensures that the available conduction band states take only discrete energy values, where the energy spacing between the two lasing levels determines the emitted frequency.

The ever increasing complexity of chip-scale devices necessitates correspondingly sophisticated theoretical modeling. In the last two decades, we have seen a steady progress in the design of quantum cascade lasers, resulting in devices with high electrical stability, emitting spectra with various desirable characteristics such as high-power single mode emission, short pulse and frequency comb generation. By contrast, it seems that theoretical or simulation models have struggled to keep up with the pace of experimental progress in the field. For example, to date most theoretical papers reduce the QCL complexity to only two energy levels which, albeit sometimes being able to give qualitative agreement with experiment, is often insufficient to achieve quantitative accuracy or explain some of the relevant physics. In addition, QCLs exhibit highly non-trivial dynamics, stemming from the intricate interplay of various coherent and incoherent processes, nonlinear light-matter interactions and complicated electro-optical phenomena, the understanding of which requires sophisticated theoretical models, unfortunately well beyond the analytically solvable such.

To this end, the thesis attempts to outline in greater detail coherent light-matter interaction models, suitable for transient analysis of terahertz (THz) quantum cascade lasers for frequency comb generation. Therefore, there are two main focal points. First, this is the development of sufficiently accurate theoretical models and corresponding algorithms for their solution. And second is the usage of these models to investigate the physics behind frequency comb generation in two main modes of QCL operation, i.e. free running and actively/passively mode locked regime.

The thesis begins with a very brief and informal introduction to lasers in general and quantum cascade lasers in particular, before presenting the essential theory on which all subsequent simulations are based. The resulting Maxwell/density matrix model is then discretized and numerical algorithms for its solution are presented, together with theoretical and numerical analysis of their accuracy (consistency) and stability. Next, follow the essential parts of the thesis, and namely the usage of the outlined models for time-domain simulations of QCLs for frequency comb generation. In that context, two different approaches to the production of frequency combs are considered, first by free running devices, where the main mode

proliferation mechanisms are a consequence of high order nonlinearities in the device, and secondly by active and passive mode locking, where comb generation is equivalent to the production of a periodic train of pulses in the time domain.

Several achievements can be mentioned. For example, this is the extension of the traditional two level Maxwell-Bloch model to multiple level such and subsequent simulations of free running THz QCLs. Importantly, the new model includes coherent tunneling between the injector and upper laser level of QCLs, and its simulation is shown to deliver results in very good agreement with available experiment, both for data in time and Fourier domains. Next, the same model is utilized to emulate laboratory experiments by numerical such, in order to characterize the multimode dynamics of longitudinal optical phonon terahertz QCLs, which results in several important insights about the behavior of these devices. Additionally, the model is adapted to simulate ultrashort pulse generation in the THz with specific emphasis on passive mode locking via a fast saturable absorber. It is also shown how one can exploit the natural "multi-pulse" regime of QCL operation to obtain very stable second and higher harmonic pulse emission. To date, no passively mode locked QCL device has been presented and it remains to be seen if this theoretical possibility could be realized experimentally. The thesis also outlines the beginnings of an extended model, suitable for self-consistent microwave-optical simulations, capturing the interaction dynamics between the intracavity QCL light and the propagating current/voltage along the device. Finally, as a small detour from the main topic, the author also investigates the possibility to engineer metamaterials for slowing down terahertz light, based on the so called tunneling induced transparency effect.

Deutsch

Quantenkaskadenlaser (QKL) sind unipolare Halbleiterlaser, die kohärente Strahlung im Terahertz- (THz) und im mittleren Infrarotbereich emittieren. Diese Bereiche gehören zu den technisch wenig erschlossenen Teilen des elektromagnetischen Spektrums. In QKL werden diese Frequenzbereiche mit Hilfe von Quantentopf-Heterostrukturen erreicht, die durch Epitaxieverfahren hergestellt werden. Mit diesen Verfahren ist es möglich, Quantentöpfe im Sub-Nanometerbereich herzustellen, die die verfügbaren Leitungsbandzustände auf diskrete Energiewerte reduzieren. Der Abstand zwischen zwei Energiewerten, die durch passende Konstruktion als Laserniveaus bestimmt werden, bestimmt dann die emittierte Frequenz.

Die ständig zunehmende Komplexität von Strukturen im Nanometerbereich erfordert eine entsprechend ausgereifte theoretische Modellierung. In den letzten zwei Jahrzehnten konnte man einen stetigen Fortschritt beim Entwurf von Quantenkaskadenlasern beobachten, der zu Strukturen mit hoher elektrischer Stabilität sowie mit verschiedenen wünschenswerten Betriebsarten – wie zum Beispiel Hochleistungsemission im Dauerstrichbetrieb, Kurzimpuls- oder Frequenzkammbetrieb - führte. Im Gegensatz dazu scheint die Entwicklung von theoretischen oder Simulationsmodellen Schwierigkeiten zu haben, mit dem Tempo des experimentellen Fortschritts Schritt zu halten. So reduzieren etwa die meisten theoretischen Arbeiten die Komplexität, in dem nur zwei Energieniveaus betrachtet werden. Obwohl dieser Ansatz manchmal eine qualitative Übereinstimmung mit dem Experiment liefern kann, ist er oft nicht ausreichend, um eine quantitative Genauigkeit zu erreichen oder die zugrunde liegende relevante Physik

zu erklären. Darüber hinaus weisen QKL eine nicht-triviale Dynamik auf, die aus dem komplizierten Zusammenspiel verschiedener kohärenter und inkohärenter Prozesse, nichtlinearer Licht-Materie-Wechselwirkungen und elektrooptischer Phänomene resultiert. Deren Verständnis erfordert aufwändige theoretische Modelle, die leider in der Regel nicht analytisch lösbar sind.

Zu diesem Zweck wird versucht, kohärente Licht-Materie-Wechselwirkungsmodelle, die für die transiente Analyse von Terahertz-QKL für den Frequenzkammbetrieb geeignet sind, näher zu beschreiben. Dabei gibt es zwei Hauptschwerpunkte. Einerseits werden erweiterte theoretische Modelle und entsprechende Algorithmen zu deren Lösung entwickelt, andererseits werden diese Modelle verwendet, um die physikalischen Grundlagen der Frequenzkammgenerierung zu untersuchen, wobei auf zwei Hauptbetriebsarten der QKL – freilaufender Betrieb und aktive/passive Modenkopplung – eingegangen wird.

Diese Arbeit beginnt mit einer sehr kurzen und informellen Einführung in die Grundlagen von Laser im Allgemeinen und Quantenkaskadenlaser im Speziellen, bevor die wesentliche Theorie vorgestellt wird, auf der alle nachfolgenden Simulationen basieren. Die Diskretisierung der resultierenden Maxwell/Dichtematrix-Gleichungen und die Verwendung numerischer Algorithmen für deren Lösung werden zusammen mit einer theoretischen und numerischen Analyse ihrer Genauigkeit (Konsistenz) und Stabilität präsentiert. Als Nächstes folgen die wesentlichen Teile der Arbeit, und zwar wird die Verwendung der skizzierten Modelle für dynamische Simulationen von QKL für Frequenzkammbetrieb beschrieben. In diesem Zusammenhang werden zwei unterschiedliche Ansätze zur Generierung von Frequenzkämmen betrachtet. Der erste Ansatz betrifft Strukturen im freilaufenden Betrieb, wobei die Moden des Frequenzkamms eine Folge von Nichtlinearitäten höherer Ordnung in dem Lasermedium sind. Als zweite Möglichkeit wird aktive und passive Modenkopplung verwendet, um eine periodische Folge von Impulsen im Zeitbereich zu erzeugen, was im Frequenzbereich einem Frequenzkamm entspricht.

Mehrere Ergebnisse können erwähnt werden. Zunächst wurde das traditionelle Maxwell-Bloch-Modell von zwei Niveaus auf mehrere Niveaus erweitert und für die Simulation von Terahertz-QKL im freilaufenden Betrieb angewendet. Dabei ist von Bedeutung, dass das neue Modell ein kohärentes Tunneln zwischen dem Injektorniveau und dem oberen Laserniveau von QKL berücksichtigt. Mit diesem Ansatz konnte eine gute Übereinstimmung von Simulationsergebnissen mit verfügbaren Experimenten erreicht werden, sowohl im Zeitbereich als auch im Frequenzbereich. Als nächstes wurde das gleiche Modell verwendet, um Laborexperimente numerisch zu emulieren und somit die Multimodendynamik von Longitudinal Optical Phonon Terahertz-QKL zu charakterisieren. Dies führte zu mehreren wichtigen Erkenntnissen über das Verhalten dieser Strukturen. Zusätzlich wurde das Modell so angepasst, dass die Erzeugung von ultrakurzen Pulsen im Terahertz-Bereich simuliert werden kann. Dabei wurde der Schwerpunkt auf die passive Modenkopplung mit einem schnellen sättigbaren Absorber gelegt. Ferner wird auch gezeigt, wie man den natürlichen Mehrpulsbetriebsmodus des QKL ausnutzen kann, um eine sehr stabile zweite (und höhere) harmonische Pulsemission zu erhalten. Bislang wurde kein passiv modengekoppelter QKL vorgestellt und es ist noch eine offene Frage, ob diese theoretische Möglichkeit experimentell realisiert werden könnte. Dann werden die Anfänge eines erweiterten Modells skizziert, das für selbstkonsistente Simulationen geeignet ist und die dynamische Wechselwirkung zwischen dem Licht in dem QKL-Resonator

und dem/der sich ausbreitenden Strom/Spannung im Mikrowellenbereich entlang der Struktur erfasst. Schließlich untersucht der Autor als kleinen Umweg vom Hauptthema auch die Möglichkeit, Metamaterialien zur Verlangsamung von Terahertz-Licht durch den sogenannten „tunneling induced transparency“ Effekt zu entwickeln.

Contents

1 Introduction

1.1 Foreword

As scientific knowledge progresses, designing successful experiments to directly test theoretical predictions is becoming increasingly difficult. In the field of quantum cascade laser (QCL) research, which this thesis attempts to penetrate into, this is partially so because of the practical inability to experimentally investigate some of the properties of these highly sophisticated, and also very delicate devices. A typical QCL has dimensions of several millimeters in length, and several micrometers in thickness and width, which makes them difficult and expensive to manufacture and analyze. The situation is further complicated due to the QCLs' multiple degrees of freedom, giving rise to electrical and optical instabilities. This, coupled to the fact that the fundamental processes, determining the laser performance, are quantum mechanical in nature, and despite that our abilities to manipulate matter at the minuscule scale have considerably increased over the last decade, makes the direct experimental observations of the inner workings of a QCL extremely difficult. Exactly at this frontier between theory and experiment, is where computational science and simulations are most helpful. Combining the advancement in physical theory and computational machinery, simulation scientists are able to conduct more and more comprehensive numerical experiments in all areas of science and engineering. In particular in the field of quantum cascade laser research, there is an increasing interest from the community in population dynamics, electron transport, active region design as well as emission characteristics [1–6]. Different models with varying degree of complexity are being developed, ranging from classical rate equation models, Monte-Carlo simulations, up to entirely quantum mechanical approaches based on density-matrix or non-equilibrium Green's function methods [7, 8]. Naturally, the end goal of all of this research is to improve the understanding of QCLs, or on a more practical note, to deliver cheap, robust and high quality technology to the scientific and engineering world.

What makes quantum cascade lasers so interesting? Since the radiative transitions in QCLs are based on intersubband transitions and are thus determined purely by active region engineering and not by the band gap of the used materials, QCLs are very potent sources of coherent and tunable light in the underdeveloped regions of the mid- and far-infrared portions of the electromagnetic spectrum. Having a stable laser in this frequency domain unlocks a great diversity of applications such as high precision optical spectroscopy [9, 10], telecommunications [11], explosive and other dangerous chemicals' fingerprint detection [12] and many others.

Ever since the first experimental realization of a quantum cascade laser by J. Faist and co-workers in 1994, in the next twenty-five years, there has been a surge of research activity on the topic. Recent advances include the creation of room temperature mid-infrared QCLs,

delivering devices emitting up to 3 W of optical power in the continuous-wave regime [13], the demonstrations of stable frequency combs in both spectral regions, emitted by free-running lasers [14–16], the generation of picosecond pulses with actively mode locked devices [17–19] and others, with the general tendency of shifting away from purely conceptual work towards applications. Despite these recent advances, there are still a great many challenges that the research community must overcome, especially in the field of terahertz QCLs, before this technology can mature. To this end, accurate and reliable numerical simulations of the light-matter interaction dynamics in QCLs can help the community gain a better understanding of the main processes that undermine the realization of the quantum cascade laser technology to its full potential. Thus the main tasks assumed at the onset of this thesis are two. First of all, the aim is to develop efficient and accurate carrier transport models, simultaneously treating the coherent nature of the light-matter interaction [20] as well the multi-level behavior of those laser systems. Secondly, the proposed models shall be used to investigate transient dynamics of QCLs, especially at higher operating currents, which is characterized by both stable and unstable multimode emission [21], and the gained knowledge shall be applied to understand frequency comb formation (by either free-running or mode locked devices) in QCLs. As the latter task needs to allow for the inclusion of non-linear optical processes, such as four-wave mixing (FWM), difference frequency generation (DFG) etc., this necessitates that the undertaken approach resolves the optical field in both space and time. Additionally, to minimize the exposure to estimation error, and to increase the generality of the proposed model, the simulation approach shall be self-consistent, in the sense that it depends on no (or at least very few) empirically chosen parameters.

To address these goals, this thesis has undertaken a multi-domain simulation approach, combining stochastic carrier transport simulations such as the ensemble Monte-Carlo (EMC) method, with semi-classical light-matter interaction models, based on a formalism coupling the quantum mechanical time evolution of the system with Maxwell's equations. While EMC simulations are comprehensive enough to treat hopping transport due to various perturbation potentials, they are too computationally demanding in order to discretize the system in space and time, and thus capture field propagation effects. On the other hand, the semi-classical model treats only a portion of the interactions quantum-mechanically, and as such is rather "light-weight" for simulation purposes, and thus allows for full discretization of the system. The coupling between those two worlds is done via the Lindblad formalism and is discussed in Chapter 2. Importantly, the combined approach leverages the advantages of each individual model and allows for self-consistent and efficient light-matter interaction simulations, capturing hopping transport, coherent interactions, propagation effects (such as spatial hole burning), dispersion, optical nonlinearities etc., and as such has the potential to deliver results with an increased quantitative accuracy.

The general organization of the thesis is the following: in the remainder of this chapter, a brief introduction on laser fundamentals in general, and quantum cascade lasers in particular is given. Next, Chapter 2 and Chapter 3 provide us with the more detailed theoretical foundations and numerical algorithms, needed for the understanding and simulation of the employed models. The second part of this thesis focuses on the main achievements by the author. Namely, Chapter 4 analyzes transient dynamics in free-running terahertz quantum cascade

lasers for frequency comb generation. Chapter 5 is concerned with the possibility of ultrashort THz pulse generation via various forms of (active and passive) mode locking of the same type of devices. Finally, Chapter 6 concludes with a small detour from the main topic of the thesis and discusses the possibility of slowing down THz light with the tunneling induced transparency effect.

The full work is based on four peer-reviewed publications, in which the author of this thesis has been the main contributor. For completeness, the titles of the publications together with their short abstracts are included below.

1 Introduction

Time domain modeling of terahertz quantum cascade lasers for frequency comb generation

Petar Tzenov[1], David Burghoff[2], Qing Hu[2], and Christian Jirauschek[1]

[1] *Institute for Nanoelectronics, Technical University of Munich, D-80333 Munich, Germany*

[2] *Department of Electrical Engineering and Computer Science, Research Laboratory of Electronics, Massachusetts Institute of Technology, Cambridge, Massachusetts 02139, USA*

Abstract: The generation of frequency combs in the mid-infrared and terahertz regimes from compact and potentially cheap sources could have a strong impact on spectroscopy, as many molecules have their roto-vibrational bands in this spectral range. Thus, quantum cascade lasers (QCLs) are the perfect candidates for comb generation in these portions of the electromagnetic spectrum. Here we present a theoretical model based on a full numerical solution of Maxwell- Bloch equations suitable for the simulation of such devices. We show that our approach captures the intricate interplay between four wave mixing, spatial hole burning, coherent tunneling and chromatic dispersion which are present in free-running QCLs. We investigate the premises for the generation of QCL based terahertz combs. The simulated comb spectrum is in good agreement with experiment, and also the observed temporal pulse switching between high and low frequency components is reproduced. Furthermore, non-comb operation resulting in a complex multimode dynamics is investigated.

Publication Journal	Optics Express **24**.20:23232-23247
Date of submission	4 Aug 2016
Date of publication	27 Sep 2016
URL	https://doi.org/10.1364/OE.24.023232

Slow terahertz light via resonant tunneling induced transparency in quantum well heterostructures

Petar Tzenov, and Christian Jirauschek
Institute for Nanoelectronics, Technical University of Munich, D-80333 Munich, Germany

Abstract: We present a theoretical and computational investigation of the possibility of achieving slow terahertz light by exploiting the tunneling induced transparency (TIT) effect in suitably engineered quantum well heterostructure devices. We design such a meta-material and show how TIT could lead to large values of the group refractive index, unfortunately at the cost of strong field attenuation due to decoherence. As a suitable alternative, we propose a grating, consisting of a buffer and a quantum cascade amplifier regions, arranged in such a way as to achieve slow light and simultaneously compensate for the large signal losses. Our calculations show that a binary message could be reliably transmitted through this system, with non-critical reduction of the signal to noise ratio, as we achieve a slow-down factor of more than 70.

Publication Journal	Proceedings of SPIE **10226**:1022603
Date of submission	26 September 2016
Date of publication	5 January 2017
URL	https://doi.org/10.1117/12.2262367

1 Introduction

Analysis of operating regimes of terahertz quantum cascade laser frequency combs

Petar Tzenov[1], David Burghoff[2], Qing Hu[2], and Christian Jirauschek[1]

[1] *Institute for Nanoelectronics, Technical University of Munich, D-80333 Munich, Germany*

[2] *Department of Electrical Engineering and Computer Science, Research Laboratory of Electronics, Massachusetts Institute of Technology, Cambridge, Massachusetts 02139, USA*

Abstract: In recent years, quantum cascade lasers (QCLs) have shown tremendous potential for the generation of frequency combs in the mid-infrared and terahertz portions of the electromagnetic spectrum. The research community has experienced success both in the theoretical understanding and experimental realization of QCL devices, capable of generating stable and broadband frequency combs. Specifically, it has been pointed out that four wave mixing (FWM) is the main comb formation process and group velocity dispersion (GVD) is the main comb-degradation mechanism. As a consequence, special dispersion compensation techniques have been employed, in order to suppress the latter and simultaneously enhance the former processes. Here, we perform a detailed computational analysis of FWM, GVD, and spatial hole burning (SHB), all known to play a role in QCLs, and show that SHB has a considerable impact on whether the device will operate as a comb or not. We therefore conclude that for a successful implementation of a quantum cascade laser frequency comb, one would need to address this effect as well.

Publication Journal	IEEE Transactions on Terahertz Science and Technology **7**.4:351-359
Date of submission	9 January 2017
Date of publication	26 April 2017
URL	https://doi.org/10.1109/TTHZ.2017.2693822

Passive and hybrid mode locking in multi-section terahertz quantum cascade lasers

Petar Tzenov[1], Ihar Babushkin,[2,3], Rostislav Arkhipov[4,5], Mikhail Arkhipov[4], Nikolay Rosanov[5,6,7], Uwe Morgner[2], and Christian Jirauschek[1]

[1] *Institute for Nanoelectronics, Technical University of Munich, D-80333 Munich, Germany*

[2] *Institute of Quantum Optics, Leibniz University Hannover, 30167 Hannover, Germany*

[3] *Max Born Institute, 12489 Berlin, Germany*

[4] *St. Petersburg State University, 199034 St. Petersburg, Russia*

[5] *ITMO University, 197101 St. Petersburg, Russia*

[6] *Vavilov State Optical Institute, Kadetskaya Liniya v.o. 14/2, St Petersburg 199053, Russia*

[7] *Ioffe Physical Technical Institute, Politekhnicheskaya str. 26, St Petersburg 194021, Russia*

Abstract: It is believed that passive mode locking is virtually impossible in quantum cascade lasers (QCLs) because of too fast carrier relaxation time. Here, we revisit this possibility and theoretically show that stable mode locking and pulse durations in the few cycle regime at terahertz (THz) frequencies are possible in suitably engineered bound-to-continuum QCLs. We achieve this by utilizing a multi-section cavity geometry with alternating gain and absorber sections. The critical ingredients are the very strong coupling of the absorber to both field and environment as well as a fast absorber carrier recovery dynamics. Under these conditions, even if the gain relaxation time is several times faster than the cavity round trip time, generation of few-cycle pulses is feasible. We investigate three different approaches for ultrashort pulse generation via THz quantum cascade lasers, namely passive, hybrid and colliding pulse mode locking.

Publication Journal	New Journal of Physics **20**.5:053055
Date of submission	24 November 2017
Date of publication	24 May 2018
URL	http://stacks.iop.org/1367-2630/20/i=5/a=053055

1.2 Laser fundamentals

The LASER, or Light Amplification by Stimulated Emission of Radiation, is probably one of the most important scientific discoveries of the twentieth century. This technology has penetrated our daily lives with unforeseen speed, and has found applications in a wide range of fields such as electronics, medical procedures, astronomy, national security and defense, natural and applied sciences and many others, to name a few.

So what is a laser? Simply put, a laser is a device that emits coherent and collimated electromagnetic radiation ranging from the ultraviolet, through the visible, up to the far-infrared electromagnetic spectrum [22]. Depending on the area of application, lasers come in wide a variety of sizes, performance characteristics, price ranges etc., from the everyday diode laser-pointers used in classrooms to powerful industrial gas lasers used in medicine and industry. All those devices, however, are based on one and the same fundamental physical principle - that of stimulated emission.

Stimulated emission is a very interesting phenomenon. It is intuitively described as a "forced" or stimulated de-excitation (i.e. transition from a higher to a lower energetic state) of a charge carrier due to its interaction with an electromagnetic (EM) field. Such a transition occurs when the incoming electromagnetic wave has energy equal to or close to the transition energy of the carrier particle. Due to energy conservation laws, this quantum process is accompanied by emission of a photon, or equivalently an electromagnetic wave, with the same momentum, polarization and phase as the incoming EM field. Quite symmetrically, if a certain material can be forced to emit energy due to interaction with radiation, then the opposite situation should also be possible, i.e. the same material should be able to absorb some of the energy of the field. Indeed, such a process occurs and it is called absorption (for the obvious reasons).

Now, armed with as little as few lines of understanding about stimulated emission and absorption, we are ready to, at least conceptually, design our first laser. First, take a material that can efficiently interact with light in the frequency domain we are interested at. Then, we also need a mechanism to ensure that the overall number of stimulated emission events is larger than that of absorption (or any other lossy processes), in order for the newly generated photons to be more than the lost ones, i.e. to achieve net amplification of the original field. Without proper understanding of those other lossy processes, we will be designing terrible lasers, but in order to illustrate a concept let us assume that the material we have chosen can have its charge carriers in one of two energy levels only, and the only excitation mechanism is absorption and also the only de-excitation mechanism is stimulated emission. Then, it is evident that if we wish to amplify our original EM signal, we will need to ensure that on average we have more charge de-excitations, i.e. stimulated emission processes, than charge excitations. Since by necessity, the net optical scattering rate ought to depend on the difference in carrier density in both levels, we thus need to design our system so that it has more charges in the upper energy state than in the lower one. Such a situation is called population inversion, and is evidently a non-equilibrium state of matter. In that sense population inversion can rarely be found in nature, even though there are some such examples [23, 24], which means that appropriate "material engineering" will be necessary in order to achieve our goal.

Next, let us now see how we can construct a very primitive laser. As we mentioned we need a lasing/interacting material, usually called an active region, which we need to make sure that it is in the state of population inversion. We do so by artificially "pumping" more charge carriers into the upper energetic state than into the lower one. In practice this pumping mechanism, or pumping scheme, can be anything from driving electrical current into the active medium, forcing population inversion with intense external radiation, or populating the medium with highly energetic "particles", which in their collisions with the constituents of our active region, drive the system out of equilibrium.

Once we have gotten our population inversion, we also need a way to efficiently direct the laser beam, or the electromagnetic field we wish to amplify, in and out of our active region. This is achieved via the so called optical cavity, which is there to confine the input/generated electric field and maximize its interaction with the amplifier. Summarizing, most lasers consist of two components - the gain medium and a feedback mechanism, with the latter usually implemented by partially reflecting mirrors. A schematic of two of the most common designs, the so called Fabry-Perot and the ring-type cavity, are depicted in Fig. 1.1.

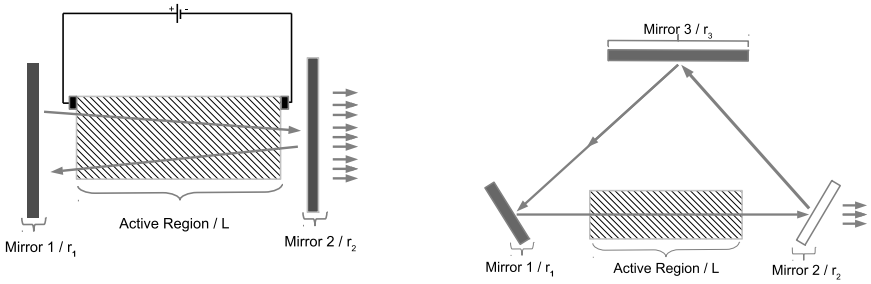

Figure 1.1 Fabry-Perot (left) and ring-type (right) laser cavity schematics. The active region, together with the mirror setup, is referred to as optical cavity.

In practice, based on the choice of lasing material, lasers can be broadly divided into the following categories:

- Semiconductor lasers - the active region is made of different semiconductive materials, such as GaAs, AlGaAs etc. (typically III-V semiconductors due to their superior properties), where the most common pumping mechanism is via current injection into the structure. Prominent examples are the diode laser and also the quantum cascade laser. The lasing action occurs due to radiative recombination of electrons from the conduction band with holes of the valence band (in diode lasers), the so called interband transitions, or intersubband transitions of electrons between states in the conduction band (as in QCLs) or holes in the valence band (not realized conceptually).

- Solid state lasers - the active region is a solid, the so called host material, usually a glass, in the form of a rod or optical fiber, or a crystal, which is then doped with charge carriers, usually metallic ions. The main pumping mechanism is optical, i.e. illumination with an external light source, and common examples are the Nd:YAG, the Ruby laser,

and the Ti:Sapphire laser, which is very important in the context of pulse and frequency comb generation. The lasing action occurs due to radiative electron decay into lower, more stable energy levels.

- Dye lasers - the active region consists of a liquid solution of organic dye, containing molecules able to fluoresce. The pumping mechanism is optical illumination, as in solid state lasers, with the lasing action occurring due to fluorescence.
- Gas lasers - the active region is in gaseous state and the pumping mechanism is gas discharge current. Prominent examples are the "HeNe" or helium-neon laser or the CO_2 laser. Here the utilized charge carriers are not necessarily electrons, where for the CO_2 laser, for instance, lasing occurs due to relaxation of vibrationally excited CO_2 molecules to a lower vibrational level.
- Other lasers such as excimer lasers, chemical lasers etc., with a plethora of different pumping mechanisms and optical cavity designs.

For a very thorough and pedagogical introduction to lasers and laser technology refer to [22, 25].

1.3 Quantum cascade lasers

As mentioned above, in traditional semiconductor lasers the lasing transition occurs due to recombination of electrons from the conduction band with holes from the valence band of the material. Those types of lasers, for e.g. the diode laser, are very cheap compact sources of coherent radiation and are intensively used for a wide range of applications. A schematic illustration of a typical semiconductor p-n junction diode laser is depicted in Fig. 1.2.

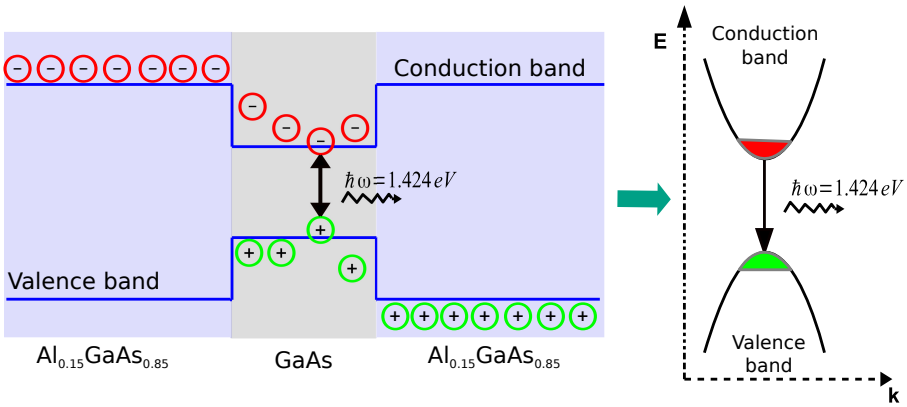

Figure 1.2 (Left) One GaAs layer sandwiched between two $Al_{0.15}GaAs_{0.85}$ layers to form a conduction/valence band well, trapping electrons/holes respectively. The transition of a single electron from the conduction band to a vacancy in the valence band is accompanied by emission of a photon with approximately the same energy as the band gap of the material. (Right) Energy-band diagram illustration of the transition. GaAs band gap value taken from [26].

As it can be seen from Fig. 1.2, the emitted radiation's frequency is determined by the band gap of the materials involved. This means that we cannot, at least at this stage, hope to

build such semiconductor lasers operating at any desired frequency. Due to the lack of low band gap semiconductors, it turns out that there is a frequency range very poorly covered by conventional semiconductor lasers [27]. These are the mid- to far-infrared wavelengths, defined to encapsulate frequencies between (10-60) THz for the former, and (0.3-10) THz for the latter. Nevertheless, coherent light emitters and detectors in that range are desired for spectroscopy and sensing applications, since many molecules have roto-vibrational bands in that region [9, 28–30].

This is where QCLs come into play, as they allow for very accurate engineering of the lasing transition, and thus give access to this underdeveloped electromagnetic region. Now, QCLs are n-doped semiconductor lasers, consisting of a stack, or an array, of quantum wells, the so called heterostructure, in which the interacting electrons are constrained to the conduction band of the medium. As illustrated in Fig. 1.3, the fundamental difference in the operating principles of QCLs as compared to conventional semiconductor lasers, is in that the electron transitions in QCLs occur within the conduction band itself, and not between the conduction and the valence band states. That is why sometimes such a radiative transition is called intersubband transition. Due to energy conservation, the emitted photon will have energy equal to the difference between the electronic states in the conduction band of the heterostructure, and will not depend in any way on the band gap. This allows scientists to overcome the band gap limitation and open the already mentioned low energy spectral regions to exploitation.

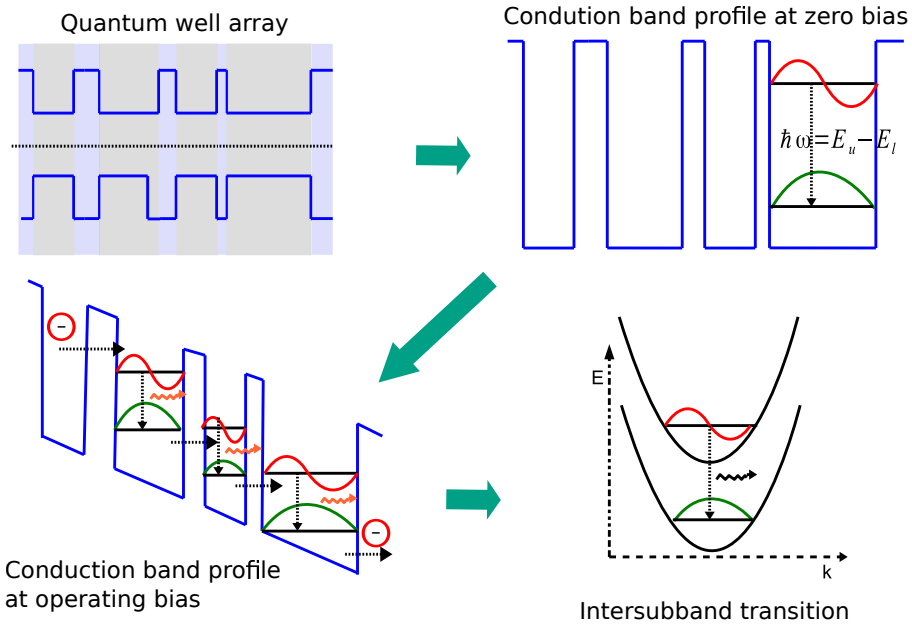

Figure 1.3 Schematic diagram of quantum cascade laser operating principles. Upper-left we have the material stack with the corresponding conduction and valence band profiles. The images on the upper-right and lower-left depict the resulting conduction band profile - a quantum well array, without and with applied bias, respectively. Lastly, the lower-right image illustrates the transition in the reciprocal lattice.

Due to quantum mechanical effects, the electrons have bound states and their wave-functions (at least those with energies close to the conduction band edge) generally span one or more quantum wells, since there is a finite probability for the electron to tunnel through an

energetic barrier. When the right voltage difference, i.e. bias, is applied onto the quantum well array, the probability of electrons to tunnel through the barriers increases due to resonant tunneling [31]. In this way, the charges that populate the conduction band start cascading down the structure, hopping from quantum well to quantum well via resonant tunneling and emitting a photon each time they undergo radiative transition. Care must be taken as this is a vast simplification of the dynamics actual devices, as typical QCLs have more bound states participating in the conduction, and in addition to tunneling, exploit other scattering mechanism for electron transport [27]. This means that a single electron can, in principle, generate multiple photons as it cascades through the system, unlike in conventional semiconductor lasers where a single charge is responsible for at most one photon. This property hints about the large efficiencies that can be obtained with QCL. Quite evidently QCLs are electrically pumped devices where the carrier transport is custom-tailored as to ensure maximum possible population inversion, via wave function engineering.

The original idea of light amplification by intersubband transitions has originally been proposed by two soviet physicists, Kazarinov and Suris already in 1971 [32], however due to technological limitations a working QCL was only first demonstrated in Bell Labs in 1994 [33]. For the last 25 years or so, there has been a surge in research activity in developing and improving the technology. Currently, QCLs have been established as potent room-temperature mid-infrared radiation sources, emitting both continuous wave and pulsed signals with high power and wall-plug efficiently [17, 34, 35]. There is a multitude of different active region and waveguide designs for optimal performance of the devices, depending on the desired application, and there are even several industrial companies producing and distributing commercial QCLs [36, 37].

The situation is a bit different for far-infrared devices, due to the ultracold temperatures needed for their operation. THz quantum cascade lasers are, due to the smaller energy spacing between the lasing levels, extremely sensitive to temperature variations. State of the art technology has allowed for a maximal operating temperature of 200 K, with this record, set in 2012, still to be improved [38]. Certain advancements have been made in, for example, achieving negative differential resistance at 290 K [39], but the search for a room-temperature THz QCL is largely still on-going [40, 41]. Nevertheless, cryogenically cooled THz QCLs can still be useful especially for the generation of frequency combs either by free-running lasers or with mode locking. A brief introduction to the concept of a frequency comb and the principles of mode locking is given in the following sections.

1.4 Mode locking of lasers and frequency comb generation

1.4.1 Mode locking

Mode locking is a method with which a fixed-phase relationship between the longitudinal modes of a laser is established in order to make the device emit short, very power-intensive pulses of light. Mode locked lasers are useful in a variety of applications ranging from laser ablation, a process when intense light is cast upon a material to alter its nano-scale structure [42], through different kind of probing experiments, to even the so called internal confinement fusion

in nuclear fusion research. To avoid confusion, it should be noted that mode locking is a more general concept than ultrashort pulse generation, i.e. the time domain profile of a phase locked laser is not necessarily a periodic train of pulses. Indeed, there are devices, such as QCLs for example, which have shown to emit mode locked, coherent multimode light, even in a free running regime of operation [14, 15]. Nevertheless in this thesis, with a slight abuse of terminology, the term mode locking will be used to refer to the multitude of methods used for the generation of optical pulses of light. With this in mind, in this section the fundamentals of mode locking, both active and passive, are introduced together with some relevant notation.

First of all, let us consider the concept of a longitudinal laser mode. Longitudinal or axial mode formation is an interference phenomena that determines the allowed frequencies at which a wave can oscillate inside a bounded region of length L. It is basically the formation of standing wave patterns with a discrete set of allowed frequencies, due to the confinement of the light inside a finite domain. Longitudinal modes are the optical analogue of normal modes for a vibrating string with its both ends fixed.

To see the interference nature of this phenomena, imagine that we have an optical cavity of length L, at both ends of which we have positioned perfectly reflecting mirrors ($r_1 = r_2 = 1.0$). Assume that at time t on position $x = 0$ there is the following electric field

$$E(t, 0) = E_0 cos(\omega t + \phi), \tag{1.1}$$

where ϕ is the phase and ω is the fields angular frequency. The signal, starting from $x = 0$ at time t, will travel through the cavity with velocity, say v, reflect from the right mirror and come back to $x = 0$ in exactly $T_R = 2L/v$ seconds. Obviously, the reflected wave will interfere with the wave crest at $x = 0$ at time $t + T_R$ and in case of destructive interference, the reflected and emitted waves will quickly cancel each other and the total electric field will vanish. Conversely, constructive interference will occur if the phase shift of the reflected wave is exactly an integer multiple of 2π. Therefore, we get

$$\omega T_R = m2\pi, \tag{1.2}$$

where $m = 0, 1, 2...$ is an integer determining the mode order, as the condition for constructive interference. Rewriting in terms of usual frequency reads

$$f_m = m\frac{v}{2L} = m\frac{c}{2Ln}. \tag{1.3}$$

Note that in Eq. (1.3) c denotes the velocity of light in vacuum and n is the refractive index. Another interesting quantity is the separation frequency between two adjacent modes, i.e.

$$\Delta f = f_m - f_{m-1} = \frac{c}{2Ln}, \tag{1.4}$$

where in general one might assume that the refractive index and hence Δf are frequency dependent (the so-called dispersion).

Generally, a laser's gain medium will have a non-vanishing gain over a wide range of longitudinal modes. This means that it is, in principle, possible to extract broadband radiation from such a device. Additionally, given a multimode emission spectrum, how can one impose a fixed phase relationship between the lasing longitudinal modes, so that in the time domain, the laser emits ultra short pulses? Generally, there are two methods to achieve that: active and passive mode locking.

Within active mode locking, pulsed operation is achieved by placing an externally controlled gain or loss modulator inside the cavity. When this component, also known as attenuator, is switched on, the losses inside the cavity overcome the gain, which prevents the device from lasing. This, naturally, leads to a buildup of population inversion, due to whatever pumping mechanism we are using, and hence storage of a large quantity of energy inside the device. Now, when the attenuator is switched off for a short time, the losses become smaller than the gain and the built-up energy is quickly released in a powerful pulse, thus depleting the gain. After some time, the attenuator is switched on again and the same process is repeated. Examples of such active mode locking mechanisms are radio frequency (RF) injection-current modulators, acousto-optical modulators or even simple mechanical shutters that that open and close in brief intervals. In the frequency domain, active mode locking is best represented as amplitude or frequency modulation of the field, with some frequency ω_m. It can be shown [43] that, if the modulation frequency is equal or close to the mode spacing of the laser, the effect of an amplitude modulating component is to couple ("lock") adjacent lasing modes and perpetually broaden the lasing spectrum. Namely, because the modulation frequency ω_m has to be driven externally, this technique is called active mode locking. When the laser cavities are very short (on the order of couple of millimeters for semiconductor lasers), then also the round trip times will be small, from where it follows that the modulation frequency has to be very large (order of GHz). Creating a controllable switching mechanism working at such high frequencies is a formidable engineering challenge, which limits the applicability of this technique, or at least the minimum pulse-width that can be achieved via active mode locking. Figure 1.4 illustrates how loss modulation via an externally driven oscillator can lead to pulse formation.

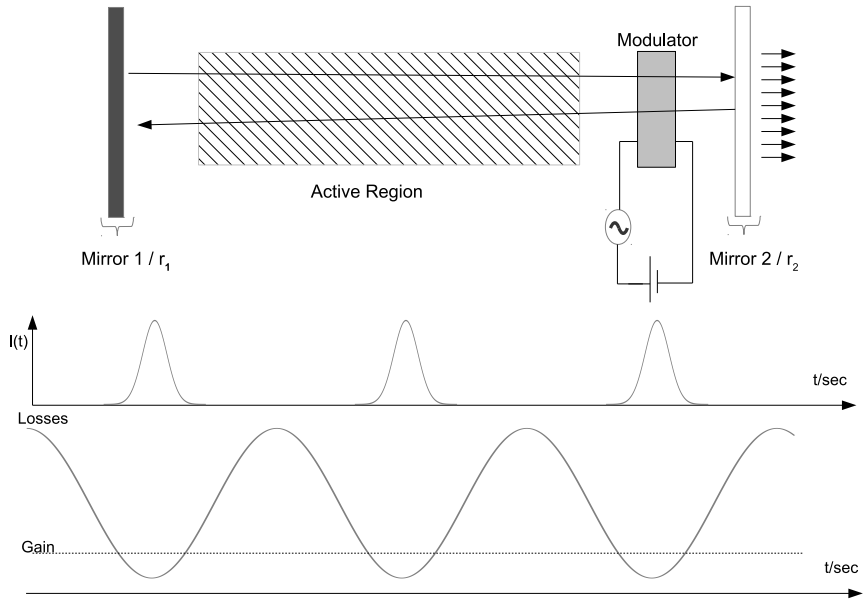

Figure 1.4 (Top) Fabry-Perot optical cavity containing an externally driven modulator component. (Bottom) Gain/Loss dynamics under harmonic modulation of the losses and resulting pulse-shape. Adapted from [43].

On the other hand, there is also passive mode locking, where the attenuating mechanism is internal to the laser and does not need to be controlled externally in any way. Passive

mode locking is a consequence of non-linear effects such as four-wave mixing, saturable absorption, Kerr-lensing and other mechanisms [44, 45], which favor multimode operation over continuous wave lasing. One of the most common methods for passive mode locking is the already mentioned saturable absorption, where the gain medium contains a special material with intensity dependent losses. This dependence is usually represented as

$$l(t) = \frac{q_0}{1 + I(t)/I_{sat}}, \tag{1.5}$$

where $I(t)$ is the intensity of the field at time t, I_{sat} is the so called saturation intensity and q_0 denotes the losses in the absence of the photon field (i.e. the "small signal" losses). From the above expression it is evident how the pulse will shape itself as it propagates through the medium. When the intensity is very large, the pulse's peak sees more net gain (less losses) than the pulse's wings, which shortens the signal on each traversal of the cavity. Naturally, this shortening process stops when the bandwidth of the pulse reaches the gain bandwidth, or the pulse-width approaches some minimal resolution, generally determined by the gain recovery dynamics of the medium. For the formation of very short pulses, passive mode locking turns out to be more effective than its active counterpart [43].

1.4.2 Frequency combs

A closely related concept to the notion of mode locking is the idea of frequency combs. A frequency comb is a device, emitting a broadband spectrum of evenly spaced frequency lines. The famous time-bandwidth product rule from Fourier analysis tells us that in the spectral domain, a periodic repetition of ultrashort pulses consists of multiple frequency lines. Building upon the previous discussion about ultrashort pulse generation, we can clearly see that a stable-pulse emitting laser can also be a frequency comb.

However, the notions of pulse-formation and frequency comb generation are not completely interchangeable, i.e. even though short periodic pulse trains form a frequency comb in the spectral domain, not all frequency combs are trains of short pulses in the time domain. Perfectly frequency modulated signal can also be a comb [46]. The only requirement for a frequency comb laser is that its spectral modes shall be separated by a constant frequency spacing [47].

An ideal frequency comb contains mode lines indexed by the following expression (see Fig. 1.5)

$$f_n = f_o + n\Delta f, \tag{1.6}$$

where n an integer denoting the mode index, Δf is the frequency spacing and $f_o < \Delta f$ is the so called carrier-envelope offset frequency. In general, both f_o and Δf are in the microwave frequency domain, e.g. a couple of GHz, which implies that Eq. (1.6) maps a set of optical modes to a set of radio frequencies. This means that one can measure optical oscillations by down-conversion to this lower frequency regime with, for example, heterodyne mixing [10, 48]. For a more intuitive picture, imagine the frequency comb as a very fine ruler in the spectral domain with which we can accurately measure different frequencies. Such a capability to count optical cycles with RF detectors promises a wide range of very significant applications in both everyday life and the frontiers of science [9, 29, 45, 47]. The importance of this new emerging technology has already received the highest sign of recognition by the international

scientific community in 2005, when the researchers Theodor Hänsch and John Hall shared the Nobel Prize in physics "*for their contributions to the development of laser-based precision spectroscopy, including the optical frequency comb technique*" [49].

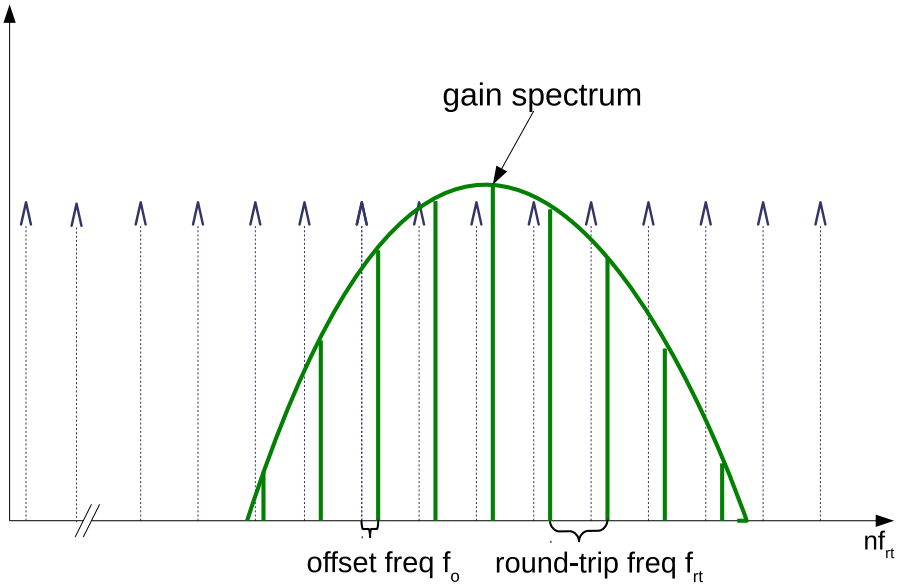

Figure 1.5 An illustration of a frequency comb spectrum. A broadband gain medium lases evenly spaced frequency lines, separated by f_{rt}. The offset frequency is also shown as f_o.

What are the difficulties in constructing frequency combs? As many lasers' gain media are broadband in nature, emitting a mixture of frequencies is not so much the problem, rather, stabilizing the mode separation frequency Δf (usually equal to the repetition rate of the signal f_{rt}) and also the carrier-envelope offset frequency f_o poses the biggest technological challenges. Building upon years of research in ultrashort pulse generation and pulse stabilization, frequency comb generation techniques based on mode locking have been the most successful so far, with the culmination of this research - the Kerr-lens mode locked Ti:Sapphire laser [50].

Following the above line of thoughts, mode locking quantum cascade lasers should lead to frequency comb generation in the mid- and far-infrared regimes. There is a very intensive ongoing research on this topic with some partial success, with the shortest pulse widths achieved so far at around 2.5 ps, produced via a complex combination of pulse seeding and active modulation of the injection current [51]. It is generally thought that active mode locking of QCLs, so that they emit short and powerful pulses, is very challenging [4], which is mainly due to the inherently fast gain recovery time (on the order of few picoseconds) in this kind of devices. Intuitively, the gain recovery time can be considered similar to the relaxation time of the upper laser level, as it determines the speed at which saturated gain can return to values above threshold. When a pulse propagates through an active region with very long gain recovery time, the peak of the pulse saturates the gain so that its wings experience less amplification, which in turn shortens the signal. By way of contrast, if the gain medium has fast gain recovery, on the order of the length of the pulse, the pulse tends to be prolonged at every pass through the active region. In Chapter 5 the possibility of ultra-short pulse generation in QCLs will be revisited. Note that to date, no passively mode locked QCL has been demonstrated.

On the other hand, there is the possibility to generate free-running frequency combs. For example, in [14] the authors demonstrated a mid-infrared frequency comb based one a free-running QCL, lasing in a spectral region where the group velocity dispersion (GVD) of the medium was close to zero. For clarity, GVD is a material determined coefficient specifying the rate at which pulses spread out in time, due to differences in the individual modes' phase velocities. Therefore the absence or the compensation of GVD is crucial for the temporal coherence of the emitted signal.

The multimode behavior of that same laser, on the other hand, was theoretically explained [4] to be due to non-linear processes such as cascaded four wave mixing occurring inside the optical cavity. Similarly, a frequency comb, with the unprecedented bandwidth of 14 $\%$ of the laser's central frequency, was later reported for the terahertz regime, again based on a free-running device [15]. In this paper, GVD was accounted for by a special dispersion compensation mechanism - a kind of corrugation grating etched into the waveguide of the QCL. It might be worth mentioning explicitly that, interestingly enough, the THz device did not produce output light in the form of pulses, but rather lased in the continuous wave regime, i.e. with approximately constant instantaneous intensity. Such a behavior is characteristic for frequency modulated signals.

1.5 Conclusion

In this chapter the central problem that this thesis addresses, namely the theoretical investigation of means for frequency comb generation with quantum cascade lasers, has been outlined. Related publications were introduced, followed by some elementary remarks about lasers in general and quantum cascade lasers in particular. Lastly, as a gentle preparation for the upcoming chapters, some basic concepts concerning pulse generation via active and passive mode locking, as well as frequency comb generation by free-running devices, were introduced.

2 Theoretical models for light-matter interaction

2.1 Introduction

This chapter introduces step by step derivation of various light-matter interaction models, suitable for transient simulations of quantum cascade lasers. The exposition begins in Sec. 2.2 with a classical description of the electromagnetic field, based on Maxwell's equations, before applying considerable simplifications to produce an alternative model, better suited for computer simulations. The coupling of the electromagnetic field to the carrier dynamics is accomplished in Sec. 2.3 via a classical rate equations approach and also a quantum mechanical model, within the framework of the density matrix. After a brief introduction to the theory of the latter, the main equations of motion for the density matrix are derived, where the carrier-photon dynamics is treated coherently (via a unitary transformation to the state), whereas additional interactions are captured in the Markov approximation via a Lindblad superoperator. From the quantum mechanical model, a classical limit (in the form of rate equations) is also presented and the assumptions under which this classical description is valid are discussed. Finally, in Sec. 2.4, the landmark two-level Maxwell-Bloch equations are developed, and several important quantities relating the quantum and the classical world are summarized.

2.2 Classical models for the optical field

In this section we consider several approaches to modeling the electromagnetic field in optical systems. Due to the typically large number of photons in laser devices, quantization of the field is not strictly necessary as a purely classical model ought to suffice in reproducing all of the relevant physics.

From classical electrodynamics we know that the electromagnetic field satisfies the celebrated Maxwell's equations, which serve as a starting point for the derivation of the main optical model, used throughout the thesis. Concretely, it will be shown how, employing the right set of assumptions about the material system and the field, this allows for the considerable simplification of Maxwell's equations, resulting in a pair of traveling wave equations. Detailed explanation is given in the following.

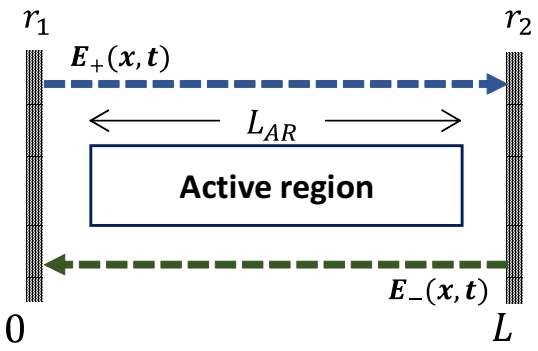

Figure 2.1 An illustration of a generic laser resonator consisting of an active region of length L_{AR} and two reflective mirrors with reflectivities r_1 and r_2.

2.2.1 Maxwell's equations

Consider a generic laser geometry as depicted in Fig. 2.1, an active section packed inside a linear cavity of certain length L. The time evolution of the electric and magnetic field vectors, $\mathbf{E}(\mathbf{r},t)$ and $\mathbf{H}(\mathbf{r},t)$, respectively, is classically described by Ampere's and Faraday's laws,

$$\nabla \times \mathbf{H} = \frac{\partial \mathbf{D}}{\partial t} + \mathbf{j}, \tag{2.1}$$

$$\nabla \times \mathbf{E} = -\frac{\partial \mathbf{B}}{\partial t}, \tag{2.2}$$

together with a pair of constitutive relations

$$\mathbf{D} = \varepsilon \mathbf{E} + \mathbf{P}, \tag{2.3}$$

$$\mathbf{B} = \mu_0 \mathbf{H} + \mathbf{M}, \tag{2.4}$$

where ∇ is the familiar nabla operator, $\mathbf{r}$ is the coordinate vector, $\mathbf{D}$ is the electric displacement field, $\mathbf{B}$ is the magnetic induction, $\mathbf{j}$ is the free carrier current density, and lastly $\mathbf{P}$ and $\mathbf{M}$ refer to the electric and magnetic polarization fields. Also in the constitutive relations, Eqs. (2.3)-(2.4), $\varepsilon = \varepsilon_0 \varepsilon_r$ denotes the material permittivity decomposed as the product of the vacuum and the relative permittivities, ε_0 and ε_r, respectively, and μ_0 is the magnetic permeability. Specifically, Eq. (2.3) assumes both linear polarization term, encoded in the dimensionless parameter ϵ_r, and an additional polarization $\mathbf{P}$, which is general enough to describe arbitrary system response to an applied external electric field $\mathbf{E}$.

In quantum cascade lasers, one can first of all neglect the magnetic polarization term, i.e. set $\mathbf{M} = 0$. Furthermore, due to quantum mechanical selection rules [52], only the resonator modes parallel to the heterostructure growth direction, in this case assumed to be the $z-$direction, can couple to the intersubband transition and thus be amplified. For slab-waveguide lasers, this condition will be generally satisfied by a transverse magnetic (TM) mode, however as a rough approximation, one can also neglect electric field components in longitudinal direction, i.e. assume a transverse electromagnetic (TEM) mode propagating

inside the resonator. Taking this and the constitutive relation assumptions into account, the original equations are reduced to the pair

$$\partial_t \hat{E}_z = \varepsilon^{-1}[-\sigma \hat{E}_z - \partial_t \hat{P}_z + \partial_x \hat{H}_y], \tag{2.5a}$$

$$\partial_t \hat{H}_y = \mu_0^{-1} \partial_x \hat{E}_z. \tag{2.5b}$$

In Eq. (2.5a), $\hat{F}_j$ is used to denote the corresponding (j^{th}) component of each of the field vectors, and additionally the free carrier current is modeled via Ohm's law as $\hat{j}_z = \sigma \hat{E}_z$, with σ denoting the material's conductivity parameter.

Despite reducing the number of differential equations from 6 to only 2, Eqs. (2.5a)-(2.5b) still depend on all three spatial coordinates. At this point, the problem can be further simplified by integrating over the transverse spatial directions, i.e. over the y and z coordinates, which in this text will be denoted via the change in notation $\iint \hat{F}_j(x, y, z) dy dz = F_j$, i.e. to indicate that an integration over y and z has been performed, we simply remove the $\hat{\cdot}$ from all field terms. The resulting system can serve as a starting point for various light-matter interaction models [53, 54], and where analytical solutions are not available, can be solved numerically via the established finite difference time domain (FDTD) method, the pseudo-spectral time-domain method (PSTD) and others [55, 56]. Unfortunately, the numerical solution of Eqs. (2.5a)-(2.5b) imposes quite stringent requirements on the discrete time step or grid size, and for short wavelength fields, or alternatively large simulation regions, can be quite time and resource consuming endeavor. Next to "brute force" implementations, various approximation and/or parallelization techniques can be employed to speed up the calculation time [57]. Since this thesis focuses on exploring the physics of quantum cascade lasers, rather than on the numerical efficiency of the underlying models, the author has taken an approximation approach to simplify the computational load. However, it must be noted that in the age of fast many-core computer architectures, it is high time for a paradigm shift in the way those "intractable" numerical problems are tackled. Instead of devising elaborate approximations, which are usually capable of treating only corner cases, one should directly approach the full complexity of the system with models (usually computationally demanding) based on first principles and physical laws, rather than approximations. Alternatively, where parallelization techniques are not possible, or do not scale efficiently, "multi-domain" models, where one combines various simulation tools, are also possible. This thesis partially incorporates the latter approach, as a combination of Schrödinger-Poisson solvers, ensemble Monte Carlo simulations together with density matrix-based models, have been used to simulate and prototype QCL dynamics. More on this will be elaborated in later chapters of this thesis.

2.2.2 The traveling wave equations

As mentioned previously, since Eqs. (2.5a)-(2.5b), even in the 1D case, are too computationally demanding to enable fast prototyping and analysis of THz QCLs, here a simplification of the Maxwell's equations will be employed. This results in the so called "traveling wave equation", which is a widely employed approximation of Eqs. (2.5a)-(2.5b), used to capture the axial dynamics of various types of lasers and optical amplifiers [58–61].

For starters, use Eq. (2.5b) to express the mixed derivative of H_y and completely remove the magnetic field from the dynamics. After some simple algebra one comes up with the one dimensional inhomogeneous wave equation

$$\frac{c^2}{n^2}\partial_x^2 E_z - \partial_t^2 E_z = \frac{\sigma}{\varepsilon_0 n^2}\partial_t E_z + \frac{1}{\varepsilon_0 n^2}\partial_t^2 P_z, \tag{2.6}$$

where $n = \sqrt{\varepsilon_r}$ denotes the background refractive index, c denotes the vacuum speed of light and $\varepsilon\mu_0 = n^2/c^2$.

Fortunately, Eq. (2.6) can be greatly simplified by employing one very common approximation, the so called slowly varying envelope approximation or SVEA for short [62]. In the SVEA approximation it is assumed that the optical field can be written as a product of an envelope function, say $E_+(x,t)$ and a carrier wave $e^{i(\beta_0 x - \omega_0 t)}$, where ω_0 is usually considered to be the angular frequency of the central mode of the laser, and β_0 is the corresponding wave number. Taking the electric field as a superposition of forward and backward propagating waves, one can write

$$E_z(x,t) = \frac{1}{2}\Big[E_+(x,t)e^{i(\beta_0 x - \omega_0 t)} + E_-(x,t)e^{-i(\beta_0 x + \omega_0 t)} + c.c.\Big], \tag{2.7}$$

where $c.c.$ denotes the complex conjugate of the preceding expression and the $+$ and $-$ signs specify the forward/backward propagating waves' envelopes, respectively. To complete the approximation, add the *slowly varying* part, which limits the spatio-temporal variations of $E_\pm$ to be seen as slow in the length/time scale of the spatial/temporal oscillation period of the carrier. What that physically means is that we consider a frequency spectrum of much smaller bandwidth than the absolute value of the central frequency ω_0, which is indeed justified for most QCL devices, even in mode locked regime of operation [15, 19, 63]. Employing SVEA will allow one to neglect partial derivatives of second and higher order, and thus substantially simplify the wave equation.

Straightforward substitution of Eq. (2.7) into the wave equation Eq. (2.6) gives two first order partial differential equations for the envelopes $E_\pm$. To see how, it will be convenient to employ a more compact notation as to simplify the partial differentiation, summation and complex conjugation. Write

$$E_z(x,t) = \frac{1}{2}\sum_{\alpha=\pm} E_\alpha e^{i(\alpha\beta_0 x - \omega_0 t)} + c.c.\,, \tag{2.8}$$

where the α is simply a sign specifier. Additionally, it is useful to decompose the polarization into a slowly varying term times a carrier wave as follows

$$P_z(x,t) = \frac{1}{2}\sum_{\alpha=\pm} P_\alpha e^{i(\alpha\beta_0 x - \omega_0 t)} + c.c.\,. \tag{2.9}$$

This assumption is reasonable as P_z will be proportional to the electric field if the interaction is linear, and will depend on higher orders of E_z for non-linear interaction [64].

Now, computing the first and second partial derivatives of the field and polarization with respect to x and t gives

$$\partial_t E_z(x,t) = \frac{1}{2}\sum_{\alpha=\pm}\left\{\partial_t E_\alpha - i\omega_0 E_\alpha\right\} e^{i(\alpha\beta_0 x-\omega_0 t)} + c.c., \tag{2.10}$$

$$\partial_x E_z(x,t) = \frac{1}{2}\sum_{\alpha=\pm}\left\{\partial_x E_\alpha + i\beta_0 E_\alpha\right\} e^{i(\alpha\beta_0 x-\omega_0 t)} + c.c., \tag{2.11}$$

$$\partial_t^2 E_z(x,t) = \frac{1}{2}\sum_{\alpha=\pm}\left\{\partial_t^2 E_\alpha - 2i\omega_0\partial_t E_\alpha - \omega_0^2 E_\alpha\right\} e^{i(\alpha\beta_0 x-\omega_0 t)} + c.c., \tag{2.12}$$

$$\partial_x^2 E_z(x,t) = \frac{1}{2}\sum_{\alpha=\pm}\left\{\partial_x^2 E_\alpha + 2i\alpha\beta_0\partial_x E_\alpha - \beta_0^2 E_\alpha\right\} e^{i(\alpha\beta_0 x-\omega_0 t)} + c.c., \tag{2.13}$$

$$\partial_t^2 P_z(x,t) = \frac{1}{2}\sum_{\alpha=\pm}\left\{\partial_t^2 P_\alpha - 2i\omega_0\partial_t P_\alpha - \omega_0^2 P_\alpha\right\} e^{i(\alpha\beta_0 x-\omega_0 t)} + c.c.. \tag{2.14}$$

Plugging into Eq. (2.6), employing the slowly varying amplitude approximation or $|\partial_t E_\pm| \ll |\omega_0 E_\pm|$, $|\partial_x^2 E_\pm| \ll |\beta_0\partial_x E_\pm|$, $|\partial_t^2 E_\pm| \ll |\omega_0\partial_t E_\pm|$ (similarly for the polarization) and finally the dispersion relation $\beta_0 = \omega_0 n/c$, the derivation simplifies to

$$\sum_{\alpha=\pm}\left\{\partial_t E_\alpha + \alpha\frac{c}{n}\partial_x E_\alpha\right\} e^{i(\alpha\beta_0 x-\omega_0 t)} + c.c = \frac{1}{2}\sum_{\alpha=\pm}\left\{-\frac{\sigma}{\varepsilon_0 n^2}E_\alpha + i\frac{\omega_0}{\varepsilon_0 n^2}P_\alpha\right\} e^{i(\alpha\beta_0 x-\omega_0 t)} + c.c.. \tag{2.15}$$

Equating terms in front of matching carrier wave components one can obtain the pair of propagation equations for the forward and backward propagating electric field envelopes ($E_\pm$)

$$\frac{n}{c}\partial_t E_\pm \pm \partial_x E_\pm = -\frac{a}{2}E_\pm + i\frac{\omega_0}{2\varepsilon_0 nc}P_\pm, \tag{2.16}$$

where $a = \sigma/(\varepsilon_0 nc)$ denotes the cavity linear loss parameter, which can also be related to the photon lifetime τ_p via $\tau_p = n/(ac)$. This pair of equations, Eq. (2.16), serves as the basis of the above mentioned traveling wave equation model and needs to be supplemented by an adequate description of the light-matter coupling, i.e. a specific form for the polarization term $P_\pm$ ought to be specified.

2.3 Models for the active region

2.3.1 Rate equation models

In order to establish a complete carrier-light model, one needs to decide on a specific form on the source term in Eq. (2.16). This can be done in various different ways and is a topic subject to its own research. For starters, assume that the polarization envelope $P_\pm$ is proportional to the electric field envelope, i.e. $P_\pm = \varepsilon_0\chi E_\pm$, with the proportionality coefficient $\chi(x,t)$, which is generally position and time dependent and is also known as the susceptibility of the material [64]. Plugging this ansatz into Eq. (2.16), multiply the latter equation by the complex conjugate of the E-field envelope, i.e. $E_\pm^*$, which yields

$$\frac{n}{c}(\partial_t E_\pm)E_\pm^* \pm (\partial_x E_\pm)E_\pm^* = -\frac{a}{2}|E_\pm|^2 + i\frac{\omega_0}{2nc}\chi|E_\pm|^2. \tag{2.17}$$

Now one can take the complex conjugate of the previous expression and add the resulting equation to Eq. (2.17), to obtain a pair of propagation equations for the intensity $I_\pm \propto |E_\pm|^2$ of the forward and backward envelopes

$$\frac{n}{c}\partial_t I_\pm \pm \partial_x I_\pm = -aI_\pm - \frac{\omega_0}{nc}\,\mathrm{Im}\{\chi\}I_\pm, \tag{2.18}$$

where $\mathrm{Im}\{\cdot\}$ denotes the imaginary part (with $\mathrm{Re}\{\cdot\}$ representing the real part). As previously mentioned, a in Eq. (2.18) is interpreted as the linear waveguide loss parameter, whereas the term $g = -\omega_0\,\mathrm{Im}\{\chi\}/[nc]$ captures the polarization response of the system and is also known as the gain coefficient. With this new notation at hand, the field propagation equations can be written in a more canonic form as

$$\frac{n}{c}\partial_t E_\pm \pm \partial_x E_\pm = -\frac{a}{2}E_\pm + \frac{g\Gamma}{2}(1-i\alpha)E_\pm, \tag{2.19}$$

where $\alpha = \mathrm{Re}\{\chi\}/\,\mathrm{Im}\{\chi\}$ is also known as the *linewidth enhancement factor*, famously derived by Henry in 1982 [65], and is responsible for the observed increase in the spectral linewidth as compared to the quantum limit. Additionally, in order to consider the fact that the electric field does not fully overlap with the active region, it is customary to multiply the gain coefficient in the above expression by the field overlap factor Γ, defined as

$$\Gamma = \frac{\iint_{S_g} |\hat{E}_z|^2 dydz}{\iint_{-\infty}^{\infty} |\hat{E}_z|^2 dydz}, \tag{2.20}$$

where in the numerator one integrates over the gain medium cross sectional area S_g [52].

Now, it is time to couple the traveling wave equations to an additional model for the gain. Its dependence on the density of active carriers N, i.e. the population inversion, and thus the injection current J, is usually parametrized as some empirical function of N, motivated by fitting theoretical curves to experimental data. For quantum well lasers, experimental evidence indicates that a logarithmic such dependence provides a good approximation, where the gain curve is given by [61]

$$g(x,t) = \frac{g_0 \log(N/N_0)}{1 + (I_+ + I_-)/I_{sat}}, \tag{2.21}$$

where g_0 is the small signal gain, N_0 is the carrier density at transparency and I_{sat} is the saturation intensity. Alternatively, one can take a more simple, linear model for the gain

$$g(x,t) = g_0(N/N_0 - 1). \tag{2.22}$$

These relations are additionally appended by a rate equation for the time evolution of N, which for example for quantum well lasers can take the form

$$\partial_t N = \frac{J}{eV_g} - \frac{c}{n}\Gamma g(N)\Phi - r_{nr}(N) - r_{sp}(N), \tag{2.23}$$

where $\Phi = n^2\varepsilon_0|E_z|^2/(2\hbar\omega_0)$ is the photon number, $r_{nr}(N)$ denotes the nonradiative electron-hole recombination rate, $r_{sp}(N)$ is the spontaneous emission rate, J is the injected current, V_g is the gain volume and e the elementary charge. The nonradiative total recombination rate can include, among other models, the SRH (Shockley-Read-Hall) recombination or Auger

recombination [26, 66], and its precise modeling is out of the scope of this work. For quantum cascade lasers, where intraband transitions do not play a role, the term r_{nr} can be dropped in favor of a rate equation model including nonradiative scattering events between the various subband levels. Additionally, since for QCLs those scattering events occur on much shorter time-scales as compared to spontaneous emission, then the r_{sp} term can also be dropped from the model. Such rate equation approaches have been extensively studied for QCLs and in some cases have proven to give quite a satisfactory agreement with experiment [67–69]. An exemplary such system for a model considering only two subband levels, the upper and the lower laser level, can be written down as [52]

$$\partial_t N_2 = \eta_2 \frac{J}{eV_g} - \tau_2^{-1} N_2 - \sigma_{21} I (N_2 - N_1), \tag{2.24}$$

$$\partial_t N_1 = \eta_1 \frac{J}{eV_g} - \tau_1^{-1} N_1 + \tau_{21}^{-1} N_2 + \sigma_{21} I (N_2 - N_1), \tag{2.25}$$

with N_2 and N_1 denoting the carrier concentration in the upper and lower laser level, respectively, I is the total optical intensity in the active region at the lasing frequency, and σ_{21} is the so called scattering cross section for stimulated emission from level 2 to level 1. Additionally, Eqs. (2.24)-(2.25) have been generalized to take into account that a η_2 fraction of the current is injected in the upper level and η_1 into the lower laser level, with $\eta_2 + \eta_1 = 1$, and also τ_2 and τ_1 denote the corresponding level lifetimes and τ_{21} the nonradiative scattering term for the transition $2 \to 1$.

Further extension of the two level rate equations model, in the case of multiple subband levels, is the $N-$level system model with time evolution equations

$$\frac{dn_j}{dt} = R_j^e + \sum_{i \neq j} \Gamma_{i,j} n_i - \Gamma_j n_j, \text{ for } j = 1, 2...N \ , \tag{2.26}$$

where n_j and R_j^e denote the population density and the electron injection rate (proportional to the injection current) in the j^{th} level, respectively, $\Gamma_{i,j} = \tau_{i,j}^{-1} = \sum_{(s)} \Gamma_{i,j}^{(s)}$ is the out-scattering rate (inverse lifetime) from subband level i to level j, which includes the contributions from all possible (radiative and nonradiative) scattering mechanisms s and $\Gamma_i = \sum_k \Gamma_{i,j}$ is the total out-scattering rate from level i. Here, for compactness of notation, the radiative scattering to and from each level due to absorption and stimulated emission, respectively, has also been taken into account with equal rates given by the formula [52]

$$\Gamma_{i,j}^{\textbf{optical}}(\omega) = \Gamma_{j,i}^{\textbf{optical}}(\omega) = \frac{\pi |d_{i,j}|^2}{\varepsilon_0 c n \hbar^2} I_\omega \mathscr{L}_{i,j}(\omega). \tag{2.27}$$

In Eq. (2.27) the various terms are defined as follows: $d_{i,j}$ is the so called dipole matrix element [70], which describes the strength of the optical coupling between levels i and j, ε_0 is the vacuum permittivity, c is the velocity of light, n is the refractive index in the active region, $\hbar$ is the reduced Plank constant and finally I_ω denotes the optical intensity at angular frequency ω and $\mathscr{L}_{i,j}(\omega)$ is the lineshape function for the transition $i \leftrightarrow j$ [22].

2.3.2 Periodic rate equation model

Since QCLs not only have multiple (M) subbands per period, but also have multiple (usually > 30) periods (N_p), a simulation based on Eq. (2.26) would need to time-step $M \times N_p$

independent levels, which is cumbersome, numerically demanding and practically unnecessary. Additionally, the arbitrary inclusion of intersubband scattering rates would generally violate the conservation of charges in the system as the sum $\sum_m \partial_t n_m \neq 0$. To truncate the system to only a few periods, and simultaneously to ensure charge conservation, one could modify the level lifetimes by incorporating periodic boundary conditions as follows.

Let us assume that the discrete energy levels consist of an "injector" level, henceforth denoted by "in", from where the electrical current enters the system, M intermediate "channel" levels, $\{i\}_{i=1}^{M}$, and one output level, "out", which serves as an extractor for the scattered electrons. In the incoherent limit, the master equation for this system [71], with phenomenologically included electron injection rate R_e, is given

$$\frac{dn_{\text{in}}}{dt} = R_e + \sum_{i\neq \text{in}} \Gamma_{i,\text{in}} n_i - \Gamma_{\text{in}} n_{\text{in}}, \tag{2.28a}$$

$$\frac{dn_j}{dt} = \sum_{i\neq j} \Gamma_{i,j} n_i - \Gamma_j n_j, \text{ for } j = 1, 2...M, \tag{2.28b}$$

$$\frac{dn_{\text{out}}}{dt} = -R_e + \sum_{i\neq \text{out}} \Gamma_{i,\text{out}} n_i - \Gamma_{\text{out}} n_{\text{out}}. \tag{2.28c}$$

To close the system, assume that all electrons that enter the extractor level, "out", are immediately re-injected into the input level "in". This "translates" to the condition that the former will be always empty, i.e. $n_{\text{out}} \equiv 0$, which from Eq. (2.28c) allows to find an expression for the carrier injection rate term R_e as $R_e = \sum_{i\neq \text{out}} \Gamma_{i,\text{out}} n_i$. Now plugging this into Eq. (2.28a) one obtains the final "periodic rate equation system"

$$\frac{dn_{\text{in}}}{dt} = \sum_{i\neq \{\text{in, out}\}} [\Gamma_{i,\text{in}} + \Gamma_{i,\text{out}}] n_i - \Gamma_{\text{in}} n_{\text{in}}, \tag{2.29a}$$

$$\frac{dn_j}{dt} = \sum_{i\neq j} \Gamma_{i,j} n_i - \Gamma_j n_j, \text{ for } j = 1, 2...M. \tag{2.29b}$$

2.3.3 Principles of quantum mechanics

The traveling wave model for light matter interaction presented by Eq. (2.19) together with Eq. (2.23) or alternatively Eqs. (2.24)-(2.25) (also Eqs. (2.29)) suffers from the substantial limitation that the spectral bandwidth of the gain is assumed infinitely wide, i.e. these set of models adopt the so called flat gain approximation. To investigate the impact of gain dispersion onto the spatio-temporal dynamics of lasers, this essentially necessitates the inclusion of additional numerical techniques to impose the bandwidth limit of the gain medium [61, 72, 73]. By contrast, coherent light-matter interaction models based on the density matrix equations intrinsically capture the spectral dependence of the gain and can serve as a theoretical basis for further extension and modeling. Namely these approaches, commonly referred to as the Maxwell-Bloch type equations, will be reviewed in this section.

This subsection begins with a quick overview of the main principles and notations used in quantum mechanics. This is by no means an exhaustive tutorial on the subject, but rather should serve to lay out foundations for the more advanced models comprising the main work

of this thesis. The interested reader is referred to the excellent textbooks by J.J. Sakurai [74], Nielsen and Chuang [75] or Rodney Loudon [76] for an exhaustive review of the subject.

Quantum mechanics is built upon several postulates, which serve as the axiomatic basis for that branch of physics. The first of those says that the state of a quantum system can be completely described by a vector in a complex vector space, equipped with an inner product, the so called Hilbert-space [75]. Employing Dirac notation, let us denote a member of this space as $|\Psi\rangle$, which is also referred to as ket-vector. Assuming a finite $N-$dimensional Hilbert space $\mathscr{H}$ with some basis set $\{|k\rangle\}_{k=1}^{N}$, from linear algebra it is known that an arbitrary vector $|\Psi\rangle \in \mathscr{H}$ can be expanded as a linear combination of the basis states

$$|\Psi\rangle = \sum_k c_k |k\rangle . \tag{2.30}$$

In Eq. (2.30) the c_k are complex-valued coefficients, the amplitude squared of which, $|c_k|^2$, is interpreted as the probability of the system being in state $|k\rangle$. In quantum mechanical language, the state $|\Psi\rangle$ is also known as a "pure state" and the expansion Eq. (2.30) is referred to as a "quantum superposition".

The set of linear transformations $\hat{O} : \mathscr{H} \to \mathscr{H}$ is the set of all linear operators acting on the Hilbert space. Another important postulate of quantum mechanics says that any physical observable O of a quantum mechanical state is represented by a Hermitian linear operator $\hat{O}$ acting on $\mathscr{H}$. Furthermore, the process of measurement of the observable O of the system, initially prepared in the pure state $|\Phi\rangle$, is mathematically described by applying the corresponding operator $\hat{O}$ onto the state, i.e. $\hat{O}|\Phi\rangle$. Due to the probabilistic interpretation of quantum mechanics, performing the same measurement on two identically prepared systems will generally yield different results, so instead one works with expectation values. For example, the expectation value of the observable O for a system initially in the state $|\Phi\rangle$ is given by the inner product

$$\langle \hat{O} \rangle = \langle \Phi | \hat{O} | \Phi \rangle . \tag{2.31}$$

The next postulate that will be mentioned here is related to time evolution and it states that any *closed* quantum mechanical system, described by the ket $|\Phi(t)\rangle$, evolves according to the Schrödinger equation

$$i\hbar \frac{d|\Phi(t)\rangle}{dt} = \hat{H}|\Phi(t)\rangle , \tag{2.32}$$

where $\hat{H}$ is a very special operator, called the Hamiltonian of the system. Another, more general formulation of this principle is that the time evolution of any *closed* system is governed by a unitary operator $\hat{U}$ acting on that system ($\hat{U}$ is called unitary if $\hat{U}\hat{U}^\dagger = \hat{U}^\dagger\hat{U} = \hat{I}$ holds, where $\hat{I}$ is the identity operator and $\hat{U}^\dagger$ is the conjugate transpose of $\hat{U}$).

2.3.4 The density matrix

As already mentioned, it is a peculiarity of quantum mechanics that two independent measurements on two identically prepared quantum systems will not, in general, yield the same

result. Such phenomena are not consequences of our "lack of knowledge" about the system(s) under investigation, but it is thought that they arise due to disturbances introduced by the measurement process. Mathematically this is modeled by assuming special relations between quantum mechanical operators. That is, if two operators corresponding to two distinct observables commute, it is possible to prepare the system such that both properties are simultaneously known, whereas if they do not commute - simultaneous knowledge of both properties is impossible (this is the famous uncertainty principle). In this context one says that a quantum mechanical system is in a pure state, if it is prepared in such a way that there is maximal knowledge about the system, which means that one knows the outcome of measurement of a complete set of compatible observables (i.e. commuting observables). It is more often the case, however, that we are concerned with physical systems full information about which is hard or impossible to obtain. The system in such a situation is said to be in a mixed state and its modeling within the ket-vector formalism is impractical. The mathematical apparatus, which will allow us to treat mixed and pure states on equal footing is the so called density matrix and will be introduced below.

Another occasion when the concept of mixed state will come in handy, is when one considers an ensemble of quantum mechanical systems, say the atoms of a crystal. It is virtually impossible to know simultaneously the exact state of every single atom of the crystal, even though it might be possible to know the pure state of a particular such atom. In this case, this statistical ensemble of atoms in pure states can be modeled as a single atom in a mixed state, which will lead to a shift in the interpretation of different quantities, e.g. from occupation probabilities to population densities and so on.

To illustrate the concept of a density matrix, let us assume that our system consists of n identical atoms, each of which is in some pure quantum mechanical state $|\phi_i\rangle$ for the i^{th} atom. Now, a measurement of the observable property $\hat{M}$ of atom i will yield the expectation value $M_i = \langle\hat{M}\rangle_i = \langle\phi_i|\hat{M}|\phi_i\rangle$ with the macroscopic average over all atoms given by

$$\langle\hat{M}\rangle = \frac{1}{n}\sum_{i=1}^{n}\langle\hat{M}\rangle_i = \frac{1}{n}\sum_{i=1}^{n}\langle\phi_i|\hat{M}|\phi_i\rangle\,. \tag{2.33}$$

Next, assume that the set of possible atomic states $\{\phi_i\}_{i=1}^{n}$ "lives" in an $N-$dimensional Hilbert space with the basis $\{|k\rangle\}_{k=1}^{N}$. Then, the atomic pure states $|\phi_i\rangle$, of the system can be given by a quantum superposition of the basis states, i.e.

$$|\phi_i\rangle = \sum_{k=1}^{N} c_i^k\,|k\rangle. \tag{2.34}$$

Insert Eq. (2.34) into Eq. (2.33) to obtain

$$\langle\hat{M}\rangle = \frac{1}{n}\sum_{i=1}^{n}\sum_{k,l=1}^{N}(c_i^k)^* c_i^l\,\langle k|\hat{M}|l\rangle \tag{2.35}$$

In this sum the $(\cdot)^*$ denotes the complex conjugate and $(c_i^k)^* c_i^l$, for $k = l$ can be interpreted as the probability of atom i to be found in basis state $|k\rangle$, whereas for $k \neq l$ is a term giving rise to "quantum interference" between states $|k\rangle$ and $|l\rangle$.

Now, Eq. (2.35) can be cast in a more compact form by defining the "density matrix" operator for atom i via

$$\hat{\rho}_i \equiv \sum_{k,l=1}^{N} (c_i^k)^* c_i^l \left|l\right\rangle \left\langle k\right| = \left|\phi_i\right\rangle \left\langle \phi_i\right| . \tag{2.36}$$

Then Eq. (2.35) is simply

$$\langle \hat{M} \rangle = \sum_{l=1}^{N} \langle l| \left[\sum_{i=1}^{n} \frac{1}{n} \hat{\rho}_i \hat{M} \right] |l\rangle = \sum_{i=1}^{n} \frac{1}{n} \mathbf{tr}(\hat{\rho}_i \hat{M}), \tag{2.37}$$

where $\mathbf{tr}(\cdot)$ denotes the trace operation, given as

$$\mathbf{tr}(\hat{O}) = \sum_{l=1}^{N} \langle l| \hat{O} |l\rangle . \tag{2.38}$$

With this definition, we see that the macroscopic expectation value of the dynamical observable $\hat{M}$ is given as the ensemble average over the traces of $\hat{M}$ multiplied by the i^{th} atom's density matrix $\hat{\rho}_i$. Similarly, one can define a density matrix quantity, representing the full ensemble as $\hat{\rho} = \sum_i p_i \hat{\rho}_i$, where the individual contribution (weight) from every atom is more generally written as $0 \leq p_i \leq 1$, with $\sum_i p_i = 1$. From there, it follows that $\langle \hat{M} \rangle = \mathbf{tr}(\hat{\rho}\hat{M})$.

In fact, writing the density matrix as an average over all atoms in the ensemble is inconvenient for the simple reason that in a usual system there could be some 10^{15} or more particles. An equivalent and more convenient definition of $\hat{\rho}$ is therefore given in terms of the atomic state basis $\{|l\rangle\}_{l=1}^{N}$, where typically $N \ll n$,

$$\hat{\rho} = \sum_{k,l=1}^{N} \rho_{l,k} \left|l\right\rangle \left\langle k\right| , \tag{2.39}$$

with the matrix element $\rho_{l,k} = \sum_i p_i (c_i^k)^* c_i^l$. From this definition it is seen that the diagonal elements $\rho_{l,l}$ of the density matrix, give the fraction of the ensemble in the state $|l\rangle$, whereas the off-diagonal elements $\rho_{l,k}$ quantify the quantum mechanical correlation (or coherence) between the l-th and the k-th basis states.

For closed systems, i.e. unitary dynamics, the time evolution of $\hat{\rho}$ is governed by the von Neumann equation, which is a direct consequence of the Schrödinger equation,

$$i\hbar \partial_t \hat{\rho} = [\hat{H}, \hat{\rho}], \tag{2.40}$$

with $\hat{H}$ being the total Hamiltonian of the system, and $[\cdot, \cdot]$ is the usual commutator of operators.

The unitarity of the time evolution of $\hat{\rho}$ is a rather strong assumption for any quantum mechanical system S of interest, as generally S will interact with the surrounding environment which will introduce deviations from the law in Eq. (2.40). Nevertheless, if one takes a larger system, consisting of S and its environment E, then the composite system $S + E$ can be considered, to a good approximation, as closed and thus its time evolution will indeed be unitary. Typically the system S is used to denote the atom of interest, whereas E refers to a phonon/photon bath. Let us initially assume that the density matrix of $S + E$ can be written as a separable tensor product of two density matrices, i.e.

$$\hat{\rho}(0) = \hat{\rho}_S(0) \otimes \left|i_E\right\rangle \left\langle i_E\right| , \tag{2.41}$$

where $\hat{\rho}_S(0)$ is the initial density matrix of S and $|i_E\rangle$ is some initial state of the environment. Since the time evolution of $S+E$ is unitary, with some operator $\hat{U}_{SE}$, it follows that

$$\hat{\rho}(t) = \hat{U}_{SE}\hat{\rho}(0)\hat{U}_{SE}^{\dagger} = \hat{U}_{SE}\hat{\rho}_S(0) \otimes |i_E\rangle \langle i_E| \hat{U}_{SE}^{\dagger}. \tag{2.42}$$

Tracing out the environment in Eq. (2.42), one obtains the density matrix of the system alone

$$\hat{\rho}_S(t) = \sum_{k_E} \langle k_E|\hat{\rho}(t)|k_E\rangle = \sum_{k_E} \langle k_E| \hat{U}_{SE}\hat{\rho}_S(0) \otimes |i_E\rangle \langle i_E| \hat{U}_{SE}^{\dagger} |k_E\rangle = \sum_{k_E} \hat{M}_{k_E}\rho_s(0)\hat{M}_{k_E}^{\dagger}, \tag{2.43}$$

where $|k_E\rangle$ is an arbitrarily chosen basis set of E and

$$\hat{M}_{k_E} = \langle k_E|\hat{U}_{SE}|i_E\rangle\,. \tag{2.44}$$

Based on this formalism, three different representative cases for this system+environment interaction will be outlined, and it will be shown how those lead to either phase-coherent or incoherent time evolution.

First, let us consider the phase-coherent case. Assume that after propagating $\hat{\rho}(0)$ in time, the environment does not change its state, but only the system S does, i.e. suppose that the unitary operator $\hat{U}_{SE}$ can be decomposed into the tensor product

$$\hat{U}_{SE} = \hat{U}_S \otimes \hat{I}_E, \tag{2.45}$$

where $\hat{U}_S$ is an operator acting on the Hilbert space $\mathscr{H}_S$ and $\hat{I}_E$ is the identity operator in $\mathscr{H}_E$. From the unitarity of $\hat{U}_{SE}$ and also the decomposition Eq. (2.45), it follows that $\hat{U}_S$ is also unitary and also that future states of the composite system are given as

$$|\Psi\rangle_S |i_E\rangle \to (\hat{U}_S |\Psi\rangle_S) |i_E\rangle\,. \tag{2.46}$$

This rather trivial case cannot be observed in practice, but to a certain degree of approximation one can get close. For example when the environment E describes a photon bath with a large photon density, such as in optical amplifiers, then it is obvious that a single transition of one carrier would not severely change the photon number in the bath and thus the statistical properties of E will be unaltered. This is namely the premise which will be employed in subsequent sections, where the coherent light-matter interaction will be treated without resorting to quantization of the electromagnetic field itself. For large photon numbers n, as assumed in this thesis, this semi-classical modeling is justified and in fact it can be shown that the fully quantum theory approaches the semi-classical model in the limit when $n \to \infty$ [76].

Next, consider a little less obvious scenario, modeling the coupling of a single, initially excited, atom with a photon field. Suppose that the atom, i.e. system S, has two possible states $|0\rangle_S$ and $|1\rangle_S$ denoting the ground and the excited state, respectively. Also, take an initially empty "environment", i.e. zero photons. Let $\gamma\delta t$ denote the probability of the atom to relax to its ground state, emitting a resonant photon in the process, within a time interval of δt seconds. Then, the evolution after time δt is non-unitary and is given as

$$|0\rangle_S |0\rangle_E \to |0\rangle_S |0\rangle_E\,, \tag{2.47}$$

$$|1\rangle_S |0\rangle_E \to \sqrt{1-\gamma\delta t}\,|1\rangle_S |0\rangle_E + \sqrt{\gamma\delta t}\,|0\rangle_S |1\rangle_E\,. \tag{2.48}$$

Next, trace out over the possible states of the environment E, and use the definition of the operators $\hat{M}_k$ to obtain

$$\hat{\rho}_S = \sum_{k\in\{0,1\}} \hat{M}_k \rho_S(0) \hat{M}_k^\dagger = \begin{bmatrix} \rho_{00} + \gamma\delta t \rho_{11} & \sqrt{1-\gamma\delta t}\rho_{01} \\ \sqrt{1-\gamma\delta t}\rho_{10} & (1-\gamma\delta t)\rho_{11} \end{bmatrix}, \tag{2.49}$$

where ρ_{ij} are the elements of the initial density matrix $\hat{\rho}_S(0)$ [77]. Finally, apply $\hat{U}_{SE}$ consecutively $m-$times to get

$$\hat{\rho}_S(t_m) = \begin{bmatrix} \rho_{00} + [1-(1-\gamma\delta t)^m]\rho_{11} & (1-\gamma\delta t)^{m/2}\rho_{01} \\ (1-\gamma\delta t)^{m/2}\rho_{10} & (1-\gamma\delta t)^m \rho_{11} \end{bmatrix}. \tag{2.50}$$

Equation (2.50) leads to the expected exponential decay of $\rho_{11}(t) = e^{-\gamma t}\rho_{11}(0)$ with the decay rate γ and a corresponding exponential loss of coherence $\rho_{01/10}$ with half of that rate, which is also familiar as lifetime broadening [22].

The last possible scenario to consider is the situation where upon interaction S does not change its energy/state, whereas the environment E undergoes a transformation. Such situations arise, for example, in modeling collisional broadening [76], where elastic collisions do not induce atomic transitions, but rather only random perturbations to the phase of S. This gives rise to the so called "pure dephasing" [76], which can be quite significant in QCLs due to intrasubband transitions [78], and can be modeled as an additional contribution to the decay rate in the time evolution of the off-diagonal elements of the density matrix.

At this point we are finished with the theoretical foundations needed to derive time-domain models for quantum cascade lasers. In the following sections we will employ the notations, definitions and principles outlined above to derive a concrete semi-classical light-matter interaction model suitable for simulating the dynamics of terahertz quantum cascade lasers, detectors and other meta-materials [5, 6, 79].

2.3.5 Unperturbed Hamiltonian

Until now no special assumptions about the nature of the quantum system under investigation had been made. At this point, a particular specialization of the physical laws to reflect the specifics of quantum cascade lasers is necessary. For example, depending on the level of detail in the undertaken modeling approach, various forms for the Hamiltonian operator can be assumed. In general $\hat{H}$ can be divided into the sum of the unperturbed system Hamiltonian, $\hat{H}_0$, and an additional term $\hat{H}_I$, which can include the physics of both single and many body interactions, such as carrier-phonon, carrier-carrier or carrier-light coupling [71]. The coherent inclusion (i.e. unitary evolution) of the full device physics into the dynamics is an enormous theoretical and practical endeavor which is out of the scope of this thesis. As an example of one such approach, one may give the so called non-equilibrium Green's function method and the interested reader may refer to the work in [7, 8, 52] for a more detailed overview. Instead, here a *divide and conquer* approach is adopted, where one treats coherently only the carrier-light coupling Hamiltonian ($\hat{H}_F$), whereas all other scattering mechanisms will be included via incoherent rate equations models, with the corresponding rates computed form Fermi's golden rule [52, 74].

The unperturbed Hamiltonian represents the bare superlattice Hamiltonian $\hat{H}_{SL}$ and an additionally applied external time-constant electric field F_0, parallel to the growth direction z, and is written as

$$\hat{H}_0 = \hat{H}_{SL} + eF_0\hat{z}, \tag{2.51}$$

where $\hat{z}$ is the position operator. In three dimensions, taking into account the periodicity of the crystal lattice via a position dependent effective mass tensor, Eq. (2.51) can be rewritten in coordinate representation as

$$\hat{H}_0 = \left[-\frac{\hbar^2}{2m^*_{\parallel}(z)}\nabla^2_{\parallel} - \frac{\hbar^2}{2}\partial_z\frac{1}{m^*_{\perp}(z)}\partial_z + V_{SL}(z) + eF_0z\right], \tag{2.52}$$

where $\nabla_{\parallel}$ and $m^*_{\parallel}(z)$ denote the in-plane direction (here assumed along the x and y coordinate axes) nabla differentiation operator and effective mass, respectively, $m^*_{\perp}(z)$ is the effective mass in the growth direction, $V_{SL}(z)$ is the superlattice potential (i.e. the conduction band profile of the heterostructure), F_0 denotes the strength (in units of V/m) of the applied bias field, and lastly $\hbar$ is the reduced Plank constant.

With this form of the Hamiltonian in mind, the next step is to look for the solution of the time-independent Schrödinger equation

$$\hat{H}_0\Psi(\vec{r}) = E\Psi(\vec{r}), \tag{2.53}$$

where $\vec{r}$ is the position vector in 3D. Due to the $x-y$ independence of the superlattice potential, as well as the applied field, one can factor $\Psi(\vec{r}) = \phi(z)F(\mathbf{r})$, where from now on $\mathbf{r}$ will be used to denote the 2D position vector in the in-plane direction, i.e. $\mathbf{r} = x\hat{e}_x + y\hat{e}_y$. Assuming $z-$independent term $m^*_{\parallel}$, simple algebraic manipulations give the general solution $\Psi_{m,\mathbf{k}}(\vec{r}) = \phi_m(z)e^{i\mathbf{k}\cdot\mathbf{r}}$ with $\mathbf{k} = (k_x, k_y)$ being the in-plane wave vector and $\phi_m(z)$ the $m-$th eigensolution of the Sturm-Liouville equation

$$\left[-\frac{\hbar^2}{2}\partial_z\frac{1}{m^*_{\perp}(z)}\partial_z + V_{SL}(z) - eF_0z\right]\phi_m(z) = E_m\phi_m(z). \tag{2.54}$$

It is worthwhile to note that $\phi_m(z)$ are formally referred to as the Wannier-Stark states and satisfy the translational symmetry relations

$$\phi_{m+N_p}(z) = \phi_m(z - L_p), \tag{2.55}$$

$$E_{m+Np} = E_m + eF_0L_p, \tag{2.56}$$

where N_p are the number of subbands considered per superlattice period and L_p is the length of the SL period [80].

Since $\hat{H}_0$ is diagonal in the basis of its eigenstates $\{\Psi_{m,\mathbf{k}}\}$, going back to Dirac notation, it can be expanded as

$$\hat{H}_0 = \sum_{m,\mathbf{k}} E_{m,\mathbf{k}} \left|\Psi_{m,\mathbf{k}}\right\rangle \left\langle\Psi_{m,\mathbf{k}}\right|, \tag{2.57}$$

where $E_{m,\mathbf{k}}$ is the energy of an electron in subband m with wave vector $\mathbf{k}$, also given as

$$E_{m,\mathbf{k}} = E_m + \frac{\hbar^2|k|^2}{2m^*_{\parallel}}, \tag{2.58}$$

where $k = |\mathbf{k}|$ is the magnitude of the wave vector.

2.3.6 Carrier-light interaction Hamiltonian

The carrier-light coupling is modeled to first order via the electric dipole approximation [76],

$$\hat{H}_F = e\hat{z}E_z(t), \tag{2.59}$$

where $\hat{z}$ denotes the position operator in $z-$direction, E_z is the corresponding component of the (classical) electric field vector and again e is the elementary charge. In the Wannier-Stark basis the matrix elements of H_F read

$$\langle \Psi_{m,\mathbf{k}_1} | \hat{H}_F | \Psi_{n,\mathbf{k}_2} \rangle = eE_z(t) \langle \phi_m | \hat{z} | \phi_n \rangle \delta(\mathbf{k}_1 - \mathbf{k}_2), \tag{2.60}$$

where the Dirac-delta $\delta(\mathbf{k}_1 - \mathbf{k}_2)$ term ensures that the optical coupling is $\mathbf{k}-$conserving and $z_{m,n} = \langle \phi_m | \hat{z} | \phi_n \rangle$ denotes the one dimensional dipole moment.

2.3.7 Time-evolution

Firstly, due to the 1D confinement of the electron inside the quantum well heterostructure, the basis of eigenstates of $\hat{H}_0$ is given as (in position representation)

$$\langle \vec{r} | \Psi_{m,\mathbf{k}} \rangle = \Psi_{m,\mathbf{k}}(\vec{r}) = \Phi_m(z) e^{i(k_x x + k_y y)}. \tag{2.61}$$

This yields the corresponding expression for the elements of the density matrix

$$\langle \Psi_{m,\mathbf{k}_1} | \hat{\rho} | \Psi_{n,\mathbf{k}_2} \rangle = \rho_{n,\mathbf{k}_2}^{m,\mathbf{k}_1}, \tag{2.62}$$

and also similar notation for the matrix elements of $\hat{H}$. Plugging this into Eq. (2.40), the time dynamical law for $\rho_{n,\mathbf{k}_2}^{m,\mathbf{k}_1}$ is obtained

$$i\hbar \partial_t \rho_{n,\mathbf{k}_2}^{m,\mathbf{k}_1} = \sum_{l,\mathbf{k}} H_{l,\mathbf{k}}^{m,\mathbf{k}_1} \rho_{n,\mathbf{k}_2}^{l,\mathbf{k}} - H_{n,\mathbf{k}_2}^{l,\mathbf{k}} \rho_{l,\mathbf{k}}^{m,\mathbf{k}_1}. \tag{2.63}$$

Next, one explicitly evaluates Eq. (2.63) by including the contribution of the unperturbed and interaction Hamiltonians and leaves out the rest of the system interactions to be treated separately. Since both $\hat{H}_0$ and $\hat{H}_F$ were shown to be $\mathbf{k}-$preserving, then it will be also reasonable to assume that for $\mathbf{k}_1 \neq \mathbf{k}_2$ it follows that $\rho_{n,\mathbf{k}_2}^{m,\mathbf{k}_1} = 0$ [71] (since there is no coherent coupling between states $|\Psi_{m,\mathbf{k}_1}\rangle$ and $|\Psi_{n,\mathbf{k}_2}\rangle$). This leads to the following set of equations

$$\partial_t \rho_{m,n;\mathbf{k}} = -i\frac{E_m - E_n}{\hbar} \rho_{m,n;\mathbf{k}} - i\frac{eE_z(t)}{\hbar} \sum_l z_{m,l}\rho_{l,n;\mathbf{k}} - z_{l,n}\rho_{m,l;\mathbf{k}}. \tag{2.64}$$

where the $\mathbf{k}-$dependence in the energy difference vanishes, since we have considered subband-independent in-plane effective mass $m_{\parallel}^*$. Since Eq. (2.64) is practically $\mathbf{k}-$independent, the degrees of freedom, and thus the computational complexity, of the end-system can be drastically reduced by summing over the possible states in $\mathbf{k}-$space. Define $\rho_{m,n} = \sum_{\mathbf{k}} \rho_{m,n;\mathbf{k}}$ and sum both sides of Eq. (2.64) to obtain

$$\partial_t \rho_{m,n} = -i\frac{E_m - E_n}{\hbar} \rho_{m,n} - i\frac{eE_z(t)}{\hbar} \sum_l z_{m,l}\rho_{l,n} - z_{l,n}\rho_{m,l}. \tag{2.65}$$

Indeed Eq. (2.65) is much simpler to solve (numerically) since we have effectively removed out the dependence on the wave vector $\mathbf{k}$ which had introduced intractable degrees of freedom in the general time evolution.

Lastly, to complete the picture, Eq. (2.65) will be supplemented with an additional term, describing the generally non-unitary nature of carrier dynamics. In the similar spirit as derived in the previous section, we will treat the rest of the intersubband scattering mechanisms via incoherent scattering rates $\Gamma_{i,f}$, where $\Gamma_{i,f}\delta t$ describes the probability of a carrier initially in state $|i\rangle$ to transition to state $|f\rangle$ within a time-interval δt. Adhering to the operator formalism introduced before, the term "$i\hbar\mathscr{G}(\hat{\rho})$" will also be added to the right hand side of Eq. (2.40) to denote those non-unitary contributions to $\partial_t\hat{\rho}$. In his seminal work in 1976 Lindblad derived the mathematical form which $\mathscr{G}(\hat{\rho})$ should have in order to describe a physically reasonable assumption [81]. For all possible $i \to j$ transitions, model $\mathscr{G}(\hat{\rho}) = \sum_{i,j}\mathscr{G}^{ij}(\hat{\rho})$, where

$$\mathscr{G}^{ij}(\hat{\rho}) = \hat{C}^{ij}\hat{\rho}\hat{C}^{ij\dagger} - \frac{1}{2}\left\{\hat{C}^{ij\dagger}\hat{C}^{ij};\hat{\rho}\right\}, \tag{2.66}$$

with $\hat{C}^{ij} = \sqrt{\Gamma_{i,j}}\,|j\rangle\langle i|$ and $\{\cdot;\cdot\}$ denoting the anti-commutator [81, 82]. Finally, in a similar manner, one also adds to Eq. (2.40) the sum

$$i\hbar\mathscr{D}(\hat{\rho}) = i\hbar\sum_{i,j}\hat{D}^{i,j}\hat{\rho}\hat{D}^{i,j\dagger}(\delta_{ij}-1) \tag{2.67}$$

to include "pure dephasing" to the time evolution of the off-diagonal elements of the density matrix with the rate $\Gamma^*_{i,j}$. Employing similar notation, $\hat{D}^{ij} = \sqrt{\Gamma^*_{i,j}}\,|j\rangle\langle i|$.

Despite their "fancy" operator-form, Eqs. (2.66)-(2.67) present a simple rate equation contribution to the "unitary" part of the von Neumann equation, which eventually do not pose any particular difficulties for their solution. As a conclusion, the complete time evolution of the reduced density matrix is written, describing the dynamics of a generic optical system, coherently interacting with a classical electric field E_z, and also including incoherent carrier scattering events, captured within the Lindblad formalism,

$$\partial_t\hat{\rho} = -\frac{i}{\hbar}\left[\hat{H}_0 + eE_z\hat{z};\hat{\rho}\right] + \sum_{i,j}\left[\hat{C}^{ij}\hat{\rho}\hat{C}^{ij\dagger} - \frac{1}{2}\left\{\hat{C}^{ij\dagger}\hat{C}^{ij};\hat{\rho}\right\} + \hat{D}^{i,j}\hat{\rho}\hat{D}^{i,j\dagger}(\delta_{ij}-1)\right]. \tag{2.68}$$

2.4 The Maxwell-Bloch equations

In this section we combine the field-evolution and carrier-transport models derived in Sec. 2.2 and Sec. 2.3 to obtain a comprehensive light-matter interaction model for dynamic simulations of quantum cascade lasers. The previously outlined framework is general enough to couple the full Maxwell's equation dynamics to an arbitrary level system, however due to its symbolic importance, here a detailed derivation and analysis of the two level Maxwell-Bloch equations in the rotating wave and the slowly varying envelope approximations will be presented.

First, take a two level system, consisting of an upper laser level $|a\rangle$ and a lower laser level $|b\rangle$, with respective eigenenergies E_a and E_b, such that $|a\rangle$ and $|b\rangle$ are radiatively coupled by

an electric field E_z with a dipole moment $z_{a,b}$. Quantum mechanically, the state is described by a 2x2 density matrix $\hat{\rho}$, where the unitary time evolution generator is the combined Hamiltonian

$$\hat{H} = \hat{H}_0 + \hat{H}_F = \begin{bmatrix} E_a & ez_{a,b}E_z \\ ez_{b,a}E_z & E_b \end{bmatrix}. \tag{2.69}$$

Taking the commutator of $\hat{H}$ with $\hat{\rho}$, plugging into the von Neumann equation Eq. (2.40), and expanding one gets

$$\partial_t \Delta_\rho = 2i\frac{ez_{a,b}}{\hbar}E_z(\rho_{a,b} - \rho^*_{a,b}), \tag{2.70a}$$

$$\partial_t \rho_{a,b} = -i\frac{E_a - E_b}{\hbar}\rho_{a,b} + i\frac{ez_{a,b}}{\hbar}E_z\Delta_\rho. \tag{2.70b}$$

Due to the Hermitian symmetry of the density matrix and the Hamiltonian, the original 4 coupled ODEs have been reduced to Eqs. (2.70) by assuming $z_{a,b} = z_{b,a} = z^*_{a,b}$ and denoting the population inversion as $\Delta_\rho = \rho_{a,a} - \rho_{b,b}$. Typically, the non-unitary time evolution of the resulting system is modeled either via rate equations, as in Eqs. (2.24)-(2.25), or by phenomenologically included "current" term, describing the steady injection of electrons into the upper laser level [21]. If one switches off the electric field, this injection current will lead to some steady state population inversion $\bar{\Delta}$ within some characteristic time constant T_1 (the population inversion lifetime). Additionally, since this non-unitary evolution does change the distribution of carriers in either level, as elaborated in Sec. 2.3.4, this would also lead to a corresponding lifetime broadening, next to which we also phenomenologically add a pure dephasing rate to obtain a total dephasing rate of $1/T_2$. Including these assumptions into Eq. (2.70), one can rewrite

$$\partial_t \Delta_\rho = 2i\frac{ez_{a,b}}{\hbar}E_z(\rho_{a,b} - \rho^*_{a,b}) - \frac{\Delta_\rho - \bar{\Delta}}{T_1}, \tag{2.71a}$$

$$\partial_t \rho_{a,b} = -i[\omega_{a,b} - i\frac{1}{T_2}]\rho_{a,b} + i\frac{ez_{a,b}}{\hbar}E_z\Delta_\rho, \tag{2.71b}$$

where $\omega_{a,b} = (E_a - E_b)/\hbar$ is the optical resonance's angular frequency. Several remarks here are in order. First of all, since we have taken that the field propagation direction is x (with heterostructure growth direction z), this implies the assumption that at every point x there is a separate two level system, with the total active region being described by a time and *position* dependent density matrix $\rho(x,t)$. Also, it is worth keeping in mind that ρ is a positive semidefinite, unitless quantity, the diagonal elements of which denote the probability of finding an electron in each respective state [75]. This means that in order to relate this microscopic, quantum mechanical description of the carrier dynamics, to a *macroscopic* classical variable of the electron ensemble, we need to take the expectation values of respective dynamical observables, and furthermore re-normalize these expectation values to the correct carrier densities. For example, for the dynamical observable O, described by the operator $\hat{O}$, the corresponding macroscopic value should be given as

$$O = N\langle\hat{O}\rangle = N\mathbf{tr}(\hat{\rho}\hat{O}), \tag{2.72}$$

where N is the carrier density in the system.

Now the coupling of Eqs. (2.70) to the Maxwell's equations Eqs. (2.5) is done straightforwardly, via the polarization term $P(x,t)$. Similarly to the polarization of a classical electric dipole [64], for the two level system $P(x,t)$ is given by

$$P(x,t) = -eN\langle\hat{z}\rangle = -eN\mathbf{tr}(\hat{\rho}(x,t)\hat{z}) = -eNz_{a,b}\left[\rho_{a,b}(x,t) + \rho_{b,a}(x,t)\right], \tag{2.73}$$

which, combined with Eq. (2.71b), allows for the explicit evaluation of

$$\partial_t P(x,t) = J(x,t) = -2eNz_{a,b}\left(\omega_{a,b}\,\mathrm{Im}\{\rho_{a,b}\}(x,t) - \frac{1}{T_2}\,\mathrm{Re}\{\rho_{a,b}\}(x,t)\right), \tag{2.74}$$

where the term $J(x,t)$ has been used to make explicit the fact that $\partial_t P$ is classically interpreted as the polarization-current density (bound charge current density) of the system.

2.4.1 Rotating wave approximation

Equations (2.5)-(2.71), coupled via Eq. (2.74) are commonly referred to as the full Maxwell-Bloch (MB) equations [53, 54]. In practice there is another, more commonly used, variant of the Maxwell-Bloch equations, also known as the optical-Bloch equations [18, 62, 64, 83–85], where the rotating wave approximation (RWA) and the SVEA have been employed to simplify the underlying system [62], which in some cases could even lead to an analytically tractable problem [86]. For the RWA, in addition to the factorization of the field into a product of a slowly varying envelope and a carrier wave Eq. (2.7), neglecting backward propagating waves for simplicity, one can also assume

$$\rho_{a,b} = \eta_{a,b}e^{i(\beta_0 x - \omega_0 t)}. \tag{2.75}$$

Now, plugging Eq. (2.75) into Eqs. (2.71), performing the multiplication, and (within the RWA) neglecting terms $\propto e^{\pm 2i\omega_0 t}$ [62], one eventually derives what will be referred to as the reduced Maxwell-Bloch equations

$$\frac{n}{c}\partial_t E_+ + \partial_x E_+ = -i\frac{N\Gamma e z_{a,b}\omega_0}{2\varepsilon_0 cn}\eta_{a,b} - \frac{a}{2}E_+, \tag{2.76a}$$

$$\partial_t \Delta_\rho = +i\frac{ez_{ab}}{\hbar}\left(E_+^*\eta_{ab} - E_+\eta_{ab}^*\right) - \frac{\Delta_\rho - \bar{\Delta}}{T_1}, \tag{2.76b}$$

$$\partial_t \eta_{ab} = i\left[(\omega_0 - \omega_{a,b}) + i\frac{1}{T_2}\right]\eta_{ab} + i\frac{ez_{ab}}{2\hbar}E_+\Delta_\rho. \tag{2.76c}$$

2.4.2 Susceptibility & gain coefficient

Here we will perform a steady state analysis of the optical Bloch equations to analyze the response of the system to an applied electric field. One very common approximation, called the "adiabatic limit", will be employed, which under the right conditions will allow to eliminate the term $\eta_{a,b}$ from the set of equations. The resulting system presents an incoherent model for light-matter interaction dynamics, which will be used to derive some useful expressions for the gain and linewidth enhancement factors, for the stimulated emission/absorption rates as well as for the susceptibility, a quantity representing the optical response of the ensemble.

In the adiabatic limit, suppose that $1/T_2 \gg |ez_{a,b}E_+/\hbar|$, which is satisfied for either weak optical fields or for fast dephasing rates. With this in mind, one can argue that $\partial_t \eta_{a,b} = 0$ can

be set. Indeed, when $1/T_2 \gg |ez_{a,b}E_+/\hbar|$ holds, any dipole oscillations induced by the electric field will quickly be dampened by the fast relaxation term and thus $\eta_{a,b}$ will be approximately stationary. Then the steady-state solution for $\eta_{a,b}$ is

$$\bar{\eta}_{a,b} = \frac{ez_{a,b}}{2\hbar} E_+ \Delta_\rho \times [\omega_0 - \omega_{a,b} - i\frac{1}{T_2}]/[(\omega_0 - \omega_{a,b})^2 + (\frac{1}{T_2})^2]. \tag{2.77}$$

Plugging Eq. (2.77) into Eq. (2.76a) and using the notation in Sec. 2.2 for the gain g and the linewidth enhancement factor α, we go back to Eq. (2.19)

$$\frac{n}{c}\partial_t E_+ + \partial_x E_+ = \frac{g}{2}(1 - i\alpha)E_+ - \frac{a}{2}E_+, \tag{2.78}$$

where this time the gain coefficient is $g = \sigma_{\omega_0}\Delta N$, with the scattering cross-section parameter

$$\sigma_{\omega_0} = \frac{\Gamma |ez_{a,b}|^2 \omega_0}{2\varepsilon_0 cn\hbar} \times \frac{1/T_2}{(\omega_{a,b} - \omega_0)^2 + (1/T_2)^2}, \tag{2.79}$$

the linewidth enhancement factor $\alpha = (\omega_{a,b} - \omega_0)T_2$, and the average number of active carriers $\Delta N = \Delta_\rho \times N$. Additionally, we can also derive an expression for the stimulated emission rate. Plugging in Eq. (2.77) into Eq. (2.76b) one obtains the rate equation for the population inversion

$$\partial_t \Delta_\rho = -\frac{|ez_{a,b}|^2}{2\hbar^2} \frac{1/T_2}{(\omega_0 - \omega_{a,b})^2 + 1/T_2^2} \times |E_+|^2 \Delta_\rho - \frac{\Delta_\rho - \bar{\Delta}}{T_1}, \tag{2.80}$$

with the stimulated emission/absorption rate

$$B_{a,b} = B_{b,a} = \frac{|ez_{a,b}|^2}{2\hbar^2} \frac{1/T_2}{(\omega_0 - \omega_{a,b})^2 + 1/T_2^2} \times |E_+|^2. \tag{2.81}$$

Lastly, using that $g = -\omega_0 \operatorname{Im}\{\chi\}/nc$ and $\alpha = \operatorname{Re}\{\chi\}/\operatorname{Im}\{\chi\}$ (as derived in Sec. 2.3.1) the complex susceptibility of the system can be found,

$$\chi = \operatorname{Re}\{\chi\} + i \operatorname{Im}\{\chi\} = \frac{\Delta N \Gamma |ez_{a,b}|^2}{2\hbar\varepsilon_0} \frac{1}{\omega_0 - \omega_{a,b} - i1/T_2}. \tag{2.82}$$

Notice that Eq. (2.82) is not the *linear* susceptibility of a two level system, even though it resembles the expression typically found in literature [62]. The fact that Eq. (2.82) contains the term $\Delta N = \Delta_\rho \times N$ means that χ will contain also optical nonlinearities, since Δ_ρ depends on $|E_+|^2$ via the rate equation Eq. (2.80).

2.5 Conclusion

In this chapter the main theoretical knowledge, needed to understand the following parts of the thesis, was introduced. Concretely, the traveling wave equation model was derived from Maxwell's equations, which was then coupled to various different methods for the theoretical treatment of the carrier dynamics. After presenting the intuitive rate equations approach, a more involved density matrix model was also derived. In the process, a short introduction of the theory of the density matrix, particularly focused on modeling of the carrier dynamics in quantum cascade lasers, by for example taking into consideration the specifics of the wave function, was outlined. Lastly, building upon the previous sections of the text, the celebrated Maxwell-Bloch equations were derived and analysis and interpretation of various quantities was presented.

3 Numerical Methods

3.1 Introduction

Except of a few limiting cases, the Maxwell-Bloch equations are not analytically solvable, and as such they need to be simulated on a computer. Numerical simulations have routinely been employed for the analysis of various light-matter interaction systems, ranging from investigations on self-pulsations in lasers [87], the coherent interaction of ultrafast pulses with matter [53], self-induced transparency mode-locking [88] and many others. Unlike the aforementioned scientific papers, which are typically concerned with very specific systems, i.e. with a well-defined set of parameters, and the equations are simulated over short time-intervals, the investigation of frequency comb formation with THz QCLs necessitates a drastically different simulation approach. First and foremost, in order to be able to capture various regimes of operation, i.e. ranging from single mode operation to coherent and incoherent multimode lasing, one cannot impose strict assumptions on the model parameters, except of course the restriction that the involved energies, lifetimes and losses are characteristic for those type of devices. Furthermore, especially for the simulation of comb-formation in free-running devices, where various mode proliferation and degradation mechanisms are at play, steady state is reached after a relatively long time-period (compared to the picosecond time-scales in the QCL active region) which necessitates millions of iterations until transients are eliminated. Therefore, for high-fidelity simulations, one must employ carefully selected algorithms, ones that do not introduce substantial numerical artifacts in the end result. As mentioned already, the situation is additionally complicated by the fact that (in general) the Maxwell-Bloch equations do not posses analytical solution, which makes the verification of the selected algorithm quite a difficult task. In this PhD thesis, building up on the results from my master thesis [89], several different algorithms for the numerical solution of the reduced Maxwell-Bloch equations will be investigated, and subsequently important properties which these algorithms must satisfy in order to deliver credible results will be outlined. Next, the proposed algorithms will be numerically tested in various simulation scenarios, in order to extract the best possible algorithm for the scientific investigations in upcoming chapters. As a final test, the selected algorithm will be additionally verified in a very specific simulation scenario, where the light-matter interaction dynamics is analytically solvable.

3.2 Discretization

In this section, three different numerical algorithms will be derived for the solution of the model advection-type equation

$$\frac{1}{c}\frac{\partial E_{\pm}}{\partial t} = \mp\frac{\partial E_{\pm}}{\partial x} + f_{\pm}(x,t) + kE_{\pm}, \tag{3.1}$$

where k is some real-valued constant (here assumed to be a negative number and hence representing linear losses) and $f_{\pm}(x,t)$ represents some (complex-valued) source term, which in the context of the Maxwell-Bloch equations models the (non-linear) optical response of the atomic system.

Before one can dive into details around the discretization methods, it will be useful to examine more carefully the various terms in Eq. (3.1), in order to understand the dynamics they are supposed to introduce. As mentioned, the term on the right hand side $kE_{\pm}$ models some linear response of the active medium to the presence of the electric field, where usually $k = -|\alpha|/2 < 0$ represents the waveguide amplitude losses ($|\alpha|$ representing the power losses). The latter typically arise due to free-carrier losses in the metal and doped semiconductor areas of the waveguide [90].

In addition, the term $f_{\pm}(x,t)$, is included to represent any nonlinear material response, e.g. optical gain, which arises in the active medium. As already mentioned in Sec. 2.3, various mathematical models can be employed to specify the term $f_{\pm}(x,t)$. If we assume, for simplicity, a ring-type of cavity, then it is reasonable to expect that the electric field will propagate in a single direction (e.g. in the positive x-direction). In that case, one of the simplest possible models for the optical gain can be given by the equation

$$f_{+}(x,t) = \frac{g(I_{+})}{2}E_{+} = \frac{g_0}{2}\frac{1}{1+I_{+}/I_{sat}}E_{+}, \tag{3.2}$$

where $I_{+} \propto |E_{+}|^2$ is the intensity of the forward propagating wave, and I_{sat} is the saturation intensity, defined as the intensity at which the gain coefficient $g(I_{+})$ is half its small signal value g_0.

With this form of $f_{+}(x,t)$ in mind, we recast Eq. (3.1), into an expression for the e-field intensity as follows

$$\frac{\partial I_{+}}{\partial t} + c\frac{\partial I_{+}}{\partial x} = c\left[\frac{g_0}{1+I_{+}/I_{sat}} - |\alpha|\right]I_{+}, \tag{3.3}$$

To gain further insight, integrate Eq. (3.3) over the full cavity length, e.g. 0-L, to obtain

$$\frac{d}{dt}\int_0^L I_{+}(x,t)dx = cI_{+}(0,t) - cI_{+}(L,t) + c\int_0^L \left[\frac{g_0}{1+I_{+}/I_{sat}} - |\alpha|\right]I_{+}(x,t)dx, \tag{3.4}$$

Ignoring the integral on the right hand side of the above equation, we see that Eq. (3.4) represents a conservation law, asserting that the *total* change in intracavity intensity is equal to the flux of intensity coming from the left side of the cavity, minus the flux of intensity exiting through the right side of the cavity, i.e. at point $x = L$. In case of periodic boundary conditions, i.e. $E_{+}(0,t) = E_{+}(L,t)$, both contributions cancel and we have the conserved quantity $Q(t) = \int_0^L I_{+}(x,t)dx$.

Next, let us examine the role of the third summand term on the right hand side of Eq. (3.4). First, due to the fact that $I_+ \geq 0$, we see that $g(I_+)$ attains its maximum g_0 at $I_+ = 0$ (hence the name *small-signal gain*) and monotonously decreases as a function of I_+. This means that in order for lasing to start whatsoever, the active region's g_0 coefficient must be larger than the power losses $|\alpha|$. If this condition is satisfied, the total intracavity intensity will gradually increase, which in turn will reduce the available gain, by virtue of Eq. (3.2). This process will continue unabated, until the system reaches *steady state* with $g(I_+) = |\alpha|$. From then on, again assuming periodic boundary conditions, the total intracavity intensity will remain constant at a value of

$$\bar{I}_+ = I_{sat}(\frac{g_0}{|\alpha|} - 1) \tag{3.5}$$

for all $x \in [0; L]$.

Furthermore, in this model one can additionally show that the obtained equilibrium is stable. To do so, let us assume that after steady state is established, the intracavity intensity gets perturbed by some small amount ΔI, i.e. $I_+ \to \bar{I}_+ + \Delta I$, which could be either a positive or a negative quantity. Plugging this into Eq. (3.4), we obtain that

$$\frac{d\bar{Q}(t) + \Delta Q(t)}{dt} = c[\bar{I}_+ + \Delta I] + c\int_0^L \left(\frac{g_0}{1 + (\bar{I}_+ + \Delta I)/I_{sat}} - |\alpha|\right)(\bar{I}_+ + \Delta I)dx, \tag{3.6}$$

where $[S]$ represents the difference $S(0,t) - S(L,t)$ and $\Delta Q = \int_0^L \Delta I dx$. Since ΔI is assumed to be small, we can expand the gain coefficient around $\bar{I}_+$ yielding

$$\frac{d\bar{Q}(t) + \Delta Q(t)}{dt} = c[\bar{I}_+ + \Delta I] + c\int_0^L \left(g(\bar{I}_+)(1 - \frac{\Delta I}{I_{sat}}) - |\alpha|\right)(\bar{I}_+ + \Delta I)dx, \tag{3.7}$$

Finally, using the equilibrium condition at $\bar{I}_+$ and eliminating higher order terms in ΔI, one can obtain a differential equation for the perturbation ΔQ

$$\frac{d\Delta Q}{dt} = c[\Delta Q] - cg(\bar{I}_+)\frac{I_+}{I_{sat}}\Delta Q. \tag{3.8}$$

In a periodic cavity $[\Delta Q] \equiv 0$ which directly yields the solution

$$\Delta Q(t + \Delta t) = e^{-cg(\bar{I}_+)\frac{I_+}{I_{sat}}\Delta t}\Delta Q(t). \tag{3.9}$$

From Eq. (3.9) we see that the perturbation will decrease exponentially to 0, with a characteristic time constant $\tau = I_{sat}/[cg(\bar{I}_+)I_+]$, which from the equilibrium condition Eq. (3.5) can be recast in the form

$$\tau = \frac{1}{c(g_0 - |\alpha|)}. \tag{3.10}$$

From the above discussion, it becomes evident how the examined system will 'self-regulate' itself to maintain equilibrium. Namely, when the total perturbation is positive $\Delta Q > 0$, the active region will provide a *negative* feedback to the system, whereas when $\Delta Q < 0$, the feedback will be positive.

Of course, in the more general situation, i.e. when $f_\pm(x,t)$ models the polarization $P_\pm$, which in turn satisfies a system of auxiliary differential equations, as in Eq. (2.76), the total system dynamics is substantially more complex and could posses both stable and unstable equilibria [84, 91].

3.2.1 The Lax-Wendroff method

After the short pedagogic discussion on the expected dynamics of the model Eq. (3.1), let us go back to the focal point of this chapter and discuss various discretization methods.

Equation (3.1) resembles the advection equation, which belongs to a more general family of conservation equations of the form

$$\frac{\partial U(x,t)}{\partial t} + \frac{\partial F(U)}{\partial x} = 0, \tag{3.11}$$

where U is the conserved quantity (or a vector of conserved quantities) and $F(U)$ is some (generally nonlinear) function of U determining the 'flux' of U at points x and t. Various numerical methods for the solution of conservation laws, such as Eq. (3.11), are familiar from the theory of computational fluid dynamics (CFD) [92]. One of the most celebrated such algorithms is the so called Lax-Wendroff method [93], and an outline of its derivation is presented in the following. It is worthwhile to note, however, that the propagation equation we are trying to solve here, i.e. Eq. (3.1), in general will *not* conserve $E_\pm$, due to the presence of the k factor as well as $f_\pm(x,t)$. Nevertheless, direct usage of numerical methods from the field of CFD is justified as Eq. (3.1) is structurally similar to Eq. (3.11), and it can be thought of as a conservation law with various sources and sinks, modeled namely by the inclusion of the polarization and linear losses terms.

Proceeding with the derivation of the Lax-Wendroff method, first of all, assume that the differential equation Eq. (3.1) is discretized over the equidistant grid $G_{\Delta x \Delta t} := \{(x_m, t_n) | x_m = m\Delta x \, , \, t_n = n\Delta t\}$, with the value of the e-field envelopes onto the grid given as $E_\pm(x_m, t_n) = E_\pm(m,n)$. As usual, to obtain a time-stepping procedure, we start with a Taylor series expansion of $E_\pm(x_m, t_{n+1})$ around the point x_m and t_n

$$E_\pm(m,n+1) = E_\pm(m,n) + \Delta t \frac{\partial E_\pm(m,n)}{\partial t} + \frac{\Delta t^2}{2}\frac{\partial^2 E_\pm(m,n)}{\partial t^2} + O(\Delta t^3). \tag{3.12}$$

Now the partial derivatives of the envelopes in t can be expressed as partial derivatives in x, due to the relation Eq. (3.1), which in turn can be discretized with suitable finite difference expressions. The following identities hold

$$\frac{\partial E_\pm}{\partial t} = \mp c \frac{\partial E_\pm}{\partial x} + c f_\pm(x,t) + ck E_\pm, \tag{3.13a}$$

$$\frac{\partial^2 E_\pm}{\partial t^2} = \mp c \frac{\partial^2 E_\pm}{\partial x \partial t} + c\frac{\partial f_\pm(x,t)}{\partial t} + ck\frac{\partial E_\pm}{\partial t}, \tag{3.13b}$$

$$\frac{\partial^2 E_\pm}{\partial t \partial x} = \mp c \frac{\partial^2 E_\pm}{\partial x^2} + c\frac{\partial f_\pm(x,t)}{\partial x} + ck\frac{\partial E_\pm}{\partial x}. \tag{3.13c}$$

Next, eliminating the mixed derivative from the equations we get

$$\frac{\partial^2 E_\pm}{\partial t^2} = c^2 \frac{\partial^2 E_\pm}{\partial x^2} + c\Big(\frac{\partial}{\partial t} \mp c\frac{\partial}{\partial x}\Big)(f_\pm(x,t) + kE_\pm), \tag{3.14}$$

which can be inserted in the Taylor expansion of Eq. (3.12). This procedure yields the Lax-Wendroff method

$$\begin{aligned} E_{\pm}(m,n+1) = E_{\pm}(m,n) + c\Delta t\Bigg\{ \mp \left[\frac{\partial E_{\pm}}{\partial x}\right]_m^n + f_{\pm}(m,n) + kE_{\pm}(m,n)\Bigg\} \\ + \frac{c^2\Delta t^2}{2}\Bigg\{ \left[\frac{\partial^2 E_{\pm}}{\partial x^2}\right]_m^n + \frac{1}{c}\left[\frac{\partial f_{\pm}}{\partial t}\right]_m^n \mp \left[\frac{\partial f_{\pm}}{\partial x}\right]_m^n \Bigg\} \\ + \frac{kc^2\Delta t^2}{2}\Bigg\{ \mp 2\left[\frac{\partial E_{\pm}}{\partial x}\right]_m^n + f_{\pm}(m,n) + kE_{\pm}(m,n)\Bigg\}, \end{aligned} \tag{3.15}$$

with the terms in square brackets being the finite difference approximations

$$\left[\frac{\partial E_{\pm}}{\partial x}\right]_m^n = \frac{E_{\pm}(m+1,n) - E_{\pm}(m-1,n)}{2\Delta x}, \tag{3.16a}$$

$$\left[\frac{\partial^2 E_{\pm}}{\partial x^2}\right]_m^n = \frac{E_{\pm}(m+1,n) - 2E_{\pm}(m,n) + E_{\pm}(m-1,n)}{\Delta x^2}, \tag{3.16b}$$

$$\left[\frac{\partial f}{\partial x}\right]_m^n = \frac{f_{\pm}(m+1,n) - f_{\pm}(m-1,n)}{2\Delta x}. \tag{3.16c}$$

A quick comment on the order of consistency of the numerical method is in order. By virtue of the Taylor expansion in Eq. (3.12) and Eq. (3.16), it is straightforward to see, by the way the scheme was constructed, that Eq. (3.15) has a local approximation error (LE) of the order $O([\Delta t \Delta x^2], [\Delta t^3])$. The LE is defined by

$$|E_{\pm}(m,n+1) - \tilde{E}_{\pm}(x_m, t_{n+1})|, \tag{3.17}$$

where $\tilde{E}_{\pm}$ is the analytical and $E_{\pm}(m,n+1)$ the numerical solution at the new time-step, assuming the initial condition $E_{\pm}(m,n) = \tilde{E}_{\pm}(x_m,t_n)$. For example, let us first examine the truncation error due to the finite difference approximation of the various spatial derivatives, e.g. $\partial f_{\pm}(x,t)/\partial x$. In Eq. (3.16) the central differences have been used to approximate the operator $\partial/\partial x$, from where it follows that the approximation error induced is $O(\Delta x^2)$. Even if the differential had been approximated only to first order accuracy in Δx, this would have not reduced the overall order of the approximation error, since all FD expressions involving $f_{\pm}$ are further multiplied by Δt^2, which reduces the total approximation error by this factor. Note that, due to the second term on the right hand side of Eq. (3.15), it is essential to use Eq. (3.16a) for $\partial E_{\pm}/\partial x$ in order to preserve the high order accuracy. Finally one gets an absolute local error of the order of $O(\Delta t^2 \Delta x)$. Similar analysis can be conducted for the approximation of the time derivative of $f_{\pm}(x,t)$, which will yield an absolute local error of the order $O(\Delta t^3)$.

Despite it's second order consistency (and conditional stability as it will be shown later), the Lax-Wendroff method is not the optimal candidate for the numerical solution of the propagation equation. To see why, let us consider the homogeneous case of Eq. (3.1), i.e. when both $k = 0$ and $f_{\pm}(x,t) \equiv 0$, for a wave propagating only in, for example, the forward direction. Applying the Lax-Wendroff method in this situation, yields the following difference equation

$$\frac{U_m^{n+1} - U_m^n}{\Delta t} + c\frac{U_{m+1}^n - U_{m-1}^n}{2\Delta x} = \frac{c^2\Delta t}{2}\frac{U_{m+1}^n - 2U_m^n + U_{m-1}^n}{\Delta x^2}, \tag{3.18}$$

where $U_m^n = E_+(m,n)$ is used. The solution to this difference equation will, in general, not satisfy the original propagation equation, but instead a different PDE, the so called *modified equation*. To find the analytical form of the latter, one needs to perform the reverse of the procedure that lead to the derivation of the numerical method, i.e. to substitute the finite differences with their Taylor expansions. Doing so, yields (for the separate terms)

$$\frac{U_m^{n+1} - U_m^n}{\Delta t} = U_t + \frac{\Delta t}{2} U_{tt} + \frac{\Delta t^2}{6} U_{ttt} + O(\Delta t^3), \tag{3.19a}$$

$$\frac{U_{m+1}^n - U_{m-1}^n}{2\Delta x} = U_x + \frac{\Delta x^2}{6} U_{xxx} + O(\Delta t^4), \tag{3.19b}$$

$$\frac{U_{m+1}^n - 2U_m^n + U_{m-1}^n}{\Delta x^2} = U_{xx} + O(\Delta x^2). \tag{3.19c}$$

Combining Eq. (3.19) and plugging into Eq. (3.18) produces the *modified equation*, which is the one actually solved by the Lax-Wendroff method,

$$\begin{aligned} U_t + cU_x = &-\frac{\Delta t}{2}(U_{tt} - c^2 U_{xx}) \\ &- \frac{\Delta t^2}{6} U_{ttt} - \frac{c\Delta x^2}{6} U_{xxx} + O(\Delta t^3, \Delta t \Delta x^2, \Delta t^2 \Delta x, \Delta x^3). \end{aligned} \tag{3.20}$$

Now, the first term on the right hand side of Eq. (3.20) is identically zero, as can be seen from Eq. (3.14), which leaves us with a second order truncation error, proportional to $\Delta x^2 U_{xxx}$. Note, that if we had expanded Eq. (3.12) only to first order in Δt, the second order derivatives on the right hand side above would have not canceled out. What that means is that during simulation, the presence of a diffusion term U_{xx} will lead to a numerical loss of energy, even for a conservative system. In fact, this kind of behavior is characteristic of first order linear numerical methods for Eq. (3.11), and its prevention requires restrictively small time-steps [94]. For the second order accurate Lax-Wendroff method, however, the dominant error term is (after expressing $U_{ttt} = -c^3 U_{xxx}$ [94])

$$U_t + cU_x = \frac{c\Delta x^2}{6}(\nu^2 - 1) U_{xxx} + \text{higher order terms}, , \tag{3.21}$$

with $\nu = c\Delta t / \Delta x$. Now, we have rid ourselves from the diffusion term, at the cost of introducing a *dispersive* term U_{xxx}. This is problematic, since this third order spatial derivative will induce nonphysical dispersion into the solution, which could have quite a dramatic effect on the credibility of the results, especially in the context of frequency comb simulations. Let us see if we can do better.

3.2.2 The Risken-Nummedal method

Equation (3.21) indicates that the third order derivative term could be eliminated if we set $c\Delta t = \Delta x$. In fact, in the homogeneous case, making that choice guarantees that the truncation error will be identically zero (i.e. the "higher order terms" will also cancel [94]) and thus the modified equation and the original equation will coincide, which also means that the numerical solution is in fact the analytical solution. Elaborating further, this could be the starting point for an improvement of the original Lax-Wendroff scheme in terms of improving its numerical dispersion error.

Such an algorithm for the computer-based solution of Eq. (3.1) was introduced already in 1968 by H. Risken and K. Nummedal in [87]. The derivation basically proceeds in an analogous way to that of the Lax-Wendroff method, with two subtle differences. First of all, the "magic time-step" condition that $c\Delta t = \Delta x$ is imposed. This ensures that the expression

$$E_{\pm}(m \mp 1, n) = E_{\pm}(m, n) \mp c\Delta t \left[\frac{\partial E_{\pm}}{\partial x}\right]_m^n + \frac{c^2\Delta t^2}{2}\left[\frac{\partial^2 E_{\pm}}{\partial x^2}\right]_m^n, \tag{3.22}$$

where the partial derivatives are approximated as in Eq. (3.16), holds. As shown above, this eliminates the dispersive terms form the modified PDE of the homogeneous part of the equation. Secondly, to discretize the inhomogeneous part of the propagation equation, the spatial derivatives of $E_{\pm}$ or $f_{\pm}$ are approximated with a forward or backward finite differences, depending on the direction of wave propagation, to yield the the RNFD (Risken-Nummedal Finite-Differences) algorithm

$$\begin{aligned} E_{\pm}(m, n+1) = {} & E_{\pm}(m \mp 1, n) + c\Delta t\big(f_{\pm}(m, n) + kE_{\pm}(m, n)\big) \\ & + \frac{c^2\Delta t^2}{2}\left\{\frac{1}{c}\left[\frac{\partial f_{\pm}}{\partial t}\right]_m^n \mp \left[\frac{\partial f_{\pm}}{\partial x}\right]_m^n \mp 2k\left[\frac{\partial E_{\pm}}{\partial x}\right]_m^n + kf_{\pm}(m, n) + k^2 E_{\pm}(m, n)\right\} \end{aligned} \tag{3.23}$$

with

$$\left[\frac{\partial E_{\pm}}{\partial x}\right]_m^n = \pm 1\frac{E_{\pm}(m, n) - E_{\pm}(m \mp 1, n)}{\Delta x}. \tag{3.24}$$

By way of construction, we saw that when $k = 0$ and $f \equiv 0$, then the RNFD method satisfies the original PDE exactly, i.e. the modified equation and the propagation equation are equivalent. In order to obtain some insight about eventual numerical issues introduced by this method, one would need to analyze not the homogeneous conservation law, but rather

$$\frac{\partial E_+}{\partial t} = -c\frac{\partial E_+}{\partial x} + ckE_+, \tag{3.25}$$

where again only the case of a forward propagating wave will be considered (for simplicity). Here, the term $f_+(x, t)$ was omitted, since it is too general to be susceptible to analysis. A tedious, but conceptually simple, calculation yields the modified equation of the RNDF method

$$U_t + cU_x - ckU = \frac{\Delta t^2 c^3 k^2}{2}U_x - \frac{\Delta t^2 k^3 c^3}{6}U + O(\Delta t^3). \tag{3.26}$$

Two things become evident from the above expression. First of all, when $k \neq 0$, then the RNFD method does not deliver the exact solution (as expected), and secondly, the leading error terms introduce small modifications of both the propagation velocity and the losses. Rewriting Eq. (3.27) becomes

$$U_t + c(1 - \frac{\mu}{2})U_x - ck(1 - \frac{\mu}{6})U = O(\Delta t^3). \tag{3.27}$$

Here $\mu = \Delta t^2 c^2 k^2$ denotes the modification factor, and represents a unitless quantity, the magnitude of which is easily calculated. For typical values of $\Delta t \approx 10^{-13}\ \mathrm{s}$, $k \approx 1000\ \mathrm{m}^{-1}$ and the velocity of light rounded to $c = 3 \times 10^8\ \mathrm{m/s}$, μ is 0.09%, which is too small to have considerable impact.

Next, the analysis of the RNFD scheme is continued, by demonstrating that it satisfies an essential numerical property, that of *monotonicity preservation*. For a partial differential equation, a monotonicity preserving scheme can be formally defined as follows [92].

Definition 3.1 *A numerical scheme for the solution of Eq. (3.11) is called monotonicity preserving if for every non-decreasing (non-increasing) initial condition*

$$\{\phi_j^0\} = \{..., \phi_{j-1}^0, \phi_j^0, \phi_{j+1}^0, ...\},$$

the numerical solution at all later time-instances

$$\{\phi_j^n\} = \{..., \phi_{j-1}^n, \phi_j^n, \phi_{j+1}^n, ...\},$$

for $n = 1, 2...$*, is non-decreasing (non-increasing).*

From the above definition one intuitively sees that if a scheme is monotonicity preserving, then the numerical solution is less likely to have phase errors. In Fig. 3.1, a hypothetical example of a Gaussian pulse, propagated with a scheme that does not posses this property [92], is shown.

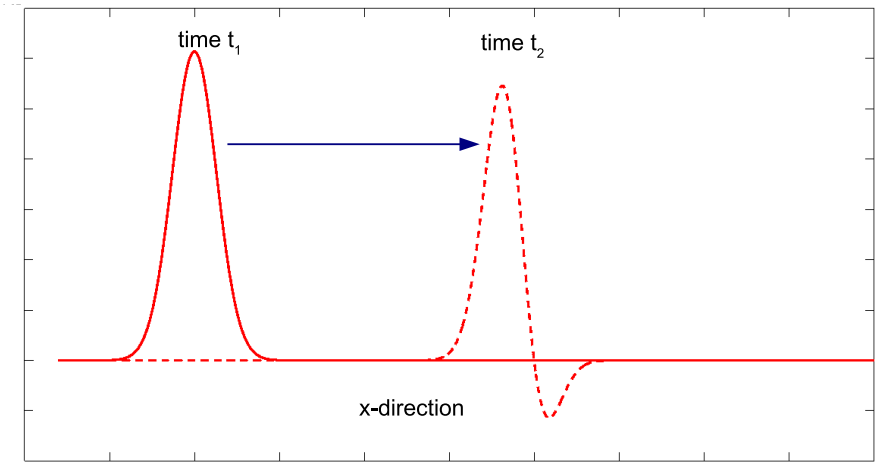

Figure 3.1 A Gaussian pulse being propagated between times t_1 and t_2 along the positive x-direction, by a scheme that does not preserve monotonicity.

It can be easily seen that, in case $f_\pm \equiv 0$, a sufficient condition for the RNFD scheme to be monotonicity preserving does exist. One can prove the following lemma, shown here for the case of a wave propagating in positive x-direction.

Lemma 3.2 *The Risken-Nummedal finite difference scheme, i.e. Eq. (3.23), for the solution of Eq. (3.25) is monotonicity preserving if* $k \geq 0$ *or, for* $k < 0 \Rightarrow \Delta t \leq \frac{1}{|ck|}$.

Proof Assume that the initial sequence $\{E_+(m,n)\}$ is non-decreasing. From Eq. (3.23), set $f_\pm(x,t) \equiv 0$, and drop the subscript $+$ for simplicity. Then the update rule reads

$$E(m, n+1) = (1 + ck\Delta t)E(m-1, n) + \frac{\Delta t^2 c^2 k^2}{2} E(m, n), \tag{3.28}$$

$$E(m+1, n+1) = (1 + ck\Delta t)E(m, n) + \frac{\Delta t^2 c^2 k^2}{2} E(m+1, n). \tag{3.29}$$

Now taking the difference Eq. (3.29) - Eq. (3.28)

$$E(m+1,n+1) - E(m,n+1) = (1+ck\Delta t)[E(m,n) - E(m-1,n)] + \frac{\Delta t^2 c^2 k^2}{2}[E(m+1,n) - E(m,n)]. \tag{3.30}$$

The second term on the right hand side is always positive, since we have assumed that the sequence at time t_n is non-decreasing, while the first term is > 0 in two cases

1. if $k \geq 0$, or
2. $k < 0$ and $(1 - |ck|\Delta t) \geq 0$, i.e. $\Delta t \leq \frac{1}{|ck|}$.

The latter condition imposes a restriction on the chosen time-step. To estimate how consequential that is, simply plug in the above quoted values for c and k, to obtain $1/|ck| \approx 3.3\,\mathrm{ps}$. This value is much longer than our characteristic time-step Δt.

As for the Lax-Wendroff scheme, we have already seen that the modified equation, among other terms, contains third order spatial derivatives of the propagating wave. This indicates that the numerical solution will *not* be monotonicity preserving. In fact, a more general statement can be proven about higher order, one-step linear numerical methods for the solution of the advection equation. This result is famous as the "Godunov's Order Barrier Theorem" [95, 96] and is re-stated below.

Theorem 3.3 *(Godunov's Barrier Theorem)*
Linear one-step second-order accurate numerical schemes for the convection equation

$$\frac{\partial \varphi}{\partial t} + c\frac{\partial \varphi}{\partial x} = 0, \quad t > 0, \quad x \in \mathbb{R} \tag{3.31}$$

cannot be monotonicity preserving, unless

$$\sigma = |c|\,\frac{\Delta t}{\Delta x} \in \mathbb{N}. \tag{3.32}$$

3.2.3 Method of lines approach

Next, the method of lines approach to derivation of numerical schemes will be introduced. The basic algorithm originates from the idea of reducing the solution of a PDE to that of a system of ordinary differential equations (ODEs), by discretizing along all but one coordinate and propagating the resulting tensor with one of the many ODE solvers from literature [97].

The semi-discretized version of Eq. (3.1) is written as

$$\frac{d\mathbf{V}^{\pm}}{dt} = \mp cD_N\mathbf{V}^{\pm} + \mathbf{F}^{\pm} + ck\mathbf{V}^{\pm}\,, \tag{3.33}$$

where $\mathbf{V}^{\pm}$ is the vector-valued representation of the solution, already discretized over a finite spatial grid, i.e. $\mathbf{V}_i^{\pm}(t) = E_{\pm}(x_i,t)$. Once the grid size and grid points have been determined, one needs to approximate all spatial derivatives by a suitable transformations in the N-dimensional vector space. In this thesis, D_N is used to denote a linear such transformation by means of a specifically chosen differentiation matrix. Lastly $\mathbf{F}^{\pm}$ is $cf_{\pm}(x,t)$, also sampled on the same spatial grid.

When we have reduced the equation to a system of ODEs, we are left their integration in time, for which a great variety of algorithms exist. In this thesis, due to its relative simplicity and high order of accuracy, I have selected the m-step Adams-Bashforth (AB) method as time-propagator. Of course other methods could also be used, such as for example Runge-Kutta or Backward Differentiation Formulas (BDF) [97], but those were not rigorously investigated, since the former method empirically delivered credible results, as it will be seen in Sec. 3.3.3. For any arbitrary m the linear, $m-$step AB method reads

$$(\mathbf{V}^{\pm})^{n+1} = (\mathbf{V}^{\pm})^{n} + \Delta t \sum_{j=0}^{m-1} a_j \Big(\mp c D_N (\mathbf{V}^{\pm})^{n-j} + (\mathbf{F}^{\pm})^{n-j} + ck(\mathbf{V}^{\pm})^{n-j} \Big) , \tag{3.34}$$

with coefficients a_j, chosen as to maximize the order of the approximation error [97].

To complete the description, the differentiation matrix D_N also needs to be specified. There are various ways to define D_N, such as for example compact high-order finite differences approximation schemes [98], or one can also use spectral differentiation matrices [99]. For the purpose of this thesis, a Chebyshev differentiation matrix D_N is chosen [99], which is known to result in extremely high order accurate (i.e. $O(\Delta x^N)$) approximation of the spatial derivative. However, this comes at a cost of increased computational complexity since D_N is essentially dense, and it is well known that dense matrix-vector multiplication is an expensive procedure.

The individual elements of D_N can be computed from the formulas [100]

$$(D_N)_{00} = \frac{2N^2+1}{6}, \qquad (D_N)_{NN} = -\frac{2N^2+1}{6}, \tag{3.35}$$

$$(D_N)_{jj} = \frac{-x_j}{2(1-x_j^2)}, \qquad j = 1, 2...N-1, \tag{3.36}$$

$$(D_N)_{ij} = \frac{c_i}{c_j} \frac{(-1)^{i+j}}{x_i - x_j}, \qquad i \neq j \quad i,j = 1, 2...N-1 \, , \tag{3.37}$$

where $c_i = 2$ if $i = 0$ or N and $c_i = 1$ otherwise.

Unfortunately, checking for the monotonicity preservation property, even in the simplest case when the time propagator is the explicit Euler scheme, yields that the above derived method is not monotonicity preserving. For more complicated time-propagators (for e.g. the AB method), it is rather difficult to prove general statements about this property. Instead, computational experiments can be conducted to uncover the degree to which numerical dispersion errors are introduced by the scheme.

Since numerical dispersion errors arise mainly when the gradient of the solution is large, one can design simple tests to capture such effects. Consider the propagation of a box-car pulse in the positive x-direction of a ring-type cavity. For simplicity, here the homogeneous version of Eq. (3.1) is propagated with the Lax-Wendroff, RNFD and the method of lines numerical schemes. The results are plotted in Fig. 3.2.

The image clearly illustrates the problems which arise with the Lax-Wendroff and the method of lines approaches. One can see how the solution immediately develops strange oscillations around the steep gradient, the origin of which is purely numerical. In contrast, the RNFD method (the solid red line on Fig. 3.2) does not suffer from these issues as it propagates the solution exactly.

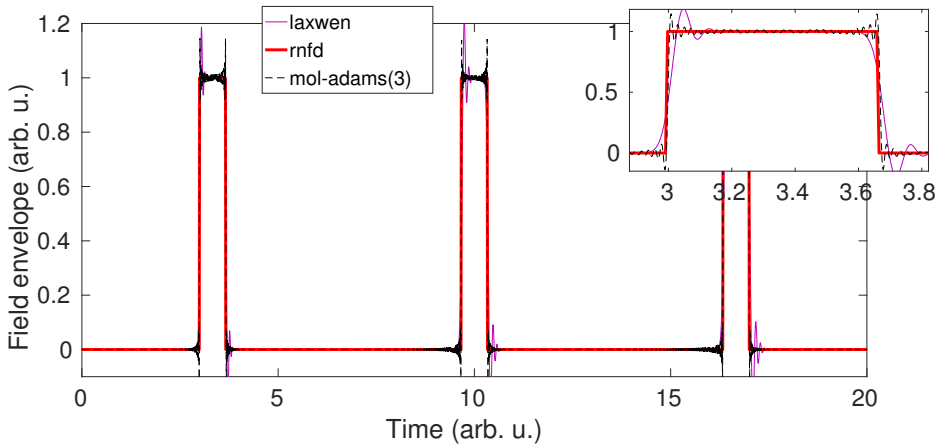

Figure 3.2 A box-car shaped pulse being propagated for with the Lax-Wendroff, RNFD and method of lines approach for a little longer than three round trips. The inset represents a zoom in of the pulse from the first round trip.

It is easy to extrapolate this in the context of simulations of free running QCLs. In this more complex scenario, such numerical errors could severely damage the quality of the solution as they could obscure important physical effects. As such, it is rather clear that the RNFD method is possibly the best algorithm to use in these cases. Nevertheless, in order to substantiate the choice of a numerical method even more, in the following section the convergence properties of each scheme will also be investigated.

3.3 Implementation and testing

3.3.1 Wave equation solvers

In this subsection it will be shown, by means of numerical experiment, that Lax-Wendroff and the RNFD schemes are second order consistent in both time and space. Of course, this could naturally be expected from the analytical derivation presented in the preceding sections, but it is always nice to verify one's implementation by investigating to what extend does each scheme satisfy its mathematically provable properties.

The method of lines approach, on the other hand, is expected to have order of consistency dominated by the accuracy of the chosen time-propagation scheme, due to the fact that the error induced by approximating the spatial derivative is much smaller than the errors during time-stepping.

As a benchmark, the following test function can be specified, which satisfies Eq. (3.1), for $k = 0$ and

$$f_+(x,t) = (x + ct)e^{i(\beta x - \omega t)}. \tag{3.38}$$

This solution is given by

$$u(x,t) = xte^{i(\beta x - \omega t)} + \text{ constant }, \tag{3.39}$$

where the usual dispersion relation $\omega/c = \beta$ holds (and here $c > 0$ is assumed).

To measure the local approximation error, the standard L_∞ metric is used, with the error at time step t_n defined as

$$\epsilon_n = ||y^n - u(x, t_n)||_\infty, \tag{3.40}$$

where y^n is the numerical solution at the current step and $u(x, t_n)$ is the analytical solution evaluated at time t_n onto all grid points x. Next, the global approximation error, after N_t-iterations of the algorithm, is given by

$$\epsilon = \max_{n=1,2..N_t} \epsilon_n. \tag{3.41}$$

Furthermore, since one would like to examine the convergence properties of the solution upon variation of both ω and N, two additional quantities can be defined, denoted by $\langle \rho_N \rangle$ and $\langle \rho_\omega \rangle$. Those are simply the averaged convergence rates of each method's global error as a function of grid size N and angular frequency ω, respectively. The term "convergence rate" denotes the exponential dependence of the error with respect to the cited quantity. For example, for two measurements of the error as a function of, e. g. the grid size N, ρ_N is calculated from

$$\rho_N = \frac{\log \epsilon(N_1) - \log \epsilon(N_2)}{\log N_2 - \log N_1}, \tag{3.42}$$

with N_i denoting the selected grid size and $\epsilon(N_i)$ the calculated global error for simulations with N_i points. In case of several measurements, each conducted on a different grid size N_i (or in that context also ω_i), the arithmetic average is taken as a qualitative measure.

For the numerical experiments, the cavity is assumed to be of length 3, the phase velocity of the wave is set to $c = 1$ and the simulation time interval is chosen to be $T = 1$ (in arbitrary units). With this setup, Table 3.1 illustrates the global approximation error for all three numerical methods, when the number of grid points N and the angular frequency ω are varied. Importantly, in all measurements, the magic time-step condition $c\Delta t = \Delta x$ holds, whereas for the method of lines approach, due to the non-equidistant nature of the computational grid, $\Delta x = x_1 - x_0$ has been chosen. Lastly, for time-propagation of the semi-discretized solution vector $\mathbf{V}(t)^+$, the 3-step Adams-Bashforth method has been used.

First of all, it is worthwhile to notice that both the Lax-Wendroff method and the RNFD method deliver equivalent results. This comes to no surprise, since it was already shown that when the magic time-step is assumed, and also when $k = 0$, these methods deliver identical results. Also, both methods are *second* order convergent, since the convergence rate $\langle \rho_N \rangle \approx 2$ in all experiments, which is in excellent agreement with the derived theoretical results and confirms the validity of our implementation. Additionally, these finite difference schemes seem to exhibit a quadratic dependence on the angular frequency parameter ω, with the numerical solution diverging from the analytical such when the ratio ω/N increases (hence the negative sign in $\langle \rho_\omega \rangle$). This is also not unexpected, since in such finite difference approximations one would need several grid points per oscillation period, in order to be able to correctly resolve the underlying frequency.

Next, one can examine the results from simulations based on the *m.o.l.-adams* approach. As mentioned, in the conducted numerical experiments the time-propagator was provided with 3 initial conditions (as needed by the 3-step AB-method), so that the error in the solution is dominated by the error originating from the discretization in time. That being said, the numerical tests indicate that the convergence rate (for small values of ω) is approximately $\rho_N \approx 4$! The

Table 3.1 RNFD (*rnfd*), Lax-Wendroff (*laxwen*) and the method of lines (*m.o.l.-adams*)'s global error ϵ as a function of the grid size N and the frequency ω.

	ω=4	ω=16	ω=64	ω=256	$\langle\rho_\omega\rangle$
rnfd					
N = 512	2.8329e-04	4.4060e-03	7.0111e-02	1.0571e+00	-1.9776
N = 1024	7.0838e-05	1.1018e-03	1.7580e-02	2.7714e-01	-1.9890
N = 2048	1.7697e-05	2.7526e-04	4.3951e-03	7.0055e-02	-1.9918
$\langle\rho_N\rangle$	2.0004	2.0003	1.9978	1.9577	
laxwen					
N = 512	2.8329e-04	4.4060e-03	7.0111e-02	1.0571e+00	-1.9776
N = 1024	7.0838e-05	1.1018e-03	1.7580e-02	2.7714e-01	-1.9890
N = 2048	1.7697e-05	2.7526e-04	4.3951e-03	7.0055e-02	-1.9918
$\langle\rho_N\rangle$	2.0004	2.0003	1.9978	1.9577	
m.o.l.-adams					
N = 512	3.0432E-07	1.2133E-06	2.2422E-05	2.9048E+00	-1.9816
N = 1024	1.8725E-08	7.4656E-08	3.7858E-07	2.5645E+00	-1.6481
N = 2048	1.1612E-09	4.6297E-09	1.8515E-08	1.3228Ee-06	-1.3169
$\langle\rho_N\rangle$	4.0042	4.0042	4.0673	5.9983	

origin of this discrepancy is currently unknown to me, but could probably be attributed to some kind of averaging effect between the global error induced by the time-stepping procedure and the global error of the spectral differentiation procedure. Next, it can be noticed that *m.o.l.-adams* delivers significantly smaller magnitudes of ϵ, and that the method is visibly less sensitive to the angular frequency ω (with the exception of the results for $\omega = 256$). Nevertheless, the calculation time needed to compute the solution (especially for $N = 2048$), is much longer due to the $O(N^2)$ complexity of the matrix-vector multiplication operation (Eq. (3.34)), which makes the usage of this method for long-time simulations impractical.

Finally, a brief mention on the stability properties of the three different algorithms must be included. I will not go in great detail, as those results were already presented elsewhere [89], and instead will expose only a brief summary of the most important points.

First of all, conventional von Neumann stability analysis of the finite difference schemes, shows that both the *rnfd* and the *lax-wen* methods are *conditionally* stable [89], with the stability condition $r < 1$ (where $r = c\Delta t/\Delta x$ is also known as the Courant number) for the *lax-wen* method. Furthermore, the analysis showed that the choice of the *magic time-step* for the *rnfd* method automatically guarantees the stability of the *rnfd* method.

On the other hand, the stability of the method of lines approach was not verified analytically, as it depends on the properties of the used time propagation scheme. Furthermore, for this algorithm there is no straightforward definition of a Courant number, because the interpolation in Sec. 3.2.3 is performed on a non-equidistant spatial grid. For these reasons the stability of the method was investigated only numerically, via simulations of the planted solution in Eq. (3.39).

Table 3.2 Stability check for the *m.o.l-adams* approach in combination with different variants of the m-step Adams-Bashforth method. For comparison, simulation data with the default version of Matlab's *ode45* time propagator has also been included. Reprinted from [89].

✓-stable x-unstable	$2-$step A.B.	$3-$step A.B.	$4-$step A.B.	$5-$step A.B.	*ode45*
r = 0.4	✓	✓	✓	✓	✓
r = 0.6	✓	✓	✓	x	✓
r = 0.8	✓	✓	✓	x	✓
r = 1.0	✓	✓	x	x	✓
r = 1.2	✓	✓	x	x	x

As it is often the case that it takes some time for the round-off error to build up and manifest itself, one needs to ensure that the simulation runs over a long enough time interval. For that purpose, the simulation time T was set to $T = 20$ (in arbitrary time-units). Additionally, the order of the m-step Adams-Bashforth method was examined by varying the parameter m and for comparison, time-stepping with the famous *Matlab* ODE solver, the adaptive Runge-Kutta method *ode45* [101], was also performed. The results were obtained for the parameters set: $c = 1$, $\omega = 4$, $T = 20$ and the domain $[0; 3]$, with $r = c\Delta t/\min(\Delta x_j)$. With those "initial conditions" the above outlined numerical tests reveal the following stability properties for *m.o.l.-adams*, summarized in Tab. 3.2.

3.3.2 Density matrix equations solver

The optical Bloch equations, e.g. Eqs. (2.76b)-(2.76c) constitute a system of ODEs describing the population dynamics of the atoms in our lasing material during its interaction with the optical field. For the numerical solution of such systems, a wide range of numerical algorithms is available. In this work, a family of multi-step Adams-Bashforth methods are suggested as a suitable tool for the task. In general, the linear $m-$step Adams-Bashforth method, for the solution of the equation

$$\frac{dy}{dt} = f(t, y) \, , \tag{3.43}$$

can be written down in the following simple form

$$y^{n+1} = y^n + \Delta t \sum_{k=0}^{m-1} c_k f(t_{n-k}, y^{n-k}) \, , \tag{3.44}$$

where the coefficients c_k are chosen so that the order of consistency of the method is maximized. As the relevant theory is well established [97, 102, 103], it is not worthwhile to go in great detail in revealing these methods' convergence and stability properties, but instead the focus is shifted on testing the numerical implementation.

A mention of a peculiar detail about the computer implementation of the multi-step Adams-Bashforth method is in order. For each m, as seen from Eq. (3.44) the $m-$step AB method needs no more and no less than m past instances of $f(t, y)$. However, in computational physics and similar disciplines, it is usual to have only a single initial condition, from which one

wishes to evolve the system in time, and similarly only the 'gradient' at the current time point (n) is known. To deal with this issue the implementation is adapted as follows. First of all, during initialization, the $m-$step Adams-Bashforth solver checks how many initial $f(t, y)$'s have been provided, and automatically chooses the coefficients c_k, in order to achieve a maximal order of the approximation error. For example, if only p instances of $f(t, y)$ (with $p < m$), are given, the implementation 'regresses' to a $p-$step Adams-Bashforth method for a single time step. After that time step, the algorithm updates its history and its coefficients, becoming a $(p+1)-$ step method and so on, until m is reached. As it will be shown further below, this does affect the quality of the algorithm as it reduces the overall order of approximation. However, for the purposes of this thesis, i.e. simulations of free running QCLs, where typically one starts with random initial conditions, this issue does not pose any serious threat.

Table 3.3 Numerical errors in the solution of Eq. (3.45), accumulated by the m-step Adams-Bashforth solver for different values of m and Δt. For each m and Δt pair, we are looking at two different cases, one where the solver has been initialized with the full set of initial conditions, i.e. 3, 4 and 5 initial points, respectively, and the scenario where only the initial point, $y(0) = 1$, was specified. Last line includes the calculated convergence rates of the solvers with respect to the choice of step-size. Reprinted from [89].

3-step A.B.		4-step A.B.		5-step A.B.		Δt
3 i.c.	1 i.c.	4 i.c.	1 i.c.	5 i.c.	1 i.c.	
2.13E-05	4.98E-04	6.19E-07	4.89E-04	1.83E-08	4.89E-04	1.56E-03
2.66E-06	1.23E-04	3.87E-08	1.22E-04	5.73E-10	1.22E-04	7.81E-04
3.33E-07	3.07E-05	2.42E-09	3.06E-05	1.79E-11	3.06E-05	3.91E-04
3.00	2.01	4.00	2.00	5.00	2.00	$\leftarrow \rho(\Delta t)$

Expectedly, with the above mentioned approach one will not gain the full order of accuracy of a $m-$step A.B. method unless the solver is initialized with exactly m initial conditions. From some tests, it turns out that for the adaptive approach, when one supplies only a single initial data (p = 1), the implementation results in a method with maximal order of accuracy up to 2.0, for $m = 3, 4, 5$. If, however, the solver is provided with a complete set of initial data points, the full $m-$th order accuracy is recovered, as predicted by theory. The implementation has been tested on the equation

$$\begin{aligned} &\frac{dy}{dt} = ky, \quad k < 0, \\ &y(0) = 1, \end{aligned} \tag{3.45}$$

which has the analytical solution $y(t) = e^{kt}$. The global approximation errors for $k = -1 + 20i$ and simulation window $T = 10$, for 3, 4 and 5-step Adams-Bashforth methods, are summarized in Tab. 3.3. The data is divided in two different categories, depending on the initial setting. First, this is when the solver has been initialized with the full set of initial conditions (i.c.), i.e. 3, 4 and 5 initial points, respectively, compared to the setup where only one initial point is specified at $y(0) = 1$.

3.3.3 Putting it all together

After having separately tested all the numerical solvers, it is clear that the Risken-Nummedal finite differences algorithm is superior to its two alternatives, the Lax-Wendroff and the method of lines approaches, for the simple reason that it is both second order consistent, stable (under the magic time-step condition) and also monotonicity preserving. Additionally, from implementation point of view, the RNFD algorithm computes several vector operations (i.e. multiplication of a vector by a number, addition of two vectors etc.), and as such has the inherent complexity of $O(N)$, where N is the number of grid points along the propagation direction, which makes it the preferred algorithm to the *m.o.l-adams* method.

For the density matrix equations, the $m-$th order Adams-Bashforth method has high order of consistency, it is easily implementable and can be programmed efficiently since its complexity is also $O(N)$. This makes it a great match to the RNFD method in terms of the accuracy it delivers, the ease of implementation and modification, as well as speed with which a single time step is evolved.

With this in mind, as a final step we are ready to test the full Maxwell-Bloch solver. As mentioned in the beginning of this chapter, the Maxwell-Bloch equations, in their general form, are almost never susceptible to analytical solution. In several few limiting cases (one of which I will present here), however, such an analytical solution does exist, and can be used as a starting point for one last test of the numerical methods.

The analytical solution I have selected, is based on the famous "Area Theorem" solution of the reduced Maxwell-Bloch equations, published by McCall and Hahn in their groundbreaking work [86]. To trace back their derivation, let us start with the reduced Maxwell-Bloch equations for an electric field interacting with a two level system, with upper laser level $|a\rangle$ and lower laser level $|b\rangle$ (see Sec. 2.4.1).

$$\frac{n}{c}\partial_t E_+ + \partial_x E_+ = -i\frac{N\Gamma e z_{a,b}\omega_0}{2\varepsilon_0 cn}\eta_{a,b}, \tag{3.46a}$$

$$\partial_t \Delta_\rho = +i\frac{ez_{ab}}{\hbar}\left(E_+^*\eta_{ab} - E_+\eta_{ab}^*\right) - \frac{\Delta_\rho - \bar{\Delta}}{T_1}, \tag{3.46b}$$

$$\partial_t \eta_{ab} = i\left[(\omega_0 - \omega_{a,b}) + i\frac{1}{T_2}\right]\eta_{ab} + i\frac{ez_{ab}}{2\hbar}E_+\Delta_\rho. \tag{3.46c}$$

First, in order to simplify notation, re-normalize the equations as follows

$$\begin{aligned} F(x,t) &= \frac{ez_{a,b}}{\hbar}E_+(x,t), \\ P(x,t) &= \frac{N\Gamma(ez_{a,b})^2\omega_0}{\hbar\varepsilon_0 cn}\eta_{a,b}, \\ D(x,t) &= \frac{N\Gamma(ez_{a,b})^2\omega_0}{\hbar\varepsilon_0 cn}\Delta_\rho. \end{aligned} \tag{3.47}$$

Secondly, assume that the envelope predominantly real, which means that the field is simply amplified, without experiencing any dispersion during its interaction with the two level system. This transforms the original Eq. (3.46) to

$$\frac{n}{c}\partial_t F + \partial_x F = -\frac{i}{2}P, \tag{3.48a}$$

$$\partial_t D = -2F\,\mathrm{Im}\,P - \frac{D-\bar{D}}{T_1}, \tag{3.48b}$$

$$\partial_t P = i\left[(\omega_0 - \omega_{a,b}) + i\frac{1}{T_2}\right]P + \frac{i}{2}FD, \tag{3.48c}$$

which, one must admit, is much more pleasant to the eye than Eqs. (3.46). In Eq. (3.48a) there is small discrepancy with our ansatz for a purely real electric field, as this assumption implies that P will be purely imaginary. This however, contradicts Eq. (3.48c), since the right hand side contains contribution to both the real and imaginary part of P. Namely,

$$\partial_t\,\mathrm{Re}\,P = -(\omega_0 - \omega_{a,b})\,\mathrm{Im}\,P - \frac{1}{T_2}\,\mathrm{Re}\,P, \tag{3.49}$$

$$\partial_t\,\mathrm{Im}\,P = (\omega_0 - \omega_{a,b})\,\mathrm{Re}\,P + \frac{1}{2}FD - \frac{1}{T_2}\,\mathrm{Im}\,P. \tag{3.50}$$

From this we see that the real part of P will vanish, provided that the detuning $\Delta\omega = \omega_0 - \omega_{a,b}$ is negligibly small, which will indeed be the case when the incoming field has a carrier frequency in or close to resonance with the optical transition frequency.

To proceed with the solution, it is also needed to assume that the inversion lifetime T_1 and the linewidth broadening time T_2 are very long so that the terms $1/T_i$ can be eliminated from the original equations. This allows to represent Eqs. (3.48b)-(3.48c) in vector form

$$\frac{d\vec{P}}{dt} = \vec{P} \times \vec{\Omega}, \tag{3.51}$$

where $\vec{P} = [2\,\mathrm{Re}\,P, 2\,\mathrm{Im}\,P, D]$ is the so called Bloch-vector and $\Omega = [F, 0, -\Delta\omega]$ [64]. Equation (3.51) is structurally familiar from the theory of classical electrodynamics, e.g. Lamor precession [104], nuclear magnetic resonance [105] and obviously optics [64], as it describes precession of the vector $\vec{P}$ around $\vec{\Omega}$ with the precession frequency proportional to the magnitude of $\vec{\Omega}$. Importantly, since T_1 and T_2 have been assumed large and thus eliminated from the equations, Eq. (3.51) describes a purely coherent interaction process, with the length of the Bloch-vector preserved at all times. Solving further, McCall and Hahn observed that upon its interaction with the e-field envelope, $\vec{P}$ will be rotated around $\vec{\Omega}$ at a net angle of

$$\theta(x) = \int_{-\infty}^{\infty} F(x,t)dt, \tag{3.52}$$

with the quantity $\theta(x)$ also known as the *pulse area* [86] (see Fig. 3.3).

While it is obvious that the two level system is modified via its interaction with F, the field envelope also experiences either attenuation or amplification depending on the sign of D, as follows from Eq. (3.48a). With the newly introduced quantities at hand, as well as some minor additional assumptions [106], one can derive a differential equation for the pulse-envelope area [86]

$$\frac{d\theta}{dx} = -\frac{\alpha}{2}\sin\theta(x), \tag{3.53}$$

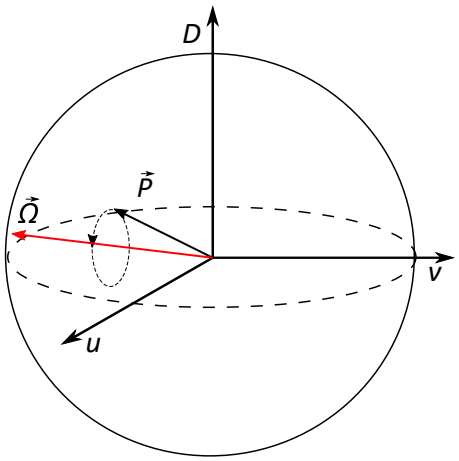

Figure 3.3 Illustration of the Bloch sphere and precession of $\vec{P}$ around $\vec{\Omega}$.

where α is the intensity absorption coefficient. The solution of this ODE is easily found to be

$$\tan\frac{\theta(x)}{2} = \tan\frac{\theta(x_0)}{2}\exp[-\frac{\alpha}{2}(x-x_0)], \tag{3.54}$$

with its various branches, plotted in Fig. 3.4.

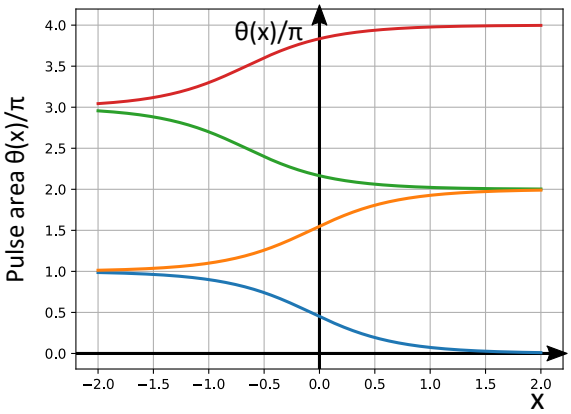

Figure 3.4 Branches of Eq. (3.54) for $\theta(x_0) = 0.9\pi, 1.1\pi, 0.9\times 3\pi, 1.1\times 3\pi$, with $x_0 = -1$ and $\alpha = 4$.

Figure 3.4 is subject to a straightforward interpretation. Depending on the initial pulse area, i.e. which branch of the solution will θ evolve in, the field will either experience amplification or attenuation. Consider for example the branch, corresponding to the blue curve in Fig. 3.4. A pulse with initial area 0.9π will exponentially decay to a zero-area pulse as it propagates through the two-level medium. On the contrary, if the envelope has initial area of $\theta(x_0) = 1.1\pi$, according to Eq. (3.54), the pulse will be reshaped and amplified to a steady state area of 2π. In fact, McCall and Hahn have shown that the only field configuration which could propagate stably (as a soliton) inside the resonant region is a sech pulse with the following (normalized) envelope

$$F_{2\pi} = \frac{2}{\tau_p}\,\mathrm{sech}\left[\frac{1}{\tau_p}\left(t-\frac{cx}{n}\right)\right], \tag{3.55}$$

which has area exactly equal to 2π.

Finally, in order to test the numerical algorithms derived in this chapter, the propagation of three different sech pulses with respective areas of π, 2π and 3π, inside a two level system with

the same parameters as in [53], has been examined. For the numerical solution of the Maxwell-Bloch system, I chose the Risken-Nummedal finite differences method from Sec. 3.2.2, and for the density matrix equations, the 3-step Adams-Bashforth method from Sec. 3.3.2.

The initial pulse width τ_p in all cases was set to 100 fs and all carriers in the system were assumed to start in their lower energetic state.

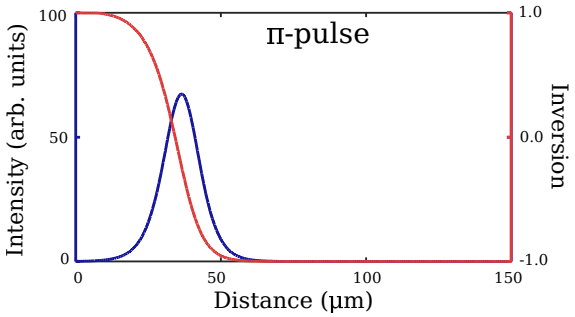

Figure 3.5 Propagation of a π-pulse through a two-level coherent medium.

Let us first look at snapshot of a π-pulse injected from the left-hand-side of the cavity in Fig. 3.5. The image clearly illustrates that the area theorem is satisfied, as the population inversion (right-axis in the figure), is completely inverted after its interaction with the pulse. This corresponds to a rotation of the vector $\vec{P} = [0, 0, -1]$ at 180 degrees in Bloch-space. Also, it was observed that after propagating some 100 μm or so, the pulse gets strongly attenuated, in another agreement with the statement of the theorem.

Next, we examine the propagation of a 2π-pulse, which according to McCall and Hahn [86], should instead propagate stably inside the cavity, whereas simultaneously inverting the population twice. Assuming the same initial conditions as in Fig. 3.5, the result for a 2π-pulse, is plotted in Fig. 3.6. It is immediately evident that the population inversion swings from -1 to

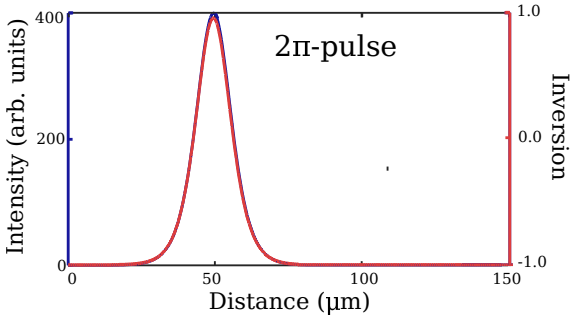

Figure 3.6 Propagation of a 2π-pulse through a two-level coherent medium.

1 and back, as the latter interacts with the optical field. Furthermore, the initial intensity of the pulse remains constant (as it gains as many photons from- as it losses to the population inversion) leading to a stable soliton propagation inside the cavity.

As a last test of the theory and the numerics, an initially 3π-pulse is propagated through the cavity and results thereof are plotted in Fig. 3.7. Now the population inversion undergoes three half-cycles, between the transitions $-1 \rightarrow 1 \rightarrow -1 \rightarrow 1$. Since this dynamics results in a net absorption (since more photons are given up than gained), the pulse intensity also gets gradually reduced from its initial value.

All of these three experiments unequivocally confirm that the area theorem is satisfied, but also more importantly that the used numerical methods yield physically interpretable solutions.

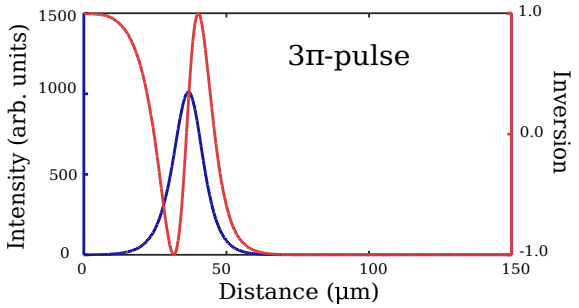

Figure 3.7 Propagation of a 3π-pulse through a two-level coherent medium.

3.4 Conclusion

After offering a comprehensive mathematical derivation of Maxwell-Bloch's equations in Chapter 2, following the good practices in computational science, this part of the thesis focused on developing numerical solvers for the system at hand. To this end three different computational schemes for the wave propagation equation, coupled with a multi-step Adams-Bashforth method for the optical Bloch equations, have been demonstrated. Analytical study as well as experiments with the proposed solvers, gave results in accordance with theory, for the *laxwen*, *rnfd* and the Adams-Bashforth methods, demonstrated convergence rates equal to those obtained from their Taylor expansions. This does not come out as a surprise, but it rather ensures us that the actual implementation of those solvers is correct. A simple lemma was also proven, showing that under some special conditions, the *rnfd* scheme is monotonicity preserving, whereas direct application of "Godunov's Barrier Theorem" and a simple check (for the method of lines approach) showed that *laxwen* and *m.o.l.-adams* do not posses that property. This favorable result for the *rnfd* that distinguishes it from the other two schemes, is technically a virtue of the choice of time step $\Delta t = \Delta x/c$.

Next, numerical study on all schemes lead to the discovery of some interesting properties of these solvers. First of all, we saw that all three schemes for the propagation equations, i.e. *laxwen*, *rnfd* and the *m.o.l.-adams*, experience decrease in accuracy with increasing oscillation frequency, ω, of the wave. This deterioration was quantified and it was reported that the first two schemes demonstrate quadratic convergence with respect to ω, whereas *m.o.l.-adams* sub-quadratic. This suggests that the latter is more robust when one has to solve highly oscillating problems. These good news, however, do not come for free, as the *m.o.l.-adams* method uses a dense pseudospectral differentiation matrix for discretization of the partial derivatives along the spatial direction. That means that at each time step, this solver has to perform a matrix-vector multiplication, an operation that is very costly.

The stability conditions for the proposed PDE solvers were also investigated, using both numerical experiments and analytical von Neumann spectral analysis for the purpose. In doing so it has been shown [89] that *laxwen* and *rnfd* are conditionally stable when the linear

Table 3.4 Summary of the wave propagation schemes and their most important properties for $k \leq 0$.

Name	Order	Stability $k < 0$	Stability $k = 0$	Monotonicity
Lax-Wendroff	2	cond. stable	cond. stable	NO
RNFD	2	stable	stable	YES if $\Delta t \leq \frac{1}{\lvert ck \rvert}$
3-M.O.L-Adams	4	cond. stable	cond. stable	NO

source term, i.e. $kE_{\pm}$, is modeled as a linear loss, i.e. $k < 0$. On the other hand, if $k > 0$, we observed unconditionally unstable behavior for both schemes, something also familiar to the computational electrodynamics scientific community. As for the *m.o.l-adams* method, the scheme's stability regions were investigated numerically when the time propagation is done via a multi-step Adams-Bashforth (with different number of steps) method or Matalab's adaptive Runge-Kutta solver "ode45" [101]. It was discovered that at some instances, the custom implementation of the Adams-Bashforth method couples much better with spectral differentiation to give looser stability constraints onto the choice of time-step. Additionally, the accuracy and stability of the multi-step Adams-Bashforth solver was briefly analyzed and it was shown that the implementation lives up to its theoretical description.

A summary of the wave propagation schemes and their properties is presented in Tab. 3.4. From Tab. 3.4, one can easily pick out the best candidate for solving the wave propagation equation. This is namely the *rnfd*-scheme due to its second order accuracy, stability and monotonicity preserving properties as well as the computational efficacy of the method. Lastly, one final test of the coupled Maxwell-Bloch solver was performed via a simulation of the coherent self-induced transparency phenomenon. The numerical results produced were analyzed and compared to the analytical solution and a satisfactory match was found, assuring that the final choice of algorithms is suitable.

4 Free running THz QC lasers

4.1 Introduction

In this chapter time domain simulations of free-running terahertz quantum cascade lasers will be considered, based on the theoretical framework introduced in Chapter 2, utilizing the numerical methods from Chapter 3. It will be shown how the Maxwell-Bloch framework serves as a wonderful tool to investigate the complexities of the transient dynamics of free-running QCLs, which have been shown to produce both coherent and incoherent multimode spectra. Furthermore, since the focus of this thesis in general is answering questions about frequency comb formation in QCLs, with the presented simulation methods various comb formation and degradation mechanisms will be investigated, with the end goal to give the research community a better insight,s as well as the tools to prototype QCL-based combs which are stable over a wide dynamic range.

Quantum cascade lasers are potentially efficient, cheap and compact generators of frequency combs in the mid- and far-infrared portions of the electromagnetic spectrum. QCL based combs in both spectral regions have been experimentally demonstrated [14, 15, 63, 107, 108], but their spectral coverage has been limited to a fraction of their central frequency. From an application point of view, frequency combs with bandwidths spanning an octave are highly desirable, since then the carrier offset frequency can be readily identified via a self-referencing scheme based on heterodyne detection [109]. However, achieving comb stability over such a broadband frequency range has proven to be difficult [16], namely due to the distorting effect of chromatic dispersion. Nevertheless, also more narrowband QCL combs could be useful for practical applications, as demonstrated using the so-called dual-comb spectroscopy technique [9, 10].

The experimentally demonstrated QCL frequency combs are based on free running lasers [14–16, 63]. Here, high order nonlinear optical processes, in particular four wave mixing (FWM), have been identified as the main mode proliferation mechanisms that contribute to comb formation [4, 110]. In contrast, it has been argued that group velocity dispersion (GVD) leads to unstable multimode operation and thus limits the full exploitation of the gain bandwidth of the material [111]. In the terahertz regime, two of the widest comb generating devices demonstrated so far have shown a strong variation of the beatnote's linewidth with changing injection current, indicating that comb operation comprises only a fraction of the whole dynamic range of these lasers [15, 16].

This chapter addresses fully time dependent simulations of free-running QCL comb operation based on a multiple level extension of the reduced Maxwell-Bloch laser equations, the theoretical basis of which was derived in Sec. 2.4. In the literature, mode locking in QCLs and the emergence of coherent optical instabilities have so far been analyzed based on numerical

solutions of the MB equations [83–85, 91, 112, 113]. Simulations are even more intricate for comb operation, since the optical field must be propagated over some 10^4 cavity round trips to obtain converging results, which in turn poses strong requirements on the accuracy and numerical efficiency of the undertaken approach. Here, extended version of the Maxwell-Bloch equations is derived, which also includes coherent resonant tunneling between the injector and upper laser level, as required for a realistic modeling of QCL-based THz combs. These equations are coupled to self-consistent ensemble Monte Carlo (EMC) carrier transport simulations which provide the non-radiative transition rates between the energy levels, eliminating the need to use empirical electron lifetimes. The addressed simulation approach considers the full transient dynamics of the system, directly solving the extended MB equations without invoking any further assumptions. In this way, also regimes of non-comb or imperfect comb operation can be analyzed, including cases where spectrally separated sub-combs exist or only part of the spectral lines are phase-locked and participate in comb operation.

The chapter is organized as follows: Section 4.2 introduces the theoretical model, based on the Maxwell-Bloch equations in the tight-binding basis approximation. In that context, Sec. 4.2.1 presents a numerical procedure to calculate the tight binding eigenstates and the corresponding level coupling terms, and Sec. 4.2.2 outlines a detailed derivation of an extended system of equations, coherently treating both the optical and resonant tunneling transitions. This approach is used in Sec. 4.3 to investigate the active region of a longitudinal optical (LO) phonon depopulation THz QCL design, experimentally shown to produce one of the most broadband THz QCL frequency combs to date [15]. Here the focus lies on effects relevant for the comb operation, in particular the gain characteristics, group velocity dispersion, four wave mixing as well as spatial hole burning (SHB). In their corresponding sections each mechanism is investigated in detail and its effect on the transient dynamics of the device is discussed. As a verification of the undertaken approach, Sec. 4.3.5 presents simulation results for comb and non-comb operation of the device in question and compares theoretical results with experimental data both in frequency and time domain. This is pushed a step further in Sec. 4.3.6, where we consider in detail the evolution of the lasing modes in the presence and absence of multimode instabilities and show how spatial hole burning could have a dramatic effect onto the laser behavior (Sec. 4.3.6). Lastly, Sec. 4.3.7 studies the influence, exerted onto the system dynamics, by the first modes that start to lase.

Some of the results, contained in this chapter, were presented on several scientific conferences and also featured in journal publications [5, 6, 114].

4.2 Model

The investigations are based on the Maxwell-Bloch laser equations, which present a suitable model for the description of light-matter interaction in microscopic systems. Specifically, here extended Bloch equations are used to describe the optical transition between the upper and lower laser level, additionally accounting for coherent resonant tunneling between the injector and upper laser level to obtain a realistic description of the investigated THz QCL design. The standard rotating wave and slowly varying envelope approximations are employed to reduce the numerical load of the solution [62, 83, 84, 112]. The effect of various scattering mechanisms

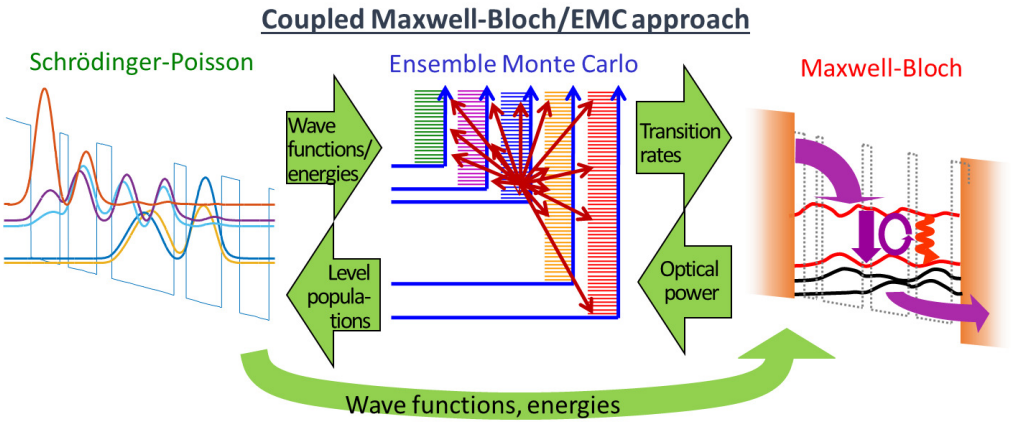

Figure 4.1 A diagram of the employed multi-domain modeling approach, combining a Schrödinger-Poisson solver, and ensemble Monte-Carlo carrier-transport simulation and density matrix/Maxwell's equations based models to enable self-consistent analysis of QCLs.

onto the carrier dynamics is then captured phenomenologically via a periodic rate equations approach, motivated by the assumed Markovian dynamics of the non-unitary interaction between the QCL system and its environment, see Sec. 2.3.4. The level eigenenergies, dipole moments and anticrossing strengths are obtained from a Schrödinger-Poisson solver [115]. The MB approach is coupled to a well-established ensemble Monte Carlo (EMC) carrier transport simulation code for QCLs [116–119], which provides the scattering rates. In that sense, the approach is self-consistent and does not require empirical parameters, with the exception of pure dephasing rates. A diagram of the undertaken "multi-domain" simulation method is illustrated in Fig. 4.1.

4.2.1 Tight-binding basis

In resonant LO-phonon THz QCLs, tunneling plays an important role especially for thick barriers where the subbands involved in the electron transport have a small energy separation, which particularly applies to the injection barriers of various QCL designs [80, 120, 121]. This effect is usually treated in the tight-binding (TB) approximation [122], where the wave functions are calculated for a single isolated period, and the electron subbands in adjacent modules are simply obtained by adequate translation in energy and space by the module length L_p [80]. The energetic coupling between levels spanning the intermodule barrier is modeled by including the corresponding anticrossing energies in the Hamiltonian matrix [120, 121].

The following briefly outlines a numerical procedure to relate these tight-binding states to the original eigenstates, and also shows how one can find the value of the anticrossing energies.

Let us begin by assuming that the computational domain consists of three identical heterostructure periods. Decompose the unperturbed Hamiltonian $\hat{H}$ of the system into a tight-binding Hamiltonian $\hat{H}_{TB}$ and a residual term, where the TB Hamiltonian is assumed to be identical to $\hat{H}$ over one particular period and have infinitely thick barriers everywhere else. Next, denote quantities belonging to each of the three periods with sub/super-script indices

L, C and R for the left, central and the right period, respectively. An illustration of $\hat{H}$ and $\hat{H}_{TB}^{C}$ for a simple two well QC structure is given in Fig. 4.2(a).

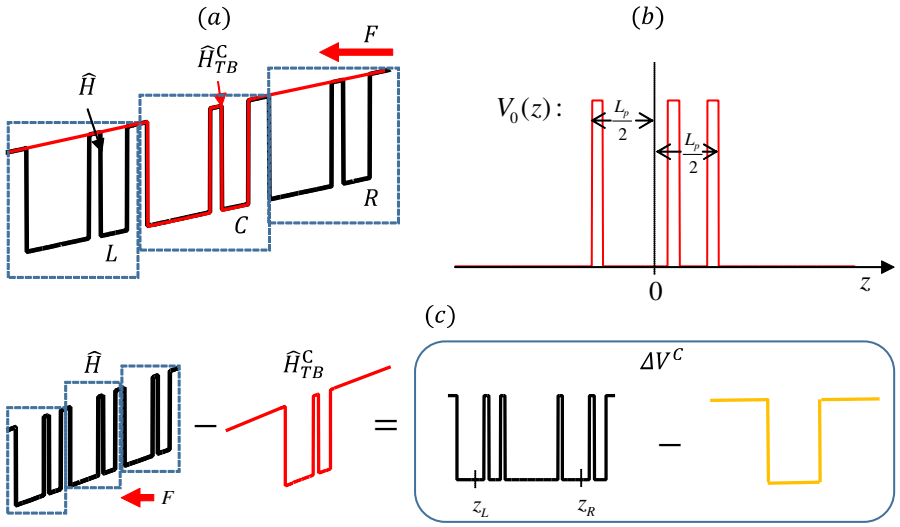

Figure 4.2 (a) Graphical illustration of the difference of the full and tight binding basis conduction band profiles, under some constant applied bias F. (b) a plot of the "naked" conduction band heterostructure profile $V_0(z)$ inside the central period and (c) a graphical representation of the decomposition of $\hat{H}$ into $\hat{H}_{TB}^{C}$ and ΔV^C.

With this notation at hand, the original three-period Hamiltonian operator takes the following form

$$\hat{H} = -\frac{\hbar}{2}\partial_z \frac{1}{m_{\perp}^{*}(z)}\partial_z + V_0(z - z_L) + V_0(z) + V_0(z - z_R) - eFz, \tag{4.1}$$

where $V_0(z)$ is illustrated in Fig. 4.2(b) and consists of the conduction band barriers in the central period and is zero otherwise, and F is some applied constant bias field. Furthermore, in the same figure L_p is the length of the period, and z_L and z_R are the mid-points along the growth direction of the left and right period, respectively (the mid point of the central period is assumed to be zero). Then, one can write

$$\hat{H} = \hat{H}_{TB}^{L} + \Delta V^L = \hat{H}_{TB}^{C} + \Delta V^C = \hat{H}_{TB}^{R} + \Delta V^R. \tag{4.2}$$

The terms ΔV^j are the residual terms when one takes the difference between the original and the tight-binding Hamiltonians, with ΔV^C graphically illustrated in Figure 4.2(c).

In the beginning of the calculation compute, using a Schrödinger-Poisson solver, the tight-binding Hamiltonian eigenstates, for example for the central period, whereas the eigenstates for the adjacent periods are the former translated in energy and space according to the applied bias and the period length, respectively. For the A^{th} period, where $A \in \{L, C, R\}$, denote the ν^{th} eigenvalue and eigenstate of $\hat{H}_{TB}^{A}$ with E_ν^A and ϕ_ν^A, respectively. Now, since all TB wave functions together form a complete basis set in the three period system, any arbitrary wave function Ψ of the full system can be given as a linear combination with some complex expansion coefficients a_ν^A, e.g.

$$\Psi = \sum_{\nu,A} a_\nu^A \phi_\nu^A = \sum_{\nu} \left(a_\nu^L \phi_\nu^L + a_\nu^C \phi_\nu^C + a_\nu^R \phi_\nu^R \right). \tag{4.3}$$

Since Ψ can span multiple periods, those wave functions will be referred to as the delocalized basis. A particular such basis is important, and namely this is the set of states Ψ in which the original Hamiltonian is diagonal. Now, one looks for the solution of the time independent Schrödinger equation

$$\hat{H}\Psi = \sum_{\nu,A} a_\nu^A (\hat{H}_{TB}^A + \Delta V^A)\phi_\nu^A = \varepsilon \sum_{\nu,A} a_\nu^A \phi_\nu^A, \tag{4.4}$$

with the eigenenergy ε.

Using Eq. (4.2) and Eq. (4.3), find the expansion coefficients a_ν^A by taking the inner product of both sides of Eq. (4.4) with the state ϕ_μ^B

$$\langle \phi_\mu^B | \hat{H} | \Psi \rangle = \sum_{\nu,A} \left[a_\nu^A (E_\nu^A \langle \phi_\mu^B | \phi_\nu^A \rangle + \langle \phi_\mu^B | \Delta V^A | \phi_\nu^A \rangle) \right] = \varepsilon \sum_{\nu,A} a_\nu^A \langle \phi_\mu^B | \phi_\nu^A \rangle . \tag{4.5}$$

This defines an eigenvalue problem. To see how, set $\mathbf{a} = [a_1^L, \ldots, a_N^L, a_1^C, \ldots, a_N^C, a_1^R, \ldots, a_N^R]$, where it is explicitly assumed that there are N tight-binding levels per period. Then Eq. (4.5) is rewritten in matrix form as

$$H\mathbf{a} = \varepsilon D\mathbf{a}, \tag{4.6}$$

determined by the matrices

$$D = \begin{bmatrix} D^{LL} & D^{LC} & D^{LR} \\ D^{CL} & D^{CC} & D^{CR} \\ D^{RL} & D^{RC} & D^{RR} \end{bmatrix}, \quad S = \begin{bmatrix} S^{LL} & S^{LC} & S^{LR} \\ S^{CL} & S^{CC} & S^{CR} \\ S^{RL} & S^{RC} & S^{RR} \end{bmatrix}, \text{ and } \quad H = \begin{bmatrix} H^{LL} & H^{LC} & H^{LR} \\ H^{CL} & H^{CC} & H^{CR} \\ H^{RL} & H^{RC} & H^{RR} \end{bmatrix}, \tag{4.7}$$

which have dimension $3N \times 3N$ and the individual elements are given from Eq. (4.5) as

$$D_{\mu\nu}^{AB} = \langle \phi_\mu^A | \phi_\nu^B \rangle , \quad S_{\mu\nu}^{AB} = \langle \phi_\mu^A | \Delta V^B | \phi_\nu^B \rangle , \quad \text{and} \quad H_{\mu\nu}^{AB} = E_\nu^B D_{\mu\nu}^{AB} + S_{\mu\nu}^{AB}. \tag{4.8}$$

As a reminder, note that in Dirac notation the inner product $\langle \phi | \hat{O} | \psi \rangle$, where $\hat{O}$ is any arbitrary quantum mechanical operator, is an integral in the position representation

$$\langle \phi | \hat{O} | \psi \rangle = \int_{-\infty}^{\infty} \phi^*(z) \hat{O} \psi(z) dz. \tag{4.9}$$

A simplistic interpretation of the integrals in Eq. (4.8) is in order. First of all, $D_{\mu\nu}^{AB}$ is the so called overlap integral, the elements of which are not necessarily zero since the wave functions of different tight-binding Hamiltonians, i.e. when $A \neq B$, are generally non-orthogonal. On the other hand $S_{\mu\mu}^{AA}$ is known as the shift integral [122], as it can be shown to induce a (negative) shift in the tight-binding eigenenergies. Lastly $S_{\mu\nu}^{AA\pm1}$ is the coupling strength integral (also known as transfer integral), which estimates the potential coupling between two wave functions sharing a barrier and is the term responsible for the energy splitting/anticrossing between two TB states close to resonance.

As mentioned above, since the tight-binding states, which will be needed as basis states in the subsequent density matrix formalism, are not eigenstates of the original Hamiltonian $\hat{H}$, the matrix representation of $\hat{H}$ in the TB basis will generally not be diagonal but will additionally

contain off-diagonal level-coupling terms, the so called anticrossing energies. For two levels, spanning a module barrier, the coupling energy is given by

$$\hbar\Omega_{\mu\nu}^{AB} = \langle\phi_\mu^A|\hat{H}|\phi_\nu^B\rangle = E_\nu^B D_{\mu\nu}^{AB} + S_{\mu\nu}^{AB} = H_{\mu\nu}^{AB}, \tag{4.10}$$

which also provides us with an interpretation for the elements of the matrix H.

To conclude, the validity of the outlined procedure is demonstrated by a numerical test. First, the quantum well heteorstructure in Fig. 4.2(a) is taken and its delocalized basis eigenstates $\{\Psi\}$ are numerically calculated by finite difference discretization of $\hat{H}$ and a Schrödinger-Poisson (SP) solver [115]. Then with the same SP solver the tight-binding eigenstates $\{\phi_\mu^A\}$ are computed by assuming that the structure has infinite barrier outside of the period of interest, say C. Finally, the matrices D, S and H are constructed and Eq. (4.6) is solved. With the knowledge of the coefficients a_ν^A and the expansion formula Eq. (4.3), one then calculates anew the delocalized states $\{\Psi'\}$, but this time as a linear combination of ϕ_ν^A states. If the procedure has been performed correctly, then the states $\{\Psi\}$ and the states $\{\Psi'\}$ shall be approximately identical. An illustration of this verification test is displayed in Fig. 4.3.

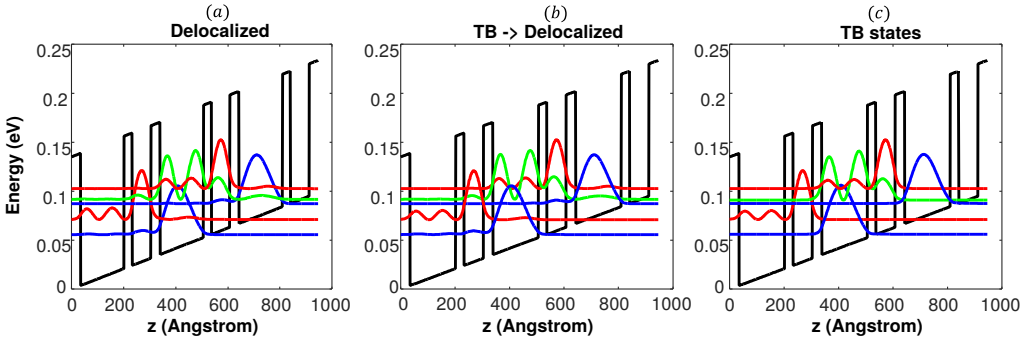

Figure 4.3 (a) The delocalized basis wave functions (WFs), i.e. the states $\{\Psi\}$ calculated directly from the SP solver. (b) The delocalized basis WFs $\{\Psi'\}$ calculated from Eq. (4.3) and (c) the tight-binding basis wave functions $\{\phi_\mu^A\}$.

4.2.2 Three level density matrix model

Next, the density-matrix based model is derived. In order to introduce some notation, consider taking a simple prototype for a resonant phonon THz QCL, depicted in Fig. 4.4. In this configuration there are four relevant bound states $|1'\rangle$, $|3\rangle$, $|2\rangle$ and $|1\rangle$ which are the injector level, the upper and lower laser levels and the depopulation level, which also serves as the injector level for the next period. The state $|1'\rangle$ couples to $|3\rangle$ via the anticrossing energy $\hbar\Omega_{1'3}$, whereas the upper and lower laser levels interact via the instantaneous Rabi frequency $\Omega_L(t) = -ez_{32}E_z(t)/\hbar$. Here, $z_{32} = \langle 3|\,\hat{z}\,|2\rangle$ is the dipole matrix element of the lasing states. The energy separation between $|1'\rangle$ and $|3\rangle$ is denoted with $\Delta E_{1'3} = \hbar\varepsilon$ and that between the upper and lower laser levels as $\Delta E_{32} = \hbar\omega_{32}$.

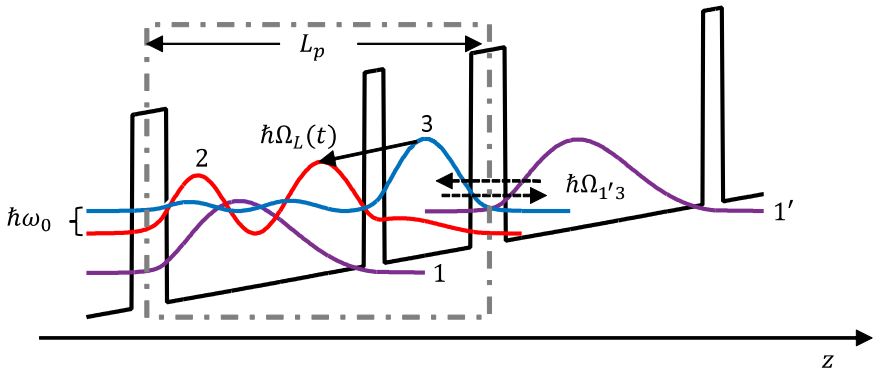

Figure 4.4 Schematic diagram of a simple three-level LO-phonon depopulation THz QCL, where the upper laser level is populated via resonant tunneling.

In this tight-binding basis, the time evolution is governed by the von Neumann equation which, with phenomenologically included scattering rates, reads

$$\frac{d}{dt}\begin{pmatrix}\rho_{1'1'} & \rho_{1'3} & \rho_{1'2}\\ \rho_{31'} & \rho_{33} & \rho_{32}\\ \rho_{21'} & \rho_{23} & \rho_{22}\end{pmatrix} = \frac{\mathrm{i}}{\hbar}\left[\begin{pmatrix}\rho_{1'1'} & \rho_{1'3} & \rho_{1'2}\\ \rho_{31'} & \rho_{33} & \rho_{32}\\ \rho_{21'} & \rho_{23} & \rho_{22}\end{pmatrix}, \overbrace{\begin{pmatrix}\frac{\hbar\varepsilon}{2} & \hbar\Omega_{1'3} & 0\\ \hbar\Omega_{1'3} & -\frac{\hbar\varepsilon}{2} & -\hbar\Omega_L(t)\\ 0 & -\hbar\Omega_L(t) & -\frac{\hbar\varepsilon}{2}-\hbar\omega_{32}\end{pmatrix}}^{\text{resonant tunneling and radiative coupling}}\right] + \underbrace{\begin{pmatrix}-\frac{\rho_{1'1'}}{\tau_{1'}}+(\frac{1}{\tau_{31'}}+\frac{1}{\tau_{31}})\rho_{33}+(\frac{1}{\tau_{21'}}+\frac{1}{\tau_{21}})\rho_{22} & \tau_{\|1'3}^{-1}\rho_{1'3} & \tau_{\|1'2}^{-1}\rho_{1'2}\\ \tau_{\|1'3}^{-1}\rho_{31'} & \frac{\rho_{1'1'}}{\tau_{1'3}}-\frac{\rho_{33}}{\tau_3}+\frac{\rho_{22}}{\tau_{23}} & \tau_{\|32}^{-1}\rho_{32}\\ \tau_{\|1'2}^{-1}\rho_{21'} & \tau_{\|32}^{-1}\rho_{32} & \frac{\rho_{1'1'}}{\tau_{1'2}}+\frac{\rho_{33}}{\tau_{32}}-\frac{\rho_{22}}{\tau_2}\end{pmatrix}}_{\text{scattering rates matrix}}. \tag{4.11}$$

In Eq. (4.11) the $\rho_{ij} = \langle i|\,\hat{\rho}\,|j\rangle$ denote the corresponding density matrix elements and the zero energy has been set at $(E_{1'} + E_3)/2$. Furthermore τ_{ij}^{-1} denotes the outscattering rate from level i to level j, τ_i is the lifetime of level i with $\tau_i^{-1} = \sum_{j\neq i}\tau_{ij}^{-1}$, and

$$\tau_{\|ij}^{-1} = \frac{1}{2}\left(\frac{1}{\tau_i}+\frac{1}{\tau_j}\right) + \frac{1}{\tau_{ij}^{pure}} \tag{4.12}$$

is the damping rate of the coherence between levels i and j, containing lifetime broadening and a "pure" dephasing time τ_{ij}^{pure} [80].

Notice that Eq. (4.11) omits the time evolution related to state $|1\rangle$, because it serves as the injector level for the next period, which allows for the elimination of this level from the model by employing "periodic" boundary conditions in the scattering rates matrix. It is vital for the simulation that these periodic boundary conditions are implemented correctly, because the model is formulated in a manner which does not phenomenologically include the injection current density J into the equations. Instead, a periodic system is assumed, where all carriers that reach the depopulation level $|1\rangle$ are immediately re-injected into the system through level $|1'\rangle$. The boundary conditions for this kind of periodicity were already introduced in Sec. 2.3.2.

The coupling of the microscopic density matrix equations to the macroscopic Maxwell's equations is again done via the incorporation of the polarization term in Maxwell's equations as the expectation value of the quantum mechanical dipole moment operator,

$$P_z = -N\Gamma \mathbf{tr}(\hat{\rho} e \hat{z}) = -N\Gamma e(z_{32}\rho_{32} + z_{23}\rho_{23}) = -N\Gamma e z_{32}(\rho_{32} + \rho_{23}), \tag{4.13}$$

where Γ is the spatial overlap factor between the optical field and the active region. Assuming no free electric charges and also weak inhomogeneity, the optical field evolution is governed by the wave equation Eq. (2.6).

Next, consider a Fabry-Perot resonator of a certain length L, and employ the rotating wave (RWA) and the slowly varying envelope approximations (SVEA) [62, 84]. The optical field inside the cavity is written as a superposition of counter-propagating waves

$$E_z(x,t) = \frac{1}{2}\left\{E_+(x,t)\exp\left[\mathrm{i}(\beta_0 x - \omega_0 t)\right] + E_-(x,t)\exp\left[-\mathrm{i}(\beta_0 x + \omega_0 t)\right] + c.c\right\}, \tag{4.14}$$

where "c.c." denotes the complex conjugate of the preceding expression, the $+$ and $-$ signs specify the positive/negative direction, respectively, and ω_0 and β_0 are again the field's carrier frequency and wave number. Since the superposition of two counter-propagating waves forms a standing wave, this will lead to the formation of an inversion grating along the propagation direction x, a phenomenon also known as spatial hole burning (SHB). Later, a separate section will be dedicated on this phenomenon as it turns out that its analysis is extremely important for the understanding of the complex multimode dynamics observed in THz QCLs. To model SHB within the SVEA+RWA approximations, make the following ansatz for the diagonal elements of the density matrix

$$\rho_{ii}(x,t) = \rho_{ii}^0(x,t) + \rho_{ii}^+(x,t)\exp\left(2\mathrm{i}\beta_0 x\right) + \rho_{ii}^-(x,t)\exp\left(-2\mathrm{i}\beta_0 x\right), \tag{4.15}$$

where $\rho_{ii}^+ = (\rho_{ii}^-)^*$ are the inversion grating's amplitudes [83]. Lastly, decompose the coherences of the density matrix as

$$\rho_{32}(x,t) = \eta_{32}^+(x,t)\exp\left[\mathrm{i}(\beta_0 x - \omega_0 t)\right] + \eta_{32}^-(x,t)\exp\left[-\mathrm{i}(\beta_0 x + \omega_0 t)\right], \tag{4.16a}$$

$$\rho_{1'2}(x,t) = \eta_{1'2}^+(x,t)\exp\left[\mathrm{i}(\beta_0 x - \omega_0 t)\right] + \eta_{1'2}^-(x,t)\exp\left[-\mathrm{i}(\beta_0 x + \omega_0 t)\right], \tag{4.16b}$$

$$\rho_{1'3}(x,t) = \rho_{1'3}^0(x,t) + \rho_{1'3}^+(x,t)\exp\left(2\mathrm{i}\beta_0 x\right) + \rho_{1'3}^-(x,t)\exp\left(-2\mathrm{i}\beta_0 x\right). \tag{4.16c}$$

Notice that Eqs. (4.16a) and (4.16b) follow the electric field ansatz since the corresponding transition energies are in close resonance with the optical field. In contrast, the ansatz Eq. (4.16c) is chosen in analogy to Eq. (4.15) for the diagonal elements since the term $\rho_{1'3}$ is expected to oscillate only slowly due to the small energetic spacing between subbands $1'$ and 3.

Finally, plugging Eqs. (4.14)-(4.16) into Eqs. (4.11)-(4.13) and Eq. (2.6) and invoking the rotating wave and slowly varying amplitude approximations, the model is reduced to its final form

1. Propagation equations

$$\frac{n}{c}\partial_t E_\pm \pm \partial_x E_\pm = -\mathrm{i}\frac{N\Gamma e z_{32}\omega_0}{\varepsilon_0 n c}\eta_{32}^\pm - \frac{a}{2}E_\pm, \tag{4.17}$$

2. Population densities

$$\frac{d\rho^0_{1'1'}}{dt} = \mathrm{i}\Omega_{1'3}\left(\rho^0_{1'3} - \rho^0_{31'}\right) + \left(\frac{1}{\tau_{31'}} + \frac{1}{\tau_{31}}\right)\rho^0_{33} + \left(\frac{1}{\tau_{21'}} + \frac{1}{\tau_{21}}\right)\rho^0_{22} - \frac{\rho^0_{1'1'}}{\tau_{1'}}, \tag{4.18a}$$

$$\frac{d\rho^+_{1'1'}}{dt} = \mathrm{i}\Omega_{1'3}\left(\rho^+_{1'3} - \rho^+_{31'}\right) + \left(\frac{1}{\tau_{31'}} + \frac{1}{\tau_{31}}\right)\rho^+_{33} + \left(\frac{1}{\tau_{21'}} + \frac{1}{\tau_{21}}\right)\rho^+_{22} - \left(\frac{1}{\tau_{1'}} + 4\beta_0^2 D\right)\rho^+_{1'1'}, \tag{4.18b}$$

$$\frac{d\rho^0_{33}}{dt} = \mathrm{i}\Omega_{1'3}\left(\rho^0_{31'} - \rho^0_{1'3}\right) + \mathrm{i}\frac{ez_{32}}{2\hbar}\left(E^*_-\eta^-_{32} + E^*_+\eta^+_{32} - c.c.\right) + \frac{1}{\tau_{1'3}}\rho^0_{1'1'} + \frac{1}{\tau_{23}}\rho^0_{22} - \frac{\rho^0_{33}}{\tau_3}, \tag{4.18c}$$

$$\frac{d\rho^+_{33}}{dt} = \mathrm{i}\Omega_{1'3}\left(\rho^+_{31'} - \rho^+_{1'3}\right) + \mathrm{i}\frac{ez_{32}}{2\hbar}\left[E^*_-\eta^+_{32} - E_+(\eta^-_{32})^*\right] + \frac{\rho^+_{1'1'}}{\tau_{1'3}} + \frac{\rho^+_{22}}{\tau_{23}} - \left(\frac{1}{\tau_3} + 4\beta_0^2 D\right)\rho^+_{33}, \tag{4.18d}$$

$$\frac{d\rho^0_{22}}{dt} = -\mathrm{i}\frac{ez_{32}}{2\hbar}\left(E^*_-\eta^-_{32} + E^*_+\eta^+_{32} - c.c.\right) + \frac{1}{\tau_{1'2}}\rho^0_{1'1'} + \frac{1}{\tau_{32}}\rho^0_{33} - \frac{\rho^0_{22}}{\tau_{21}}, \tag{4.18e}$$

$$\frac{d\rho^+_{22}}{dt} = -\mathrm{i}\frac{ez_{32}}{2\hbar}\left[E^*_-\eta^+_{32} - E_+(\eta^-_{32})^*\right] + \frac{1}{\tau_{1'2}}\rho^+_{1'1'} + \frac{1}{\tau_{32}}\rho^+_{33} - \left(\frac{1}{\tau_2} + 4\beta_0^2 D\right)\rho^+_{22}, \tag{4.18f}$$

3. Coherence terms

$$\frac{d\rho^0_{1'3}}{dt} = -\mathrm{i}\varepsilon\rho^0_{1'3} + \mathrm{i}\Omega_{1'3}\left(\rho^0_{1'1'} - \rho^0_{33}\right) + \mathrm{i}\frac{ez_{32}}{2\hbar}\left(E^*_+\eta^+_{1'2} + E^*_-\eta^-_{1'2}\right) - \tau^{-1}_{\parallel 1'3}\rho^0_{1'3}, \tag{4.19a}$$

$$\frac{d\rho^\pm_{1'3}}{dt} = -\mathrm{i}\varepsilon\rho^\pm_{1'3} + \mathrm{i}\Omega_{1'3}\left(\rho^\pm_{1'1'} - \rho^\pm_{33}\right) + \mathrm{i}\frac{ez_{32}}{2\hbar}E^*_\mp\eta^\pm_{1'2} - \left(\tau^{-1}_{\parallel 1'3} + 4\beta_0^2 D\right)\rho^\pm_{1'3}, \tag{4.19b}$$

$$\frac{d\eta^\pm_{32}}{dt} = \mathrm{i}\left(\omega_0 - \omega_{32}\right)\eta^\pm_{32} + \mathrm{i}\frac{ez_{32}}{2\hbar}\left[E_\pm(\rho^0_{33} - \rho^0_{22}) + E_\mp(\rho^\pm_{33} - \rho^\pm_{22})\right] - \mathrm{i}\Omega_{1'3}\eta^\pm_{1'2} - \tau^{-1}_{\parallel 32}\eta^\pm_{32}, \tag{4.19c}$$

$$\frac{d\eta^\pm_{1'2}}{dt} = \mathrm{i}\left(\omega_0 - \omega_{32} - \varepsilon\right)\eta^\pm_{1'2} + \mathrm{i}\frac{ez_{32}}{2\hbar}\left(E_\pm\rho^0_{1'3} + E_\mp\rho^\pm_{1'3}\right) - \mathrm{i}\Omega_{1'3}\eta^\pm_{32} - \tau^{-1}_{\parallel 1'2}\eta^\pm_{1'2}. \tag{4.19d}$$

Notice that in Eq. (4.17) a linear loss coefficient a is phenomenologically added, and in Eq. (4.18b), Eq. (4.18d), Eq. (4.18f) and Eq. (4.19b) a diffusion term $4\beta_0^2 D$ is included, describing the rate at which carriers diffuse away from peaks of the population grating. Here D denotes the diffusion constant, which for GaAs/AlGaAs systems is $46\,\mathrm{cm}^2/\mathrm{s}$ [17, 91]. The fields $E_\pm$ in Eq. (4.17) satisfy the boundary conditions $E_+(0) = rE_-(0)$ and $rE_+(L) = E_-(L)$ [83], with the (amplitude) reflection coefficient r.

4.3 Theoretical analysis of a LO phonon depopulation THz QCL with a strong injector anticrossing

In this section the three level model, outlined in Sec. 4.2, is extended to simulate the QCL design in [15]. This laser is based on a resonant LO phonon depopulation active region lasing at the central frequency $f_0 \approx 3.5\,\mathrm{THz}$, and has been shown to produce a stable comb spectrum containing more than 70 equidistant longitudinal modes in a free running regime of operation. At optimum bias, field autocorrelation measurements indicate multimode lasing,

and radio frequency (RF) measurements produce a very strong and narrow beatnote with a minimum reported full width at half-maximum (FWHM) linewidth of approximately $1.53\,\mathrm{kHz}$, indicating that at least part of the modes are phase-locked [14–16, 63]. Furthermore, a novel comb coherence detection technique, shifted-wave interference Fourier-transform (SWIFT) spectroscopy, has been developed to prove the stability of the THz comb over a large number of round trips [123]. To correctly model this device, one needs to first determine operating regimes where the "single resonant tunneling and single optical transition" assumption, made in Sec. 4.2, is justified.

Figure 4.5(a) illustrates the calculated wave functions at a bias of $11\,\mathrm{kV/cm}$ obtained with the tight-binding approximation. From graphical inspection it can be seen that there are in total five relevant levels per period, which are referred to, according to their assumed role, as $|ULL\rangle$ for the upper laser level, $|LLL1\rangle$ for the higher energy level from a pair of lower laser levels, $|LLL2\rangle$ for the lower energy level from the same pair, $|DEP1\rangle$ for the higher energy level from a doublet of depopulation levels, and finally $|DEP2\rangle$ for the lowest energy level. Furthermore, since the structure is periodic, the depopulation levels from the previous period are denoted as $|INJ1\rangle$ and $|INJ2\rangle$.

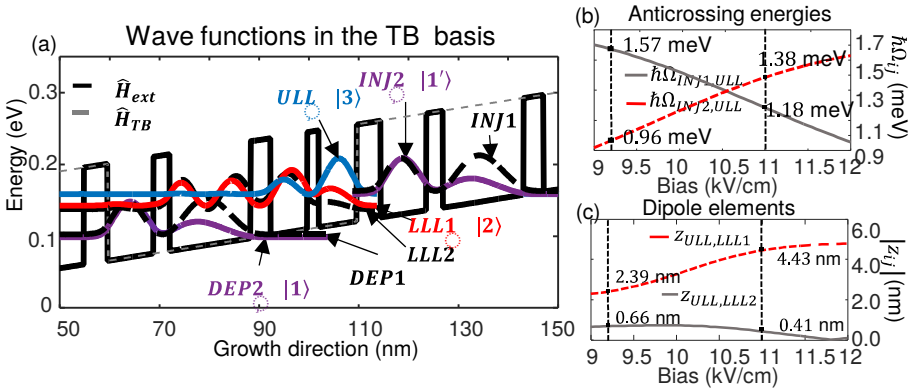

Figure 4.5 (a) The modulus squared of the wave functions of the THz QCL in [15] within the tight-binding approximation. (b) The anticrossing coupling strengths between the pair of injector levels, $|INJ1\rangle$, $|INJ2\rangle$, and the upper laser level $|ULL\rangle$, computed via the method outlined in Sec. 4.2.1. (c) Dipole elements calculated for the possible transitions $ULL \leftrightarrow LLL1$ and $ULL \leftrightarrow LLL2$.

Figure 4.5(b) and Fig. 4.5(c) depict the calculated coupling strengths $\hbar\Omega_{ij}$ between the injector states and the upper laser level for different biases, as well as the magnitudes of the dipole matrix elements, $|z_{ij}|$, between the upper laser level and the doublet of lower laser levels. The anticrossing (AC) energies were calculated via the method described in Sec. 4.2.1, and the numerical values were verified by diagonalization of the tight-binding Hamiltonian. Focusing on bias values at around $11\,\mathrm{kV/cm}$, the calculations show that there is almost perfect energetic alignment between $|INJ2\rangle$ and $|ULL\rangle$, whereas $|INJ1\rangle$ and $|ULL\rangle$ are separated by approximately $\Delta E_{INJ1,ULL} \approx 4.3\ \mathrm{meV}$ (not shown in the figure). Even though the anticrossing energies $\hbar\Omega_{INJ1,ULL} \approx 1.18\ \mathrm{meV}$ and $\hbar\Omega_{INJ2,ULL} \approx 1.38\ \mathrm{meV}$ are of comparable strength, the strong resonance condition between the pair $|INJ2\rangle$, $|ULL\rangle$ enhances the tunneling probability, i.e. reduces the tunneling time, between those levels [27], as compared to the tunneling transition between $|INJ1\rangle$ and $|ULL\rangle$. This means that the

majority of the tunneling electrons will prefer the $|INJ2\rangle \leftrightarrow |ULL\rangle$ transport channel and hence our model, which includes only a single tunneling transition, ought to correctly capture the microscopic dynamics of the real device. From dipole moment calculations in Fig. 4.5(c), one can see that the optical transition at $11\,\mathrm{kV/cm}$ is most likely to occur between the pair $|ULL\rangle$, $|LLL1\rangle$, and thus the state $|2\rangle$ in the model can be assigned to be subband $|LLL1\rangle$ from the system under investigation. Similarly, due to the discussion above, one can set the injector level in the model, i.e. $|1'\rangle$, to state $|INJ2\rangle$. Finally, $|3\rangle$ is mapped to subband $|ULL\rangle$. The remaining states $|INJ1\rangle$ and $|LLL2\rangle$ are then treated within a rate equations approach and included into the scattering rates matrix by adequately extending Eq. (4.11).

Table 4.1 Simulation parameters for a THz QCL, modeled after the device in [15]. The modal overlap factor and the facet reflectivities are selected based on [90] for a metal-metal waveguide with thickness $10\,\mu\mathrm{m}$ and width of $20\,\mu\mathrm{m}$.

Parameter	Symbol	Value
Avg. carrier density	N	5.6×10^{15} cm^{-3}
Overlap factor	Γ	0.9
Linear amplitude loss	l_0	11 cm^{-1}
Dipole matrix element	ez_{32}	4.0 nm $\times e$
Refractive index	n_0	3.6
Diffusion constant	D	46 cm^2/s
Left mirror reflect.	R_L	0.8
Right mirror reflect.	R_R	0.8
1'$\rightarrow$3 pure deph. time	$\tau_{1'3}^{\text{pure}}$	0.6 ps
3 $\rightarrow$2 pure deph. time	τ_{32}^{pure}	1 ps
1'$\rightarrow$2 pure deph. time	$\tau_{1'2}^{\text{pure}}$	1 ps
3 $\leftrightarrow$ 2 resonance energy	ΔE_{32}	15.82 meV
1'$\leftrightarrow$ 3 detuning energy	$\Delta E_{1'3}$	-0.43 meV
1'$\leftrightarrow$ 3 anticrossing	$\hbar\Omega_{1'3}$	-1.3447 meV

In Tab. 4.1 the parameter set used for the simulations is summarized and in Tab. 4.2, the scattering rates between each pair of the active region subbands calculated with our ensemble Monte Carlo simulation code [52] are shown. The code includes all relevant scattering mechanisms reported to play a role in quantum cascade lasers, including longitudinal optical phonons, acoustic phonons, interface roughness and impurity scattering as well as electron-electron scattering. The calculated rates include all these mechanisms and are presented in units of ps^{-1}.

4.3.1 Gain and dispersion characterization

In order to extract the spectral gain profile as well as the strength of the chromatic dispersion induced by the active region design, simulations are performed emulating the THz time-domain spectroscopy (THz-TDS) technique, often used for gain characterization of THz QCLs [124–126].

Table 4.2 Total scattering rates between each pair of relevant subbands of the device in [15] for a bias of $10.8\,\mathrm{kV/cm}$. The rates are presented in ps^{-1}.

	INJ1	INJ2	ULL	LLL1	LLL2	DEP1	DEP2
INJ1	0	0.8179	0.0200	0.0016	0.0007	0.0025	0.0029
INJ2	0.4906	0	0.0451	0.0016	0.0007	0.0024	0.0031
ULL	0.0471	0.0894	0	0.1252	0.1101	0.0503	0.0464
LLL1	0.0329	0.0425	0.0794	0	0.4949	0.7787	0.6196
LLL2	0.0214	0.0280	0.0357	0.2810	0	1.0196	1.0960
DEP1	0.0026	0.0037	0.0029	0.0031	0.0042	0	0.8179
DEP2	0.0017	0.0026	0.0018	0.0013	0.0042	0.4906	0

The model is applied to a ring cavity configuration with length $L = 2.5\,\mathrm{mm}$ with neglected spatial hole burning effects, which are not expected to play a role for this simulation. As illustrated in Fig. 4.6, a weak unchirped Gaussian pulse is propagated inside the cavity for one round trip of length L. At each time step t_n of this simulation, as well as at different points x_j along the cavity length, the electric field envelope E_j^n is recorded for further data processing. From this data the real and imaginary parts of the refractive index can be calculated in a straightforward manner, as briefly discussed below.

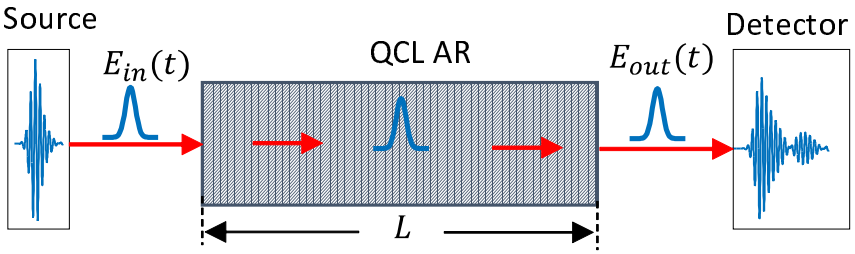

Figure 4.6 Diagram of the performed numerical "experiment" used to infer the spectral gain and dispersion.

In a ring cavity, there are only forward propagating waves (no standing waves) and thus the electric field can be written as $E_z(x,t) = \mathrm{Re}\{f(x,t)\exp\left[\mathrm{i}(\beta_0 x - \omega_0 t)\right]\}$, where f is the (slowly varying) envelope function. Let us denote the electric field of the injected seed pulse at the input facet of our cavity as $E_{in}(t)$ and the field of the detected pulse as $E_{out}(t)$. Their Fourier transforms are $E_{in}(\omega)$ and $E_{out}(\omega)$, with the angular frequency ω. The corresponding envelope functions are $f_{in}\,(t)$ and $f_{out}\,(t)$, with the Fourier transforms $F_{in}\,(\omega)$ and $F_{out}\,(\omega)$, respectively. For a weak seed pulse the light-matter interaction is linear, and the active region can be described by its complex refractive index $\underline{n}\,(\omega) = n'\,(\omega) + \mathrm{i}n''\,(\omega)$, with the amplitude gain coefficient given by $g(\omega) = -n''(\omega)\omega/c$. The dependence between the seed and output fields is then given by $E_{out}(\omega) = E_{in}(\omega)\exp\left(\mathrm{i}\omega\underline{n}L/c\right)$, which corresponds to $F_{out}(\omega-\omega_0)\exp(\mathrm{i}\beta_0 L) = F_{in}(\omega-\omega_0)\exp\left(\mathrm{i}\omega\underline{n}L/c\right)$. From this, one obtains

$$n'(\omega) = \frac{c}{L\omega}\angle\{F_{out}(\omega-\omega_c)/F_{in}(\omega-\omega_0)\} + \frac{c\beta_0}{\omega}, \tag{4.20}$$

$$n''(\omega) = -g(\omega)c/\omega = -\frac{c}{L\omega}\ln\{|F_{out}(\omega-\omega_0)|/|F_{in}(\omega-\omega_0)|\}. \tag{4.21}$$

Figure 4.7 shows the results from numerical THz-TDS simulations at a bias of $10.8\,\mathrm{kV/cm}$ for the active region in [15] for a single round trip of the seed THz pulse. Since the aim

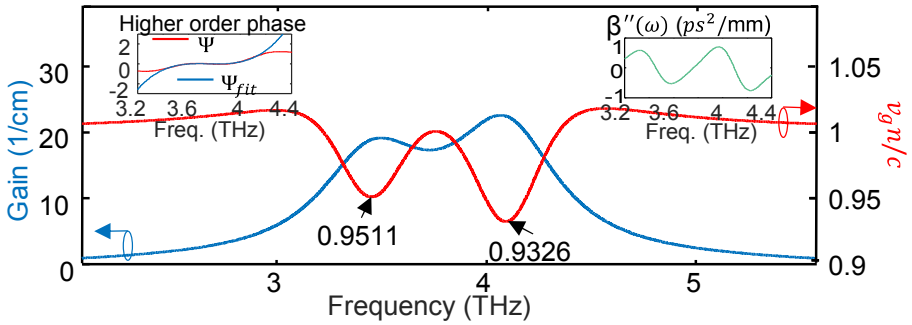

Figure 4.7 Simulated spectral gain profile (blue curve, left y-axis) together with the normalized group velocity $v_g n/c$ (red curve, right y-axis). (Left inset) The higher order phase acquired by the test pulse. (Right inset) The second derivative of the wave number with respect to the angular frequency.

is to probe the unsaturated gain profile, for these numerical experiments a weak Gaussian seed pulse has been used with an initial field amplitude (normalized to its Rabi-frequency) of $0.5\,\mathrm{ns}^{-1}$ and FWHM duration of $0.707\,\mathrm{ps}$, corresponding to a FWHM bandwidth of $623\,\mathrm{GHz}$ for a transform limited pulse. In Fig. 4.7 the blue curve illustrates the simulated spectral amplitude gain, obtained from Eq. (4.21). One can clearly observe a pronounced splitting of the gain spectra into two frequency lobes, one centered around $3.55\,\mathrm{THz}$ and another one around $4.21\,\mathrm{THz}$. The red curve in Fig. 4.7 depicts the frequency resolved group velocity, calculated from $v_g = [\partial\beta(\omega)/\partial\omega]^{-1}$ with $\beta(\omega) = n'(\omega)\omega/c$, and normalized to the central frequency's phase velocity c/n. Due to the strong resonances at $3.55\,\mathrm{THz}$ and $4.21\,\mathrm{THz}$, the low and high frequency components are delayed with respect to each other as $v_g n/c$ approaches 0.9511 and 0.9326 for the low and high frequency gain peaks, respectively, where this ratio depends on the strength of the corresponding transition. The upper left inset of Fig. 4.7 depicts the calculated higher order phase $\Psi = \beta(\omega)L$ (with the linear part removed) together with a third order polynomial fit to it, Ψ_{fit}, and shows that the dispersion relation within the spectral range of interest (i.e. from $3.5\,\mathrm{THz}$ to $4.2\,\mathrm{THz}$) is approximately cubic. Additionally, the top right inset illustrates the second derivative of the wave number with respect to frequency, i.e. $\beta''(\omega)$, which is a measure of GVD.

From the above analysis it can be concluded that even in the absence of bulk or waveguide dispersion, the doubly peaked resonant nature of the transition will cause significant dispersion in the cavity which is expected to deteriorate the comb performance. Here a question naturally arises: "How does the presence of strong chromatic dispersion impact the mode proliferation process?" If the multimode behavior of free-running QCLs is due to FWM, as suggested in [4, 110], then one would intuitively expect that such a high GVD will violate the phase matching condition and thus render this nonlinear process ineffective. However, from experiment [15, 16], multimode operation of both mid-infrared and THz QCLs could be observed, even in the presence of strong dispersion. To investigate further this question, the nature of this mode generation mechanism is analyzed and the amount of phase mismatch induced by the resonant transition is estimated.

4.3.2 Four Wave Mixing (FWM)

Both theoretical [4] and experimental [110] investigations have confirmed that four wave mixing (FWM), induced by the large third order nonlinearity $\chi^{(3)}$, acts as the main comb-formation mechanism in free-running mid- and far-infrared QCL devices. For example, a series of pump-probe experiments were performed in [110], where a mid-infrared QC amplifier was pumped with two single mode lasers, emitting a pair of frequencies, f_1 and f_2 (with $f_1 < f_2$), lying well under the gain spectrum of the device, Fig. 4.8(a). Outcoupled light was consecutively recorded and subsequent spectral analysis revealed the clear footprints of degenerate four wave mixing, i.e. the generation of a pair of conjugate modes at the Stokes and anti-Stokes frequencies of $f_s = 2f_1 - f_2$ and $f_a = 2f_2 - f_1$, respectively. Combined with the inherently broadband gain of QCLs, this effect could support the generation of more sidebands in a cascaded manner, ideally spanning the full bandwidth of the laser. Since FWM is an energy conserving process, in this way it should lead to an equidistant multimode spectrum and thus a frequency comb.

However, this does not always occur due to the competition of FWM with various comb-degradation mechanisms. These include group velocity dispersion (GVD) and multimode instabilities such as the Risken-Nummedal-Graham-Haken (RNGH) instability [87, 127], which has a lower threshold in QCLs due to spatial hole burning (SHB) [84]. From these the former, i.e. GVD, has been shown to play a major role in blocking the formation of a nice equidistantly-spaced spectrum [123, 128]. That is why state of the art QCL frequency combs usually employ sophisticated dispersion compensating mechanisms (DCMs), either based on a chirped corrugation structure embedded into the laser cavity [15] or GTI-mirrors positioned behind one of the facets of the laser [128]. Both techniques have been shown to be very successful in eliminating the dispersion, leading to comb formation. However, there is still lack of clear understanding as to why lasers operating at negative GVD are easier to phase-lock [128] or why the DCMs can be effective only within a narrow range from the overall operating regime [15].

With the Maxwell-Bloch model presented earlier, one can investigate the effect of different parameters on the efficacy of FWM by essentially emulating laboratory experiments similar to those in [110]. Figure 4.8(c) and Fig. 4.8(d) show data from two such computations, where a traveling wave amplifier was simulated, seeded through the left facet by two modes with frequencies f_1 and f_2. In both cases, the simulations were based on the THz QCL from [15], biased at 11 kV/cm which is approximately the bias aligning the injector and the upper laser levels, i.e. $\varepsilon \approx 0$. All scattering rates and other relevant active region parameters were calculated with the aid of Schrödinger-Poisson and ensemble Monte Carlo codes [52] and their values are not considerably different from the data published in Tab. 4.2. Importantly, here the left and right amplitude reflectivities have been set to only 5%, chosen to be sufficiently low as to ensure the elimination of spatial hole burning from the simulation, and thus isolate FWM as the only mode proliferation mechanism.

Concretely, in Fig. 4.8(c), the system was pumped from the left facet and the electric field at the right end of a cavity of length $L = 2.5$ mm was collected, for a total simulation time of 1 ns. The logarithmic optical power spectrum clearly shows the emergence of signals at the

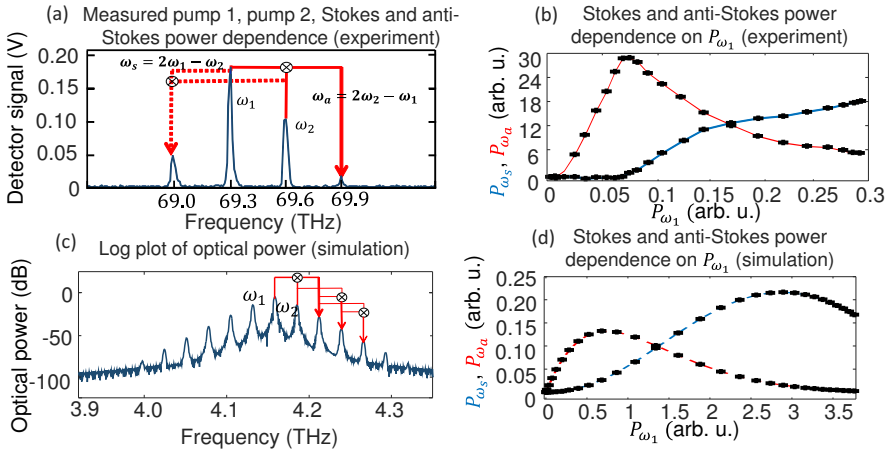

Figure 4.8 (a) Optical spectra obtained from pump-probe experiments with a mid-IR QCL, presented in [110], where the authors pumped the device with two optical modes, ω_1 and ω_2, and observed sideband generation at the Stokes and anti-Stokes frequencies, ω_s and ω_a, respectively. (b) Experimental data, again from [110], illustrating the dependence of the output power of the Stokes and anti-Stokes frequencies on to the input power of the ω_1 mode, while keeping the input power in the ω_2 mode constant. (c) Simulation of the pump-probe experiment in (a), performed for a THz QCL with the Maxwell-Bloch model presented in this chapter. (d) The same plot as in (b) however this time the data comes from time-domain simulations performed with the same model.

Stokes (f_s) and anti-Stokes (f_a) frequencies in excellent agreement with experimental data in Fig. 4.8(a). Based on the formalism in [129], one knows that the amplitudes of the generated sidebands at f_a and f_s will experience the following dependence on the pump amplitudes, i.e. A_{ω_1} and A_{ω_2}, and the nonlinear susceptibility $\chi^{(3)}$:

$$\begin{aligned} A_{\omega_a} &\propto \chi^{(3)}(-\omega_a;\omega_2,-\omega_1,\omega_2)A_{\omega_1}A_{\omega_2}^2, \\ A_{\omega_s} &\propto \chi^{(3)}(-\omega_s;\omega_1,-\omega_2,\omega_1)A_{\omega_1}^2A_{\omega_2}. \end{aligned} \tag{4.22}$$

Figure 4.8(d) shows namely this dependence when the strength of the first pump at f_1 is varied, whereas all other parameters are kept fixed. Denoting with P_{ω_j} the spectral power in the $j-$th mode, it can be seen that in the weak pumping regime, P_{ω_a} exhibits linear dependence on P_{ω_1}, whereas P_{ω_s} quadratic. Further, in agreement with experiment, Fig. 4.8(b), there can be also observed saturation effects and, more interestingly, the previously reported threshold behavior of P_{ω_s}, emerging only after P_{ω_1} is large enough as compared to P_{ω_2} [110]. One can push this analysis a little further and estimate the spectral dependence of the non-linear susceptibility from the relation [129]

$$\chi^{(3)}(-\omega_s;\omega_1,-\omega_2,\omega_1) \propto A_{\omega_s}/[\omega_s A_{\omega_1}^2 A_{\omega_2}]. \tag{4.23}$$

The results from this procedure are graphed in Fig. 4.9, as a contour plot of $\chi^{(3)}$ as a function of f_1 and f_2. As expected [110], the strength of the nonlinearity decreases as the detuning between the seed frequencies is increased. Additionally, Fig. 4.9 reports that $\chi^{(3)}$ is strongest in the interval between 3.6 THz and 3.9 THz, which is natural since this spectral range fits under the gain spectrum, and one can also observe that the FWM efficacy decreases as the detuning between the seed modes is increased. The latter is another result in qualitative

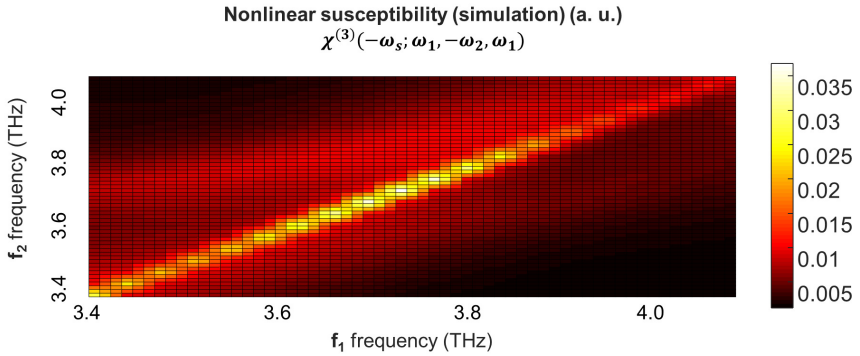

Figure 4.9 Simulation of the nonlinear susceptibility $\chi^{(3)}$ (in arbitrary units) as a function of the two seed frequencies, f_1 and f_2.

agreement with experiment [110]. Even though this approach lacks the robustness of a direct mathematical proof, these calculations unequivocally confirm that it is indeed four wave mixing which is observed, and not other multi-mode generation effects.

Lastly, a couple of words on the efficacy of FWM for multimode lasing. The phase mismatch for the anti-Stokes component of the degenerate FWM process is [64]

$$L\Delta\beta = \left[2\beta(\omega_2) - \beta(\omega_1) - \beta(\omega_a)\right] L, \tag{4.24}$$

where $\beta(\omega)$ is the "wave number" $\leftrightarrow$ "frequency" dispersion relation. For a Fabry-Perot laser of length L, the intracavity mode spacing is $\Delta\omega = \pi c/\left(nL\right)$, so Taylor-expanding around ω_2 up to third order in $\Delta\omega$ yields, with $\omega_1 = \omega_2 - \Delta\omega$ and $\omega_a = 2\omega_2 - \omega_1 = \omega_2 + \Delta\omega$,

$$L\Delta\beta = -L\Delta\omega^2 \left.\frac{\partial^2\beta}{\partial\omega^2}\right|_{\omega_2} + O(\Delta\omega^4) \approx -\frac{1}{L}\left(\frac{\pi c}{n_0}\right)^2 \left.\frac{\partial^2\beta}{\partial\omega^2}\right|_{\omega_2}. \tag{4.25}$$

Plugging in typical values of $L = 5$ mm, $n = 3.6$ and $\partial_\omega^2\beta \approx 2\,\mathrm{ps}^2/\mathrm{mm}$ as an upper estimate for GVD, one obtains a phase mismatch of $L\left|\Delta k\right| = 0.0274\,\mathrm{rad}$, which is negligible. This means that despite significant dispersion present in the cavity, under the favorable conditions of broadband gain, strong third order nonlinearity and some kind of multimode instability mechanism, such lasers can potentially emit a multitude of longitudinal modes even in a free running regime of operation, as reported in numerous experiments [14, 16, 63, 124]. This, however, does not mean that such GVD is not strong enough to hamper the comb formation over the full spectral bandwidth. It will be elaborated further in Sec. 4.3.5 on the detrimental effect of GVD onto the comb coherence, where we will consider simulations of devices with and without GVD compensation.

4.3.3 Spatial Hole Burning (SHB)

An additional mode proliferation mechanism, highly relevant for quantum cascade lasers, is spatial hole burning. This effect arises due to interference of counter-propagating waves in lasers with Fabry-Perot type cavities, and it has been shown to induce multimode instabilities and also hamper active mode locking of QCL devices [83, 84, 112]. The principle, under which SHB leads to multimode lasing, is straightforward to understand [22].

Assuming single mode lasing with angular frequency ω_1 and wave number β_1, the forward and backward propagating components of the field, with intensities $I_1^+ = cn\varepsilon_0|E_+|^2/2$ and $I_1^- = cn\varepsilon_0|E_-|^2/2$, will interfere to produce the total intracavity intensity

$$I_1(x) = I_1^+ + I_1^- + 2\sqrt{I_1^+ I_1^-}\cos(2\beta_1 x + \theta_1), \tag{4.26}$$

where θ_1 is the phase difference between the forward and backward propagating field (taken as zero for simplicity). For a cavity with equal facet reflectivities, i.e. $r_L = r_R = r$, both of which are close to 1, one can take that the intensity of the field in both directions is approximately constant and has equal value, i.e. $I_1^+ = I_1^- = I_1$. Thus the above expression simplifies to

$$I_1(x) = 4I_1\cos^2(\beta_1 x). \tag{4.27}$$

During lasing, the net gain seen by the mode will be equal to the round trip losses, giving the condition [130]

$$\sigma_1 \int_0^l N(x)I_1(x)dx = \int_0^l aI_1(x)dx, \tag{4.28}$$

where the left hand expression is proportional to the net gain and the right hand side to the total round trip losses, with $a = a_w + a_m$ being the distributed loss parameter, incorporating both waveguide and mirror losses.

The steady state dependence of the population inversion on intensity can be given by the formula

$$N(x) = N\Delta(x) = N\Delta^{\text{eq}}/[1 + I_1(x)/I_{sat}]. \tag{4.29}$$

Here, N is the average electron density, Δ^{eq} is the equilibrium population inversion, $I_{sat} = cn\varepsilon_0\hbar^2/(2\mu^2 T_1 T_2)$ is the saturation intensity of the material [22], with T_1 the inversion lifetime parameter, T_2 the total dephasing time, μ the dipole matrix element (in units C $\cdot$ m), and $\sigma_1 = \sigma(\omega_1)$ is the gain cross-section at the particular lasing frequency ω_1.

For multimode lasing, the above threshold condition Eq. (4.28) outlines a procedure for the estimation of the modal intensity under SHB. Assume that there are a total of k candidate cavity modes for lasing, specified by the set $\mathscr{M}_k = \{(\omega_1, \beta_1, I_1), (\omega_2, \beta_2, I_2), \ldots, (\omega_k, \beta_k, I_k)\}$, where the triplet (ω_j, β_j, I_j) denotes the $j-$th mode angular frequency, wave number and intensity, respectively. If one neglects interference effects, then each mode, e.g. the i^{th}, ought to approximately satisfy the balance equation

$$\sigma(\omega_i)N\Delta^{\text{eq}} \int_0^L \frac{I_i\cos^2(\beta_i x)dx}{1 + 4\sum_{j=1}^k I_j\cos^2(\beta_j x)/I_{sat}} = \int_0^L a(x)I_i\cos^2(\beta_i x)dx, \tag{4.30}$$

which will have to hold irrespective if the mode is lasing (in which case we get $I_i = 0$ and thus the identity $0 \equiv 0$) or not. Equation (4.30) can be rewritten in the following form

$$I_i = F_i(I_1, I_2, ...I_k) = \frac{\sigma(\omega_i)N\Delta^{\text{eq}}}{\int_0^L a(x)\cos^2(\beta_i x)dx} \times \int_0^L \frac{I_i\cos^2(\beta_i x)dx}{1 + 4\sum_{j=1}^k I_j\cos^2(\beta_j x)/I_{sat}}, \tag{4.31}$$

which is a system k equations for k unknowns (the mode intensities). Furthermore, since Eq. (4.31) is written in the form of an iterated function, one can try a fixed point iteration algorithm

$$I_i^{m+1} = F_i(I_1^m, I_2^m, ...I_k^m), \quad \text{for } i = 1, 2, \ldots, k, \tag{4.32}$$

where m is the iteration index, to find the steady state solution and determine the lasing modes. As a proof of concept, an exemplary such fixed-point iteration was performed for a hypothetical laser with a single optical transition, homogeneously broadened with a Lorentzian lineshape, cross-section given by the formula Eq. (2.79), and suitably chosen other parameters (not mentioned here since the exact values are not relevant). Importantly the central frequency was chosen at $f_0 = 3$ THz and the total losses were set to $a = 15\,\mathrm{cm}^{-1}$. Results from the fixed-point iteration in Eq. (4.32) are plotted in Fig. 4.10(a)-(c) and clearly illustrate how spatial hole burning enables multimode emission, even in homogeneously broadened lasers. Figure 4.10(a) shows the time-evolution of the field modes, whereas Figure 4.10(b) shows the saturated gain at the end of the algorithm, i.e. after $m = 500$ iterations. Note how, at steady state, each of the modal amplitudes is "chosen" in such a way so that the modal gain will exactly balance the losses (plotted with a horizontal red line in Fig. 4.10(b)).

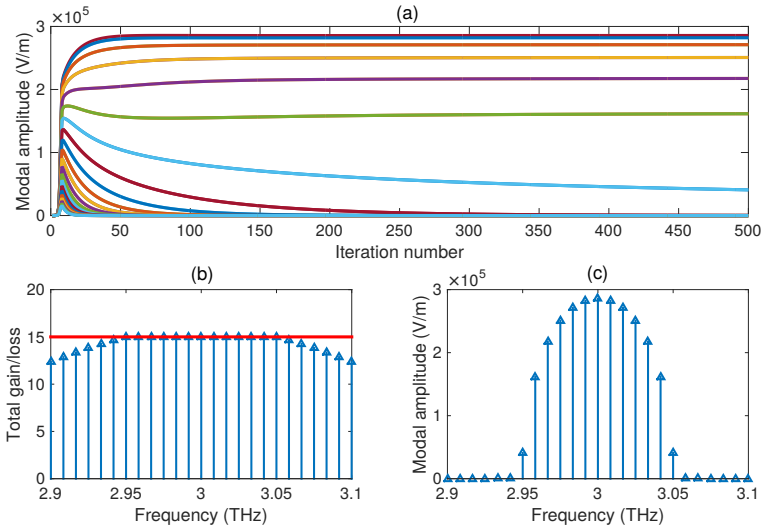

Figure 4.10 Results from fixed-point iteration simulations of Eq. (4.32). (a) Electric field modal amplitude versus iteration number. (b) Modal round trip gain versus frequency and (c) electric field amplitude versus frequency after 500 iterations (i.e. steady state solution).

The obtained results do raise some immediate concerns. First of all, even to the author's own surprise, the fixed-point iteration algorithm does converge to a steady state solution, with constant values for the intensities I_j, without exhibiting any irregular variation in the modal amplitudes. This is in stark contrast with experimental data, which reports an "incoherent" multimode spectrum when the laser is pumped high above threshold and SHB is strong [21, 84]. It might be that the steady state loss=gain relation, Eq. (4.30), utilizes a too simplistic model for the dependence of carrier inversion onto the intracavity intensity, or that nonlinear effects such as self- and cross- phase modulation (stemming from intensity dependent refractive index and hence frequency $\leftrightarrow$ wave number dispersion relation) might play a role. Additionally, at each iteration m one might need to consider random perturbations of the modal photon density, arising due to spontaneous emission or external "environmental" factors jeopardizing the frequency stability of the laser. All of these extensions are out of the scope of this thesis, so the interested reader is encouraged to further pursue these questions.

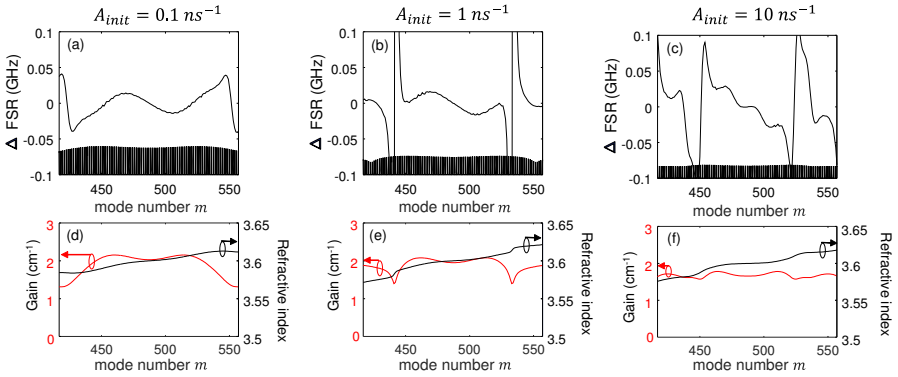

Figure 4.11 Results from simulations of a numerical pump-probe experiment, performed with our model in [5]. (a), (b) and (c) display the variation of the free spectral range as a function of the mode index m, for values of the pump pulse amplitude, expressed in terms of the Rabi-frequency, of 0.1 ns^{-1}, 1 ns^{-1} and 10 ns^{-1}, respectively. For illustrative purposes we also plot the cavity modes (black lines), calculated via $f_m = m \times c/[2Ln'(f_m)]$, with amplitudes weighted by the normalized gain. (d), (e) and (f) Spectral gain (left y-axis) and the real part of the refractive index (right y-axis) as a function of the mode index m and for different pump pulse amplitudes. All simulations were performed at an applied bias of 11 kV/cm, where the upper-lower laser level transition frequency was calculated as $f_0 = 3.88$ THz. The refractive index at f_0 was set to $n = 3.6$ and the simulated cavity length was chosen as $L = 5$ mm, giving a free spectral range $FSR(f_0) = 8.3$ GHz and a corresponding central mode index $m_0 = 487$.

4.3.4 Comb degradation mechanisms

It is known that chromatic dispersion, i.e. frequency dependence of the refractive index, affects the equidistance of the Fabry-Perot modes, and thus hampers the formation of a comb. Direct estimation of the GVD of a device is difficult, as it has a strong dependence on the system parameters, waveguide design, as well as the power spectral density of the lasing modes (due to self- and cross- phase modulation effects) [128]. This also makes the theoretical treatment very challenging and therefore impedes the computer aided design of QCL frequency combs.

Again, one finds that the Maxwell-Bloch equations provide a suitable framework for the rigorous treatment of dispersion, as the density matrix equations intrinsically capture polarization effects, and thus dispersion due to optical gain. The model can be extended by the phenomenological inclusion of different dispersive components, e.g. waveguide or bulk dispersion, via complementary ordinary differential equations, modeling this additional material response in the time domain [55].

Here we restrict ourselves to modeling only dispersion due to optical resonances, i.e. gain dispersion, and in the following several computational experiments to characterize its impact on the equidistance of the cavity modes are performed.

Again, the simulation technique introduced in Sec. 4.3.1 is applied. There the general idea was to treat the gain medium of length L as a nonlinear filter with some unknown transfer function. If one were able to extract the magnitude and frequency response of this transfer function, this information could be used to infer the real and imaginary part of the refractive index. This can be done quite easily by simulating the passage of a pulse, with suitably chosen spectral width and amplitude, through the medium, recording the pulse at the output

facet of the simulation region, and finally processing the input and output data in frequency domain. The real power of this method lies in its universality, as it allows us to characterize the time-dependent behavior of the system under different operating conditions, by simply varying the model parameters.

From basic laser theory [22], it is well known that a Fabry-Perot cavity of length L will sustain longitudinal modes, determined by the relation $f_m = m \times c/[2Ln'(f_m)]$, where m is some (large) integer, f_m denotes the frequency of the m^{th} mode, c the velocity of light in vacuum and $n'(f_m)$ is the corresponding value of the real part of the refractive index. The spacing at the m^{th} longitudinal mode is also known as the free spectral range (FSR) and is given by $FSR(m) = f_{m+1} - f_m \approx c/[2Ln'(f_m)]$, which is generally index-dependent.

In free-running QCLs, due to their broadband nature and ultrafast carrier dynamics [4], there will be a strong competition between FWM and dispersion, the outcome of which will determine the emission spectrum of the device. This is because, while the former is an energy conserving process and thus tends to homogenize the mode spacing, the latter has a detrimental influence as it results in an FSR depending on frequency. It has been shown that at operation regimes where the different components of dispersion cancel each other out [16], or when special dispersion compensation mechanisms are employed [15], four wave mixing can defeat intracavity dispersion via the injection-locking effect [22], resulting in a broad comb spectrum. Generally, however, those comb regimes cover only a fraction of the whole dynamic range of the device and are usually limited to near-threshold operation. In fact, a clear explanation of why FWM loses to GVD is somehow missing. It has been suggested [128] that in cases of large dispersion the phase-matching condition for FWM is violated and therefore the process becomes inefficient. However, in Sec. 4.3.2, it was shown, via a simple Taylor expansion, that for the type of FWM depicted above, values of the GVD coefficient as high as 2 ps^2/mm cannot introduce a sufficiently strong phase-mismatch [5]. Here one can observe another comb-degrading effect, which can be related to spatial hole burning-induced instabilities, and could turn out to be also one of the reasons for the breakdown of comb-like operation at high pump currents.

First, the frequency dependence of the refractive index is investigated in detail, using the computational method outlined in the beginning of this section, when the amplitude of the input pump pulse is varied. In doing so, one can analyze the net effect of different intensity-dependent phenomena, such as gain saturation and also self- and cross-phase modulation, onto the system dynamics.

For these simulations take the QCL of Ref. [15], and again apply the technique from Sec. 4.3.1. This time, the cavity length is set to 5 mm and the pump pulse is propagated only once before post-processing. Figure 4.11 illustrates the results from this procedure when the strength of the input pulse is varied. The latter is chosen as an unchirped Gaussian, with an intensity full-width at half maximum (FWHM) duration of 1 ps, corresponding to a FWHM bandwidth of 440 GHz, whereas the amplitude A_{init} is normalized to the Rabi-frequency of the material.

As a figure of merit for the effect of chromatic dispersion on the comb-spacing, one can calculate the frequency dependent variation of the free spectral range via [131]

$$\Delta FSR(m) = (f_{m+1} - f_m) - (f_m - f_{m-1}). \tag{4.33}$$

Figures 4.11(a)-4.11(c) illustrate the dependence of ΔFSR upon the pump pulse intensity. For completeness Fig. 4.11(d), Fig. 4.11(e) and Fig. 4.11(f) also plot the shapes of the calculated spectral gain and the real part of the refractive index.

The plots in Fig. 4.11(a)-Fig. 4.11(f) show large variations in ΔFSR upon gain saturation. This is due to the fact that causality imposes an intimate relationship between the real and imaginary parts of the refractive index, via the Kramers-Kronig relations [132]. In particular, one can see from Fig. 4.11(b)-(c) and Fig. 4.11(e)-(f) that at places where the saturated spectral gain has a large curvature, due to the dependence $\Delta FSR(m) \propto \partial^2 f_m/\partial m^2$, this would lead to strong variation of the free spectral range and thereby very uneven mode spacing. This reveals that dispersion control is a highly non-trivial problem, deeply rooted in the laser dynamics (e.g. the fluctuations in the mode intensities), which might explain the difficulties of designing a dispersion compensation mechanism which can be effective over a broad range of operating conditions.

As mentioned in the previous section, spatial hole burning is directly related to amplitude and phase instabilities in QCLs due to the effective lowering of the RNGH-threshold, and therefore deserves a more detailed study. A thorough analytical investigation of SHB was already performed in [84] via a linear stability analysis of the Maxwell-Bloch equations. The authors showed how, in the presence of spatial hole burning, a two level system with a population inversion lifetime T_1 and a dephasing time T_2, will experience parametric gain, with maximum values at frequencies separated from the central frequency by the following distance-squared

$$\Omega_{max}^2 \approx \frac{1}{T_1}\sqrt{\frac{p-1}{3T_1T_2}}, \tag{4.34}$$

where p is the pump parameter and $p = 1$ means that the laser is biased exactly at threshold. When driven high above threshold, many QCLs, candidates for frequency comb emitters, show the spectral splitting, predicted by the above formula, confirming the correctness of the analysis [83].

Ideally, SHB will not play a significant effect if the pumping is weak, i.e. $p \approx 1$, or the peaks of the parametric gain are well outside the gain full width at half maximum bandwidth, i.e. $\Delta\omega_{FWHM}$. Assuming, for simplicity, that $T_1 \approx T_2$, one could impose the condition

$$T_1 \ll T_1^{max} = \frac{1}{\Delta\omega_{FWHM}}\sqrt{\frac{p-1}{3}}, \tag{4.35}$$

from where it is evident that for lasers with extremely fast gain recovery, spatial hole burning could not be expected to play a significant role. The order of magnitude of the gain recovery time needed, in order to suppress SHB, can be calculated directly. For a value of $p = 2$, for example, and a value of $\Delta\omega_{FWHM} \approx 2\pi \times 1$ THz, this yields $T_1^{max} \approx 0.06$ps, which is unfortunately too fast to be realistic.

Another method to suppress spatial hole burning is by incorporating the gain medium into a ring cavity instead of a Fabry-Perot one. In [133] it has been demonstrated that integrating

the active region into an external ring cavity leads to dramatic improvement of the quality of active mode locking and consecutively the emission of short pulses by a mid-infrared QCL, known to be infamously hard to mode lock. A more accessible method for reducing SHB is by creating a cavity with asymmetric mirror reflectivities such that the outcoupling is much stronger at, for example, the right facet of the cavity than the left. In such a scenario, the intensity of the right to left propagating component of each mode will be much smaller than the one in the opposite direction, which will lead to suppression of the interference term in Eq. (4.26) and thus reduction of the depth of the inversion grating. In Sec. 4.3.6, this latter scenario is simulated, and it is shown how, when SHB is weak, a free-running laser can settle in a regime of stable phase- and amplitude-coherent operation and therefore emit a frequency comb.

4.3.5 Simulations of comb operation and comparison to experiment

In this section, simulation results for comb operation of the device in [15] are presented, now considering counter-propagating waves in the Fabry-Perot cavity with a length $L = 5\,\mathrm{mm}$, giving rise to spatial hole burning. The simulations only use the device specifications and well known material parameters as an input, with the exception of empirical dephasing times, which were adapted from [121]. Again, the electron wave functions and eigenenergies are computed with a Schrödinger-Poisson solver, and the carrier lifetimes are extracted from Monte Carlo carrier transport simulations. The used model parameters are listed in Tab. 4.1 and the scattering rates are in Tab. 4.2. The simulation time lasts $\sim$15000 round trips to obtain results close to steady state.

In Fig. 4.12, the calculated spectra and beatnotes are compared from simulations without dispersion compensation, Fig. 4.12(c) and Fig. 4.12(d), and with dispersion compensation, Fig. 4.12(e) and Fig. 4.12(f), to experimental data, Fig. 4.12(a) and Fig. 4.12(b). Here, the simulation bias is set slightly below "injector" $\leftrightarrow$ "upper laser level" resonance, i.e., at $10.8\,\mathrm{kV/cm}$.

In both the dispersion compensated and uncompensated case, there is a reasonable agreement with the experimental optical power spectra, Fig. 4.12(a), however substantial differences arise when one considers the corresponding beatnotes.

Let us first discuss the simulation results in Fig. 4.12(c) and Fig. 4.12(d). While experimental data show a strong and narrow beatnote with an FWHM linewidth of approximately $0.55\,\mathrm{MHz}$, Fig. 4.12(b), in Fig. 4.12(d) one observes a multi-beatnote signal distributed around $8.14\,\mathrm{GHz}$. This deviates from the experimental value of around $6.8\,\mathrm{GHz}$ because the experimental implementation of GVD compensation in the cavity results in an increased effective cavity length. In the RF spectrum of Fig. 4.12(d), two peaks can be distinguished, one at $8.149\,\mathrm{GHz}$ and another at $8.151\,\mathrm{GHz}$, both with a FWHM of approximately $3\,\mathrm{MHz}$ (Fourier transformation of 10^4 round trips yields a frequency resolution of $0.83\,\mathrm{MHz}$, where at least two frequency intervals are required to resolve the peak). From the group velocity delay plot in Fig. 4.7 as well as from the spectra, one can deduce that since the high frequency lobe's spectral components carry more power and have lower group velocity v_g, the stronger peak in the beatnote belongs to those frequency components, whereas the weaker one is associated with

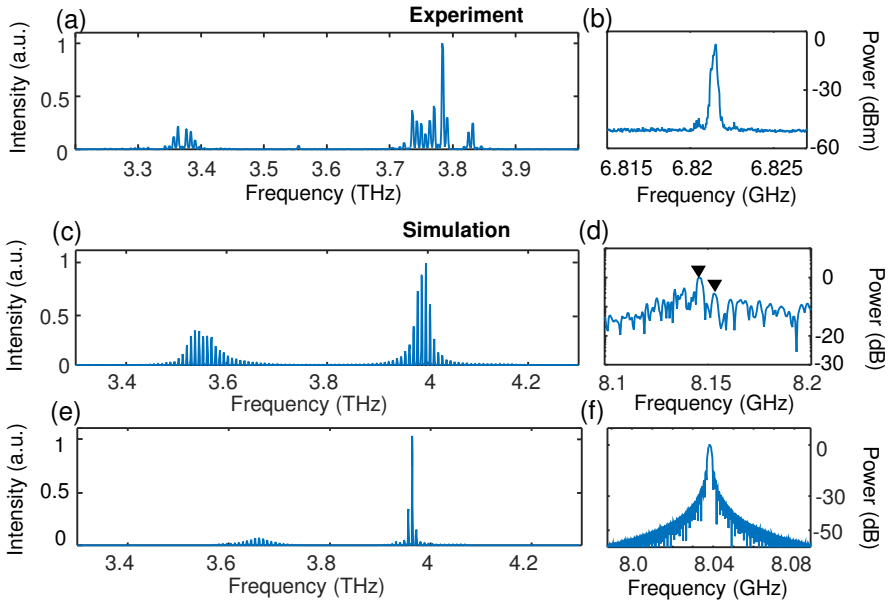

Figure 4.12 Optical power spectra (left column) and beatnotes (right column) from experiment and simulations of the device in [15]. (a), (b) Experimental data for the dispersion compensated laser, at driving current of 0.9 A. Simulation results without dispersion compensation (c)–(d) and with dispersion compensation (e)–(f). The experimentally detected beatnote in (b) has a FWHM of approx. 0.553MHz, whereas the simulated beatnote in (f) has a resolution limited FWHM of 1.66MHz. The strongest peak in (d) has a FWHM of 3.04 MHz.

the lower frequency modes. This means that there ought to be two co-propagating pulses, albeit with a different v_g, which interfere in the beatnote measurement to produce the chaotic RF spectrum in Fig. 4.12(d). The amount of noise in this non-comb regime of operation can be therefore traced mainly to the timing-jitter induced by the difference in group velocities of those pulses. This will be elaborated further below, when the results in time domain are considered.

The situation drastically changes when dispersion compensation is added to the simulations. To cancel the accumulated higher order phase components, after each round trip one Fourier-transforms the electric field envelope, subtracts from the resulting phasor the phase Ψ, extracted analogously to the simulation in Fig. 4.7, and inverse Fourier-transforms the result. The obtained, with this procedure, spectral power density and RF spectra are plotted in Fig. 4.12(e) and Fig. 4.12(f). One can see that such a procedure equilibrates the difference in the group velocities of different lasing modes, which results in a single, strong and narrow beatnote with a linewidth corresponding to the numerical frequency resolution, as expected from the experimental results for comb operation in Fig. 4.12(b).

In [123] it was shown that the strong injector anticrossing leads to a splitting of the emitted comb spectra in frequency domain and to an effect which was coined as "temporal hole burning" in time domain. To compare our simulation results to experiment, a low-pass and high-pass finite impulse response filter are applied to the simulated electric field, in order to separate the low and high frequency lobe components of the signal, respectively. Since the experimental design is dispersion compensated, let us first first consider this scenario, corresponding to the results in Fig. 4.12(e) and Fig. 4.12(f). The smoothed experimental and

simulated instantaneous intensity are depicted in Fig. 4.13(a) and Fig. 4.13(b), respectively, with a smoothing length of $10\,\mathrm{ps}$ in experiment and $3\,\mathrm{ps}$ in simulation.

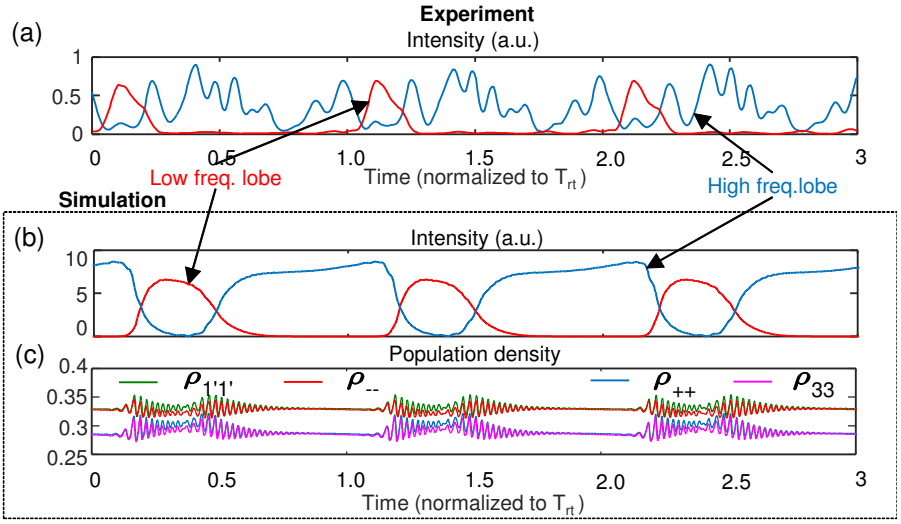

Figure 4.13 Time domain separation of the optical field into high and low frequency lobe components. (a) Measured intensity over time from [123] for the same THz comb device as in [15], driven with $0.9\,\mathrm{A}$ current. (b) Simulated intensity over time for a dispersion compensated QCL evolved for ∼15000 round trips. (c) Time dependence of the electron populations in the injector and upper laser level (i.e. $\rho_{1'1'}$, ρ_{33}) as well as the dressed states (i.e. ρ_{++}, ρ_{--}).

This approach already yields decent agreement between experiment and simulation as both data demonstrate a pulse switching behavior between the high and low frequency lobe components of the spectra. The high frequency lobe pulse (blue curve) has a longer time duration than the low lobe signal (red curve). This results from the difference in relative strengths of the corresponding spectral lobes, as the high lobe components experience more gain, as evident in Fig. 4.7. Furthermore, in the experimental trace an additional oscillatory substructure emerges, the reason for which remains to be clarified. However, a possible explanation could be the presence of windowing effects of the Fourier transform spectrometer.

The dependence of the relative strengths of both lobes on the bias has already been discussed in [121], however its implications on the time domain behavior of the laser were not considered in greater detail. To summarize the conclusions in [121], the inclusion of a strong injector anticrossing leads to a splitting of the injector $|1'\rangle$ and upper laser level $|3\rangle$ into a doublet of so-called "dressed states". The higher energy level is denoted by $|+\rangle$ (also known as the "anti-symmetric" state), and the other level by $|-\rangle$ (i.e. the "symmetric" state). These states are separated by approximately the anticrossing energy $2\hbar\Omega_{1'3}$ (depending on the detuning), which can be readily confirmed from experiment [124]. The relative radiative coupling strength of states $|+\rangle$ and $|-\rangle$ with the lower laser level depends on the detuning from resonance. Assuming low intracavity intensity, it can be shown that below the resonant bias, i.e., for $\hbar\varepsilon < 0$, the high frequency lobe of the gain dominates the transition, whereas above resonance the low lobe does [121]. As simulations and experimental data show, this results in a longer high frequency pulse.

Figure 4.13(c) displays the calculated density matrix elements ρ_{33}, ρ_{++}, ρ_{--} and $\rho_{1'1'}$ as a function of time. For all four terms, dampened Rabi-oscillations occurring upon a pulse switching event are observed, which manifest the intramode beating of the high and low lobe. The period of these oscillations is approximately $2.84\,\mathrm{ps}$, giving a frequency of $350\,\mathrm{GHz}$, which is namely the beat frequency between the high and low lobes of the dispersion compensated laser's spectrum (see Fig. 4.12). One can also clearly observe that whenever the high frequency lobe lases, state $|+\rangle$ gets more strongly depleted, whereas whenever the low lobe is switched on, state $|-\rangle$ saturates.

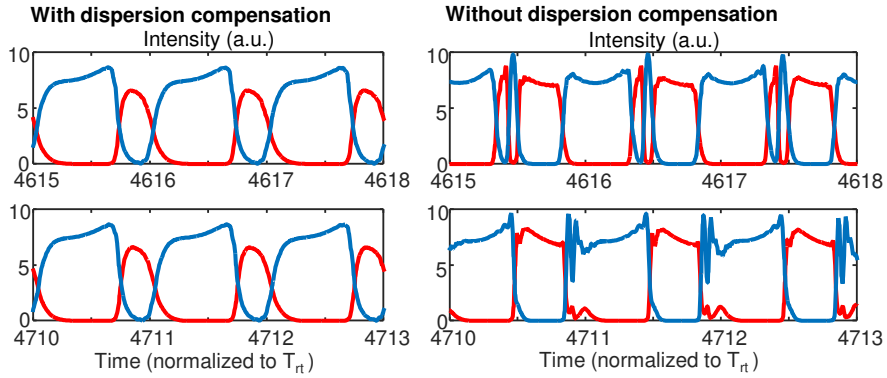

Figure 4.14 Simulated high (blue) and low (red) frequency pulses for a numerically dispersion compensated (left column) and an uncompensated (right column) THz QCL. Data from round trip 4615-4618 (top) and 4710-4713 (bottom) are shown.

To illustrate the implications of the existence of co-propagating high and low frequency lobe pulses in the presence of GVD, the simulated instantaneous intensities with (left column) and without (right column) dispersion compensation are shown in 4.14 for different temporal intervals. Temporal hole burning, or pulse switching, is clearly present in both cases. With dispersion compensation, the periodicity is preserved over many round trips, as can be seen by comparing the intensity traces for the two displayed temporal intervals. By contrast, in the presence of GVD the high and low frequency lobes constantly compete with each other, which leads to a complex non-periodic temporal shape of the signal. Thus, while the signal from a low GVD QCL has a minimal timing jitter, which results in a narrow and strong beatnote, the one from a dispersion uncompensated device operates in a multi-pulse regime with a complicated temporal and spectral profile, and thus never quite reaches a steady state. From this it follows that a coherent comb cannot be formed over the full spectrum, but either no comb or sub-combs can be observed [16, 63].

One can naturally extrapolate these conclusions to a situation where the effects of material and waveguide dispersion add to a much more complicated dispersion profile, as compared to the one in Fig. 4.7. In such a case, the competition between electric field signals propagating with various different group velocities will lead to a chaotic and unstable beatnote, characteristic for multimode non-comb behavior of QCLs [16, 63].

Lastly, it is noteworthy to add that with these density matrix simulations, the temporal hole burning effect could be reproduced at different values of the applied bias ranging between 10.7 and 11.4 kV/cm (not shown here). For lower or alternatively higher biases, lasing occurred

only in the dominant frequency lobe, due to the large difference between the corresponding components of the gain, and thus no pulse switching could be observed. Also it was found that the temporal overlap increases as the spectral gap between the high and low lobes is decreased, i.e. with decreasing anticrossing energy $\hbar\Omega_{1'3}$, as well as with broadening of the radiative transition's linewidth.

4.3.6 In-depth analysis of the modal dynamics and the impact of spatial hole burning

In the following a more detailed study of the presented results from long-time simulations of the hypothetical THz QCL for a self-starting, free-running configuration under different boundary conditions is performed. In the subsequent analysis the simulations are always started with some sufficiently small (and randomly chosen) value for the envelope $f(x, t = 0)$, physically corresponding to some random fluctuations of the field, and the system is evolved for 3000 to 4000 round trips until the envelope could be assumed to reach steady state. Within this analysis, it is found that spatial hole burning has a dramatic effect on the comb performance, one that appears even more relevant than dispersion. To see how SHB affects the dynamics, the time evolution of the phase and amplitude of each of the lasing modes in the spectrum is studied in greater detail.

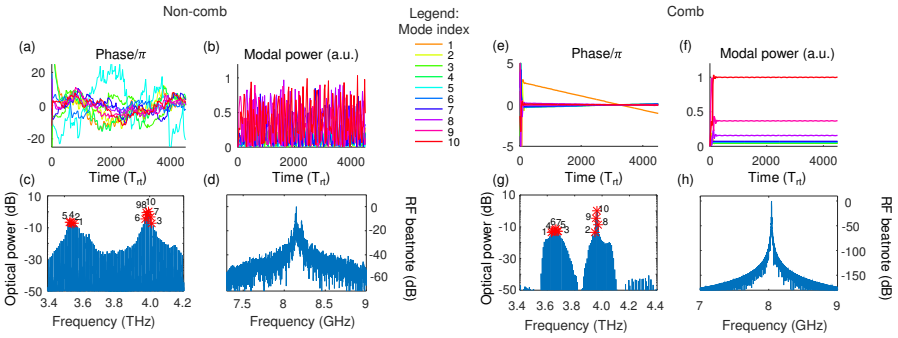

Figure 4.15 Simulations of non-comb and comb regime of operation of a THz QCL where both mirror reflectivites were set to 100%. (a)-(d) Modal phase, modal power, optical log-spectrum and radio-frequency (RF) beatnote, respectively, of a dispersion uncompensated device. (e)-(h) Modal phase, modal power, optical log-spectrum and RF beatnote, respectively, of a dispersion compensated device. The modal phases and powers were obtained via the short-time Fourier transform with a Hanning window function of duration 5 round trips (round trip time is approximately $T_{rt} = 120$ ps) for a total simulation time of 4500 round trips. The phases are presented after filtering out the constant linear time-drift, obtained with least squares estimation. We plot the results for the 10 strongest modes (ordered in increasing order from 1 to 10) in the corresponding spectra in c) and g), the locations of which are indicated by star-shaped markers. The color coding for each mode is presented in the legend.

In order to establish a criterion as to what this time evolution should be in the case of a comb and a non-comb regime of operation, the simulations from Sec. 4.3.5 of the same device with and without dispersion compensation are revisited, remembering that in the former case the laser emitted a comb, whereas in the later - an incoherent multimode spectrum. Here, a

deeper look into the data is presented, where we track the time-evolution of the amplitudes and phases of the 10 strongest lasing modes in both cases.

The results are summarized in Fig. 4.15. Note that for these simulations the laser was biased at 10.8 kV/cm, which is when the injector level is energetically below the upper laser level (i.e. $\varepsilon < 0$). A quick comparison of Fig. 4.15(a)-(d) and Fig. 4.15(e)-(h) reveals a striking difference in the time-domain dynamics of both scenarios. In Fig. 4.15(a)-(d), demonstrating the non-comb operational regime, one observes irregular fluctuation of phase and amplitude without any noticeable regularity or tendency for convergence. In fact, it almost seems that all individual modes switch on and off at random time intervals. This is namely a manifestation of multimode phase and amplitude instabilities and could be due to the RNGH-instability effect, discovered independently by Risken and Nummedal [87] as well as Graham and Haken [127]. In contrast, whenever the laser operates as a comb, i.e. Fig. 4.15(e)-(h), after several hundred round trips the lasing modes quickly converge to their steady state values with very little variation what so ever. Thus the modes are lasing constantly and are clearly phase-locked.

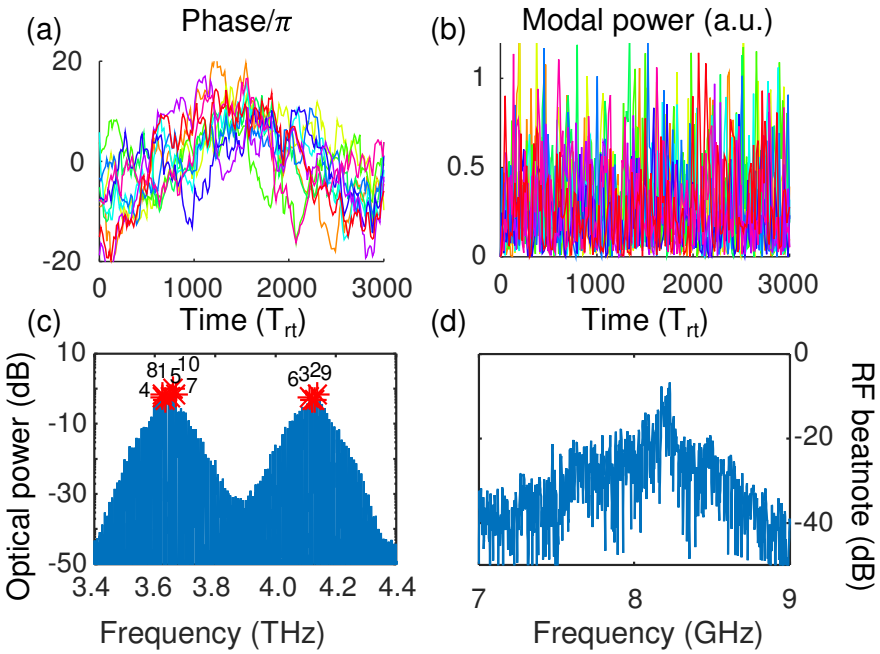

Figure 4.16 Simulation results of a free-running THz QCL, biased at 11 kV/cm, where both the left and the right facet reflectivities were set at 100%, in order to support a *strong* spatial hole burning effect. (a) and (b) illustrate the modal phase and power of the top ten strongest lasing modes in the spectrum. (c) Optical power log-spectrum (normalized) and (d) RF beatnote of the simulated device. The modal characteristics, i.e. (a) and (b), were extracted using the short-time Fourier transform with a Hanning window of 5 round trips over a total simulation time of 3000 round trips. The color coding is identical to Fig. 4.15.

Now, let us investigate whether SHB has any impact on the laser spectrum. First the device under study is simulated when biased at 11 kV/cm, in a free-running regime of operation, without dispersion compensation, when both outcoupling mirror reflectivities were set to 100%. Since equal facet reflectivities favor the formation of standing waves, this will lead to a strong SHB.

Unsurprisingly, the simulation results reveal a similar behavior to the one in Fig. 4.15(a)-(c), with irregular variation of the spectral modes in Fig. 4.16(a)-(b) and a highly irregular beatnote signal around $f_{rt} = 8.3$ GHz, Fig. 4.16(d). One can conclude, quite expectedly, that when there is no dispersion compensation and spatial hole burning is strong, the laser fails to produce a comb.

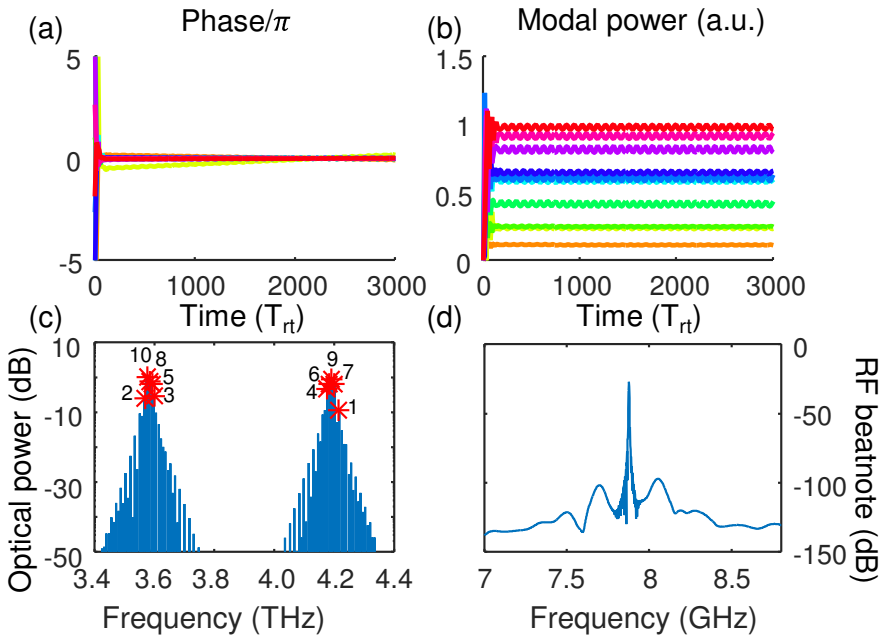

Figure 4.17 Simulation results for the same configuration as in Fig. 4.16, with the difference that the right reflectivity coefficient was set to 5%, whereas the left was maintained at 100%, in order to support a *weak* spatial hole burning effect. (a) and (b) depict the modal phase and power of the top 10 strongest modes, visible in the optical spectrum in (c). (c) Optical log-spectrum produced by the simulation with the top 10 modes indicated by red star-shape markers and corresponding mode index. (d) RF beatnote, calculated from the simulation.

Next, consider simulations for a free-running laser with asymmetrically chosen outcoupling losses, where the left reflection coefficient was maintained at 100% and the right one was set to 5%. As discussed in Sec. 4.3.3, this strengthens the unidirectionality of the emission and thus suppresses SHB. Notice that here also no dispersion compensation has been employed, in contrast to the simulation results in Fig. 4.15(e)-(h). The plots in Fig. 4.17(a)-(d) show that by only eliminating spatial hole burning one can recover the comb-like stable behavior.

Additionally, similarly to the spectrum in Fig. 4.15(g), Fig. 4.17(c) shows that the comb-like behavior seems to come at the expense of significantly reduced spectral bandwidth (as compared to e.g. Fig. 4.16(c)). Note again that this was experimentally observed in Ref. [21], where the elimination of SHB was shown to result in a sparse, but coherent multimode spectrum.

4.3.7 Seeding the comb formation

Before the analysis of free-running THz QC lasers is concluded, it will be worthwhile to discuss the various possible regimes of multimode dynamics. From the previous Sec. 4.3.6,

it seemed that eliminating spatial hole burning is the "ultimate remedy" for recovering of the comb-like characteristics of the emission spectrum. Unfortunately, this is not always the case, as eliminating SHB will (a) reduce the number of lasing modes and thus the covered spectral range and (b) might still result in an unstable, incoherent multimode behavior as experimentally confirmed in [21].

Due to the two separate transitions in the laser under investigation, let us study the effect of spectral cross-talk between the corresponding frequency lobes. Until now, the self-consistently extracted experimental parameters had such values as to ensure a minimal overlap between modes belonging to the high and the low frequency lobes, as is also observed in the corresponding experiment [15]. Even though such a device (i.e. a comb with a gap in the spectrum) could be deemed as defect, time-domain simulations indicate that whenever the cross-talk between the two optical transitions is minimal, the device is easier to phase lock. This could be due to the fact that in the presence of cross-talk, one lobe tries to impose its own FSR (via FWM) onto the other (and vice versa), which results in a constant competition for gain between modes from separate gain lobes. In case the FSR of both lobes is different, which will most probably be the case namely due to asymmetrical saturation effects, see Fig. 4.7, this will incur a constant mode competition which might not "settle" in favor of one particular choice for the FSR, but rather destabilize the modal dynamics altogether.

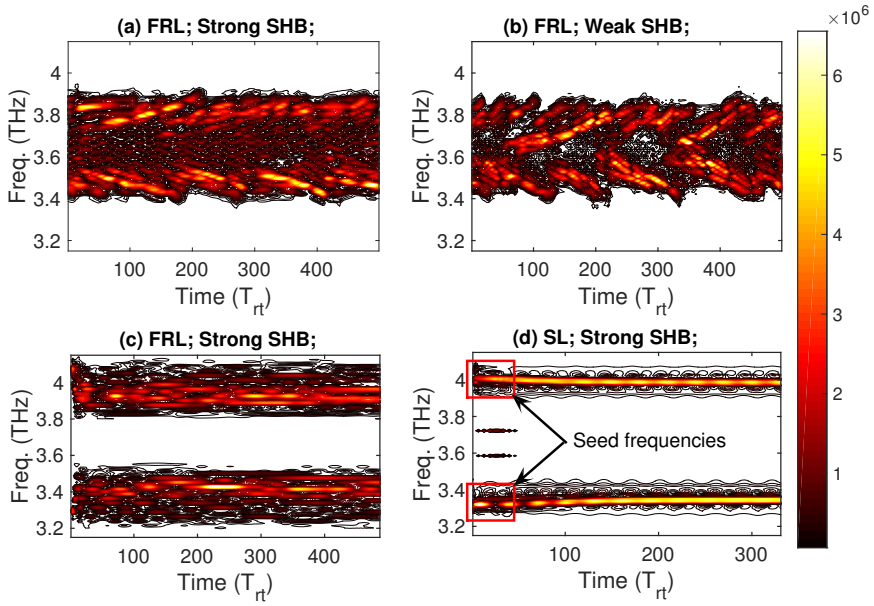

Figure 4.18 Simulations of a free-running laser (FRL) with symmetrically (a) and asymmetrically (b) chosen reflection coefficients. (c) Simulations of a free-running laser with the effect of pure dephasing removed, yielding an optical spectrum with minimal cross-talk between the distinct optical transitions. (d) Simulations with the same parameter set as in (c), however in the case where the lasing has been seeded with two pairs of resonant modes, one located under each frequency lobe of the gain.

To illustrate this effect, simulations of the same resonant LO-phonon QCL, biased at 11 kV/cm, with slightly altered pure dephasing parameters (see Tab. 4.1), are presented. Namely, the value of τ_{32}^{pure} was decreased to 0.4 ps (in effect increasing the linewidth of both transitions), in order to ensure that both spectral lobes are sufficiently "close" to each other and thus induce spectral cross-talk. Results from those simulations are illustrated in Fig. 4.18(a) and

Fig. 4.18(b), with the former presenting the case when SHB is strong due to equally set facet reflectivities, and the latter illustrating weak SHB due to asymmetric reflection coefficients. The abbreviations in the figure read: FRL - free-running laser, SL - seeded laser, SHB - spatial hole burning.

Let us look in depth at the results of Fig. 4.18(a)-(b), showing the spectrogram, computed with a short-time Fourier Transform, of the electric field. We see that both in the presence and absence of SHB, the spectrum consists of multiple modes, which drift away from the center of the spectrum towards its periphery. This is probably to due to cascaded FWM, which "transports" the maximum modal power from inside to the outside of the gain spectrum. Such a peculiar behavior, which to the best of the author's knowledge has not been reported before, seems to be due to the presence of a large overlap in the spectra of both transitions. Furthermore, in this case, the elimination of SHB in Fig. 4.18(b) does nothing to stabilize the spectrum.

On the other hand, Fig. 4.18(c)-(d) reveal simulations when the contribution of the pure dephasing time τ_{32}^{pure} has been removed completely, in order to ensure minimal spectral-cross talk between the distinct gain lobes. In Fig. 4.18(c) one sees the spectrogram from free-running laser simulations, whereas Fig. 4.18(d) illustrates the case when the same laser (i.e. with the same parameter set as in (c)) has been seeded with two pairs of modes, with one pair located under each gain lobe. In both simulations, the facet reflectivities were set to 100%, as a prerequisite for strong spatial hole burning.

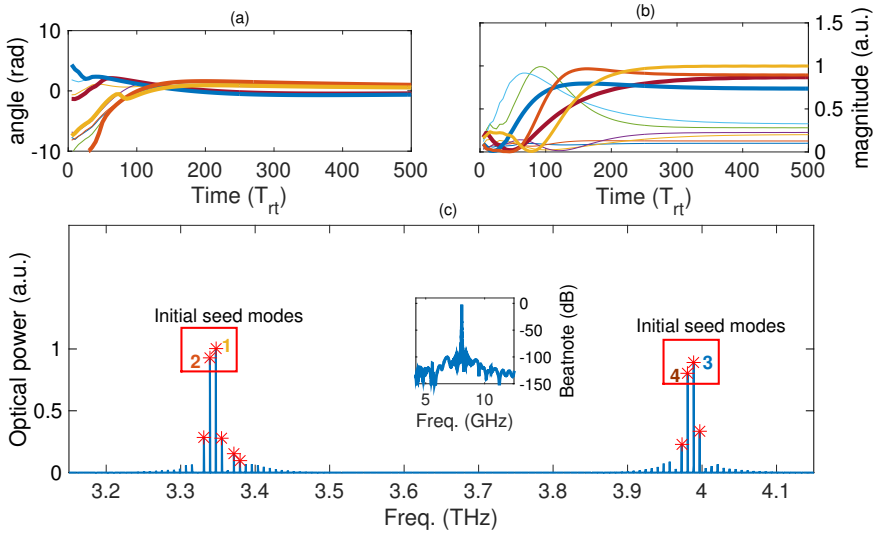

Figure 4.19 Detailed "look" into the simulation results from Fig. 4.18(d). Time-dependence of the modal phase (a) and amplitude (b) of the 10 strongest lasing frequencies from the optical power spectrum in (c).

From Fig. 4.18(c) we see that reducing the spectral cross-talk "straightens" the spectrum as now the evolution of the modal-power maximum proceeds somewhat parallel to the arrow of time, i.e. a significant drift of this peak is not observed. Nevertheless, from the spectrogram alone, one can quickly conclude that the laser emission will not satisfy the requirements for a frequency comb, since the modal amplitudes are not constant in time, but instead vary

without any discernible pattern. Indeed, beatnote calculations for the spectrum of that same simulation (not shown here), reveal a strong peak at the approximate round trip frequency of 8.2 GHz, surrounded by two side-bands around 1 GHz apart, indicating amplitude modulation. By contrast, when one considers calculations with the same parameter set as in Fig. 4.18(c), however with the lasing being started with two pairs of seed frequencies, both having the same FSR, one observes that the comb behavior is recovered, albeit again at the expense of a reduced spectral bandwidth. The full modal analysis of this simulation is presented in Fig. 4.19(a)-(c). The phase and amplitude of the top 10 lasing modes quickly settles to some constant value, without any sign of amplitude modulation, Fig. 4.19(a)-(b). In Fig. 4.19(c), the spectrum consists of two distant narrow-band frequency lobes, with the initial seed frequencies, indexed accordingly, carrying also the most energy. One can see that even in the presence of SHB the laser can act as a frequency comb, provided the correct comb formation mechanism has been "ignited" in some adequate way.

4.4 Conclusion

In this chapter a theoretical model was presented, which is suitable for the analysis of transient dynamics of THz quantum cascade lasers designed for frequency comb operation. It was shown on multiple instances how the simulation results agree well with experimental data both in the time and frequency domain. The reader has hopefully also gained a deeper insight into the intricate coupling between various comb generation and comb degradation mechanisms at play in free-running QCLs. Since the complexity of the theoretical model does not allow for a mathematical solution, the underlying dynamics was investigated via *numerical* experiments through simulations. Of course this technique to perform the analysis of complex systems does not yield comparable intuitive understanding as a rigorous analytical result, however it is probably more powerful as it delivers results with better empirical accuracy (due to the increased explanatory power of the model), and as such allows us to "design" these numerical experiments in a targeted way in order to gain knowledge about the device.

5 Mode locked THz QC lasers

5.1 Introduction

In the previous chapter it was shown how, due the intrinsically multimode nature of QCL emission spectra, these devices can be used for the generation of coherent frequency combs, even in free-running regime of operation, i.e. without taking any particular effort to introduce phase-locking in the lasing modes. While free-running QCLs rely on four wave mixing for their mode proliferation, group velocity dispersion and multimode instabilities can easily deteriorate the phase and amplitude stability of the device, making the formation of frequency combs a daunting task. The question naturally arises, as to what effect will an intentional phase control have onto the spectrum of the device? What familiar techniques are there, possibly from other areas of laser science, to introduce a fixed phase relationship between the spectral lines and thus recover the comb-like characteristics of the QCL emission?

Naturally, it is also of great scientific and practical interest to enable the formation of short, mode locked pulses of light with QCLs. This would be a major advancement for THz and mid-infrared (MIR) spectroscopy as it will open up the stage for ultrafast optical experiments, such as for example time-resolved THz spectroscopy [134], with compact, on-chip, direct sources. Additionally, since mode locked pulses are frequency combs in the Fourier domain, ultrashort pulse generation via QCLs will provide an alternative approach to obtain broadband frequency combs.

Unfortunately, experience shows that QCLs are notoriously difficult to mode lock [18], with the shortest pulse widths achieved so far being around 2.5 ps in the THz via active modulation of the injection current [51]. It is believed that, due to the ultrafast processes that govern intersubband transitions, active mode locking of QCLs is feasible only close to lasing threshold, whereas passive mode locking (PML), in the traditional sense, is virtually impossible [17]. This is because the intrinsically short carrier relaxation times, typically several times smaller than the cavity round trip time, obstruct the formation of short bursts of light since the trailing edges of any propagating pulse would be amplified by the fast recovering gain [43].

In the author's opinion there is no fully conclusive evidence to support these claims, especially in the THz, as the gain recovery dynamics has not been extensively studied. In fact, to my best knowledge, to present date there have been only two publications experimentally investigating the gain recovery time in bound-to-continuum (BTC) THz devices, and none in resonant-phonon QCLs. Interestingly, both experimental results indicate sub-threshold lifetimes on the order of several tens of picoseconds [135, 136]. These measurement techniques are based on a pump-probe experimental method where a perturbing resonant pump pulse is injected into the gain medium followed by a temporally detuned probe pulse interacting with the saturated gain. In the publication in Ref. [135], the photocurrent induced by stimulated

emission between the upper and the lower laser level was recorded as a function of the delay between both pulses, and a Gaussian fit was used to infer the speed of the recovery of population in the upper laser state. The measured lifetimes were ≈ 50 ps which, as it will be shown, are long enough to enable mode locking. In fact one might argue that BTC QCLs are among the most optimal devices for mode locking, since the energy exchange between the propagating pulse and the saturable gain is most efficient when the carrier dynamics is faster than the round trip time.

This chapter is concerned with theoretical models for both active and passive mode locking of quantum cascade lasers. The method to realize passive mode locking is based on well established techniques for quantum dot and conventional semiconductor lasers [73, 88, 137–140], where PML is routinely achieved based on a saturable absorber (SA) and a gain medium as separate components of a multi-section wave guide. Here absorption is implemented by reverse biasing the gain medium. Carrying this concept to QCLs was first suggested by Franz Kärtner [141], whereas Talukder and Menyuk were the first to point out that rather than reverse biasing the gain, carefully chosen positive biases should be used for QCLs [142]. In this work the authors simulated passive mode locking for mid-infrared devices, where the intensity dependent saturation was implemented via a (slow) quantum coherent absorber. Along these lines simulations for PML in THz QCLs have also been presented [143, 144]. In this chapter, it is expanded upon previous works by i) using an extended theoretical model, ii) showing that guided by classical principles one can achieve passive mode locking by simply using a fast saturable absorber instead [145], and iii) in addition to the conventional PML approach, the possibility of hybrid and colliding pulse mode locking will be also discussed. The way in which the fast saturable absorber (FSA) enables mode locking is twofold [59, 61]. First, the FSA provides more gain for shorter pulses, strong enough to bleach the material, while at the same time it also suppresses weak background fluctuations. Secondly, it also acts as a compensator for the dispersion introduced by the gain medium, as both gain and loss interact resonantly with the intracavity intensity, albeit with different signs in the polarization term. As a result, if the gain and absorber sections are packed into a compact structure, with the small round trip time only several times longer than the relaxation time in the gain section, very stable mode locking with one or two pulses per round trip arises.

Next to passive mode locking, a theoretical model for the computational treatment of the active mode locking of QCLs is also presented. This envisaged approach is based on coupling between the Maxwell-Bloch equations, used for carrier-light interaction dynamics, and a transmission line approach, used for simulating the electrical characteristics of the device. Due to the provably strong interaction between the modulation voltage wave and the THz field propagating inside the cavity [18, 146], such microwave-optical simulations could provide the community with a deepened understanding of the operational principles of mode locked QCLs and hopefully enable the generation of few-cycle THz and mid-infrared pulses therefrom.

This chapter is organized as follows: Sec. 5.2 investigates, via semi-analytical calculations and computer simulation, the possibility to passively mode lock ring cavity terahertz quantum cascade lasers. On the other hand, Sec. 5.3 discusses different variants of PML for Fabry-Perot QCLs, where next to conventional passive mode locking the more exotic colliding pulse mode locking and hybrid mode locking are considered. Lastly, in Sec. 5.4, the microwave-optical

model based on the transmission line/Maxwell-Bloch equations is presented together with some preliminary tests of its validity.

Some of the results, contained in this chapter, were presented on several scientific conferences and also featured in a journal publication [143, 147].

5.2 Passive mode locking of ring cavity QCLs

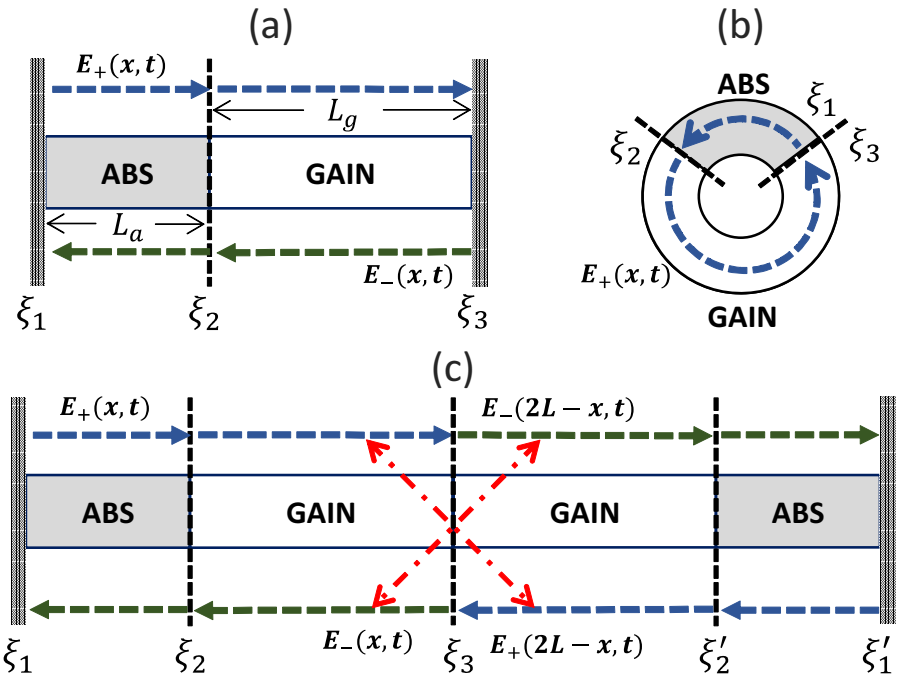

Figure 5.1 (a) A two-section Fabry-Perot cavity, consisting of an absorber of length L_a and a gain section of length L_g. (b) Monolithic ring-shaped multi-section resonator. (c) The Fabry-Perot cavity of (a) reflected off its right outcoupling facet (at coordinate ξ_3) to form a quasi-ring resonator.

In the next few sections a study of the possibility to passively mode lock multi-section ring cavity quantum cascade lasers will be presented. Despite the multilevel dynamics of these devices, we initially assume that the gain and the saturable absorber regions can each be represented as a two level system, which will allow us to analytically reason about the equations. Furthermore, since the inclusion of spatial hole burning also complicates the theoretical treatment, it is necessary to also presuppose that the field propagates inside a ring laser as illustrated in Fig. 5.1(b). Being aware of the fact that the typical QCL cavity design is the linear Fabry-Perot resonator [27], this approximation is nevertheless used, as the ring model is much easier to analyze. One might also argue that this is admissible if one takes the original Fabry-Perot cavity in Fig. 5.1(a) and unwraps/mirrors it with respect to one of the outcoupling facets as graphically depicted in Fig. 5.1(c). Then, instead of treating

counter-propagating fields $E_{\pm}(x,t)$, one defines a single quantity $E(x,t)$ over the doubled cavity length $L = L_a + L_g$ as

$$E(x,t) = \begin{cases} E_+(x,t) & x \in [0,L) \\ E_-(2L-x,t) & x \in (L,2L], \end{cases} \tag{5.1}$$

and, assuming no outcoupling losses, employs the "periodic" boundary condition $E(0,t) = E(2L,t)$, which is the same as $E_+(0,t) = E_-(0,t)$. The treatment of more realistic models, including counter propagating waves and spatial hole burning, is reserved for a later section, where results from computer simulations are presented.

Taking into account the multi-section structure of the laser, let us write down the well known Maxwell-Bloch equations for a two level system in the rotating wave and slowly varying amplitude approximation. This model couples the slowly varying field amplitude $E(x,t)$ to the 2×2 density matrices ρ_k of each section, written in terms of the population inversion, Δ_k, and the envelope of the polarization, η_k, with $k = \{g,a\}$ indexing the gain and absorber, respectively. It is worth mentioning that, due to the nature of the employed approximations, the results will be limited to pulses with duration longer than ~1 ps. The equations now read

$$\frac{\partial E}{\partial x} + \frac{n}{c}\frac{\partial E}{\partial t} = -i\frac{\Gamma_k \mu_k \omega_0}{\varepsilon_0 c n} N_k \eta_k - \frac{a_k}{2} E, \tag{5.2a}$$

$$\partial_t \Delta_k = i\frac{\mu_k}{\hbar}\left(E^*\eta_k - E\eta_k^*\right) - \frac{\Delta_k - \Delta_k^{\mathsf{eq}}}{T_{1k}}\,, \tag{5.2b}$$

$$d_t \eta_k = -i(\omega_k - \omega_0)\eta_k + i\frac{\mu_k}{2\hbar} E\Delta_k - \frac{\eta_k}{T_{2k}}\,, \tag{5.2c}$$

where ω_k denotes the resonance frequency in the $k = \{$g,a$\}$ medium, μ_k the corresponding dipole moment (in units C· m), a_k denotes the distributed power losses, $\Gamma_k \approx 1$ the (dimensionless) field overlap factor, Δ_k^{eq} is the quasi-equilibrium inversion in each section, and the rest of parameters are as defined in Chapter 2. Also define the "pump strength" as

$$p = \Delta_g^{\mathsf{eq}}/\Delta_g^{\mathsf{th}} \approx J_g/J_g^{\mathsf{th}}, \tag{5.3}$$

which is approximately the ratio between the injected current in the gain section and the current at lasing threshold, with Δ_g^{th} being the value of the gain inversion at threshold.

5.2.1 Threshold gain

Here, the steady state solution of the Maxwell-Bloch equations at threshold is examined. Neglect, for a second, the effect of the saturable absorber losses onto the threshold condition. Then at and below the threshold pumping, the electric field is zero, so from Eqs. (5.2), for $k = g$, one gets the steady state solution $\bar{\Delta}_g = \Delta_g^{\mathsf{eq}} = \Delta_g^{\mathsf{th}}$. At threshold, the peak of the gain, attained at some angular frequency ω, will exactly balance the losses. This condition establishes that

$$\frac{N_g \Gamma_g \mu_g^2 \omega}{2\varepsilon_0 c\hbar n} \times \frac{\gamma_g}{\gamma_g^2 + (\omega - \omega_g)^2} \times \bar{\Delta}_g = \frac{1}{2}\sigma_g(\omega) N_g \Delta_g^{\mathsf{th}} = \frac{a_g}{2}, \tag{5.4}$$

where $\gamma_g = T_{2g}^{-1}$ is the dephasing rate and $\sigma_g(\omega)$ is the gain cross-section at that particular frequency, given by

$$\sigma_g(\omega) = \frac{\Gamma_g \mu_g^2 \omega}{\hbar \varepsilon_0 n c} \times \frac{\gamma_g}{\gamma_g^2 + (\omega - \omega_g)^2}. \tag{5.5}$$

This yields the threshold population inversion as

$$\Delta_g^{\text{th}} = \frac{a_g}{\sigma_g(\omega) N_g}, \tag{5.6}$$

where the primary lasing frequency, i.e. ω, will generally be the cavity mode yielding the largest possible value of $\sigma_g(\omega)$ and thus smallest possible value for the inversion Δ_g^{th}. Since it is reasonable to assume that $\omega \approx \omega_g \approx \omega_0$, then the threshold inversion reduces to the formula $\Delta_g^{\text{th}} = a \times \varepsilon_0 c \hbar n / \left[N_g \Gamma_g \mu_g^2 \omega_0 T_{2g} \right]$.

Now, one can include the effect of the saturable absorber, i.e. consider the losses experienced by the optical field upon its resonant interaction with this non-inverted medium. Assuming an absorber with inversion $\Delta_a^{\text{eq}} < 0$, length L_a, and distributed losses a_a, then the condition in Eq. (5.6) becomes

$$\begin{aligned}
&\sigma_g(\omega) N_g \Delta_g^{\text{th}} L_g + \sigma_a(\omega) N_a L_a \Delta_a^{\text{eq}} = a_g L_g + a_a L_a, \\
&\Leftrightarrow \\
&\Delta_g^{\text{th}} = \frac{a_g}{\sigma_g(\omega) N_g} + \frac{a_a L_a}{\sigma_g(\omega)^g N_g L_g} - \frac{\sigma_a(\omega) N_a L_a \Delta_a^{\text{eq}}}{\sigma_g(\omega) N_g L_g}, \\
&\Leftrightarrow \\
&\Delta_g^{\text{th}} = \frac{a_g L_g}{G_g} + \frac{a_a L_a}{G_g} - \frac{G_a}{G_g} \times \Delta_a^{\text{eq}},
\end{aligned} \tag{5.7a}$$

where subscript indices g/a denote the respective quantities of the gain/absorber section and $G_j = \sigma_j N_j L_j$. From Eq. (5.2)), one can immediately see that, if $G_a \times \Delta_a^{\text{eq}} > G_g$, then $\Delta_g^{\text{th}} > 1$, and no lasing will start whatsoever.

5.2.2 Gain recovery time

Here an exact expression for the gain recovery time will be derived, based on the two level approximation. Assume that the pulse has just interacted with the system at a particular point along the length of the gain medium, and at time $t = t_0$, saturated the inversion to $\Delta_g(t_0)$. The gain recovery time will be defined as the time it takes for the population inversion to recover to the threshold value Δ_g^{th} from its initial value of $\Delta_g(t_0)$.

Immediately after passage of the pulse (i.e. when $E \approx 0$), the population inversion obeys the following simple ordinary differential equation

$$\dot{\Delta}_g(t) = -\frac{\Delta_g(t) - \Delta_g^{\text{eq}}}{T_{1g}}, \tag{5.8}$$

which has the solution

$$\Delta_g(t) = \left[\Delta_g(t_0) - \Delta_g^{\text{eq}} \right] e^{-\frac{t - t_0}{T_{1g}}} + \Delta_g^{\text{eq}}. \tag{5.9}$$

Now substituting $\Delta_g^{\text{eq}} = p\Delta_g^{\text{th}}$ and requiring that at $t = t_1$ the gain has recovered to the threshold value Δ_g^{th}, one obtains

$$\Delta_g^{\text{th}} = \left[\Delta_g(t_0) - p\Delta_g^{\text{th}}\right] e^{-\frac{\tau_{gr}}{T_{1g}}} + p\Delta_g^{\text{th}}, \tag{5.10}$$

which can be solved for the gain recovery time $\tau_{gr} = t_1 - t_0$, leading to the expression

$$\tau_{gr} = T_{1g} \ln \frac{p\Delta_g^{\text{th}} - \Delta_g(t_0)}{\Delta_g^{\text{th}}(p-1)}. \tag{5.11}$$

To investigate the dependence of the maximal saturation $\Delta_g(t_0)$ onto the different parameters, address the equation for the population inversion in the adiabatic limit (see Chapter 2)

$$\dot{\Delta}_g(t) = -\frac{\mu_g^2}{\hbar^2} T_{2g} |E|^2 \Delta_g(t) - \frac{\Delta_g - \Delta_g^{(\text{eq})}}{T_{1g}}. \tag{5.12}$$

Assuming instantaneous response of the system to the applied field, the population inversion will reach its minimum as a function of time, at a point where $\dot{\Delta}_g = 0$ and $E = E_0$, with E_0 being the peak value of the propagating pulse. This readily gives the solution

$$\Delta_g(t_0) = \frac{p\Delta_g^{\text{th}}}{1 + \mu_g^2 T_{1g} T_{2g} |E|^2/\hbar^2} \geq \frac{p\Delta_g^{\text{th}}}{1 + |E_0|^2/W_{sat}^g}, \tag{5.13}$$

with $W_{sat}^g = 1/[T_{1g} T_{2g} \mu_g^2/\hbar^2]$. By simple substitution, we come to the equation

$$\tau_{gr}^* = T_{1g} \ln \left[\frac{p}{(p-1)} \times \frac{|E_0|^2/W_{sat}^g}{(1 + |E_0|^2/W_{sat}^g)} \right], \tag{5.14}$$

which is an upper bound for τ_{gr} and can, in principle, be determined by a suitably designed experiment. It will be shown, by means of computer simulations, that τ_{gr} is an important system parameter, which serves as a good indicator for the regime of mode locking achieved.

5.2.3 Background stability condition

In order for the proposed mode locking scheme to be of any practical interest, one needs to investigate its robustness upon variation of the experimental parameters. A semi-analytical procedure, based on a model by Vladimirov and Turaev [73], provides a good indication of the parametric regions where both fundamental and higher harmonic mode locking are possible, even though it gives quite a conservative estimate. The main idea is based on the insight that when a pulse is formed inside the cavity, two distinct time-scales govern the evolution of the population inversion in the system. Due to the very large dipole moments in QCLs, and consequently large coupling strengths, the stimulated emission rate in these devices could be an order of magnitude larger than the nonradiative transition rates. When a pulse is formed, the two scattering processes, i.e. radiative and non-radiative, act on a single two level system at different times. This allows us to solve separately the gain and absorber equations, Eqs. (5.2), for the two distinct cases and then build the global solution by "matching" the partial ones at the boundary.

Start by writing the traveling wave equation for both gain and absorber sections for a field with a carrier frequency ω_0,

$$\frac{\partial E}{\partial x} + \frac{n}{c}\frac{\partial E}{\partial t} = -i\frac{N_k \Gamma_k \mu_k \omega_0}{\varepsilon_0 c n}\eta_k. \tag{5.15}$$

In the adiabatic limit, where one assumes that $1/T_{2g} \gg \mu_g E/\hbar$, express the coherence term (η_k) in Eq. (5.15) via its steady state solution

$$\eta_k = \frac{\mu_k}{2\hbar} E \Delta_k \times \frac{(\omega_k - \omega_0) + i\gamma_{\parallel k}}{(\omega_k - \omega_0)^2 + \gamma_{\parallel k}^2}. \tag{5.16}$$

Plugging back Eq. (5.16) into Eq. (5.15), rewrite Eq. (5.15) into the familiar form

$$\frac{\partial E}{\partial x} + \frac{n}{c}\frac{\partial E}{\partial t} = \frac{g_k \Gamma_k}{2}(1 - i\alpha_k)\Delta_k E, \tag{5.17}$$

where $g_k = \sigma_k(\omega_0)N_k$ is the differential gain/absorption coefficient, $\alpha_k = (\omega_k - \omega_0)T_{2k}$ is the linewidth enhancement factor.

Following the work of Vladimirov and Turaev [73], perform a change of coordinates in a co-moving frame $(t, x) \rightarrow (\tau, \xi)$ where $\tau = (t - xn/c)/T_{1a}$ is the retarded time normalized to the inversion lifetime in the absorber (T_{1a}), $\xi = x$ is the position coordinate. Additionally, also normalize the electric field by its saturation value in the gain medium, i.e. $[T_{1g}T_{2g}\mu_g^2/\hbar^2]^{1/2}E(\tau, \xi) \rightarrow A(\tau, \xi)$. Then Eq. (5.17) becomes

$$\frac{\partial A}{\partial \xi} = \frac{g_k \Gamma_k}{2}(1 - i\alpha_k)\Delta_k A(\tau, \xi), \tag{5.18}$$

while the equations for the inversion transform to

$$\partial_\tau \Delta_g(\tau, \xi) = \gamma\left(\Delta_g^{\mathsf{eq}} - \Delta_g\right) - \gamma|A|^2\Delta_g, \tag{5.19a}$$

$$\partial_\tau \Delta_a(\tau, \xi) = \Delta_a^{\mathsf{eq}} - \Delta_a - s|A|^2\Delta_a. \tag{5.19b}$$

In Eqs. (5.19a)-(5.19b), $\gamma = T_{1a}/T_{1g}$, and $s = W_{sat}^g/W_{sat}^a$, with $W_{sat}^j = 1/[T_{1j}T_{2j}\mu_j^2/\hbar^2]$, denotes the ratio of the saturation value of the electric field squared in the gain and the absorber sections, respectively. Note that the linear losses have been excluded from the propagation Eq. (5.18), which will eventually be accounted for via the out-coupling losses parameter κ. Next, define

$$Q(\tau) = g_a \Gamma_a \int_{\xi_1}^{\xi_2} \Delta_a d\xi, \tag{5.20a}$$

$$G(\tau) = g_g \Gamma_g \int_{\xi_2}^{\xi_3} \Delta_g d\xi, \tag{5.20b}$$

as the total (dimensionless) losses and gain experienced by the field when propagating through the absorber medium, assumed here to be located between ξ_1 and ξ_2, and the gain medium distributed from ξ_2 to ξ_3, see Fig. 5.1(b).

Now using the definition in Eq. (5.20), the formal solution of Eq. (5.18) can be written as

$$A(\tau, \xi_2) = \exp\{\frac{1 - i\alpha_a}{2}Q(\tau)\}A(\tau, \xi_1), \tag{5.21}$$

$$A(\tau, \xi_3) = \exp\{\frac{1 - i\alpha_g}{2}G(\tau)\}A(\tau, \xi_2). \tag{5.22}$$

After one full round trip (in re-normalized coordinates $T = T_{rt}/T_{1a}$) in the ring cavity, the field is transformed according to

$$A(\tau + T, \xi_1) = \sqrt{\kappa}\exp\{\frac{1 - i\alpha_g}{2}G(\tau) + \frac{1 - i\alpha_a}{2}Q(\tau)\}A(\tau, \xi_1), \tag{5.23}$$

where the periodicity condition $A(t, \xi + L) = A(t + T, \xi)$ has been used. To complete the system we need to find the time-evolution of the quantities $G(\tau)$ and $Q(\tau)$. Directly using Eq. (5.19) and Eq. (5.20), results in

$$\partial_\tau Q(\tau) = q_0 - Q(\tau) - s\Big(|A(\tau, \xi_2)|^2 - |A(\tau, \xi_1)|^2\Big), \tag{5.24}$$

$$\partial_\tau G(\tau) = g_0 - \gamma G(\tau) - \gamma\Big(|A(\tau, \xi_3)|^2 - |A(\tau, \xi_2)|^2\Big), \tag{5.25}$$

for the absorber and the gain, respectively. Here, $g_0 = g_g\Gamma_g\gamma\Delta_g^{\text{eq}}L_g$ denotes the (total) small signal gain (multiplied by the scaling factor γ) in the active region of length L_g, and analogously $q_0 = g_a\Gamma_a\Delta_a^{\text{eq}}L_a$ the small signal losses in the absorber.

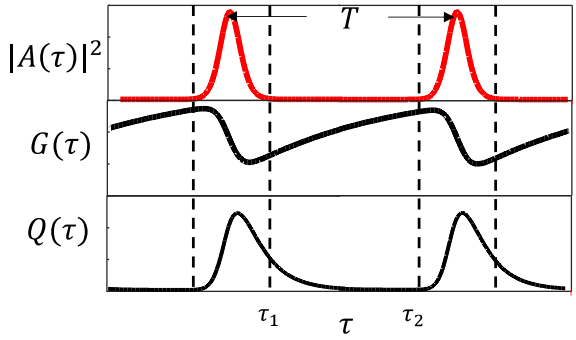

Figure 5.2 The field intensity $|A(\tau)|^2$, total gain $G(\tau)$ and losses $Q(\tau)$, as a function of the retarded time coordinate τ.

At this point, assume twofold dynamics of the population inversion in both the gain and the absorber, as illustrated in Fig. 5.2. First this is the dynamics when the photon flux is negligible. Then the evolution of the two level populations are governed by the corresponding nonradiative lifetimes T_{1g} and T_{1a}. On the other hand, whenever there is a large number of light quanta interacting with either system, the population inversion is mainly governed by stimulated emission and absorption. Adhering to Vladimirov and Turaev's style, the latter is referred to as the fast section, whereas the former will be called the slow section. This being said, assume that the slow section occurs between co-moving time coordinates τ_1 and τ_2, whereas the fast section takes place between τ_2 and T where T is the (normalized) round trip time. Finally suppose that $\tau_2 - \tau_1 \approx T$ approximately holds.

With these arguments in sight, the strategy for the solution is obvious. One would solve separately Eqs. (5.24)-(5.25) for each of the two $\tau-$intervals and then fit the integration constants so that the solution is continuous at the interfaces. First, in the case when there is no photon density at a particular coordinate (τ, ξ), then the population dynamics can be straightforwardly solved for, yielding

$$Q_2 = Q_1 e^{-T} + q_0(1 - e^{-T}), \tag{5.26}$$

$$G_2 = G_1 e^{-\gamma T} + \frac{g_0}{\gamma}(1 - e^{-\gamma T}), \tag{5.27}$$

with $G_j = G(\tau_j)$ for $j = 1, 2$ (and similarly for Q_j) and also $\tau_2 - \tau_1 \approx T$.

On the other hand, in the fast section, the absorber dynamics approximately obeys the following laws

$$\begin{aligned}\partial_\tau Q(\tau) &\approx -s(|A(\tau,\xi_2)|^2 - |A(\tau,\xi_1)|^2) \\ &= -s(e^{Q(\tau)} - 1)|A(\tau,\xi_1)|^2,\end{aligned} \tag{5.28}$$

where Eq. (5.21) has been used. Analogously, using both Eq. (5.21) and Eq. (5.22) one finds for the gain

$$\begin{aligned}\partial_\tau G(\tau) &\approx -\gamma(|A(\tau,\xi_3)|^2 - |A(\tau,\xi_2)|^2) \\ &= -\gamma(e^{G(\tau)} - 1)e^{Q(\tau)}|A(\tau,\xi_1)|^2.\end{aligned} \tag{5.29}$$

To solve the above equations, it is easier to further define the (dimensionless) pulse area

$$P(\tau) = \int_0^\tau |A(\tau',\xi)|^2 d\tau', \tag{5.30}$$

for $\tau \in [0, \tau_1]$ and also recognize that $|A(\tau,\xi)|^2 = dP/d\tau$ and that $P(0) = 0$ and $P(\tau_1) = \Delta P$.

Now, we can proceed with the solutions. First, solve the equation for Q as a function of the pulse area P, which yields

$$\ln \frac{e^Q}{1 - e^Q} = sP \Rightarrow e^Q = \frac{e^{sP}}{1 + e^{sP}}. \tag{5.31}$$

Next, integrating over the fast section and noting that $Q(P = 0) = Q_2$ and $Q(P = \Delta P) = Q_1$, obtain

$$Q_1 - Q_2 - \ln \frac{e^{Q_1} - 1}{e^{Q_2} - 1} = s\Delta P. \tag{5.32}$$

A similar procedure yields the solution for G as a function of the pulse area

$$e^G = \frac{(1 + e^{sP})^{\gamma/s}}{1 + (1 + e^{sP})^{\gamma/s}} \tag{5.33}$$

for the indefinite integral which, when evaluated over the desired interval, leads to

$$G_1 - G_2 - \ln \frac{e^{G_1} - 1}{e^{G_2} - 1} = \ln \left[\frac{1 + e^{s\Delta P}}{2}\right]^{\gamma/s}. \tag{5.34}$$

Finally integrating the square of Eq. (5.23) over $\tau \in [0; \tau_1]$ and using the solutions from Eqs. (5.31)-(5.33), one obtains

$$\begin{aligned}\int_0^{\tau_1} |A(\tau + T, \xi_1)|^2 d\tau &= \kappa \int_0^{\tau_1} \exp\{G(\tau) + Q(\tau)\}|A(\tau,\xi_1)|^2 d\tau \\ &\Leftrightarrow \\ \Delta P &= \frac{\kappa}{\gamma} \ln \frac{e^{G_2} - 1}{e^{G_1} - 1}.\end{aligned} \tag{5.35}$$

Equations (5.26)-(5.27), Eq. (5.32) and Eqs. (5.34)-(5.35) comprise a system for the unknowns G_1, G_2, Q_1, Q_2 and ΔP, which can be solved via many "off the shelf" numerical methods. More importantly, obtaining the values of G_i and Q_i will allow us to examine the parametric

regimes where fundamental and higher harmonic mode locking is possible. According to New [148], a sufficient condition for the formation of ultrashort pulses in passively mode locked devices is that upon the passage of the pulse, for the whole duration until its return on the next round trip, the saturated gain shall remain lower than the total losses. This can be mathematically expressed as

$$G_1 + Q_1 + \ln \kappa < 0, \tag{5.36a}$$

$$G_2 + Q_2 + \ln \kappa < 0, \tag{5.36b}$$

which indeed requires that there is no net round-trip gain in the time interval $[\tau_1; \tau_2]$. This criterion is also known as the New's background stability condition, and is widely employed in the analysis of mode locking of semiconductor lasers [73, 148].

In the next few paragraphs, it is time to finally utilize Vladimirov & Turaev's model to get a rough estimate of the possibility of passively mode locking of THz quantum cascade lasers. Namely, we will investigate parametric regimes where the New stability condition Eqs. (5.36) holds. As already mentioned, the above model gives a rather conservative estimate of the parametric regions where mode locking is possible. The reason for this is twofold. First of all, as Vladimirov and Turaev themselves suggested [73], the background stability criterion in Eqs. (5.36) is not a necessary condition for the formation of a mode locked pulse. Even if the dynamics of the system is such that it allows some background intensity to build up after the passage of the main pulse, the condition does not take into account the fact that this perturbation can be later absorbed by the FSA and thus will not disrupt the pulse formation. Secondly, the so derived stability criterion adiabatically eliminates the off-diagonal element of the density matrix η and thus neglects the influence of quantum coherence effects onto the light-matter interaction. In fact, it has been suggested that in special configurations such effects can enable ultrashort pulses, beyond the bandwidth limit of the gain, via self-induced transparency mode locking [88, 149–151].

Adhering to the original idea, the model accounts for a fast saturable absorber, coupled to a slow saturable gain. For the absorber, assume an inversion recovery time $T_{1a} = 3$ ps whereas for the gain section this parameter is set to 30 ps. Furthermore, the ratio of the dipole moments in the absorber and the gain medium, i.e. $d = \mu_a/\mu_g$, is chosen to be 2, since this would yield smaller saturation intensities in the FSA and thus satisfy the familiar passive mode locking (PML) condition that "the absorber should saturate stronger than the gain" [43]. Notice that this choice is also in-line with the assumed values for the T_{1g} parameter for the gain section, as values for the dipole moment $z_{ul} \approx 2$ nm are characteristic for diagonal QCL designs, which also exhibit longer upper state lifetimes [17].

With this in mind, Equations (5.26)-(5.27), Eq. (5.32) and Eqs. (5.34)-(5.35) are solved for the parameters in Tab. 5.1, with varying values for p and the total strength of the absorber q_0, which is adjusted by changing the doping density N_a. Then this solution is inserted into Eqs. (5.36) for two values of the assumed round trip time, first $T_{rt} = 30$ ps, and secondly for $T_{rt} = 15$ ps, effectively modeling fundamental mode locking (FML) and second harmonic mode locking (SH-ML), respectively. The results are plotted in Fig. 5.3, where the (black) solid curve denotes the outer boundary for parametric regions where FML is predicted, and the (red) dashed line the boundary for SH-ML.

Table 5.1 The parameters for the absorber (A) and gain (G) section of a two-section ring QCL. In the table below $e \approx 1.602 \times 10^{-19}$C denotes the elementary charge.

Parameter	Unit	A	G
Dipole matrix el. (μ_k)	nm· e	4	2
Resonant angular freq. (ω_k)	ps^{-1}	$3.4 \times 2\pi$	$3.4 \times 2\pi$
Recovery time (T_{1k})	ps	3	30
Dephasing time (T_{2k})	ps	0.5	0.5
Length (L_k)	mm	0.5	2.0
Doping density (N_k)	cm^{-3}	$3{\times}10^{14}$	$3{\times}10^{15}$
Linear power loss (a)	cm^{-1}	0	10

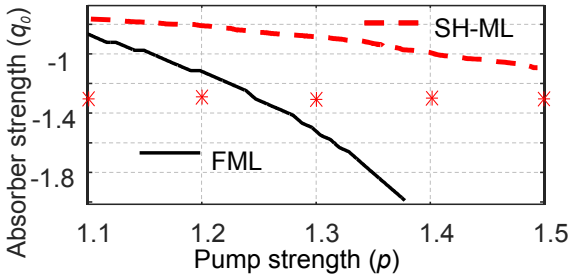

Figure 5.3 Solutions of Equations (5.26)-(5.27), Eq. (5.32) and Eqs. (5.34)-(5.35) for two different cases when $T_{rt} = 30$ ps and $T_{rt} = 15$ ps, effectively modeling fundamental mode locking (FML) and second harmonic mode locking (SH-ML). The solid line indicates the upper bound for FML, and the dashed line the same for SH-ML

To compare this semi-analytical result with Eqs. (5.2), the full system of equations is propagated over several hundreds of round trips, for the basis set of parameters in Tab. 5.1. This time only the gain pump parameter p was varied, whereas the absorber characteristics were kept constant. For $p = \{1.1, 1.2, 1.3, 1.4, 1.5\}$ the corresponding values of q_0, for which the full simulations were performed, are denoted with a red asterisk on Fig. 5.3.

Figures 5.4(a)-5.4(c) illustrate the intracavity intensity and inversion, the position dependence of the pulse full-width at half maximum (FWHM) and its power, as well as the resulting spectrum, for $p = 1.1$ and $T_{1g} = 30$ ps. Interestingly, the steady state solution is not a stable soliton, but rather one observes a slightly "breathing" pulse, with the pulse power and duration varying with spatial position according to Fig. 5.4(b). While the pulse is amplified as it propagates inside the gain, it also broadens due to the anomalous dispersion introduced in this medium. By contrast, when it enters the absorber, the pulse is compressed due to the opposite sign of the group velocity dispersion (GVD), confirming that the FSA also acts as a dispersion compensator for the gain.

When p is varied, from Fig. 5.4(d) we see that the pulse full width at half maximum exhibits a $1/\sqrt{(p-1)}$ dependence, whereas the intracavity power is proportional to $(p-1)^2$. Next, Fig. 5.4(e) illustrates the gain recovery time, calculated with Eq. (5.11), as a function of the pump strength p. We see that while τ_{gr} drops with increasing p, by virtue of Eq. (5.11), it

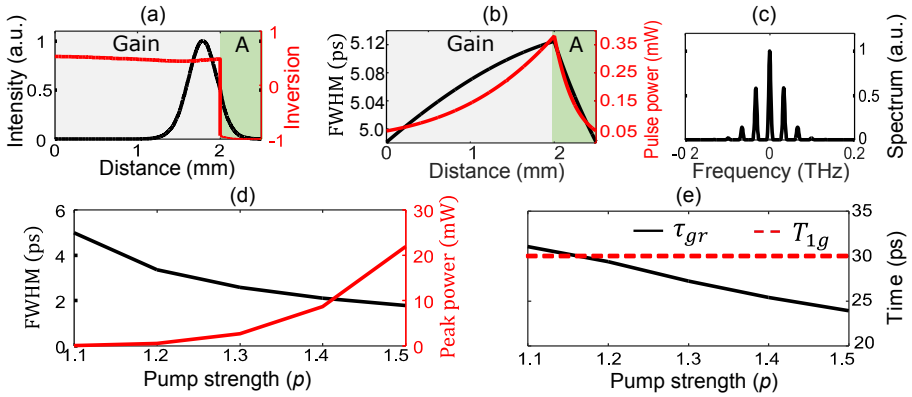

Figure 5.4 Dynamics of a two section ring cavity QCL for $T_{1g} = 30$ ps and other parameters given by Table 5.1. (a) A snapshot of the intensity (left y-axis) and population inversion distribution in the cavity (right y-axis), (b) positional dependence of the pulse full width at half maximum (left y-axis), its power (right y-axis) and (c) spectrum for value of the pump parameter $p = 1.1$. (d) Dependence of FWHM pulse duration, peak power as well as (e) the gain recovery time τ_{gr} on the pump strength p.

remains sufficiently long as to enable fundamental mode locking over the full dynamic range, as compared to the results from Fig. 5.3.

In fact, $T_{1g} = 30$ ps is a rather large value for QCLs. As a next step, consider a more realistic scenario with $T_{1g} = 10$ ps, in which case richer dynamics can be observed as a function of the system parameters, as both fundamental and second harmonic mode locking emerge. To obtain a deeper insight into the conditions that enable either types of mode locking, it is reasonable to perform a "parameter scan", i.e. a series of simulations as a function of the strength of the absorber q_0 and the pump parameter p.

Results from this computation are displayed in Fig. 5.5(a), where the gain recovery time τ_{gr} is plotted as a function of q_0 and p. Again, in order to increase or decrease q_0, the value of the carrier density in the absorber N_a is tweaked accordingly. The spheres in Fig. 5.5 denote discrete grid points for which Eqs. (5.2) have been evolved for 600 round trips, whereas the intermediate points on that same plot are obtained via bi-linear interpolation from the original coarser grid. The color coding of the small spheres also indicates the mode locking regime that has been observed at this particular simulation, with blue for fundamental mode locking and red for second harmonic mode locking. A clear relationship between q_0, p, τ_{gr} and the mode locking regime can be inferred from Fig. 5.5(a). We see that for *stronger* total absorption q_0 and *lower* values for p, i.e simulations close to lasing threshold, the gain recovery time τ_{gr} is longer (at $q_0 \approx -1.9$ and $p = 1.1$, $\tau_{gr} \approx 21$ ps) which enables the formation of a single pulse inside the cavity. By contrast, whenever p increases and q_0 is weakened (i.e. decreased $|q_0|$), the gain recovery time drops to values even shorter than $T_{1g} = 10$ ps, which hampers FML and instead leads to the formation of two pulses propagating inside the cavity. This can be explained intuitively by the fact that the round trip time is approximately 30 ps, and so the pulse splits into two identical copies, such that, as seen by the inversion, the effective round trip time reduces to about half of the original value.

Finally, Fig. 5.5(b) and Fig. 5.5(c) illustrate "corner cases", when $\tau_{gr} = 21.7$ ps is the longest possible gain recovery observed in the parameter scan and the minimum case when $\tau_{gr} = 6.5$ ps, respectively. In the former scenario, there is a single pulse formed, the spectrum of

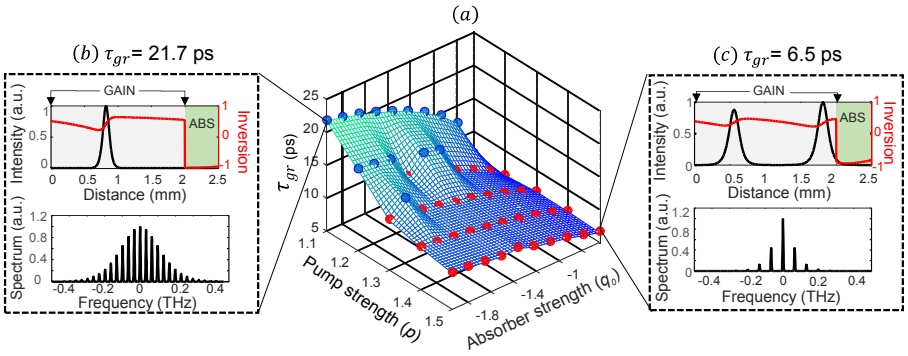

Figure 5.5 (a) A plot of τ_{gr} as a function of the pump parameter p and the absorber strength parameter q_0. The black and red spheres denote the grid points over which simulations of Eqs. (5.2) were performed over 600 round trips, whereas the intermediate points are bi-linearly interpolated from the former. The basic simulation parameters are the same as in Tab. 5.1, with the exception of T_{1g} which was set to the more "pessimistic" value of 10 ps. Additionally, (b) and (c) show snapshots of the pulse propagating inside the cavity and the corresponding spectra, for the corner cases where τ_{gr} is maximal and minimal, respectively.

which contains more than 25 frequency components, equidistantly separated by the round trip frequency, spanning a spectral FWHM bandwidth of around 400 GHz. In contrast, in the second harmonic case, two pulses propagate inside the cavity, which results in a spectrum with mode spacing equal to twice the round trip frequency, as expected.

Despite the rather unlikely application of ring cavity QCLs for passive mode locking (due to the challenging fabrication and also the trickiness of outcoupling light from the device), the above study has deepened our insight about the underlying system dynamics. Quite expectedly, for mode locking to succeed, it is evident that the saturable absorber shall be as strong as possible, but not too strong as it will violate the threshold condition Eq. (5.7). Additionally, we have seen that the gain recovery time, τ_{gr}, is a dynamical system parameter, depending on the pump above threshold p, as well as the strength of the light matter interaction, which proves to give quite a reliable indication of the observed mode locking regime. Concretely, since τ_{gr} is seen to decrease with larger values of p, one can deduce that in lasers with fast gain recovery, fundamental mode locking can be observed only close to threshold, with higher harmonic mode locking or multi-pulse emission, high above it. All of these insights will be used in the following section, where an extension of Eqs. (5.2) is employed to treat the multi level dynamics of bound to continuum QCLs as well as incorporate counter propagating waves and spatial hole burning, which are inevitable in Fabry-Perot QCLs.

5.3 Various regimes of mode locking in Fabry-Perot QCLs

After having reasoned both analytically and numerically about the possibility of passively mode locking ring cavity QCLs, it is time to will consider the more widely employed Fabry-Perot (FP) cavity designs. The conceptualized waveguides are illustrated in Fig. 5.6 for two different configurations, the A-G and G-A-G alignments, favoring conventional and colliding pulse mode locking, respectively. The general geometry consists of two or more sections with different biases and effective dipole moments. This can be realized either via wafer-bonding of

separately designed and grown structures, or by designing a single heterostructure operating either as a gain or absorber medium, depending on the driving current [152]. Despite the more challenging fabrication as compared to having epitaxially stacked gain and absorption layers, or external cavity multi-section QCLs [133], monolithic wave guides are an essential ingredient as they offer two obvious advantages: i) these structures provide short round trip lengths, i.e. relatively small round trip times, and also ii) arranging the gain and absorber in series, as depicted in the figure, allows for independent control of the injection current in all sections.

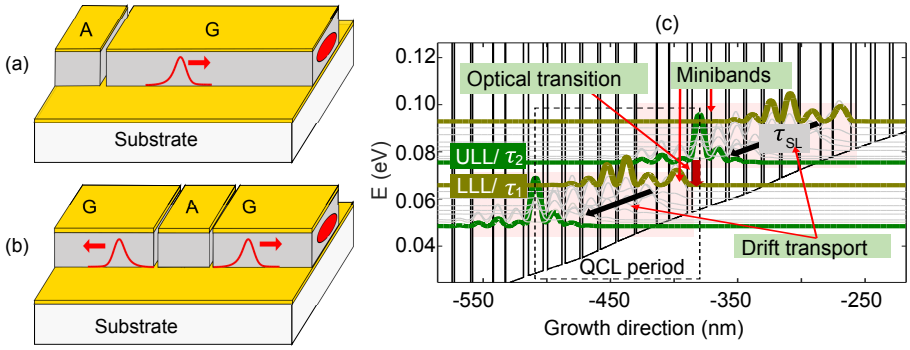

Figure 5.6 An example of multi-section Fabry-Perot (FP) cavity geometry, consisting of spatially separated gain (G) and absorber (A) regions for (a) conventional passive mode locking and (b) colliding pulse mode locking. (c) Conduction band diagram and wave functions of a typical bound to continuum (BTC) GaAs/$Al_{0.15}GaAs_{0.85}$ THz quantum cascade laser (the structure is analogous to that in Ref. [153]). The upper and lower laser levels, ULL and LLL, are outlined with thick lines. The electron transport in the device is characterized by drift transport (scattering) inside the miniband and optical transition between minibands.

Before introducing the equations of motion for the envisaged system, a careful consideration of the transport processes in a BTC quantum cascade laser is in order. An exemplary such active region is illustrated in Fig. 5.6(c). Typically, electron transport through the heterostructure can be described by three different lifetimes, the superlattice relaxation time, i.e. τ_{SL}, defined as the transit time of a carrier from the top of the miniband to the upper laser level, τ_2 defined as the lifetime of the upper laser level and lastly τ_1 denoting the same for the lower laser level [68]. A usual modeling approach in literature is to eliminate the population of the lower laser level, ρ_{11}, from the system of equations by assuming that $\rho_{11} \approx 0$ at all times [52, 84, 142]. This choice can be justified by the relatively fast out-scattering from this level to lower energetic states in the miniband, compared to the other non-radiative lifetimes in the system, i.e. $\tau_1 \ll \tau_2, \tau_{SL}$. Such an approximation is valid for determining the steady state solutions of the rate equations in the absence of an optical field, however it breaks down when one additionally considers photon assisted scattering, since the latter dramatically reduces the upper laser level lifetime [68]. Concretely, when $1/\tau_1 < 1/\tau_2 + 1/\tau_{st}(|E|^2)$, where $\tau_{st}(|E|^2)$ is the stimulated emission/absorption lifetime and E is the electric field, the dynamics of the lower laser level can no longer be excluded, as the QCL essentially operates as a three level system [68]. A value of $\tau_1 \approx 2$ ps was reported for the first THz BTC-QCL [154], indicating that typical values for the lower laser level lifetime are of that order. Keeping this in mind, again a density matrix model is employed to describe the electron transport through the triplet ρ_{SL}, ρ_{22} and ρ_{11} for the population density of the electrons in the miniband, the upper laser level

and the lower laser level, respectively. A similar system was used in the work of Choi et al. to provide evidence for the quantum coherent dynamics in mid-infrared QCLs, where an excellent agreement between simulation and experimental data was achieved [20]. Expanding on the usual two level Bloch equations approach, write down the Maxwell-Bloch (MB) equations for the three level system, however excluding the effect of resonant tunneling, in the rotating wave and slowly varying amplitude approximations, taking into account counter-propagating waves and spatial hole burning. The resulting model for the gain is given by

$$\frac{\partial E_\pm}{\partial x} \pm \frac{n}{c}\frac{\partial E_\pm}{\partial t} = -i\frac{\Gamma_g \mu_g \omega_0}{\varepsilon_0 c n} N_g \eta_\pm - \frac{a_g}{2} E_\pm, \tag{5.37a}$$

$$\frac{d\rho^0_{SL}}{dt} = \frac{\rho^0_{11}}{\tau_1} - \frac{\rho^0_{SL}}{\tau_{SL}}\,, \tag{5.37b}$$

$$\frac{d\rho^0_{22}}{dt} = \frac{\rho^0_{SL}}{\tau_{SL}} - \frac{\rho^0_{22}}{\tau_2} + i\frac{\mu_g}{2\hbar}\big[(E^g_+)^*\eta_+ + (E^g_-)^*\eta_- - c.c.\big], \tag{5.37c}$$

$$\frac{d\rho^0_{11}}{dt} = \frac{\rho^0_{22}}{\tau_2} - \frac{\rho^0_{11}}{\tau_1} - i\frac{\mu_g}{2\hbar}\big[(E^g_+)^*\eta_+ + (E^g_-)^*\eta_- - c.c.\big], \tag{5.37d}$$

$$\frac{d\rho^+_{SL}}{dt} = \frac{\rho^+_{11}}{\tau_1} - \frac{\rho^+_{SL}}{\tau_{SL}}\,, \tag{5.37e}$$

$$\frac{d\rho^+_{22}}{dt} = \frac{\rho^+_{SL}}{\tau_{SL}} - \frac{\rho^+_{22}}{\tau_2} + i\frac{\mu_g}{2\hbar}\big[(E^g_-)^*\eta_+ - (E^g_+)\eta^*_-\big], \tag{5.37f}$$

$$\frac{d\rho^+_{11}}{dt} = \frac{\rho^+_{22}}{\tau_2} - \frac{\rho^+_{11}}{\tau_1} - i\frac{\mu_g}{2\hbar}\big[(E^g_-)^*\eta_+ - (E^g_+)\eta^*_-\big], \tag{5.37g}$$

$$\frac{d\eta_\pm}{dt} = -i(\omega_g - \omega_0)\eta_\pm + i\frac{\mu_g}{2\hbar}\big[E^g_\pm(\rho^0_{22} - \rho^0_{11}) + E^g_\mp(\rho^\pm_{22} - \rho^\pm_{11})\big] - \frac{\eta_\pm}{T_{2g}}. \tag{5.37h}$$

The symbols $\eta_\pm$ denote the forward and backward propagating slowly varying coherence terms between levels 1 and 2. Similarly as before (see Chapter 4) the population of the j^{th} state is expanded as

$$\rho_{jj} = \rho^0_{jj} + \rho^+_{jj} e^{2i\beta_0 x} + (\rho^+_{jj})^* e^{-2i\beta_0 x}, \tag{5.38}$$

where ρ^0_{jj} is the average population, ρ^+_{jj} denotes the (complex) amplitude of the grating. The rest of the simulation parameters for both absorber and gain are specified in Table 5.2.

On the other hand, in order to impose a minimal set of assumptions about the absorber, it will be modeled as a two level density matrix system in the rotating wave and slowly varying amplitude approximation with average inversion Δ^0, inversion grating amplitude Δ^+ and a coherence term $\pi_\pm$. Again, sub-/superscript a is used to specify where a particular parameter or variable relates solely to the saturable absorber. The usual MB equations read

$$\frac{\partial E^a_\pm}{\partial x} \pm \frac{n}{c}\frac{\partial E^a_\pm}{\partial t} = -i\frac{\Gamma_a \mu_a \omega_0}{\varepsilon_0 c n} N_a \pi_\pm - \frac{a}{2} E^a_\pm, \tag{5.39a}$$

$$\frac{d\Delta^0}{dt} = i\frac{\mu_a}{\hbar}\big[(E^a_+)^*\pi_+ + (E^a_-)^*\pi_- - c.c.\big] - \frac{\Delta^0 - \Delta^{\text{eq}}}{T_{1a}}, \tag{5.39b}$$

$$\frac{d\Delta^+}{dt} = i\frac{\mu_a}{2\hbar}\big[(E^a_-)^*\pi_+ - (E^a_+)\pi^*_-\big] - \frac{\Delta^+}{T_{1a}}\,, \tag{5.39c}$$

$$\frac{d\pi_\pm}{dt} = -i(\omega_a - \omega_0)\pi_\pm + i\frac{\mu_a}{2\hbar}\big[E^a_\pm\Delta^0 + E^a_\mp\Delta^\pm\big] - \frac{\pi_\pm}{T_{2a}}. \tag{5.39d}$$

In the following, by means of computer simulations, various schemes are investigate, which might enable the generation of ultrashort pulses with THz QCLs. Besides conventional

Table 5.2 The parameters for the absorber (A) and gain (G) section of the two-section ring QCL from Fig. 5.6(a). In the tables below $e \approx 1.602 \times 10^{-19}$C denotes the elementary charge.

Parameter	Unit	Value (G)	Value (A)
Dipole matrix el. (μ_j)	nm·e	2	6
Resonant angular freq. (ω_j)	ps^{-1}	$3.4 \times 2\pi$	$3.4 \times 2\pi$
Gain superlattice transport time (τ_{SL})	ps	40	$\times$
Gain upper laser level lifetime (τ_2)	ps	40	$\times$
Gain lower laser level lifetime (τ_1)	ps	2	$\times$
Absorber lifetime (T_{1a})	ps	$\times$	3
Dephasing time ($T_{2a/g}$)	fs	200	160
Length (L_j)	mm	1	0.125
Doping density (N_j)	cm^{-3}	5×10^{15}	1×10^{15}
Overlap factor (Γ_j)	dimensionless	1.0	1.0
Linear power loss (a)	cm^{-1}	10	10

passive mode locking, colliding pulse and hybrid mode locking are also treated as alternative approaches to improve the pulse characteristics. Importantly, for the envisaged design to work, a slowly saturable gain, with inversion recovery time only several times faster than the round trip time, must be coupled with a fast saturable absorber [61]. To model this scenario assume a parameter set as presented in Table 5.2, with values believed to be realistic for THz QCLs. Specifically, for the BTC-QCL lifetimes assumed in Table 5.2, simulations similar to Ref. [155] yield a gain inversion lifetime of $T_{1g} \approx 12$ ps, while for the 1.125 mm FP cavity the round trip time is about 28 ps. In all of the following sections, the presented results are obtained from simulations of free-running, self-starting devices. To solve Eq. (5.37) and Eq. (5.39), the numerical method outlined in Chapter 3 are used, where all simulations are started from random noise.

5.3.1 Passive mode locking (PML)

As we have seen in Sec. 5.2, the higher the coupling between the absorber and optical field, the more beneficial are the conditions for pulse formation. This, in fact, is one of the main results from the classical theory of passive mode locking, i.e. the condition that the absorber should saturate faster than the gain [145], and will serve as a starting point for further calculations. The non-linear saturation parameter is given by $\varepsilon_j = \mu_j^2 T_{1j} T_{2j}/\hbar^2$ and denotes the inverse of the saturation value of the electric field squared $|E|^2$ in each active region ($j = \{a, g\}$). When the condition $r = \varepsilon_a/\varepsilon_g > 1$ is met, the propagating pulse will bleach the absorber more strongly than the amplifier and thus will open a net round trip gain window. In fact, simulations for quantum dot lasers have shown [61] that the pulse duration decreases approximately exponentially with increasing value of r. Conversely, classical theory and also additional simulations (results not shown here) predict that no mode locking is possible when $r < 1$ [61, 145].

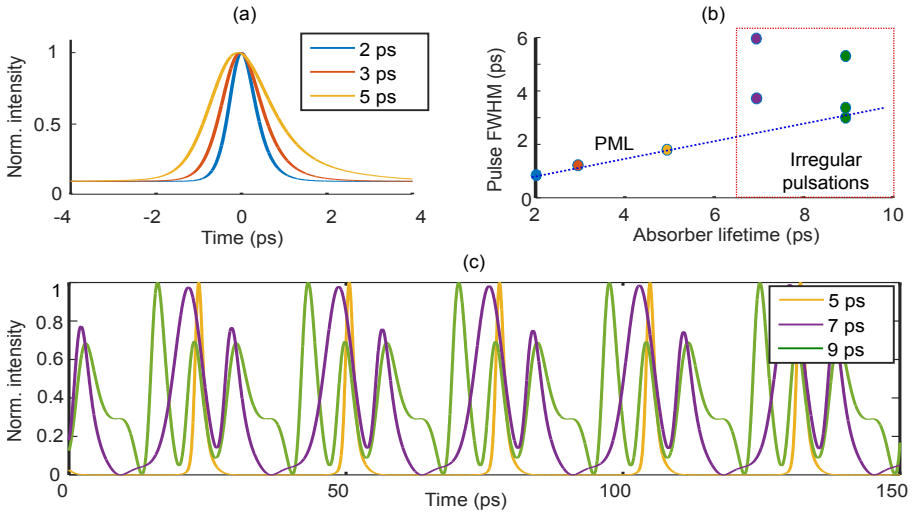

Figure 5.7 (a) Normalized pulse intensity vs time for values of the absorber lifetime of 2 ps, 3 ps and 5 ps. (b) The intensity FWHM duration as T_{1a} is varied between 2-9 ps, where for $T_{1a} = 7$ ps and 9 ps, the FWHM values of the main and also the satellite pulses are presented. (c) The normalized optical intensity for T_{1a} =5, 7 and 9 ps.

Another requirement for successful mode locking is that the absorber should have a fast recovering population inversion. One can easily see the benefits of a short T_{1a} lifetime. Upon entering the absorber, the pulse front will saturate the active medium, which on the other hand will be quick enough to recover prior to arrival of the pulse tail. This type of dynamics would naturally shorten the pulse as the duration of the net gain window will decrease with decreasing T_{1a}. Following this logic, one might expect to obtain shorter pulses with decreasing absorber lifetimes, which is indeed confirmed by the simulations. Importantly, absorbers with fast carrier recovery ought to be easy to realize based on resonant phonon QCL designs, taking advantage of strong longitudinal optical phonon scattering.

Similarly to their zero-dimensional counterparts (quantum dot lasers), QCLs could be passively mode locked provided systems with suitably chosen parameters are designed. To illustrate this possibility Eq. (5.37) and Eq. (5.39) have been simulated with a parameter set characteristic for QCLs (see Table 5.2).

To investigate the importance of absorber lifetime for PML of QCLs, the recovery time of the absorber is varied between 2 and 9 ps and the coupled system is simulated for around 400 round trips. Since the change of T_{1a} also changes the value of r, for each simulation the absorber dipole moment needs to be re-adjusted in order to maintain constant r. This is necessary in order to have controlled numerical experiments where only T_{1a} and not r changes. Finally, the gain carrier density was also adjusted from its value in Table 5.2, in order to ensure that in all subsequent simulations the active medium was biased at $p = 1.2$ times above threshold.

The results from these simulations are presented in Fig. 5.7(a) and Fig. 5.7(b) and display behavior in agreement with expectation. When the absorber lifetime is sufficiently short, Fig. 5.7(a), as T_{1a} increases so does also the pulse duration. In fact, for the PML regime of lasing in Fig. 5.7(b) a clear linear relationship between T_{1a} and the intensity full width at half maximum (FWHM) pulse duration is observed. On the other hand, for slower absorbers,

the complicated interplay between the optical field and the active region dynamics produces irregular pulsations (IP) with no well defined temporal profile. From Fig. 5.7(c) we see that the onset of this regime occurs already for absorber lifetimes $T_{1a} \geq 7$ ps and is characterized by multiple pulses with varying intensity. Additionally, for those cases one can also observe modulation of the pulse amplitude with a period spanning several tens of round trips, a phenomenon baring resemblance to Q-switched mode locking [156]. These results unequivocally validate the important role of the absorber lifetime for the pulsation dynamics and confirm that for successful mode locking of QCLs, besides slowly saturable gain media, also absorbers with short T_{1a} lifetime and large $r = \varepsilon_a/\varepsilon_g$ ratio are essential.

5.3.2 Colliding pulse mode locking (CPML)

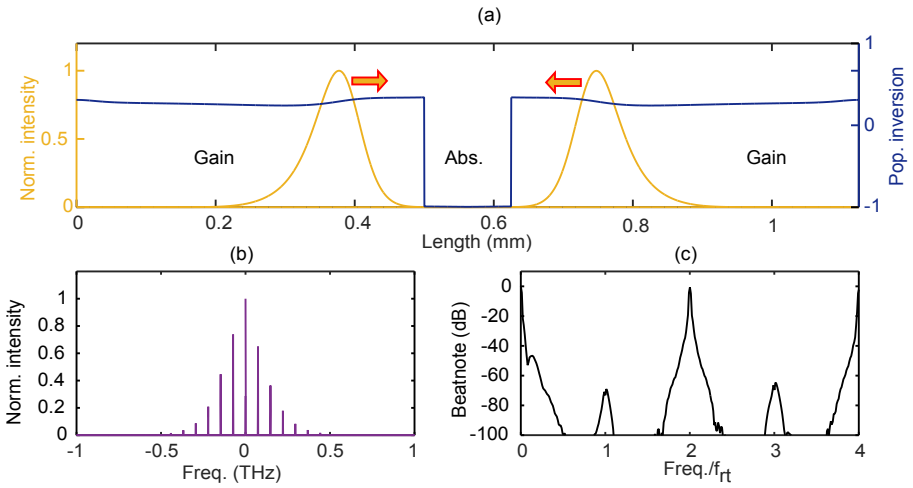

Figure 5.8 (a) A snapshot of the optical intensity (left y-axis) and population inversion (right y-axis) inside the cavity. (b) Optical spectrum of the field emitted from the right facet of the cavity. (c) A log plot of the beatnote signal versus frequency (normalized to the cavity round trip frequency f_{rt}) produced by the device.

A special type of passive mode locking, useful for shortening even further the pulse duration, but probably more importantly to achieve high repetition rates, is the so called colliding pulse mode locking, where two gain sections of equal length are symmetrically placed around the absorber [59, 157]. When such a geometric arrangement is achieved, two identical pulses per round trip can be emitted from the device, resulting in a doubled repetition rate equal to the second harmonic of the round trip frequency. In fact, it could be expected that CPML will be easier to achieve via BTC quantum cascade lasers as devices with short gain recovery time will naturally favor such multi-pulse regime of operation [143, 158].

To understand why CPML occurs, consider the schematic in Fig. 5.6(b), illustrating a multi-section cavity design in the G-A-G (gain-absorber-gain) configuration. Let us assume that a single pulse with amplitude E_0 propagates inside a gain medium with some group velocity v_g. Close to the resonator mirrors, during its forward pass the pulse will saturate the gain and there will be not enough time for the latter to recover in order to re-amplify the reflected signal. This leads to a reduction of the effective length of the gain medium by $\Delta L = v_g \tau_{gr}/2$, which is half the distance traveled by the pulse in time τ_{gr}, where $\tau_{gr} \neq T_{1g}$ denotes the time it

takes for the gain to recover to its threshold value. Since τ_{gr} is a monotonously increasing function of $|E_0|^2$, as such ΔL will be shorter if the pulse would split into two identical copies with *half* the total intensity each, since then τ_{gr} will also decrease. The most stable two-pulse configuration in a G-A-G Fabry-Perot cavity are indeed pulses, colliding in the cavity center, as those will saturate the absorber more deeply and further reduce the round trip losses.

To confirm these expectations, Eq. (5.37) and Eq. (5.39) are simulated in the G-A-G arrangement for the parameter set in Table 5.2. Figure 5.8 illustrates the results. After about 50 round trips the laser emission transforms into two identical counter-propagating pulses which collide inside the center of the cavity, Fig. 5.8(a). The spectrum in Fig. 5.8(b) consists of more than 15 modes separated by twice the round trip frequency, f_{rt}, whereas beatnote calculations, Fig. 5.8(c), indicate a strong component at the second harmonic of f_{rt}. This second harmonic regime is stable over hundreds of round trips, with the beatnote linewidth in Fig. 5.8(c) being limited by the Fourier transform resolution of the simulations. Such a device essentially represents a very stable local oscillator with a repetition frequency of around ≈71 GHz [159].

5.3.3 Hybrid mode locking (HML)

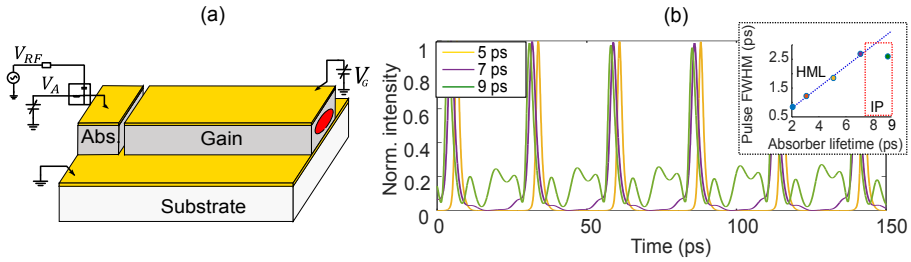

Figure 5.9 (a) Schematic diagram of hybrid mode locking with radio frequency (RF) modulation of the absorber bias. (b) Intensity profile for T_{1a} =2-5 ps. (Inset) Intensity FWHM vs absorber lifetime for the hybrid configuration of (a) and the same parameter set as the one which produced the results in Fig. 5.7(b).

As shown above, the multi-section gain/saturable absorber system might lase in a regime of irregular pulsations [59]. In order to enforce phase-locking of the modes, one can additionally modulate the current/voltage of the gain or the absorber at the round trip frequency of the optical field. Such a hybrid approach could be envisaged for QCLs, where the applied bias of the absorber is superimposed with a sinusoidally varying radio frequency source via a bias-T, and the gain medium is pumped with a DC current (see Fig. 5.9(a)) [140, 160].

To simulate this technique the term $m_0 \sin(2\pi f_{rt} t)$ is introduced in the right hand side of Eq. (5.39b), modeling the RF source [112], where the modulation amplitude is set to 25 % of the DC current, i.e. $m_0 = 0.25 \times \Delta_a^{\text{eq}}/T_{1a}$. Again, the simulations from Fig. 5.7 were repeated to evaluate how effective this active+passive mode locking will be as compared to the simple PML case. The results are plotted in Fig. 5.9(b).

From Fig. 5.9(b), within the fast absorber regime (i.e. $T_{1a} = 2 - 5$ ps), we see that the applied RF modulation does not seem to have any significant impact on the pulse widths, as the calculated FWHM-values are of almost the same magnitude as in Fig. 5.7(b). This is not

so surprising as the laser already operates in a mode locked regime and so additional RF-injection would have little to no effect on the dynamics. However, substantial improvement in the pulse structure and duration is observed for slower absorbers as the satellite pulsations are strongly suppressed in favor of more regular pulses. In particular, comparing the time-domain profile of the intensity in Fig. 5.7(c) and Fig. 5.9(b), we see that as a result of this additional active modulation, the pulse at $T_{1a} = 7$ ps has completely recovered its integrity whereas the pulse substructures for $T_{1a} = 9$ ps are drastically reduced. Again, drawing insights from the quantum dot laser community [161, 162], one might expect that with this HML technique an improvement in the overall stability of the pulse train and mode locking parameter range can be achieved, as compared to when utilizing the passive mechanism alone.

5.4 Coupled microwave and optical simulations of QCLs

The modeling of HML dynamics presented above suffers from a serious flaw. By incorporating a RF modulation in Eq. (5.39b), the dependence of the numerous system parameters on the applied bias, F, is completely neglected. This is a bad approximation as the wave functions themselves, their eigenenergies, dipole moments, anticrossing terms and scattering rates etc., are, generally, a function of the field F [116, 163]. Now, any variation of the system parameters could also alter the level populations and hence the 2D current density J through the laser, which in turn will affect the value of the applied bias F. This twofold feedback mechanism, i.e. the influence of the voltage drop onto the carrier dynamics and vice versa, is characteristic for QCLs and thus, in order to achieve reliable simulation results, an additional time domain model for the injection current is necessary.

Here a possible solution to the above introduced problem is outlined, where a coupled transmission-line/Maxwell-Bloch equations approach is envisaged for the study of microwave-optical interactions in quantum cascade lasers. The author must acknowledge that the original idea stems from his correspondence with Dr. David Burghoff and Dr. Christian Jirauschek, however most of the analytical work done is the author's own contribution. Furthermore, the model to be presented is only at a preliminary stage of development as time constraints have delayed its full completion. Nevertheless, the proposed mathematical model could serve as a first step in an attempt to extend the traditional Maxwell-Bloch equations beyond their known limitations and hence capture more of the physics at play in real devices.

To gain a deeper understanding of the underlying physical picture, let us consider the schematic diagram of Fig. 5.10. Assume an ideal DC source, applying constant voltage V_{DC} coupled through a bias-T to an RF source, generating a time-varying signal $V_{RF}(t)$. The output of the bias-T is connected to a coaxial cable of length l and internal impedance Z_0 (usually 50 Ω), which is terminated at the QCL waveguide position x_k. The QCL resonator is considered as a double-metal waveguide, which in fact is the preferred guiding structure for THz devices, especially for active mode locking applications [3, 19, 146].

In such structures the total electromagnetic field will be comprised of a THz field, which is the light actually emitted by the QCL, and a GHz field, the origin of which is in the propagating voltage variations along the waveguide. Despite the fact that there is only one electromagnetic field, it will be more convenient to treat the THz and GHz waves via separate mathematical

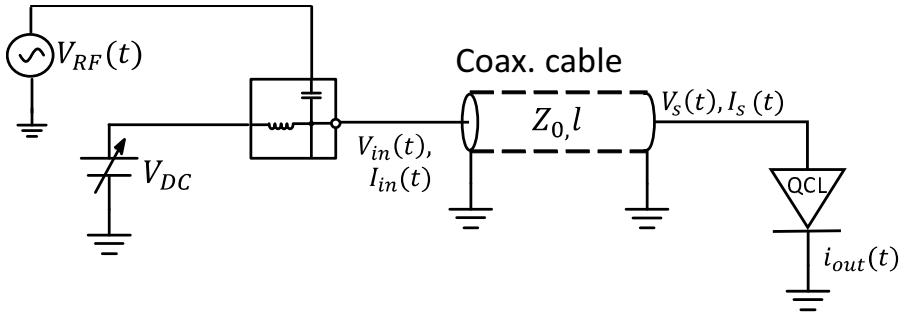

Figure 5.10 A general schematic for DC+RF voltage injection into a double-metal QCL waveguide. The current from the RF source is combined with a DC signal before being transported over a coaxial cable transmission line (TL) to the QCL. The QCL waveguide is also seen as a micro-strip transmission line, at some position x_k of which the source current is being injected.

models, the former with the usual Maxwell-Bloch equations, and the latter via the well known transmission line equations. The coupling between those two worlds will be done via the voltage $u(x,t)$ and current density $J(x,t)$, along the QCL longitudinal direction, in a manner as illustrated in Fig. 5.11. After pre-computing, with the aid of our Schrödinger-Poisson and ensemble Monte Carlo codes, the bias dependence of all relevant system parameters (eigenenergies, dipole moments, scattering rates etc.), this "input data" is provided to the algorithm as a model for the QCL. Using this data, from the current value of the voltage $u(x,t)$ (the bias is given as $F = u/h$, where h is the height of the QCL), one interpolates the aforementioned parameters, and with these new numbers propagates for one time-step the Maxwell-Bloch system. From the new state of the density matrix, one computes the QCL current density $J(x,t)$ and feeds it into the transmission line equations solver, in order to calculate an update for the voltage $u(x,t) \rightarrow u(x,t+dt)$. This iteration is repeated in the same manner until the end of the simulation time is reached, i.e. $t \geq t_{sim}$.

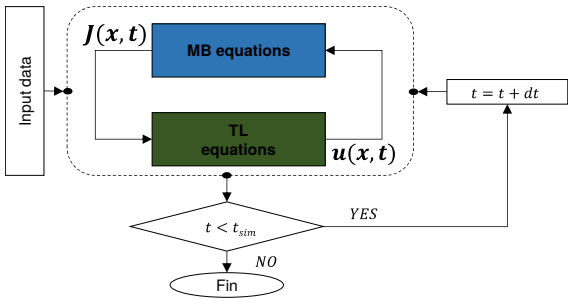

Figure 5.11 Coupled transmission-line/Maxwell-Bloch equations algorithm, suitable for microwave-optical simulations of electrically pumped lasers.

5.4.1 Current injection through a coaxial cable

Until this point, quite some time was spent in modeling the QCL carrier-light interaction dynamics via various forms of the Maxwell-Bloch equations. In the following paragraphs a model is outlined for the transmission line structures delivering the applied current/voltage to the QCL device. Since direct discretization of the coaxial cable (typically of length over

several cm) would necessitate the propagation over many thousands of grid points, assume a lossless cable, as then analytical solutions to the underlying equations are readily available. As a further simplification also frequency independent distributed parameters will be used.

Formally, the coaxial cable is modeled as a lossless transmission line with distributed capacitance C and inductance L and total length l. The telegrapher's equations for voltage V and current I along the cable are simply

$$\frac{\partial V}{\partial x} = -L\frac{\partial I}{\partial t}, \tag{5.40a}$$

$$\frac{\partial I}{\partial x} = -C\frac{\partial V}{\partial t}, \tag{5.40b}$$

with the additionally specified initial and boundary conditions,

$$V(x=0,t) = V_{in}(t), \tag{5.41a}$$

$$V(x=l,t) = V_s(t), \tag{5.41b}$$

$$I(x=0,t) = I_{in}(t), \tag{5.41c}$$

$$I(x=l,t) = I_s(t), \tag{5.41d}$$

$$V(x,t=0) = 0, \tag{5.41e}$$

$$I(x,t=0) = 0. \tag{5.41f}$$

Note that it has been assumed that initially there are no currents & voltages inside the cable, which is justified if the source is slowly turned on.

Below, the results from [164] will be adapted for the particular case where one treats a *lossless* transmission line with constant, frequency independent distributed inductance L and capacitance C. Using the Laplace transform, Eqs. (5.40) turn into

$$\frac{\partial \mathcal{V}(x,s)}{\partial x} = LI(x,0) - Ls\mathcal{I}(x,s), \tag{5.42a}$$

$$\frac{\partial \mathcal{I}(x,s)}{\partial x} = CV(x,0) - Cs\mathcal{V}(x,s), \tag{5.42b}$$

where $\mathcal{I}(x,s) = \mathscr{L}\{I(x,t)\}[s]$ and $\mathcal{V}(x,s) = \mathscr{L}\{V(x,t)\}[s]$ are the Laplace transforms of the current and voltage in the coaxial cable, respectively. As done in [164] , change the variables from $\mathcal{I}$ and $\mathcal{V}$ to $\mathcal{P}(x,s)$ and $\mathcal{Q}(x,s)$ defined as $\mathcal{P}(x,s) = (\mathcal{V} + Z_0\mathcal{I})/2$ and $\mathcal{Q}(x,s) = (\mathcal{V} - Z_0\mathcal{I})/2$, with the intuitive interpretation of forward and backward propagating voltage, respectively. Then $\mathcal{P}$ and $\mathcal{Q}$ obey the differential equations

$$\frac{\partial \mathcal{P}}{\partial x} + \lambda(s)\mathcal{P} = \frac{LI_0(x) + CZ_0V_0(s)}{2}, \tag{5.43a}$$

$$\frac{\partial \mathcal{Q}}{\partial x} - \lambda(s)\mathcal{Q} = \frac{LI_0(x) - CZ_0V_0(s)}{2}, \tag{5.43b}$$

where I_0 and V_0 are the initial current and voltage and $\lambda(s) = s\sqrt{LC}$. As mentioned above, since the initial conditions are set to zero, one can immediately come up with the analytical solutions of Eqs. (5.43)

$$\mathcal{P}(x,s) = \frac{\mathcal{V}(x,s) + Z_0\mathcal{I}(x,s)}{2} = A(s)e^{-\lambda(s)x}, \tag{5.44}$$

$$\mathcal{Q}(x,s) = \frac{\mathcal{V}(x,s) - Z_0\mathcal{I}(x,s)}{2} = B(s)e^{\lambda(s)x}, \tag{5.45}$$

with A and B being $s-$dependent constants, appropriately chosen as to satisfy the boundary conditions (BC)

$$V(0,t) = V_{in}(t), \tag{5.46a}$$
$$V(l,t) = V_s(t), \tag{5.46b}$$
$$I(0,t) = I_{in}(t), \tag{5.46c}$$
$$I(l,t) = I_s(t). \tag{5.46d}$$

Applying the BCs we get that A and B are given by

$$A = \frac{\mathcal{V}(0,s) + Z_0\mathcal{I}(0,s)}{2}, \tag{5.47}$$
$$B = e^{-\lambda(s)l}\frac{\mathcal{V}(l,s) - Z_0\mathcal{I}(l,s)}{2}. \tag{5.48}$$

Finally, re-expressing $\mathcal{I}$ and $\mathcal{V}$ in terms of $\mathcal{P}$ and $\mathcal{Q}$ the final solution (in the frequency domain) is obtained

$$\mathcal{V}(x,s) + Z_0\mathcal{I}(x,s) = e^{-\lambda(s)x}\left[\mathcal{V}(0,s) + Z_0\mathcal{I}(0,s)\right], \tag{5.49}$$
$$\mathcal{V}(x,s) - Z_0\mathcal{I}(x,s) = e^{-\lambda(s)(l-x)}\left[\mathcal{V}(l,s) - Z_0\mathcal{I}(l,s)\right]. \tag{5.50}$$

What remains is to inverse-Laplace transform the above equations in order to obtain the solutions in the time-domain. For this procedure, use the fact that the inverse Laplace transform of $\mathcal{F}(s)\cdot\mathcal{G}(s)$, where $\mathcal{F}(s) = \mathscr{L}\{f(t)\}[s]$ and similarly $\mathcal{G}(s) = \mathscr{L}\{g(t)\}[s]$, is the convolution of f and g, i.e.

$$\mathscr{L}^{-1}\{\mathcal{F}(s)\cdot\mathcal{G}(s)\}[t] = \int_0^t f(\tau)g(t-\tau)d\tau. \tag{5.51}$$

In case of a lossless transmission line, which is what has been assumed for the coaxial cable, the convolutions are done with Dirac-delta functions since the inverse Laplace transform of the exponent $\mathscr{L}^{-1}\{e^{-\lambda(s)x}\}[t] = \mathscr{L}^{-1}\{e^{-s\sqrt{LC}x}\}[t] = \delta(t-\sqrt{LC}x)$. Using the convolution theorem and this previous fact, the following analytical expression is obtained

$$\begin{aligned} V(x,t) &= \frac{V(0,t-\sqrt{LC}x) + V(l,t-\sqrt{LC}(l-x))}{2} + Z_0\frac{I(0,t-\sqrt{LC}x) - I(l,t-\sqrt{LC}(l-x))}{2} \\ &= \frac{V_{in}(t-\sqrt{LC}x) + V_s(t-\sqrt{LC}(l-x))}{2} + Z_0\frac{I_{in}(t-\sqrt{LC}x) - I_s(t-\sqrt{LC}(l-x))}{2}, \end{aligned} \tag{5.52}$$

and similarly

$$\begin{aligned} I(x,t) &= \frac{V(0,t-\sqrt{LC}x) - V(l,t-\sqrt{LC}(l-x))}{2Z_0} + \frac{I(0,t-\sqrt{LC}x) + I(l,t-\sqrt{LC}(l-x))}{2} \\ &= \frac{V_{in}(t-\sqrt{LC}x) - V_s(t-\sqrt{LC}(l-x))}{2Z_0} + \frac{I_{in}(t-\sqrt{LC}x) + I_s(t-\sqrt{LC}(l-x))}{2}. \end{aligned} \tag{5.53}$$

Equations (5.52)-(5.53) have a straightforward physical interpretation. They simply state that the current/voltage at time t and position x inside the coaxial cable, are the appropriately

taken superposition of the current/voltage coming from the left boundary and these arriving from the right boundary of the cable. In this context, the expression $1/\sqrt{LC}$ is nothing else but the propagation velocity of the electromagnetic wave inside the cable. Now, since we are interested only at what happens at the boundary, substitute $x = l$ and $x = 0$ in the above equations to obtain the relationships

$$I(l,t) = I_s(t) = \frac{V_{in}(t - l\sqrt{LC}) - V_s(t)}{2Z_0} + \frac{I_{in}(t - l\sqrt{LC}) + I_s(t)}{2}, \tag{5.54}$$

$$I(0,t) = I_{in}(t) = \frac{V_{in}(t) - V_s(t - l\sqrt{LC})}{2Z_0} + \frac{I_{in}(t) + I_s(t - l\sqrt{LC})}{2}, \tag{5.55}$$

from where the boundary currents can be expressed in terms of the boundary voltages at time t

$$I_{in}(t) = \frac{V_{in}(t) - V_s(t - l\sqrt{LC})}{Z_0} + I_s(t - l\sqrt{LC}), \tag{5.56a}$$

$$I_s(t) = \frac{V_{in}(t - l\sqrt{LC}) - V_s(t)}{Z_0} + I_{in}(t - l\sqrt{LC}). \tag{5.56b}$$

Notice that Eqs. (5.56) gives a recurrent relationship for the currents in terms of the voltages in the present time t and the past values of the boundary currents. Hence, with knowledge of two out of those four quantities (at each boundary), $I_{in/s}(t)$ and $V_{in/s}(t)$, as well as the initial conditions, the other two are completely determined. What now remains is to fix the left hand side boundary conditions for the input voltage (the right boundary conditions will be given from the "coupling" to the QCL transmission line). As the coaxial cable is assumed to be connected to a DC+RF voltage source set

$$V(0,t) = V_{in}(t) = V_{DC} + V_{RF}(t) = V_{DC} + m_A \sin(\omega_m t), \tag{5.57}$$

with m_A and ω_m the modulation amplitude (in Volts) and angular frequency, respectively.

5.4.2 QCL transmission line model

After finding the solution for a the coaxial cable, the focus shifts on the electrical modeling of the QCL structure. As already explained above, the laser resonator is treated as a (possibly lossy) micro-strip transmission line with frequency-independent distributed capacitance C_{QCL}, inductance L_{QCL}, resistance R_{QCL} and conductance G_{QCL}. The transmission line equations for the QCL voltage $u(x,t)$ and current $i(x,t)$ are

$$\frac{\partial u(x,t)}{\partial x} = -L_{QCL}\frac{\partial i(x,t)}{\partial t} - R_{QCL} i(x,t), \tag{5.58a}$$

$$\frac{\partial i(x,t)}{\partial x} = -C_{QCL}\frac{\partial u(x,t)}{\partial t} - G_{QCL} u(x,t) - wJ(x,t), \tag{5.58b}$$

where w is the width of the QCL and $J(x,t)$ denotes the current density through the structure (i.e. the current through the QCL stages). In Eqs. (5.58), an additional Ohmic leakage current component has been included, specified by the distributed conductance parameter G_{QCL}, as well as any general current density $J(x,t)$ flowing through the gain medium. Formally $J(x,t)$ ought to incorporate both types of current, however the distinction here is made for

convenience, as generally $wJ(x,t)$ could be used to denote the current contribution calculated from the density matrix equations, whereas $G_{QCL}u(x,t)$ can model any additional flow of electrons which cannot be captured by the Bloch carrier model (such as for example the leakage of electrons into the continuum [40]).

Next, the QCL voltage $u(x,t)$, current density $J(x,t)$ and line current $i(x,t)$ are discretized on the traditional staggered I-V type of Yee grid [56], i.e. take current on $i(x_{j-\frac{1}{2}},t_n) = i^n_{j-\frac{1}{2}}$, the voltage on grid points $u(x_j,t_{n-\frac{1}{2}}) = u_j^{n-\frac{1}{2}}$, and the current density on $J(x_j,t_{n-\frac{1}{2}}) = J_j^{n-\frac{1}{2}}$, for $j = 1,2...M$ and $n = 1...N_t$.

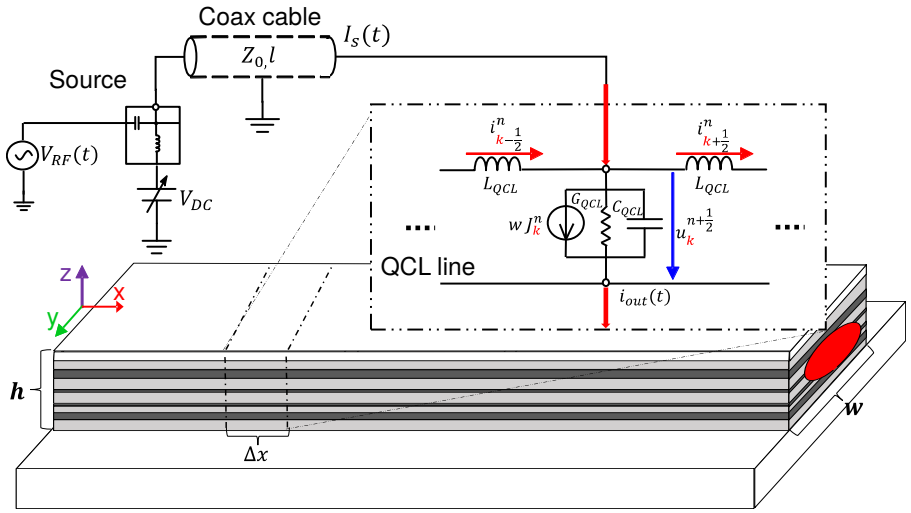

Figure 5.12 Illustration for the QCL-coaxial cable interface. The inset denotes the equivalent circuit representation of a differential element of the QCL with length Δx.

To understand the coupling between coaxial cable and QCL waveguide, let us revisit our schematic from Fig. 5.10 redrawn in Fig. 5.12, this time with a bit more focus on the QCL geometry. As illustrated in the figure, it has been assumed that x is the propagation direction, z the growth direction and y the transverse waveguide direction. With this notation, the parallel plate QCL current, denoted by $i(x,t)$, flows along the $x-$direction, whereas the voltage drop $u(x,t)$ and the current density $J(x,t)$, are aligned with the growth direction, i.e. z. Since we consider only a single QCL module, within the periodic rate equations model (see Sec. 2.3.2), we have indirectly assumed a homogeneous distribution of J and u along the growth direction.

Now, it is time to focus on the interface between the coaxial cable and the QCL transmission line. As mentioned before, it is assumed that the bonding pads are located at grid point x_k (aligned with the voltage grid). For this particular configuration one can apply Kirchhoff's voltage and current laws to derive the boundary conditions connecting the QCL with the coaxial cable. From the current balance law at grid point x_k calculate

$$\begin{aligned} I_s^n + i^n_{k-\frac{1}{2}} &= i^n_{k+\frac{1}{2}} + C_{QCL}\Delta x\frac{\partial u_k^n}{\partial t} + w\Delta x J_k^n + G_{QCL}\Delta x u_k^n \\ &\approx i^n_{k+\frac{1}{2}} + C_{QCL}\Delta x\frac{u_k^{n+\frac{1}{2}} - u_k^{n-\frac{1}{2}}}{\Delta t} + \frac{w\Delta x}{2}(J_k^{n+\frac{1}{2}} + J_k^{n-\frac{1}{2}}) + \frac{G_{QCL}\Delta x}{2}(u_k^{n+\frac{1}{2}} + u_k^{n-\frac{1}{2}}), \end{aligned} \tag{5.59}$$

where the time derivative of u_k^n is approximated with finite difference expression, centered around (x_k, t_n), and also $J_k^n \approx (J_k^{n+\frac{1}{2}} + J_k^{n-\frac{1}{2}})/2$ and similarly for u_k^n. Secondly, applying Kirchhoff's voltage law, for the closed loop between the end of the coaxial cable and going through the QCL transmission line at x_k, yields

$$V_s^n = u_k^n = \frac{u_k^{n+\frac{1}{2}} + u_k^{n-\frac{1}{2}}}{2}. \tag{5.60}$$

For the rest of the grid points the following (standard) staggered discretization applies

$$u_j^{n+\frac{1}{2}} = \alpha u_j^{n-\frac{1}{2}} - \beta(i_{j+\frac{1}{2}}^n - i_{j-\frac{1}{2}}^n) - \gamma(J_j^{n+\frac{1}{2}} + J_j^{n-\frac{1}{2}}), \quad \text{for } j = 1, 2, ..., k-1, k+1, ..., M-1, \tag{5.61}$$

$$i_{j-\frac{1}{2}}^{n+1} = \delta i_{j-\frac{1}{2}}^n - \varepsilon(u_j^{n+\frac{1}{2}} - u_{j-1}^{n+\frac{1}{2}}) \quad \text{for } j = 2, 3..., M, \tag{5.62}$$

where $\alpha, \beta, \gamma, \delta, \varepsilon$ are constants, given by

$$\alpha = \frac{2C_{QCL} - \Delta t G_{QCL}}{2C_{QCL} + \Delta t G_{QCL}}, \tag{5.63a}$$

$$\beta = \frac{2\Delta t}{\Delta x(2C_{QCL} + \Delta t G_{QCL})}, \tag{5.63b}$$

$$\gamma = \frac{w\Delta t}{2C_{QCL} + \Delta t G_{QCL}}, \tag{5.63c}$$

$$\delta = \frac{2L_{QCL} - \Delta t R_{QCL}}{2L_{QCL} + \Delta t R_{QCL}}, \tag{5.63d}$$

$$\varepsilon = \frac{2\Delta t}{\Delta x(2L_{QCL} + \Delta t R_{QCL})}. \tag{5.63e}$$

As for the left and right hand side boundary conditions, assume "open" circuit boundaries, i.e. that $i(x = 0, t) = 0$ and $i(x = l, t) = 0$, which can be approximated on the chosen grid with

$$i_{\frac{1}{2}}^{n+1} = 0, \tag{5.64}$$

$$u_M^{n+\frac{1}{2}} = u_{M-1}^{n+\frac{1}{2}}. \tag{5.65}$$

5.4.3 Interface currents

As mentioned already, in Eqs. (5.56a)-(5.56b) there is a recurrent relation between the values of $I_{in}(t)$ and $I_s(t)$, which is given by

$$I_{in}^n = \frac{V_{in}^n - V_s^{n-m}}{Z_0} + I_s^{n-m}, \tag{5.66a}$$

$$I_s^n = \frac{V_{in}^{n-m} - V_s^n}{Z_0} + I_{in}^{n-m}, \tag{5.66b}$$

where n is the present time index and $m = \sqrt{LC}l/dt$ is the number of iterations it takes for the microwave signal to propagate through the coaxial cable of length l. The numerical update

rule for $u_k^{n+\frac{1}{2}}$ can be found from the boundary condition of Eq. (5.59), using the recurrence relations in Eqs. (5.66)

$$\frac{V_{in}^{n-m}}{Z_0} - \frac{u_k^{n+\frac{1}{2}} + u_k^{n-\frac{1}{2}}}{2Z_0} + I_{in}^{n-m} + i_{k-\frac{1}{2}}^n$$
$$= i_{k+\frac{1}{2}}^n + C_{QCL}\Delta x \frac{u_k^{n+\frac{1}{2}} - u_k^{n-\frac{1}{2}}}{\Delta t} + \frac{w\Delta x}{2}(J_k^{n+\frac{1}{2}} + J_k^{n-\frac{1}{2}}) + \frac{G_{QCL}\Delta x}{2}(u_k^{n+\frac{1}{2}} + u_k^{n-\frac{1}{2}}). \tag{5.67}$$

Rearranging Eq. (5.67) leads to

$$u_k^{n+\frac{1}{2}}\left(\frac{C_{QCL}\Delta x}{\Delta t} + \frac{1}{2Z_0} + \frac{G_{QCL}\Delta x}{2}\right) = u_k^{n-\frac{1}{2}}\left(\frac{C_{QCL}\Delta x}{\Delta t} - \frac{1}{2Z_0} - \frac{G_{QCL}\Delta x}{2}\right)$$
$$+ \frac{V_{in}^{n-m}}{Z_0} + I_{in}^{n-m} + i_{k-\frac{1}{2}}^n - i_{k+\frac{1}{2}}^n - \frac{w\Delta x}{2}(J_k^{n+\frac{1}{2}} + J_k^{n-\frac{1}{2}}), \tag{5.68}$$

which can be solved for $u_k^{n+\frac{1}{2}}$ to find the next value of u at the "QCL" $\leftrightarrow$ "coaxial cable" interface.

5.4.4 Numerics for the transmission line model

In this subsection the numerics for solving the QCL transmission line equations Eqs. (5.58) are summarized, for two distinct types of grids, the above introduced I-V grid, where the current discretization *spatially* precedes the voltage, and the V-I grid where the opposite choice is made.

The I-V grid is specified as (for $j = 1, 2, ..., M$ and $n = 1, 2, ..., N_t$)

$$i_{j-\frac{1}{2}}^n = i[(j - \frac{1}{2})\Delta x, n\Delta t], \tag{5.69}$$
$$u_j^{n-\frac{1}{2}} = u[j\Delta x, (n - \frac{1}{2})\Delta t], \tag{5.70}$$
$$J_j^{n-\frac{1}{2}} = J[j\Delta x, (n - \frac{1}{2})\Delta t]. \tag{5.71}$$

The time-stepping procedure for Eqs. (5.58) can be written as

$$u_j^{n+\frac{1}{2}} = \alpha u_j^{n-\frac{1}{2}} - \beta(i_{j+\frac{1}{2}}^n - i_{j-\frac{1}{2}}^n) - \gamma(J_j^{n+\frac{1}{2}} + J_j^{n-\frac{1}{2}}), \quad \text{for } j = 1, 2, ..., k-1, k+1, ..., M-1, \tag{5.72}$$

$$i_{j-\frac{1}{2}}^{n+1} = \delta i_{j-\frac{1}{2}}^n - \varepsilon(u_j^{n+\frac{1}{2}} - u_{j-1}^{n+\frac{1}{2}}) \quad \text{for } j = 2, 3..., M, \tag{5.73}$$

with the coefficients as specified in Eqs. (5.63). If $k \neq M$ we have the "open-circuit" boundary conditions

$$i_{\frac{1}{2}}^{n+1} = 0, \tag{5.74}$$
$$u_M^{n+\frac{1}{2}} = u_{M-1}^{n+\frac{1}{2}}, \quad \text{if } k \neq M, \tag{5.75}$$

and the update of $u_k^{n+\frac{1}{2}}$ is found from

$$u_k^{n+\frac{1}{2}}\left(\frac{C_{QCL}\Delta x}{\Delta t} + \frac{1}{2Z_0} + \frac{G_{QCL}\Delta x}{2}\right) = u_k^{n-\frac{1}{2}}\left(\frac{C_{QCL}\Delta x}{\Delta t} - \frac{1}{2Z_0} - \frac{G_{QCL}\Delta x}{2}\right)$$
$$+ \frac{V_{in}^{n-m}}{Z_0} + I_{in}^{n-m} + i_{k-\frac{1}{2}}^n - i_{k+\frac{1}{2}}^n - \frac{w\Delta x}{2}(J_k^{n+\frac{1}{2}} + J_k^{n-\frac{1}{2}}). \tag{5.76}$$

If the current injection is assumed to occur at the beginning of the QCL waveguide, i.e. at $x = 0$, it is more convenient to incorporate a V-I discretization grid for the numerical solution, i.e. (for $j = 1, 2, ..., M$ and $n = 1, 2...N_t$)

$$i_j^n = i[j\Delta x, n\Delta t], \tag{5.77}$$

$$u_{j-\frac{1}{2}}^{n-\frac{1}{2}} = u[(j-\frac{1}{2})\Delta x, (n-\frac{1}{2})\Delta t], \tag{5.78}$$

$$J_{j-\frac{1}{2}}^{n-\frac{1}{2}} = J[(j-\frac{1}{2})\Delta x, (n-\frac{1}{2})\Delta t]. \tag{5.79}$$

The numerical method now reads

$$u_{j-\frac{1}{2}}^{n+\frac{1}{2}} = \alpha u_{j-\frac{1}{2}}^{n-\frac{1}{2}} - \beta(i_j^n - i_{j-1}^n) - \gamma(J_{j-\frac{1}{2}}^{n+\frac{1}{2}} + J_{j-\frac{1}{2}}^{n-\frac{1}{2}}), \quad \text{for } j = 2, ..., k-1, k+1, ..., M, \tag{5.80}$$

$$i_j^{n+1} = \delta i_j^n - \varepsilon(u_{j+\frac{1}{2}}^{n+\frac{1}{2}} - u_{j-\frac{1}{2}}^{n+\frac{1}{2}}) \quad \text{for } j = 1, 2, 3..., M-1, \tag{5.81}$$

with the similar "open-circuit" boundary conditions

$$u_{\frac{1}{2}}^{n+\frac{1}{2}} = u_{\frac{3}{2}}^{n+\frac{1}{2}}, \quad \text{if } k \neq 1, \tag{5.82}$$

$$i_M^{n+1} = 0. \tag{5.83}$$

Lastly, the injection condition at grid point $x_{k-\frac{1}{2}} = (k-\frac{1}{2})\Delta x$ gives us the update equation

$$u_{k-\frac{1}{2}}^{n+\frac{1}{2}}\left(\frac{C_{QCL}\Delta x}{\Delta t} + \frac{1}{2Z_0} + \frac{G_{QCL}\Delta x}{2}\right) = u_{k-\frac{1}{2}}^{n-\frac{1}{2}}\left(\frac{C_{QCL}\Delta x}{\Delta t} - \frac{1}{2Z_0} - \frac{G_{QCL}\Delta x}{2}\right)$$
$$+ \frac{V_{in}^{n-m}}{Z_0} + I_{in}^{n-m} + i_{k-1}^n - i_k^n - \frac{w\Delta x}{2}(J_{k-\frac{1}{2}}^{n+\frac{1}{2}} + J_{k-\frac{1}{2}}^{n-\frac{1}{2}}). \tag{5.84}$$

5.4.5 Discussion and preliminary verification of the model

To simulate the QCL operation, the formalism introduced in Sec. 2.3.7 can be employed. Therein electronic states are described with a density matrix of a suitably chosen dimension, the time evolution of which is given by Eq. (2.68), with the additional assumption that *all* parameters are voltage (or equivalently bias) dependent. To couple the carrier transport equations to the transmission line model, one will need to additionally define a particular form for the current density $J(x,t)$ through the laser cascade. An illustration of all possible contributions to the electron current in a QCL is shown in Fig. 5.13.

Generally, the total current along the active region growth direction is the sum of three distinct components: the incoherent/scattering current due to the non-radiative transport in the structure, a coherent component of the current which is due to interaction with the optical field and/or due to resonant tunneling, and lastly a possible "leakage current" contribution, originating from electrons escaping the structure through the continuum. When the mathematical model for the density matrix is implemented as to conserve the electron number (see Sec. 2.3.2), the latter component of the current density cannot be derived from the density matrix alone, but can rather be incorporated via the Ohmic relation as in Eq. (5.58b).

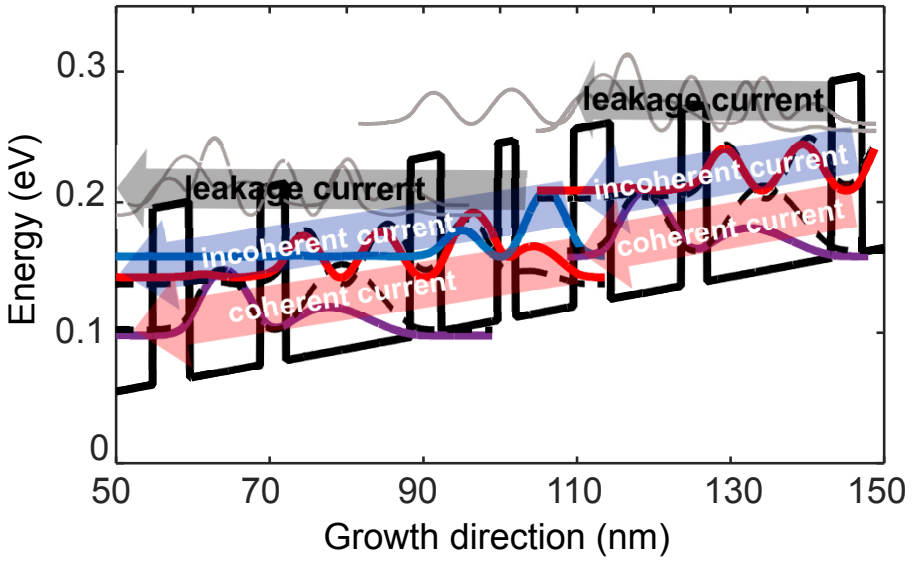

Figure 5.13 Exemplary QCL heterostructure, wave functions together with a highlight of the various contributions to the total current density flowing through the QCL. The flow of coherent and incoherent currents is constrained in the quantum well heterostructure, whereas the leakage current flows through the continuum of states.

The scattering and coherent currents can be found from the density matrix model as the expectation value of the time derivative of the position operator

$$J = Ne\frac{d}{dt}\langle\hat{z}\rangle = Ne\frac{d}{dt}\mathbf{tr}(\hat{\rho}\hat{z}) = Ne\mathbf{tr}(\frac{d}{dt}\hat{\rho}\hat{z}). \tag{5.85}$$

Since the focus here is not on the particular quantum mechanical model used for the QCL, a concrete expression for Eq. (5.85) will not be given. Instead let us focus on investigating the effects of J and $G_{QCL}u$ onto the transmission line dynamics. Take Eq. (5.58b). Integrate over the QCL cavity length L and assume that current i_0 is injected at $x = 0$, to obtain

$$\begin{aligned}
&\int_0^L \frac{\partial i(x,t)}{\partial x}dx = -\left[G_{QCL} + C_{QCL}\frac{d}{dt}\right]\int_0^L u(x,t)dx - w\int_0^L J(x,t)dx \\
&\Leftrightarrow \\
&i_0 - \underbrace{\left[w\int_0^L J(x,t)dx + G_{QCL}\int_0^L u(x,t)dx\right]}_{I_{out}} = C_{QCL}\frac{d}{dt}\int_0^L u(x,t)dx,
\end{aligned} \tag{5.86}$$

where $i(x = L, t) \equiv 0$ and $i(x = 0, t) = i_0$ have been used. A straightforward interpretation comes from the capacitor "structure" of the micro-strip transmission line. Equation (5.86) simply tells us that if the net current flow is positive, then the capacitor will gradually charge (increasing the voltage drop) and discharge for negative values of the net current. This yields the "steady state condition" for DC-pumped laser, i.e. $i_0 = i_{out}$.

Next, a numerical test for the algorithm in Sec. 5.4.4 will be presented. Since this will only be a proof of concept *experiment*, the density matrix model will be neglected in the underlying simulation, and instead a lossless QCL waveguide is modeled by setting to zero the conductance G_{QCL}, current density J, and the resistance $R_{QCL} = 0$. Additionally, assume that the QCL and the coaxial cable are impedance-matched, both with impedance $Z_0 = 50$,

while the QCL transmission line is terminated at $x = L$ with a resistive load with impedance Z_L. Note that terminating the line with a finite value for the impedance alters the corresponding boundary condition from its open circuit variant. A numerically stable formulation for the BCs of a transmission line, terminated by a resistive load, can be found in [165].

Standard transmission line theory tells us that when $Z_L \neq Z_0$, the supplied voltage wave ought to reflect from the terminal at which the load is connected, with a ratio between the forward and backward propagating voltages given by the reflection coefficient

$$\Gamma = \frac{V^-}{V^+} = \frac{Z_L - Z_0}{Z_L + Z_0}, \tag{5.87}$$

where $V^{\pm}$ denote respectively the forward and backward propagating waves. The latter can be easily found using the relations

$$I_s(t) = I_s^+ - I_s^- = \frac{V_s^+ - V_s^-}{Z_0}, \tag{5.88}$$

$$V_s(t) = V_s^+ + V_s^-, \tag{5.89}$$

and are given by

$$V_s^+ = \frac{V_s + Z_0 I_s}{2}, \tag{5.90}$$

$$V_s^- = \frac{V_s - Z_0 I_s}{2}, \tag{5.91}$$

where the end point of the coaxial cable has been chosen for reference (the same analysis can be done for every other point either along the cable or the QCL).

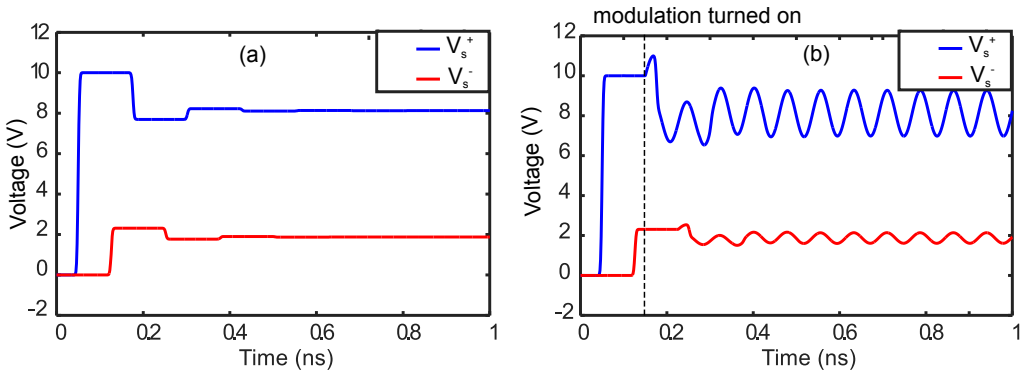

Figure 5.14 (a) Forward and backward propagating voltages as a function of time in the DC pumping regime, with a time-constant source voltage $V_{in}(t) = 10$ V. (b) Same as in (a), with the additional inclusion of a harmonic modulation of the input voltage with amplitude 1 V and modulation frequency $f_{RF} = 13$ GHz, i.e. $V_{in}(t) = [10 + \sin(2\pi f_{RF} t)]$ V.

To test this, two distinct cases are simulated, first when V_{in} is a DC voltage of 10 V (Fig. 5.14) and second, when it is a DC voltage of 10 V + a radio frequency (RF) voltage of 1 V with modulation frequency $f_{RF} = 13$ GHz. For both scenarios, assume that the coaxial cable and the QCL transmission line are lossless and have an impedance $Z_{QCL} = Z_0 = \sqrt{L/C} = 50\ \Omega$. Furthermore, the coaxial cable is connected to the $x = 0$ coordinate of the QCL transmission line, and also that the resistive load has resistance $Z_L = 80\ \Omega$.

According to Eq. (5.87), we see that both V_s^+ and V_s^- shall have the same sign (positive valued) (since $Z_L > Z_0$) and that their ratio shall be approximately $30/130 \approx 0.2308$. Simulating the system yields numerical results in perfect accordance with the analytical theory. For example in Fig. 5.14(a), after some initial transients the forward voltage settles at around $V_s^+ \approx 8.125$ V whereas the backward such $V_s^- \approx 1.875$ V, yielding a numerical reflection coefficient of 0.2308. The same reflection coefficient is also found for the case when RF modulation is abruptly switched on after 170 ps of the simulation time, see Fig. 5.14(b). Also note that in accordance with the initial conditions in Eq. (5.41), $V_s(t = 0)$ is set to zero. In order to have a smooth solution, i.e. one without spurious oscillations due to discontinuities in the initial/boundary conditions, one needs to slowly turn on the source voltage from zero to its desired value, just like in the lab, slowly enough for the quantities V, I, u and i, to be able to adapt and settle to their steady state values. The switching-on of the source is implemented by multiplying $V_{in}(t)$ by some sigmoidally shaped function, with sufficiently smooth raise time. In this case the cumulative distribution function of the normal distribution has been used,i.e.

$$V_{in}(t) \leftarrow \frac{1}{2}\left[1 + \text{erf}\left(\frac{t - t_0}{2\sigma_t^2}\right)\right] V_{in}(t), \tag{5.92}$$

where erf$(\cdot)$ is the error function, and t_0 and σ_t denote some suitably chosen mean and standard deviation, respectively.

5.5 Conclusion

In this chapter we have discussed feasible approaches to ultrashort pulse generation in terahertz quantum cascade lasers. First on the agenda was passive mode locking, where in the corresponding sections it was argued that, due to the relatively long inversion lifetimes in bound-to-continuum THz QCLs, these devices would be more suitable for PML as compared to resonant LO-phonon structures. The realization of this mechanism was suggested based on a paradigmatic model for PML via a fast saturable absorber, implementable via multi-section monolithic Fabry-Perot cavities. It was shown that, if the sections are designed correctly, the formation of picosecond pulses, with FWHM limited by the gain bandwidth of the device, could be possible. The presented calculations show that besides a suitably engineered gain medium with slowly recovering population inversion, a fast saturable absorber with very strong coupling to the optical field is essential. Carefully conducted simulation experiments indicate that the multi-section configuration is prone to entering into a regime of irregular pulsations if the absorber recovery time is very large, which should be an important point to consider in future designs. Furthermore, besides conventional passive mode locking, alternative approaches to pulse generation in QCLs, i.e. hybrid and colliding pulse mode locking, have been considered. We have seen how, by utilizing active modulation of the injection current in the absorber, the former method recovers the regular pulsations from a regime of irregular such. On the other hand, CPML might be easier to achieve with THz QCLs as multi-pulse lasing is the naturally preferred mode of operation in fast gain recovery active media. Lastly, an extension to the widely used Maxwell-Bloch equations to include microwave-optical interaction dynamics was presented. This approach, based on the coupled Maxwell-Bloch and transmission line

equations, could serve as a theoretical basis for the computational prototyping and design of actively mode locked quantum cascade lasers.

6 Metamaterials for slowing down THz light

6.1 Introduction

This thesis will conclude with a slight deviation from the main topic of THz quantum cascade lasers, instead focusing on metamaterials with custom-tailored and sometimes exotic properties. Concretely, this chapter will outline a theoretical and computational investigation on the possibility of achieving slow terahertz light by exploiting the tunneling induced transparency (TIT) effect in suitably engineered quantum well heterostructures. Such a metamaterial will be designed and simulated, showing how TIT could lead to large values of the group refractive index, unfortunately at the cost of relatively strong field attenuation due to decoherence. As a suitable alternative, the construction of an array is proposed, stacked with alternating buffer and quantum cascade amplifier regions, arranged in such a way as to achieve slow light and simultaneously compensate for the large signal losses. Calculations show that a simple 8-bit binary message could be reliably transmitted through this system, with non-critical reduction of the signal to noise ratio, and a slow-down factor of more than 70 as compared to the velocity of light in vacuum c.

Some of the results, contained in this chapter, were presented on a scientific conference [79].

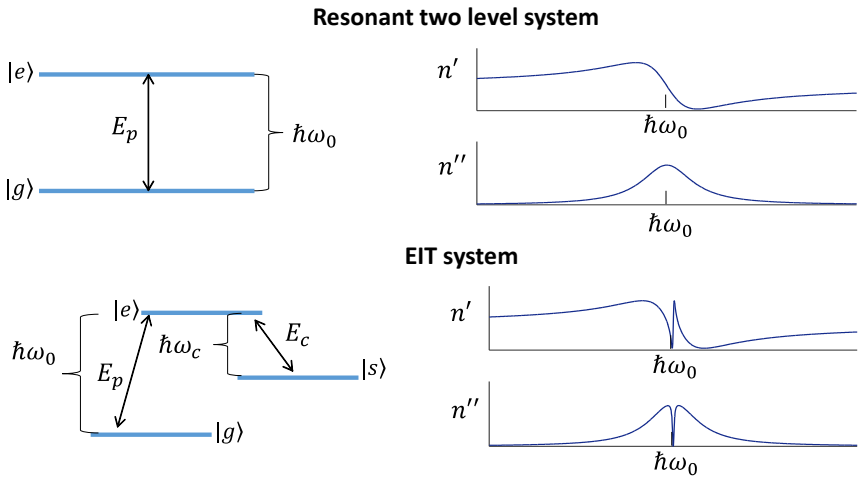

Figure 6.1 Comparison between the real and imaginary part of the refractive index, as seen by a probe field E_p in resonance with a regular two level system (top row) and a three level EIT system (bottom row).

It has been known for a long time that optical resonances can modify the group velocity (v_g) of light, leading to smaller or larger values than c. For homogeneously broadened transitions, such effects are hard to detect experimentally due to the inherently strong absorption of the incident probe field. An alternative, where optical losses due to stimulated absorption can be

partially or even completely canceled while retaining the large values of the group index, is the so called electromagnetically induced transparency (EIT) effect. Comparison between the real n' and imaginary n'' parts of the refractive index for a usual two level system resonance and EIT is shown in Fig. 6.1. For EIT, in addition to the probe field E_p there is an additional *control* beam E_c, which is used to induce the hole in the optical spectrum.

The first laboratory observation of EIT was reported in [166], where the authors demonstrated an approximately 20-fold decrease in the absorption of ultraviolet light in a ^{38}Sr vapor cell, via quantum mechanical interference effects [167, 168]. These first results initiated a very intensive and fruitful research on the topic, with probably one of the highlights of all of these collective efforts being the reduction of v_g to a mere 17 m/s in ultra-cold atomic vapor [169]. Possible applications include the construction of optical buffers [170], imaging [171, 172] and quantum memory, where light is not only slowed down but needs to be completely stopped [173]. In view of the potential commercialization of these technologies, it is very important to be able to implement the desired optical properties on a chip [174], and preferably with solid state media [175]. Furthermore, with the rapid development of semiconductor growth and processing technology, it has become even more tempting to realize slow or ultrafast light with suitably engineered quantum wells and/or quantum dots.

To understand the mechanism, in which photons are slowed down upon resonantly interacting with the EIT system, it is useful to borrow a very instructive analogy presented in [176]. Figure 6.2 illustrates the process of trapping a photon in a three level system containing the ground state $|g\rangle$, the excited state $|e\rangle$ and an additional so called "spin state" $|s\rangle$.

The key of obtaining very large slow-down factors is in making the dressed state produced by the beating between $|s\rangle$ and $|g\rangle$ as long-lived as possible. This is typically achieved in media where the $s \leftrightarrow g$ transition is forbidden whatsoever (via selection rules), for example between specially selected levels of ultra-cold lead vapor [167, 168]. Carefully tuning the frequency and amplitude of the control beam, would allow not only the selection of the appropriate $s-$level but also the tuning of the slow-down factor. Despite the great success of the EIT effect in slowing down or even stopping electromagnetic radiation, it also suffers from drawbacks as ultra cold temperatures are typically needed. Additionally, the realization of this effect necessitates the usage of two optical fields, which complicates the experimental setup.

Tunneling induced transparency (TIT) is an effect similar to EIT, with the difference that the reduction in the absorption spectrum is induced by a strong tunneling coupling between a pair of quantum states, rather than a control electric field. Both quantum well [177] and quantum dot [178] configurations have been proposed as possible implementations of TIT, but unfortunately experimental success seems to be limited to the observation of Fano-interference in quantum well heterostructures [179, 180], suggesting that more accurate theoretical modeling is needed. Below, we entertain the possibility of achieving slow light in such semiconductor metamaterials, with a slow-down factor of 70 and above all with minimal pulse attenuation. The theoretical approach is based on self-consistent simulations, involving heterostructure design via a Schrödinger-Poisson (SP) solver [115], and parameter study, with the aid of an ensemble Monte-Carlo (EMC) code [52, 117, 118], as well as full time-domain simulations of the field propagation inside the optically active material, via the Maxwell-Bloch laser equations [5, 52, 83, 91].

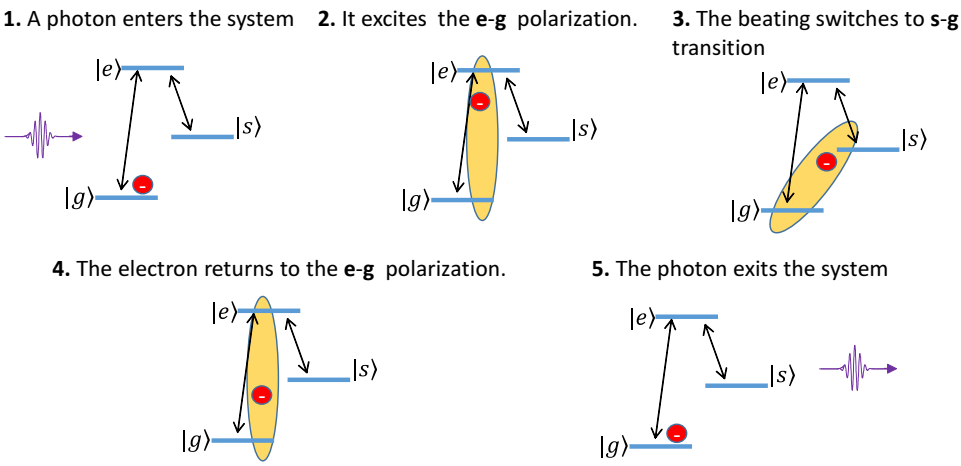

Figure 6.2 Intuitive explanation of EIT. **1.** A probe photon enters the (initially non-inverted) system. **2.** The coherent electro-optical interaction excites Rabi-oscillations between the excited state $|e\rangle$ and the ground state $|g\rangle$. **3.** The control beam transfers the coherent oscillations from the $e \leftrightarrow g$ transition to the (hopefully long-lived) $s \leftrightarrow g$ transition. **4.** Eventually, the charge returns to the original $e \leftrightarrow g$ oscillation. **5.** The charge returns to the ground state and releases the photon in the process. Adapted from [176].

This chapter is organized as follows: Section 6.2 outlines the theoretical model and the equations involved. In Sec. 6.3 an analytical expression for the group refractive index and the transmission coefficient (Sec. 6.4) are derived. In Sec. 6.5 a prototypical heterostructure design is presented together with a parameter analysis to demonstrate that it yields group index values as large as 140, however at the cost of a large signal attenuation. Lastly, in Sec. 6.6, a possible solution of the strong absorption problem is suggested, via incorporating an amplifying element in our design.

6.2 Theoretical model

The model is based on a three level Λ-type system, realized by bound states in the conduction band of a quantum well heterostructure, where a pair of states, which are denoted $|g\rangle$ for the ground and $|e\rangle$ for the excited state, is coupled via a signal field E_z oscillating with the central frequency ω_0, which is approximately in resonance with the $g \leftrightarrow e$ transition frequency ω_{eg}. On the other hand, an additional "spin" state is coupled to $|e\rangle$ via the tunneling coupling energy $\hbar\Omega_{se}$ (for explanation of the origin of the term $\hbar\Omega_{se}$ and a detailed discussion on the tight-binding basis see Sec. 4.2.1). A thick barrier separates the states $|e\rangle$ and $|s\rangle$ in space, and its width or the applied voltage can be adjusted to control the coupling strength. A schematic representation of the envisioned system is illustrated in Fig. 6.3.

To capture the optical quantum interference effects, leading to TIT, a non-classical carrier model is needed. Again, one finds that employing a density matrix approach to describe the statistical behavior of the atomic ensemble in the system, coupled to the classical Maxwell's equations via a polarization term, i.e. solving the Maxwell-Bloch equations, gives an excellent

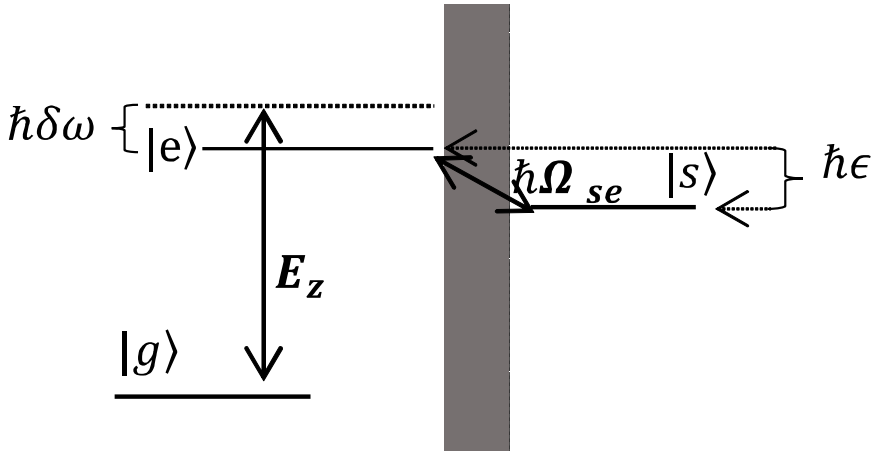

Figure 6.3 Schematic illustration of a Λ 3-level model, consisting of an excited and ground state, $|e\rangle$ and $|g\rangle$ respectively, separated via a thick barrier from a third level $|s\rangle$. The states $|g\rangle$ and $|e\rangle$ are coupled via the signal field E_z, while $|e\rangle$ and $|s\rangle$ via the tunneling coupling energy $\hbar\Omega_{se}$.

representation of the physical system. Including space dependence and employing the slowly varying envelope and rotating wave approximations, the familiar equations read

$$\partial_t f + \partial_x f = -i\frac{N\Gamma e z_{eg}\omega_0}{\epsilon_0 nc}\eta_{eg}, \tag{6.1a}$$

$$\frac{d\rho_{ss}}{dt} = i\Omega_{se}(\rho_{se}-\rho_{es}) + \Gamma_{es}\rho_{ee} + \Gamma_{gs}\rho_{gg} - \Gamma_s\rho_{ss}, \tag{6.1b}$$

$$\frac{d\rho_{ee}}{dt} = i\Omega_{se}(\rho_{es}-\rho_{se}) + i\frac{ez_{eg}}{2\hbar}\left(f^*\eta_{eg} - c.c.\right), +\Gamma_{se}\rho_{ss} + \Gamma_{ge}\rho_{gg} - \Gamma_e\rho_{ee}, \tag{6.1c}$$

$$\frac{d\rho_{gg}}{dt} = -i\frac{ez_{eg}}{2\hbar}\left(f^*\eta_{eg} - c.c.\right) + \Gamma_{sg}\rho_{ss} + \Gamma_{eg}\rho_{ee} - \Gamma_{gg}\rho_{gg}, \tag{6.1d}$$

$$\frac{d\rho_{se}}{dt} = -i\epsilon\rho_{se} + i\Omega_{se}(\rho_{ss}-\rho_{ee}) + i\frac{ez_{eg}}{2\hbar}f^*\eta_{sg} - \Gamma_{\parallel se}\rho_{se}, \tag{6.1e}$$

$$\frac{d\eta_{eg}}{dt} = i(\omega_0-\omega_{eg})\eta_{eg} + i\frac{ez_{eg}}{2\hbar}f(\rho_{ee}-\rho_{gg}) - i\Omega_{se}\eta_{sg} - \Gamma_{\parallel eg}\eta_{eg}, \tag{6.1f}$$

$$\frac{d\eta_{sg}}{dt} = i(\omega_0-\omega_{eg}-\epsilon)\eta_{sg} + i\frac{ez_{eg}}{2\hbar}f\rho_{se} - i\Omega_{se}\eta_{eg} - \Gamma_{\parallel sg}\eta_{sg}, \tag{6.1g}$$

with the usual envelope ansatz

$$E_z(x,t) = \frac{1}{2}\left[f(x,t)e^{i(\beta_0 x-\omega_0 t)} + c.c.\right], \tag{6.2}$$

$$\rho_{eg} = \eta_{eg}e^{i(\beta_0 x-\omega_0 t)}, \tag{6.3}$$

$$\rho_{sg} = \eta_{sg}e^{i(\beta_0 x-\omega_0 t)}, \tag{6.4}$$

decomposing the electric field and the coherences into a product of slowly varying envelopes and a carrier wave with angular frequency ω_0 and wave number $\beta_0 = n\omega_0/c$. The rest of the parameters are as defined throughout the previous chapters of this text.

6.3 Group index derivation

Based on the density matrix model in Eqs. (6.1), an analytical formula for the group refractive index of the TIT system can be found. First, consider the linear polarization, given by

$$P(x,t) = \epsilon_0 \chi^{(1)} E_z(x,t) = \epsilon_0 \frac{1}{2}\left[\chi^{(1)} f(x,t) e^{i(\beta_0 x - \omega_0 t)} + c.c.\right] = -N\Gamma e z_{eg}\left[\eta_{eg}(x,t) e^{i(\beta_0 x - \omega_0 t)} + c.c.\right], \tag{6.5}$$

from where one can derive an expression for the linear susceptibility

$$\chi^{(1)} = -2\frac{N\Gamma e z_{eg}}{\epsilon_0}\eta_{eg}(x,t)/f(x,t). \tag{6.6}$$

The steady state solution of η_{eg} is directly computed from Eqs. (6.1), and in the weak field limit (i.e. $|ez_{eg}f/\hbar| \ll |\Omega_{se}|$) reads

$$\eta_{eg} = -[\frac{\Omega_{se}^2}{\gamma_{se}\left(\gamma_{sg}\gamma_{eg} - \Omega_{se}^2\right)} \times (\rho_{ss} - \rho_{ee}) + \frac{\gamma_{sg}}{\left(\gamma_{sg}\gamma_{eg} - \Omega_{se}^2\right)} \times (\rho_{ee} - \rho_{gg})] \times \frac{ez_{eg}}{2\hbar} f(x,t), \tag{6.7}$$

where $\gamma_{sg} = (\delta\omega - \epsilon + i\Gamma_{\parallel sg})$, $\gamma_{eg} = (\delta\omega + i\Gamma_{\parallel eg})$, $\gamma_{se} = \epsilon - i\Gamma_{\parallel se}$, and $\delta\omega = \omega_0 - \omega_{eg}$ is the detuning of the probe field from resonance. Assuming that the populations of $|s\rangle$ and $|e\rangle$ are almost equal, $\chi^{(1)}$ simplifies to

$$\chi^{(1)} = \frac{N\Gamma e^2 z_{eg}^2}{\epsilon_0 \hbar} \times \frac{\gamma_{sg}}{\gamma_{sg}\gamma_{eg} - \Omega_{se}^2} \times (\rho_{ee} - \rho_{gg}), \tag{6.8}$$

which is the standard expression for the linear susceptibility of the 3 level Λ-system, familiar from the theory of electromagnetically induced transparency[167, 170]. Note that the term that has been dropped in Eq. (6.7) can be associated with the so called Raman gain in the system [121] and can be exploited for gain assisted slow light [181] or inversion-less lasing [182].

Let us also assume a background susceptibility $\chi_0 = n^2 - 1$, taken to be constant for narrow frequencies around the central carrier frequency. Then the total (complex) refractive index $\underline{n} = n' + in''$ is given by

$$\underline{n}^2 = n^2 + \chi^{(1)}, \tag{6.9}$$

which can be Taylor expanded to yield

$$\underline{n} = n + \frac{1}{2n}\chi^{(1)} = n(1 + r\Omega_p \times \frac{\gamma_{sg}}{\gamma_{sg}\gamma_{eg} - \Omega_{se}^2}). \tag{6.10}$$

In Eq. (6.10) $r = (\rho_{ee} - \rho_{gg}) \approx -1$ is the population inversion factor and

$$\Omega_p = \frac{N\Gamma e^2 z_{eg}^2}{2n^2\epsilon_0\hbar} > 0 \tag{6.11}$$

is the modified plasma frequency. Assuming $\epsilon \approx 0$, the group refractive index is finally given by

$$n_g = n + \omega_0 \,\mathrm{Re}\{\frac{\partial \underline{n}}{\partial \delta\omega}\}\Big|_{\delta\omega=0} = n\Big(1 - r\omega_0\Omega_p \times \frac{\Omega_{se}^2 - \Gamma_{\parallel sg}^2}{[\Omega_{se}^2 + \Gamma_{\parallel sg}\Gamma_{\parallel eg}]^2}\Big). \tag{6.12}$$

6.4 Transparency under decoherence

The power transmission coefficient over propagation length dL is simply

$$T(\omega) = \exp(-2\omega c^{-1}\,\mathrm{Im}\{\underline{n}(\omega)\}dL), \tag{6.13}$$

where $n'' = \mathrm{Im}\{\underline{n}(\omega)\}$ denotes the imaginary part of the refractive index. Calculating n'' from Eq. (6.10), one can quickly see that absorption will vanish in case of $\Gamma_{\parallel sg} = 0$ and $\delta\omega = (\omega - \omega_{eg}) = 0$, which is exactly what is termed as tunneling induced transparency [178]. Unfortunately, the relatively small coherence times, i.e. large $\Gamma_{\parallel sg}$, in solid state materials present a great obstacle in realizing slow light in such non-gaseous media.

This problem is tackled in two different ways. First of all, in Sec. 6.5, a quantum well heterostructure is presented, which has been designed in order to minimize the decoherence between the spin and the ground state of Fig. 6.3, and simultaneously maximize the value of the group index. It is found, however, that despite the optimal structure design, $s \leftrightarrow e$ lifetimes are still on the order of nanoseconds. Thus reasonable values of n_g can be only achieved at the cost of a considerable electric field attenuation. Therefore, in Sec. 6.6 we discuss a prototype system, incorporating an amplifying element, as means to compensate for this defect in the optical buffer.

6.5 Coherent three well system

With the use of a Schrödinger-Poisson solver, coupled to the ensemble Monte Carlo simulation code, a quantum well heterostructure corresponding to the model in Fig. 6.3 can be engineered. The SP solver is used to calculate the eigenstates and with the EMC code one evaluates the scattering rates at a fixed temperature, here chosen to be 10 K. The resulting structure and the corresponding system parameters are displayed in Fig. 6.4 and Tab. 6.1, respectively. The

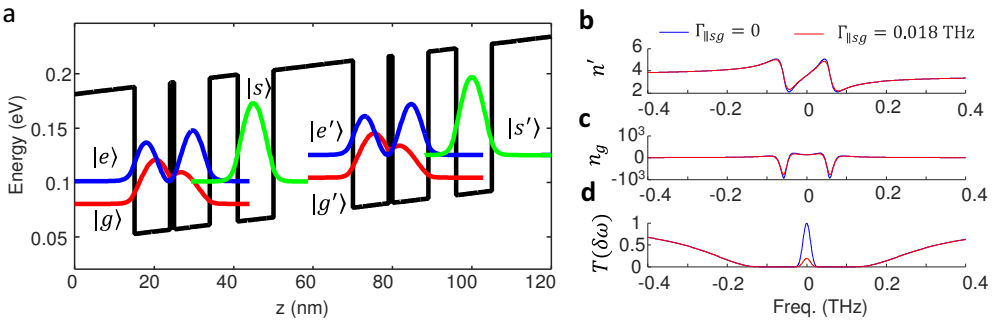

Figure 6.4 (a) The three well design calculated with the SP solver. The assumed barrier/well material is $Al_{15}GaAs_{0.85}$/GaAs, and the heterostructure has the following thicknesses (with the barriers in boldface): **100**/90/**10**/90/**90**/90/**100** in 10^{-10} m. Shown is the calculated real refractive index, (b), group index, (c), and transmission coefficient, (d), centered at the $e \leftrightarrow g$ resonance frequency ω_{eg}.

structure consists of three quantum wells per period where the left pair of wells is separated by a thick 9 nm barrier from the third well, confining the $|s\rangle$ state. At a bias of approximately 4.4 kV/cm, there is a strong repulsion between the states $|s\rangle$ and $|e\rangle$, which leads to their splitting

by twice the coupling energy $2\hbar\Omega_{se}$. From the plots in Fig. 6.4(b)–Fig. 6.4(d), we see that around $\delta\omega = 0$ the real refractive index n' has a very steep slope, which results in a group refractive index of approximately $n_g = 136$, Fig. 6.4(c), when calculated with Eq. (6.12). On the other hand, decoherence of $\Gamma_{\parallel sg} = 0.018$ THz yields a very strong absorption coefficient ($\alpha \approx 165$ cm^{-1}), which results in only 20% of the incident light being transmitted through a 0.1 mm long medium. In the next section, a possible solution to this problem is proposed, based on the construction of a grating structure, consisting of alternating slow-light and amplification regions.

6.6 Gain compensated slow light system

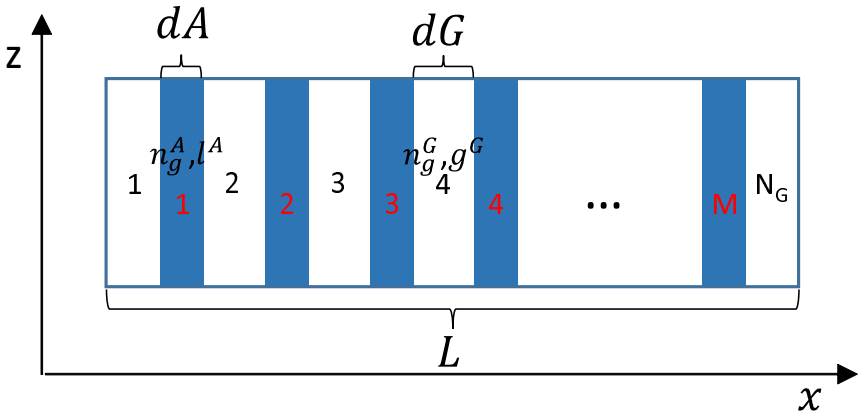

Figure 6.5 Schematic diagram of the buffer/amplification grating structure. The buffer consists of M slow-light regions (blue), each of length dA, with loss coefficient and group index l^A and n_g^A, respectively. The amplifier consists of N_G short gain media (white), each of which has a length of dG, a small signal gain g^G and a group index n_g^G.

A rather obvious remedy for the strong absorption of the signal field is to try to compensate for the attenuated light with a quantum cascade amplifier [183] with some desired properties. What would those be though? To answer this question, let us start off by assuming a patterned grating consisting of M of the quantum well heterostructures from the model in Fig. 6.4(a), alternating with N_G quantum cascade amplifier regions, as illustrated in Fig. 6.5. Let us assume that each slow light region has length dA and each amplifier region length dG, then the total length is $L_A = MdA$ for the buffer region, and $L_G = N_G dG$ for the amplifier. Specify the slow-down factor S as the ratio of the light's traversal time of the active region in Fig. 6.5 versus its traversal time of a cold cavity of length L. Then S is

$$S = \left(\frac{L_A n_g^A}{c} + \frac{L_G n_g^G}{c}\right) \times \frac{c}{L} = \frac{L_A n_g^A}{L} + (1 - \frac{L_A}{L}) n_g^G \approx \frac{L_A n_g^A}{L}, \tag{6.14}$$

where it has been taken that $n_g^A \gg n_g^G$. On the other hand, any input intensity, I_{in}, will be attenuated and amplified upon propagation through this composite material. At the output facet, the intensity will thus be given by

$$I_{out} = I_{in} \exp\left(g^G L_G - \alpha L^A\right), \tag{6.15}$$

where g^G is the power gain coefficient of the amplifier and α is the absorption coefficient in the optical buffer. To achieve transparent pulse propagation, the system needs to satisfy $g^G L_G = \alpha L^A$, which combined with Eq. (6.14) yields the relation

$$g^G L_G = \alpha S \times L/n_g^A. \tag{6.16}$$

For the old parameter values $n_g^A = 136$, α = 165 cm^{-1} and gain region length $L_G = L/2$, solve for the gain coefficient to obtain $g^G = 36.3971$ cm^{-1}, for a desired slow-down factor of 60. Such values for g^G are perfectly reasonable for state of the art QCL technology.

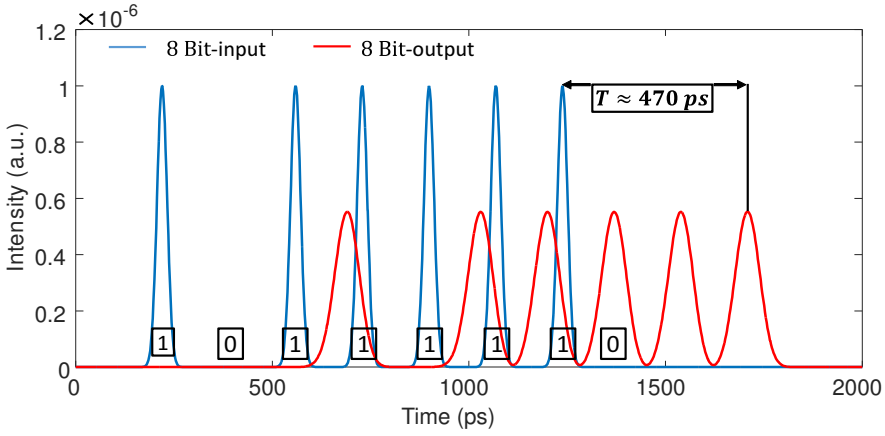

Figure 6.6 Simulation results from a binary message sent through a grating structure of length $L = 2$ mm. The blue curve shows the input bits (10111110) and the red one the output bits.

Another point worth mentioning here is that none of Eqs. (6.14)-(6.15) require that the slow-light and gain regions in Fig. 6.5 should be alternating. So why does one make that choice? This point becomes important when one considers the highly nonlinear dispersion of the slow-light material, depicted in Fig. 6.4(b). Significant pulse distortion will occur if the propagation length in the medium is longer than the corresponding dispersion length, and therefore this is prevented by adequately choosing the length dA and distributing the slow-light/gain regions in alternating fashion.

To illustrate that the above schematic can be used for implementation of optical buffers, the transmission of a binary message, i.e. the number $(125)_{10} = (10111110)_2$, has been simulated though a grating structure of total length $L = 2$ mm. The gain medium was simulated as a two-level Maxwell-Bloch system [52], amplifying at the central frequency ω_0 with the rest of the parameters specified in Table 6.1.

Figure 6.6 shows the results of this simulation, where the input message (blue) is superposed in time with the output signal (red). We immediately see that each bit takes around 470 ps to traverse the 2 mm cavity, which gives us a total slow-down factor of $S \approx 70.45$. Furthermore,

Table 6.1 Parameter values for the slow-light region (left) of Fig. 6.4a and for the amplifying medium (right) modeled as a two-level system [52].

Parameter	Value	Units
$\Gamma_{\parallel se}$	0.2145	THz
$\Gamma_{\parallel eg}$	0.2038	THz
$\Gamma_{\parallel sg}$	0.0180	THz
z_{eg}	4.6	nm
Ω_{se}	$0.0587\times2\pi$	THz
ω_c	$5.0433\times2\pi$	THz
N	7.89×10^{21}	m^{-3}

Parameter	Value	Units
Gain recovery time	10	ps
Dephasing time	2.35	ps
Steady state inversion (w_0)	1	
Waveguide losses (l_0)	10	cm^{-1}
z_{eg}	4.6	nm
ω_c	$5.0433\times2\pi$	THz
N	5.2×10^{20}	m^{-3}

calculations reveal that the signal to noise ratio has been deteriorated due to dispersion, but not to a such an extend as to make the message unreadable. The input signal is composed of Gaussian pulses with intensity full width at half maximum (FWHM) of 30 ps, yielding a spectral bandwidth of 14.6 GHz at FWHM, which is within the transparency region induced by the tunneling splitting, Fig. 6.4(c).

Lastly, Fig. 6.7 illustrates a snapshot from simulations when two of the input bits are simultaneously present inside the cavity. The green-shaded regions denote the slow-light media, whereas in the white areas are located the quantum cascade amplifiers. For this simulation both regions' lengths have been set equal, i.e. $L_G = L_A = 1$ mm, with the input bits injected from the left facet.

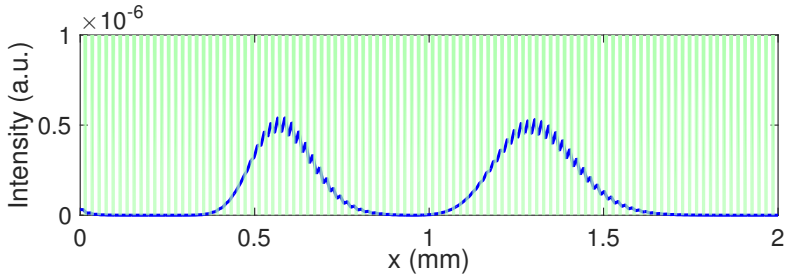

Figure 6.7 Signal propagation inside the cavity. The shaded area delineates the slow-light regions whereas the transparent area indicates the amplifying material. For this simulation $M = 100$ and $L_G = L_A = 1$ mm.

6.7 Conclusion

In this chapter we considered the usage of quantum well heterostructures for slowing down terahertz light, by harnessing the tunneling induced transparency effect. Such an approach offers the possibility to electrically control the optical properties of the system via simply varying the applied bias, however it suffers from the drawback that the inherently short coherence times in these media lead to a significant absorption of the signal field. As a possible solution, the construction of a buffer/amplifier composite grating structure was proposed, intended to compensate for the strong attenuation in the slow-light region. The actual processing and

growth of the envisaged grating structure could provide an insurmountable difficulty into the practical realization of this experiment. The problem lies in the fine level of control needed to stack two or more micro-structures in a manner as illustrated in Fig. 6.5. Other obvious drawbacks of the proposed approach are that such a schematic could be constrained to work under only very low temperatures and also that there might be reflections at the buffer/amplifier interfaces. In a publication presented at a renowned international conference [184], the latter issue has already been addressed it was shown that an optimal grating structure can be chosen so that reflections do not pose a threat to the success of the experiment.

7 Conclusion and perspectives

The presented work focused on theoretical and computer-aided investigation of various mechanisms for frequency comb formation in terahertz quantum cascade lasers. The main workhorse model was the so called Maxwell/density matrix equations model, which was shown to reliably capture the most important physical effects, known to play a role in determining the multimode dynamics of QCLs. The most important contributions of this thesis are as follows.

First, based on a version of the Maxwell/density matrix equations, a versatile semi-classical method for the time-domain simulation of light-matter interaction in QCL-heterostructures was derived. The model extended previously known theoretical results by including the coherent interaction dynamics between a pair of tunneling levels, namely the injector and the upper laser level. It was later shown by simulations that this extension is essential in order to reproduce experimental results in both frequency and time domain.

Next, solid numerical methods, suitable for the long-time simulations of THz quantum cascade lasers for frequency comb generation, were developed. These algorithms were thoroughly tested both theoretically and numerically, resulting in the selection of an optimally performing scheme to be used for the time-propagation of the electro-optical ensemble. The selected method was shown to have a good order of accuracy and importantly was proven to be devoid of low order dispersion errors, which is a virtue of its monotonicity preserving property.

Following the careful numerical study, the derived algorithms were employed to investigate the physics of both free running and mode locked QCLs, namely in the context of frequency comb generation. For the former scenario, it was shown that free running QCLs can suffer from multimode instabilities due to the intricate interplay between various comb forming and comb-degrading mechanisms. Specifically, the destabilizing influence of spatial hole burning (SHB) and spectral cross-talk onto the emission was identified and possible remedies were examined. For example, in the former case the processing of a device with asymmetric facet reflectivies was suggested, whereas in the latter it was shown how combination between laser seeding and careful gain design (i.e. one with minimal spectral cross-talk) could lead to a more coherent spectrum. The original idea, which motivated the investigations in Chapter 4, was to eventually outline a rough *recipe*, containing a set of necessary conditions for the formation of a comb from a free running laser. It must be admitted that this ambitious task was not fully accomplished, however recent publications (issued after the aforementioned research was conducted) have partially confirmed some of the findings presented. For example in [21] the detrimental effect of SHB was clearly demonstrated. However, it still remains to be seen if clever laser seeding experiments will be able to kick-start the comb formation and turn an unstable multimode spectrum to a stable one, as stipulated in Chapter 4.

Next, the possibility to actively participate in the phase locking of the lasing modes, by means of mode locking techniques, was also theoretically considered. Both passive and active mode locking were examined in Chapter 5, where some important insights about the possibility to passively mode lock (PML) QCLs were presented. For example, contrary to the popular opinion that PML is unattainable with QCLs, provided a suitable design is employed, it was shown that ultra-short terahertz pulses can be emitted by virtue of a classical PML with a fast saturable absorber. In fact, THz QCLs might be, in a sense, some of the most optimal lasers to passively mode lock, as when the gain recovery time has the same order of magnitude as the cavity round trip time, maximum energy can be transferred from the population inversion to the photon field. Additionally, it was shown that higher harmonic mode locking is also achievable with THz QCLs, and it was elaborated that this technique will probably be easier to implement than fundamental PML. In fact, there is some experimental evidence backing-up these conclusions, e.g. experiments showing spectrum with components separated by a higher harmonic of the round trip frequency [185], or the proven inherently multi-pulsed time-domain profile of free running devices [158]. It is worthwhile to mention that this part of the dissertation, contrary to the results in Chapter 4, has a predictive character, i.e. it did not aim to reproduce experimental results, but rather intended to stimulate such research.

In addition to passive mode locking, a comprehensive theoretical model for the microwave-optical simulations of transmission line effects in quantum cascade lasers was also introduced in Chapter 5. Even though, because of time constraints, the presented research was left only at preliminary stage of development, it nevertheless remains a promising avenue for further theoretical study. This is because transmission line effects, manifested in injection locking of the beatnote, self-mixing effects etc., could potentially be exploited for various applications, for example for imaging and ultra-short pulse generation via active mode locking [85, 146, 186].

Lastly, the weaknesses of the derived model as well as possible perspectives for future research should be outlined. As already mentioned, the slowly varying envelope (SVEA) and rotating wave approximations (RWA) are too restrictive on the MB-equations for modeling of QCLs with arbitrary characteristics. This is so, for example because the regimes in which the assumed approximations apply, do not allow for the simulation of a broadband device. Additional limitation is the average intensity which could be simulated by those models, since within the RWA one is constrained to solving only for relatively weak optical fields (ones for which the related Rabi-frequency is not close to the optical transition frequency). Another constraint, which I find as probably the biggest limitation when using the reduced Maxwell/density matrix equations, is that one is bound to include only one or at most two optical transitions in the simulation. This is so, because employing SVEA and RWA on a device with multiple optical transitions, results in a very large system of equations, which is somewhat cumbersome to derive and is error-prone to implement. On the other hand some QCLs, especially bound-to-continuum (BTC) designs, can contain a multitude of levels clustered into *minibands*, and as such the exact optical transitions are difficult to identify. In order to be able to accurately model such structures, one should instead try to construct a full Maxwell/density matrix approach, capable of simulating arbitrary interaction Hamiltonians and arbitrary number of laser levels, also without employing any of the above mentioned approximations. Then the resulting equations will be simpler to write down and the models easier to extend, however

the main obstacles will then lie in the development of reliable numerical algorithms and their implementation.

As for future prospects, I firmly believe that the next logical step would be indeed to simulate QCLs from first principles, possibly also quantizing the electromagnetic field, in order to capture finer details in the dynamics of these devices. Additionally, a promising subject for further research could be the investigation of colliding-pulse mode locking with THz QCLs, which in fact is a two-fold research topic, partly necessitating accurate gain region design, by means of e.g. Monte Carlo simulations, and also extensive time-domain simulations by means of the methods described in Chapter 5. Lastly, for free-running devices, one could dive deeper (by means of simulations) in investigating the initial processes that determine the multimode stability of the laser, as seminal works on Kerr-frequency comb sources indicate the immense importance of the initial dynamics in deciding which operating regime will the laser settle in [131]. Further insights along this line might lead to free running QCL combs with greater bandwidths, which are stable over a wide portion of their dynamic range.

Bibliography

[1] S. Kumar, *Development of terahertz quantum-cascade lasers*. PhD thesis, Massachusetts Institute of Technology, 2007.

[2] A. Bismuto, R. Terazzi, B. Hinkov, M. Beck, and J. Faist, "Fully automatized quantum cascade laser design by genetic optimization," *Applied Physics Letters*, vol. 101, p. 021103, 2012.

[3] A. K. Wójcik, P. Malara, R. Blanchard, T. S. Mansuripur, F. Capasso, and A. Belyanin, "Generation of picosecond pulses and frequency combs in actively mode locked external ring cavity quantum cascade lasers," *Applied Physics Letters*, vol. 103, p. 231102, 2013.

[4] J. Khurgin, Y. Dimelik, A. Hugi, and J. Faist, "Coherent frequency comb produced by self-frequency modulation in quantum cascade lasers," *Applied Physics Letters*, vol. 104, p. 081118, 2014.

[5] P. Tzenov, D. Burghoff, Q. Hu, and C. Jirauschek, "Time domain modeling of terahertz quantum cascade lasers for frequency comb generation," *Optics Express*, vol. 24, p. 23232, 2016.

[6] P. Tzenov, D. Burghoff, Q. Hu, and C. Jirauschek, "Analysis of operating regimes of terahertz quantum cascade laser frequency combs," *IEEE Transactions on Terahertz Science and Technology*, vol. 7, pp. 351–359, 2017.

[7] A. Wacker, "Gain in quantum cascade lasers and superlattices: A quantum transport theory," *Physical Review B*, vol. 66, p. 085326, 2002.

[8] A. Wacker, M. Lindskog, and D. O. Winge, "Nonequilibrium Green's function model for simulation of quantum cascade laser devices under operating conditions," *IEEE Journal of Selected Topics in Quantum Electronics*, vol. 19, pp. 1–11, 2013.

[9] S. B. Gustavo Villares, Andreas Hugi and J. Faist, "Dual-comb spectroscopy based on quantum-cascade-laser frequency combs," *Nature Photonics*, vol. 5, p. 5192, 2014.

[10] Y. Yang, D. Burghoff, D. J. Hayton, J.-R. Gao, J. L. Reno, and Q. Hu, "Terahertz multiheterodyne spectroscopy using laser frequency combs," *Optica*, vol. 3, pp. 499–502, 2016.

[11] M. B. S. Blaser, D. Hofstetter and J. Faist, "Free-space optical data link using Peltier-cooled quantum cascade laser," *Electronics Letters*, vol. 37, p. 778, 2001.

[12] E. F. N. Robin S. M. Chrystie and A. Farooq, "Ultra-fast and calibration-free temperature sensing in the intrapulse mode," *Optics Letters*, vol. 39, p. 6620, 2014.

[13] A. Müller and J. Faist, "The quantum cascade laser: ready for take-off," *Nature Photonics*, vol. 4, p. 291, 2010.

[14] A. Hugi, G. Villares, S. Blaser, H. Liu, and J. Faist, "Mid-infrared frequency comb based on a quantum cascade laser," *Nature*, vol. 492, p. 229, 2012.

[15] D. Burghoff, T.-Y. Kao, N. Han, X. Cai, Y. Yang, D. J. Hayton, J.-R. Gao, J. L. Reno, and Q. Hu, "Terahertz laser frequency combs," *Nature Photonics*, vol. 8, p. 462, 2014.

[16] M. B. Markus Rösch, Giacomo Scalari and J. Faist, "Octave-spanning semiconductor laser," *Nature Photonics*, 2015.

[17] C. Y. Wang, L. Kuznetsova, V. M. Gkortsas, L. Diehl, F. X. Kärtner, M. A. Belkin, A. Belyanin, X. Li, D. Ham, H. Schneider, P. Grant, C. Y. Song, S. Haffouz, Z. R. Wasilewski, H. C. Liu, and F. Capasso, "Mode-locked pulses from mid-infrared quantum cascade lasers," *Optics Express*, vol. 17, p. 12929, 2009.

[18] F. Wang, K. Maussang, S. Moumdji, R. Colombelli, J. R. Freeman, I. Kundu, L. Li, E. H. Linfield, A. G. Davies, J. Mangeney, *et al.*, "Generating ultrafast pulses of light from quantum cascade lasers," *Optica*, vol. 2, p. 944, 2015.

[19] A. Mottaghizadeh, D. Gacemi, P. Laffaille, H. Li, M. Amanti, C. Sirtori, G. Santarelli, W. Hänsel, R. Holzwart, L. H. Li, *et al.*, "5-ps-long terahertz pulses from an active-mode-locked quantum cascade laser," *Optica*, vol. 4, p. 168, 2017.

[20] H. Choi, V.-M. Gkortsas, L. Diehl, D. Bour, S. Corzine, J. Zhu, G. Höfler, F. Capasso, F. X. Kärtner, and T. B. Norris, "Ultrafast Rabi flopping and coherent pulse propagation in a quantum cascade laser," *Nature Photonics*, vol. 4, p. 706, 2010.

[21] T. S. Mansuripur, C. Vernet, P. Chevalier, G. Aoust, B. Schwarz, F. Xie, C. Caneau, K. Lascola, C.-e. Zah, D. P. Caffey, T. Day, L. J. Missaggia, M. K. Connors, C. A. Wang, A. Belyanin, and F. Capasso, "Single-mode instability in standing-wave lasers: the quantum cascade laser as a self-pumped parametric oscillator," *Physical Review A*, vol. 94, p. 063807, 2016.

[22] A. E. Siegman, *Lasers*. University Science Books, 1986.

[23] M. C. Gather and S. H. Yun, "Single cell biological lasers," *Nature Photonics*, vol. 5, p. 406, 2011.

[24] S. Johansson and V. Letokhov, "Astrophysical lasers and nonlinear optical effects in space," *New Astronomy Reviews*, vol. 51, p. 443, 2007.

[25] W. T. Silfvast, *Laser Fundamentals*. Cambridge University Press, 2004.

[26] S. Sze, *Physics of Semiconductor Devices*. John Wiley and Sons, second ed., 1996.

[27] B. Williams, "Terahertz quantum-cascade lasers," *Nature Photonics*, vol. 1, p. 517, 2007.

[28] P. Han and X.-C. Zhang, "Coherent,broadband midinfrared terahertz beam sensors," *Applied Physics Letters*, vol. 73, p. 3049, 1998.

[29] T. Udem, R. Holzwarth, and T. W. Hänsch, "Optical frequency metrology," *Nature*, vol. 416, p. 233, 2002.

[30] B. Williams, S. Kumar, Q. Hu, and J. Reno, "High-power terahertz quantum-cascade lasers," *Electronics Letters*, vol. 42, p. 89, 2006.

[31] C. Sirtori, F. Capasso, J. Faist, A. L. Hutchinson, D. L. Sivco, and A. Y. Cho, "Resonant tunneling in quantum cascade lasers," *IEEE Journal of Quantum Electronics*, vol. 34, pp. 1722–1729, 1998.

[32] R. F. Kazarinov and R. A. Suris, "Possibility of the amplification of electromagnetic waves in a semiconductor with a superlattice," *Soviet Physics-Semiconductors*, vol. 5, p. 707, 1971.

[33] J. Faist, F. Capasso, D. L. Sivco, C. Sirtori, A. L. Hutchinson, and A. Y. Cho, "Quantum Cascade Laser," *Science*, vol. 264, p. 553, 1994.

[34] A. Bismuto, R. Terazzi, M. Beck, and J. Faist, "Electrically tunable, high performance quantum cascade laser," *Applied Physics Letters*, vol. 96, p. 141105, 2010.

[35] F. Xie, C. G. Caneau, H. P. LeBlanc, M. tsung Ho, J. Wang, S. Chaparala, L. C. Hughes, and C. en Zah, "High power and high temperature continuous-wave operation of distributed Bragg reflector quantum cascade lasers," *Applied Physics Letters*, vol. 104, p. 071109, 2014.

[36] "http://www.alpeslasers.ch/."

[37] B. Engineering, "http://www.blockeng.com."

[38] S. Fathololoumi, E. Dupont, C. Chan, Z. Wasilewski, S. Laframboise, D. Ban, A. Mátyás, C. Jirauschek, Q. Hu, and H. Liu, "Terahertz quantum cascade lasers operating up to 200 K with optimized oscillator strength and improved injection tunneling," *Optics Express*, vol. 20, pp. 3866–3876, 2012.

[39] A. Albo, Q. Hu, and J. L. Reno, "Room temperature negative differential resistance in terahertz quantum cascade laser structures," *Applied Physics Letters*, vol. 109, p. 081102, 2016.

[40] A. Albo and Q. Hu, "Investigating temperature degradation in THz quantum cascade lasers by examination of temperature dependence of output power," *Applied Physics Letters*, vol. 106, p. 131108, 2015.

[41] A. Albo and Y. V. Flores, "Temperature-driven enhancement of the stimulated emission rate in terahertz quantum cascade lasers," *IEEE Journal of Quantum Electronics*, vol. 53, pp. 1–5, 2017.

[42] S. C. Singh, H. Zeng, C. Guo, and W. Cai, *Nanomaterials: processing and characterization with lasers*. John Wiley & Sons, 2012.

[43] H. A. Haus, "Mode-locking of lasers," *IEEE Journal of Selected Topics in Quantum Electronics*, vol. 6, p. 1173, 2000.

[44] C. W. Thiel, "Four-Wave Mixing and its Applications."

[45] A. M. Weiner, *Ultrafast Optics*. John Wiley & Sons, Inc., 2009.

[46] A. Hugi, *Single-mode and comb operation of broadband quantum cascade lasers*. PhD thesis, Diss., Eidgenössische Technische Hochschule ETH Zürich, Nr. 21138, 2013, 2013.

[47] J. Ye and E. Steven T. Cundiff, *Femtosecond Optical Frequency Comb: Principle, Operation, and Applications*. Springer US, 2005.

[48] D. Burghoff, Y. Yang, and Q. Hu, "Computational multiheterodyne spectroscopy," *Science Advances*, vol. 2, 2016.

[49] "http://www.nobelprize.org/nobel_prizes/physics/laureates/2005/."

[50] T. Udem, J. Reichert, R. Holzwarth, and T. Hänsch, "Accurate measurement of large optical frequency differences with a mode-locked laser," *Optics Letters*, vol. 24, p. 881, 1999.

[51] D. Bachmann, M. Rösch, M. J. Süess, M. Beck, K. Unterrainer, J. Darmo, J. Faist, and G. Scalari, "Short pulse generation and mode control of broadband terahertz quantum cascade lasers," *Optica*, vol. 3, p. 1087, 2016.

[52] C. Jirauschek and T. Kubis, "Modeling techniques for quantum cascade lasers," *Applied Physics Reviews*, vol. 1, p. 011307, 2014.

[53] R. W. Ziolkowski, J. M. Arnold, and D. M. Gogny, "Ultrafast pulse interactions with two-level atoms," *Physical Review A*, vol. 52, p. 3082, 1995.

[54] J. R. Freeman, J. Maysonnave, S. Khanna, E. H. Linfield, A. G. Davies, S. S. Dhillon, and J. Tignon, "Laser-seeding dynamics with few-cycle pulses: Maxwell-Bloch finite-difference time-domain simulations of terahertz quantum cascade lasers," *Physical Review A*, vol. 87, p. 063817, 2013.

[55] A. Taflove and S. C. Hagness, *Computational Electrodynamics*. Artech house publishers, 2000.

[56] K. Yee, "Numerical solution of initial boundary value problems involving Maxwell's equations in isotropic media," *IEEE Transactions on antennas and propagation*, vol. 14, pp. 302–307, 1966.

[57] M. Riesch, N. Tchipev, H.-J. Bungartz, and C. Jirauschek, "Solving the Maxwell-Bloch equations efficiently on parallel architectures," in *European Quantum Electronics Conference*, p. EJ_P_2, Optical Society of America, 2017.

[58] B. Tromborg, H. E. Lassen, and H. Olesen, "Traveling wave analysis of semiconductor lasers: modulation responses, mode stability and quantum mechanical treatment of noise spectra," *IEEE Journal of Quantum Electronics*, vol. 30, pp. 939–956, 1994.

[59] D. Jones, L. Zhang, J. Carroll, and D. Marcenac, "Dynamics of monolithic passively mode-locked semiconductor lasers," *IEEE Journal of Quantum Electronics*, vol. 31, p. 1051, 1995.

[60] S. Bischoff, J. Mørk, T. Franck, S. Brorson, M. Hofmann, K. Fröjdh, L. Prip, and M. Sørensen, "Monolithic colliding pulse mode-locked semiconductor lasers," *Quantum and Semiclassical Optics: Journal of the European Optical Society Part B*, vol. 9, p. 655, 1997.

[61] K. Williams, M. Thompson, and I. White, "Long-wavelength monolithic mode-locked diode lasers," *New Journal of Physics*, vol. 6, p. 179, 2004.

[62] R. W. Boyd, *Nonlinear Optics*. Academic Press, third ed., 2010.

[63] M. Wienold, B. Röben, L. Schrottke, and H. Grahn, "Evidence for frequency comb emission from a Fabry-Pérot terahertz quantum-cascade laser," *Optics Express*, vol. 22, pp. 30410–30424, 2014.

[64] P. N. Butcher and D. Cotter, *The Elements of Nonlinear Optics*, vol. 9. Cambridge University Press, 1991.

[65] C. Henry, "Theory of the linewidth of semiconductor lasers," *IEEE Journal of Quantum Electronics*, vol. 18, pp. 259–264, 1982.

[66] W. Shockley and W. Read Jr, "Statistics of the recombinations of holes and electrons," *Physical Review*, vol. 87, p. 835, 1952.

[67] K. Donovan, P. Harrison, and R. Kelsall, "Self-consistent solutions to the intersubband rate equations in quantum cascade lasers: Analysis of a GaAs/Al x Ga 1- x As device," *Journal of Applied Physics*, vol. 89, pp. 3084–3090, 2001.

[68] H. Choi, L. Diehl, Z.-K. Wu, M. Giovannini, J. Faist, F. Capasso, and T. B. Norris, "Gain recovery dynamics and photon-driven transport in quantum cascade lasers," *Physical Review Letters*, vol. 100, p. 167401, 2008.

[69] Q. Yang, B. Hinkov, F. Fuchs, W. Bronner, K. Köhler, J. Wagner, R. Maulini, and J. Faist, "Rate equations analysis of external-cavity quantum cascade lasers," *Journal of Applied Physics*, vol. 107, p. 043109, 2010.

[70] F. Wooten, *Optical properties of solids*. Academic press, 2013.

[71] R. C. Iotti and F. Rossi, "Microscopic theory of semiconductor-based optoelectronic devices," *Reports on Progress in Physics*, vol. 68, p. 2533, 2005.

[72] U. Bendelow, M. Radziunas, J. Sieber, and M. Wolfrum, "Impact of gain dispersion on the spatio-temporal dynamics of multisection lasers," *IEEE Journal of Quantum Electronics*, vol. 37, pp. 183–188, 2001.

[73] A. G. Vladimirov and D. Turaev, "Model for passive mode locking in semiconductor lasers," *Physical Review A*, vol. 72, p. 033808, 2005.

[74] J. Sakurai and J. Napolitano, *Modern Quantum Mecanics*. Addison Wesley, second ed., 2010.

[75] M. A. Nielsen and I. L. Chuang, *Quantum Computation and Quantum Information (Cambridge Series on Information and the Natural Sciences)*. Cambridge university press, 2004.

[76] R. Loudon, *The Quantum Theory of Light*. Oxford University Press, third edition ed., 2000.

[77] H.-P. Breuer and F. Petruccione, *The theory of open quantum systems*. Oxford University Press on Demand, 2002.

[78] T. Ando, "Line width of inter-subband absorption in inversion layers: Scattering from charged ions," *Journal of the Physical Society of Japan*, vol. 54, pp. 2671–2675, 1985.

[79] P. Tzenov and C. Jirauschek, "Slow terahertz light via resonant tunneling induced transparency in quantum well heterostructures," in *19th International Conference and School on Quantum Electronics: Laser Physics and Applications*, vol. 10226, p. 1022603, International Society for Optics and Photonics, 2017.

[80] H. Callebaut and Q. Hu, "Importance of coherence for electron transport in terahertz quantum cascade lasers," *Journal of Applied Physics*, vol. 98, p. 104505, 2005.

[81] G. Lindblad, "On the generators of quantum dynamical semigroups," *Communications in Mathematical Physics*, vol. 48, pp. 119–130, 1976.

[82] B. A. Burnett and B. S. Williams, "Density matrix model for polarons in a terahertz quantum dot cascade laser," *Physical Review B*, vol. 90, p. 155309, 2014.

[83] C. Y. Wang, L. Diehl, A. Gordon, C. Jirauschek, F. X. Kärtner, A. Belyanin, D. Bour, S. Corzine, G. Höfler, M. Troccoli, J. Faist, and F. Capasso, "Coherent instabilities in semiconductor laser with fast gain recovery," *Physical Review A*, vol. 75, p. 031802, 2007.

[84] A. Gordon, C. Y. Wang, L. Diehl, F. X. Kärtner, A. Belyanin, D. Bour, S. Corzine, G. Höfler, H. C. Liu, H. Schneider, T. Maier, M. Troccoli, J. Faist, , and F. Capasso, "Multimode regimes in quantum cascade lasers: From coherent instabilities to spatial hole burning," *Physical Review A*, vol. 77, p. 053804, 2008.

[85] Y. Wang and A. Belyanin, "Active mode-locking of mid-infrared quantum cascade lasers with short gain recovery time," *Optics Express*, vol. 23, pp. 4173–4185, 2015.

[86] S. L. McCall and E. L. Hahn, "Self-induced transparency," *Physical Review*, vol. 183, p. 457, 1969.

[87] H. Risken and K. Nummedal, "Self-Pulsing in Lasers," *Journal of Applied Physics*, vol. 39, p. 4662, 1968.

[88] R. Arkhipov, M. Arkhipov, I. Babushkin, and N. Rosanov, "Self-induced transparency mode locking, and area theorem," *Optics Letters*, vol. 41, p. 737, 2016.

[89] P. Tzenov, "Derivation, discretization and simulation of multiple level Maxwell-Bloch equations for quantum cascade lasers," masters' thesis, Technical University of Munich, 2014.

[90] S. Kohen, B. S. Williams, and Q. Hu, "Electromagnetic modeling of terahertz quantum cascade laser waveguides and resonators," *Journal of Applied Physics*, vol. 97, p. 053106, 2005.

[91] N. Vukovic, J. Radovanovic, V. Milanovic, and D. Boiko, "Multimode RNGH instabilities of Fabry-Pérot cavity QCLs: impact of diffusion," *Optical and Quantum Electronics*, vol. 48, pp. 1–10, 2016.

[92] P. Wesseling, *Principles of Computational Fluid Dynamics*. Springer, 2001.

[93] P. D. Lax and B. Wendroff, "Systems of conservation laws," *Communications on Pure and Applied Mathematics*, vol. 13, p. 217, 1960.

[94] J. C. Tannehill, D. A. Anderson, and R. H. Pletcher, *Computational Fluid Mechanics and Heat Transfer*. Taylor and Fracis, second ed., 1997.

[95] S. K. Godunov, "A difference method for numerical calculation of discontinuous solutions of the equations of hydrodynamics," *Matematicheskii Sbornik*, vol. 89, pp. 271–306, 1959.

[96] S. K. Godunov, *Different Methods for Shock Waves*. PhD thesis, Moscow State University, 1954.

[97] J. C. Butcher, *Numerical Methods for Ordinary Differentail Equations*. John Wiley, 2003.

[98] M. H. Carpenter, D. Gottlieb, and S. Abarbanel, "The stability of numerical boundary treatments for compact high-order finite difference schemes," *Journal of Computational Physics*, vol. 108, p. 272, 1993.

[99] L. N. Trefethen, *Spectral Methods in Matlab*. SIAM - Society for Industrial and Applied Mathematics, 2001.

[100] D. Gottlieb, M. Y. Hussaini, and S. A. Orszag, "Introduction: Theory and Applications of Spectral Methods," *Spectral Methods for Partial Differential Equations, SIAM*, 1984.

[101] "http://de.mathworks.com/help/matlab/ref/ode45.html."

[102] A. Iserles, *A First Course in the Numerical Analysis of Differential Equations*. Cambridge University Press, 1996.

[103] C. W. Gear, *Numerical Initial Value Problems in Ordinary Differential Equations*. Prentice Hall, first ed., 1971.

[104] J. D. Jackson, *Classical electrodynamics*. AAPT, 1999.

[105] F. Bloch, "Nuclear Induction," *Physical Reviews*, vol. 70, pp. 460–474, Oct 1946.

[106] V. A. Alekseev and B. Y. Zel'dovich, "Derivation of the area theorem in self-induced transparency," *Soviet Journal of Quantum Electronics*, vol. 5, no. 5, p. 589, 1975.

[107] Q. Lu, M. Razeghi, S. Slivken, N. Bandyopadhyay, Y. Bai, W. Zhou, M. Chen, D. Heydari, A. Haddadi, R. McClintock, M. Amanti, and C. Sirtori, "High power frequency comb based on mid-infrared quantum cascade laser at $\lambda \sim 9$ μm," *Applied Physics Letters*, vol. 106, p. 051105, 2015.

[108] F. Cappelli, G. Villares, S. Riedi, and J. Faist, "Intrinsic linewidth of quantum cascade laser frequency combs," *Optica*, vol. 2, pp. 836–840, 2015.

[109] J. Ye, *Femtosecond Optical Frequency Comb: Principle, Operation and Applications*. Springer Science & Business Media, 2005.

[110] P. Friedli, H. Sigg, B. Hinkov, A. Hugi, S. Riedi, M. Beck, and J. Faist, "Four-wave mixing in a quantum cascade laser amplifier," *Applied Physics Letters*, vol. 102, p. 222104, 2013.

[111] G. Villares and J. Faist, "Quantum cascade laser combs: effects of modulation and dispersion," *Optics Express*, vol. 23, pp. 1651–1669, 2015.

[112] V.-M. Gkortsas, C. Wang, L. Kuznetsova, L. Diehl, A. Gordon, C. Jirauschek, M. Belkin, A. Belyanin, F. Capasso, and F. Kärtner, "Dynamics of actively mode-locked quantum cascade lasers," *Optics Express*, vol. 18, p. 13616, 2010.

[113] M. A. Talukder and C. R. Menyuk, "Self-induced transparency modelocking of quantum cascade lasers in the presence of saturable nonlinearity and group velocity dispersion," *Optics Express*, vol. 18, pp. 5639–5653, 2010.

[114] P. Tzenov, D. Burghoff, Q. Hu, and C. Jirauschek, "Temporal dynamics of THz quantum cascade laser frequency combs with strong injector anticrossing," in *International Conference and School on Quantum Electronics*, pp. 102260N–102260N, International Society for Optics and Photonics, 2017.

[115] C. Jirauschek, "Accuracy of transfer matrix approaches for solving the effective mass Schrödinger equation," *IEEE Journal of Quantum Electronics*, vol. 45, pp. 1059–1067, 2009.

[116] C. Jirauschek, G. Scarpa, P. Lugli, M. S. Vitiello, and G. Scamarcio, "Comparative analysis of resonant phonon THz quantum cascade lasers," *Journal of Applied Physics*, vol. 101, p. 086109, 2007.

[117] C. Jirauschek and P. Lugli, "Monte-Carlo-based spectral gain analysis for terahertz quantum cascade lasers," *Applied Physics Letters*, 2009.

[118] C. Jirauschek, "Monte Carlo study of intrinsic linewidths in terahertz quantum cascade lasers," *Optics Express*, vol. 18, pp. 25922–25927, 2010.

[119] C. Jirauschek, "Monte Carlo study of carrier-light coupling in terahertz quantum cascade lasers," *Applied Physics Letters*, vol. 96, p. 011103, 2010.

[120] S. Kumar and Q. Hu, "Coherence of resonant-tunneling transport in terahertz quantum-cascade lasers," *Physical Review B*, vol. 80, p. 245316, 2009.

[121] E. Dupont, S. Fathololoumi, and H. Liu, "Simplified density-matrix model applied to three-well terahertz quantum cascade lasers," *Physical Review B*, vol. 81, p. 205311, 2010.

[122] G. Bastard, *Wave Mechanics Applied to Semiconductor Heterostructures*. John Wiley & Sons, 1990.

[123] D. Burghoff, Y. Yang, D. J. Hayton, J.-R. Gao, J. L. Reno, and Q. Hu, "Evaluating the coherence and time-domain profile of quantum cascade laser frequency combs," *Optics Express*, vol. 23, pp. 1190–1202, 2015.

[124] D. P. Burghoff, *Broadband terahertz photonics*. PhD thesis, Massachusetts Institute of Technology, 2014.

[125] N. Jukam, S. Dhillon, Z. Y. Zhao, G. Duerr, J. Armijo, N. Sirmons, S. Hameau, S. Barbieri, P. Filloux, C. Sirtori, X. Marcadet, and J. Tignon, "Gain measurements of THz quantum cascade lasers using THz time-domain spectroscopy," *IEEE Journal of Selected Topics in Quantum Electronincs*, vol. 14, pp. 436–442, 2008.

[126] M. Martl, J. Darmo, C. Deutsch, M. Brandstetter, A. M. Andrews, P. Klang, G. Strasser, and K. Unterrainer, "Gain and losses in THz quantum cascade laser with metal-metal waveguide," *Optics Express*, vol. 19, pp. 733–738, 2011.

[127] R. Graham and H. Haken, "Quantum theory of light propagation in a fluctuating laser-active medium," *Zeitschrift für Physik A*, vol. 213, pp. 420–450, 1968.

[128] G. Villares, S. Riedi, J. Wolf, D. Kazakov, M. J. Süess, P. Jouy, M. Beck, and J. Faist, "Dispersion engineering of quantum cascade laser frequency combs," *Optica*, vol. 3, pp. 252–258, 2016.

[129] R. L. Sutherland, *Handbook of Nonlinear Optics*. CRC press, 2003.

[130] J. Zayhowski, "Limits imposed by spatial hole burning on the single-mode operation of standing-wave laser cavities," *Optics Letters*, vol. 15, pp. 431–433, 1990.

[131] T. Herr, K. Hartinger, J. Riemensberger, C. Wang, E. Gavartin, R. Holzwarth, M. Gorodetsky, and T. Kippenberg, "Universal formation dynamics and noise of Kerr-frequency combs in microresonators," *Nature Photonics*, vol. 6, pp. 480–487, 2012.

[132] J. S. Toll, "Causality and the dispersion relation: logical foundations," *Physical Reviews*, vol. 104, pp. 1760–1770, 1956.

[133] D. Revin, M. Hemingway, Y. Wang, J. Cockburn, and A. Belyanin, "Active mode locking of quantum cascade lasers in an external ring cavity," *Nature Communications*, vol. 7, p. 11440, 2016.

[134] R. Ulbricht, E. Hendry, J. Shan, T. F. Heinz, and M. Bonn, "Carrier dynamics in semiconductors studied with time-resolved terahertz spectroscopy," *Reviews of Modern Physics*, vol. 83, p. 543, 2011.

[135] R. P. Green, A. Tredicucci, N. Q. Vinh, B. Murdin, C. Pidgeon, H. E. Beere, and D. A. Ritchie, "Gain recovery dynamics of a terahertz quantum cascade laser," *Physical Review B*, vol. 80, p. 075303, 2009.

[136] D. R. Bacon, J. R. Freeman, R. A. Mohandas, L. Li, E. H. Linfield, A. G. Davies, and P. Dean, "Gain recovery time in a terahertz quantum cascade laser," *Applied Physics Letters*, vol. 108, p. 081104, 2016.

[137] E. Avrutin, J. Marsh, and E. Portnoi, "Monolithic and multi-gigahertz mode-locked semiconductor lasers: constructions, experiments, models and applications," *IEEE Proceedings-Optoelectronics*, vol. 147, p. 251, 2000.

[138] E. Rafailov, M. Cataluna, W. Sibbett, N. Ilinskaya, Y. M. Zadiranov, A. Zhukov, V. Ustinov, D. Livshits, A. Kovsh, and N. Ledentsov, "High-power picosecond and femtosecond pulse generation from a two-section mode-locked quantum-dot laser," *Applied Physics Letters*, vol. 87, p. 081107, 2005.

[139] E. Rafailov, M. Cataluna, and W. Sibbett, "Mode-locked quantum-dot lasers," *Nature Photonics*, vol. 1, p. 395, 2007.

[140] R. Arkhipov, A. Pimenov, M. Radziunas, D. Rachinskii, A. G. Vladimirov, D. Arsenijević, H. Schmeckebier, and D. Bimberg, "Hybrid mode locking in semiconductor lasers: simulations, analysis, and experiments," *IEEE Journal of Selected Topics in Quantum Electronics*, vol. 19, p. 1100208, 2013.

[141] F. Kärtner, "Instabilities and mode locking of quantum cascade lasers." IQCLSW 2008 Conference, September 14-19, 2008, Ascona, Switzerland, 2008.

[142] M. A. Talukder and C. R. Menyuk, "Quantum coherent saturable absorption for mid-infrared ultra-short pulses," *Optics Express*, vol. 22, p. 15608, 2014.

[143] P. Tzenov, R. Arkhipov, I. Babushkin, O. Sayadi, N. Rosanov, U. Morgner, and C. Jirauschek, "On passive mode locking in THz quantum cascade lasers," in *Lasers and*

Electro-Optics Europe & European Quantum Electronics Conference (CLEO/Europe-EQEC, 2017 Conference on), p. 1, IEEE, 2017.

[144] M. A. Talukder, "Ultra-short pulses from quantum cascade lasers for terahertz time domain spectroscopy," in *Image Sensing Technologies: Materials, Devices, Systems, and Applications IV*, vol. 10209, p. 1020906, International Society for Optics and Photonics, 2017.

[145] H. A. Haus, "Theory of mode locking with a fast saturable absorber," *Journal of Applied Physics*, vol. 46, p. 3049, 1975.

[146] P. Gellie, S. Barbieri, J.-F. Lampin, P. Filloux, C. Manquest, C. Sirtori, I. Sagnes, S. P. Khanna, E. H. Linfield, A. G. Davies, H. Beere, , and D. Ritchie, "Injection-locking of terahertz quantum cascade lasers up to 35 GHz using RF amplitude modulation," *Optics Express*, vol. 18, p. 20799, 2010.

[147] P. Tzenov, I. Babushkin, R. Arkhipov, M. Arkhipov, N. Rosanov, U. Morgner, and C. Jirauschek, "Passive and hybrid mode locking in multi-section terahertz quantum cascade lasers," *New Journal of Physics*, vol. 20, no. 5, p. 053055, 2018.

[148] G. New, "Pulse evolution in mode-locked quasi-continuous lasers," *IEEE Journal of Quantum Electronics*, vol. 10, p. 115, 1974.

[149] C. R. Menyuk and M. A. Talukder, "Self-induced transparency modelocking of quantum cascade lasers," *Physical Review Letters*, vol. 102, p. 023903, 2009.

[150] R. M. Arkhipov, M. Arkhipov, and I. Babushkin, "On coherent mode-locking in a two-section laser," *JETP Letters*, vol. 101, p. 149, 2015.

[151] R. Arkhipov, M. Arkhipov, and I. Babushkin, "Self-starting stable coherent mode-locking in a two-section laser," *Optics Communications*, vol. 361, p. 73, 2016.

[152] B. Schwarz, P. Reininger, D. Ristanić, H. Detz, A. M. Andrews, W. Schrenk, and G. Strasser, "Monolithically integrated mid-infrared lab-on-a-chip using plasmonics and quantum cascade structures," *Nature Communications*, vol. 5, p. 4085, 2014.

[153] S. Barbieri, J. Alton, H. E. Beere, J. Fowler, E. H. Linfield, and D. A. Ritchie, "2.9 THz quantum cascade lasers operating up to 70 K in continuous wave," *Applied Physics Letters*, vol. 85, p. 1674, 2004.

[154] R. Köhler, A. Tredicucci, F. Beltram, H. E. Beere, E. H. Linfield, A. G. Davies, D. A. Ritchie, R. C. Iotti, and F. Rossi, "Terahertz semiconductor-heterostructure laser," *Nature*, vol. 417, p. 156, 2002.

[155] M. A. Talukder, "Modeling of gain recovery of quantum cascade lasers," *Journal of Applied Physics*, vol. 109, p. 033104, 2011.

[156] L. R. Brovelli, D. Kopf, and M. Kamp, "Control of solid state laser dynamics by," *Optical Engineering*, vol. 34, p. 2024, 1995.

[157] Y.-K. Chen and M. C. Wu, "Monolithic colliding-pulse mode-locked quantum-well lasers," *IEEE Journal of Quantum Electronics*, vol. 28, p. 2176, 1992.

[158] I.-C. Benea-Chelmus, M. Rösch, G. Scalari, M. Beck, and J. Faist, "Intensity autocorrelation measurements of frequency combs in the terahertz range," *Physical Review A*, vol. 96, p. 033821, 2017.

[159] G. Sonnabend, D. Wirtz, and R. Schieder, "Evaluation of quantum-cascade lasers as local oscillators for infrared heterodyne spectroscopy," *Applied Optics*, vol. 44, p. 7170, 2005.

[160] G. Fiol, D. Arsenijević, D. Bimberg, A. Vladimirov, M. Wolfrum, E. Viktorov, and P. Mandel, "Hybrid mode-locking in a 40 GHz monolithic quantum dot laser," *Applied Physics Letters*, vol. 96, p. 011104, 2010.

[161] D. J. Derickson, P. Morton, J. Bowers, and R. Thornton, "Comparison of timing jitter in external and monolithic cavity mode-locked semiconductor lasers," *Applied Physics Letters*, vol. 59, p. 3372, 1991.

[162] M. Thompson, C. Marinelli, K. Tan, K. Williams, R. Penty, I. White, I. Kaiander, R. Sellin, D. Bimberg, D.-J. Kang, *et al.*, "10 GHz hybrid modelocking of monolithic InGaAs quantum dot lasers," *Electronics Letters*, vol. 39, p. 1121, 2003.

[163] C. Jirauschek, H. Okeil, and P. Lugli, "Monte Carlo analysis of the terahertz difference frequency generation susceptibility in quantum cascade laser structures," *Optics Express*, vol. 23, pp. 1670–1678, 2015.

[164] J. S. Roychowdhury, A. R. Newton, and D. O. Pederson, "Algorithms for the transient simulation of lossy interconnect," *IEEE Transactions on Computer-aided Design of Integrated Circuits and Systems*, vol. 13, pp. 96–104, 1994.

[165] S. D. Gedney, "Introduction to the finite-difference time-domain (FDTD) method for electromagnetics," *Synthesis Lectures on Computational Electromagnetics*, vol. 6, pp. 1–250, 2011.

[166] K.-J. Boller, A. Imamoglu, and S. E. Harris, "Observation of electromagnetically induced transparency," *Physical Review Letters*, vol. 66, p. 2593, 1991.

[167] A. Kasapi, M. Jain, G. Yin, and S. E. Harris, "Electromagnetically induced transparency: propagation dynamics," *Physical Review Letters*, vol. 74, p. 2447, 1995.

[168] M. Fleischhauer, A. Imamoglu, and J. P. Marangos, "Electromagnetically induced transparency: Optics in coherent media," *Reviews of Modern Physics*, vol. 77, p. 633, 2005.

[169] L. V. Hau, S. E. Harris, Z. Dutton, and C. H. Behroozi, "Light speed reduction to 17 metres per second in an ultracold atomic gas," *Nature*, vol. 397, pp. 594–598, 1999.

[170] J. B. Khurgin, "Optical buffers based on slow light in electromagnetically induced transparent media and coupled resonator structures: comparative analysis," *JOSA B*, vol. 22, pp. 1062–1074, 2005.

[171] R. M. Camacho, C. J. Broadbent, I. Ali-Khan, and J. C. Howell, "All-optical delay of images using slow light," *Physical Review Letters*, vol. 98, p. 043902, 2007.

[172] O. Firstenberg, M. Shuker, N. Davidson, and A. Ron, "Elimination of the diffraction of arbitrary images imprinted on slow light," *Physical Review Letters*, vol. 102, p. 043601, 2009.

[173] M. Lukin, "Colloquium: Trapping and manipulating photon states in atomic ensembles," *Reviews of Modern Physics*, vol. 75, p. 457, 2003.

[174] B. Wu, J. F. Hulbert, E. J. Lunt, K. Hurd, A. R. Hawkins, and H. Schmidt, "Slow light on a chip via atomic quantum state control," *Nature Photonics*, vol. 4, pp. 776–779, 2010.

[175] A. Turukhin, V. Sudarshanam, M. Shahriar, J. Musser, B. Ham, and P. Hemmer, "Observation of ultraslow and stored light pulses in a solid," *Physical Review Letters*, vol. 88, p. 023602, 2001.

[176] J. B. Khurgin, "Slow light in various media: a tutorial," *Advances in Optics and Photonics*, vol. 2, pp. 287–318, 2010.

[177] P. Ginzburg and M. Orenstein, "Slow light and voltage control of group velocity in resonantly coupled quantum wells," *Optics Express*, vol. 14, pp. 12467–12472, 2006.

[178] H. Borges, L. Sanz, J. Villas-Bôas, O. D. Neto, and A. Alcalde, "Tunneling induced transparency and slow light in quantum dot molecules," *Physical Review B*, vol. 85, p. 115425, 2012.

[179] J. Faist, F. Capasso, C. Sirtori, K. W. West, and L. Pfeiffer, "Controlling the sign of quantum interference by tunnelling from quantum wells," *Nature*, vol. 390, pp. 589–591, 1997.

[180] H. Schmidt, K. Campman, A. Gossard, and A. Imamoglu, "Tunneling induced transparency: Fano interference in intersubband transitions," *Applied Physics Letters*, vol. 70, pp. 3455–3457, 1997.

[181] D. Sun and P.-C. Ku, "Slow light using P-doped semiconductor heterostructures for high-bandwidth nonlinear signal processing," *Journal of Lightwave Technology*, vol. 26, pp. 3811–3817, 2008.

[182] O. Kocharovskaya, P. Mandel, and Y. Radeonychev, "Inversionless amplification in a three-level medium," *Physical Review A*, vol. 45, p. 1997, 1992.

[183] Y. Ren, R. Wallis, Y. Shah, D. Jessop, R. Degl'Innocenti, A. Klimont, V. Kamboj, H. Beere, and D. Ritchie, "Single mode terahertz quantum cascade amplifier," *Applied Physics Letters*, vol. 105, p. 141102, 2014.

[184] B. Glauber, P. Tzenov, and C. Jirauschek, "Slow light via tunneling induced transparency in quantum well heterostructures," in *The European Conference on Lasers and Electro-Optics*, p. CD_P_41, Optical Society of America, 2017.

[185] M. Piccardo, P. Chevalier, T. S. Mansuripur, D. Kazakov, Y. Wang, N. A. Rubin, L. Meadowcroft, A. Belyanin, and F. Capasso, "The harmonic state of quantum cascade lasers: origin, control, and prospective applications," *Optics express*, vol. 26, no. 8, pp. 9464–9483, 2018.

[186] P. Dean, Y. L. Lim, A. Valavanis, R. Kliese, M. Nikolić, S. P. Khanna, M. Lachab, D. Indjin, Z. Ikonić, P. Harrison, A. D. Rakić, E. H. Linfield, and A. G. Davies, "Terahertz imaging through self-mixing in a quantum cascade laser," *Optics Letters*, vol. 36, pp. 2587–2589, Jul 2011.